INSTITUTE OF PHYSICS PUBLISHING REPORTS ON PROGRESS IN PHYSICS

Rep. Prog. Phys. **68** (2005) 577–683 doi:10.1088/0034-4885/68/3/R03

Non-linear dynamics of semiconductor superlattices

Luis L Bonilla[1,3] **and Holger T Grahn**[2]

[1] Escuela Politécnica Superior, Universidad Carlos III de Madrid,
Avenida de la Universidad 30, 28911 Leganés, Spain
[2] Paul-Drude-Institut für Festkörperelektronik, Hausvogteiplatz 5–7, 10117 Berlin, Germany

E-mail: bonilla@ing.uc3m.es

Received 29 October 2004
Published 8 February 2005
Online at stacks.iop.org/RoPP/68/577

Abstract

In the last decade, non-linear dynamical transport in semiconductor superlattices (SLs) has witnessed significant progress in theoretical descriptions as well as in experimentally observed non-linear phenomena. However, until now, a clear distinction between non-linear transport in *strongly* and *weakly coupled* SLs was missing, although it is necessary to provide a detailed description of the observed phenomena. In this review, strongly coupled SLs are described by spatially continuous equations and display self-sustained current oscillations due to the periodic motion of a charge dipole as in the Gunn effect for bulk semiconductors. In contrast, weakly coupled SLs have to be described by spatially discrete equations. Therefore, weakly coupled SLs exhibit a more complex dynamical behaviour than strongly coupled ones, which includes the formation of stationary electric field domains, pinning or propagation of domain walls consisting of a charge monopole, switching between stationary domains, self-sustained current oscillations due to the recycling motion of a charge monopole and chaos. This review summarizes the existing theories and the experimentally observed non-linear phenomena for both types of semiconductor SLs.

---

[3] Author to whom any correspondence should be addressed.

0034-4885/05/030577+107$90.00

Contents

1. Introduction

In 1970, Esaki and Tsu [1] invented an artificial crystal, which they called a semiconductor superlattice (SL), in order to develop a device that exhibits Bloch oscillations. A SL in its simplest form contains a large number of periods, with each period consisting of at least two layers, which are semiconductors or insulators with different energy gaps, but with similar lattice constants, e.g. GaAs and AlAs. These SLs are synthesized by molecular-beam epitaxy or related epitaxial growth techniques in the vertical direction [2]. The conduction band edge of an infinitely long ideal SL is modulated so that in the vertical direction it looks like a one-dimensional crystal, which is formed by a periodic succession of a quantum well (GaAs) and a barrier (AlAs). An electron inside the SL subject to a constant electric field F can perform Bloch oscillations with frequency $\omega_{\mathrm{B}} = eFl/\hbar$, where l denotes the SL period, e the elementary charge and $\hbar$ Planck's constant. These coherent Bloch oscillations can be observed, if their frequency is larger than the inverse scattering time (of the order of picoseconds) which yields experimentally achievable electric-field strengths of 10^4–10^5 V cm^{-1} for an SL period $l = 10$ nm [3]. While the original idea by Esaki and Tsu [1] was to devise a Bloch oscillator based on a strongly coupled SL, which exhibits wave functions that are extended over many periods, it took more than 20 years to demonstrate the existence of Bloch oscillations in SLs [4]. This happened because a lot of the initial research on SLs including the early experimental work of Esaki and Chang [5] was actually performed on weakly coupled SLs. In this type of SL, the wave function extends at most over two adjacent wells, and the transport through the SL is dominated by sequential resonant tunnelling [6] and not by miniband transport [7] as in strongly coupled SLs. Many early experiments on these weakly coupled SLs indicated the existence of interesting non-linear phenomena. Typical experiments of vertical charge transport use an undoped or doped SL of finite length placed in the central part of a diode (forming a p–i–n or n^+–n–n^+ structure) with respective contacts at either end of the diode. Depending on the bias condition, the SL configuration, the doping density, the temperature or other control parameters, the current through the SL and the electric field distribution inside the SL display a great variety of non-linear phenomena such as pattern formation, current self-oscillations and chaotic behaviour.

To describe and understand non-linear charge transport in SLs, it is essential to distinguish between *weakly coupled* and *strongly coupled* SLs. Weakly coupled SLs contain rather thick barriers separating the SL quantum wells, i.e. the barrier width is much larger than the typical electron wavelength inside the barrier. Therefore, a description of the electronic properties of weakly coupled SLs can be based on the subband structure of the corresponding isolated quantum well together with resonant tunnelling across the barrier of two adjacent wells. In contrast, the quantum wells of strongly coupled SLs are separated by thin barriers so that the electronic properties of strongly coupled SLs can be described in terms of extended states such as Bloch functions. The simplest mathematical models applied to a SL give rise to balance equations involving mesoscopic quantities such as the electric field, the electron density and the drift velocity. The task of deriving these equations from first principles is far from being completed. In this review, we shall summarize the current situation and point out what needs to be done to carry out the necessary first-principle derivations. However, our main task is to describe and study the non-linear dynamics of the charge and field distribution in SLs in terms of tractable models. In dealing with non-linear phenomena, deriving equations in poorly understood limiting cases is often less useful than understanding the qualitative behaviour of different models and the phenomena that can be described by their governing equations.

A fundamental difference between weakly and strongly coupled SLs is that the former are governed by *spatially discrete* balance equations, whereas the latter are governed by *spatially* *continuous* equations. Both types of equations may have solutions whose electric field profiles display regions of high electric field coexisting with regions of low electric field. The resulting dynamical behaviour is very different for these two types of equations. For strongly coupled SLs, which are described by continuous balance equations, the field profile consists of a charge dipole moving with the flow of electrons, which resembles closely the Gunn effect in bulk semiconductors [8]. Under dc voltage bias, this basic motion results in self-sustained oscillations of the current through the SL due to the periodic movement of dipole domains. In contrast, in weakly coupled SLs, which are described by discrete balance equations, electric-field domains (EFDs) are separated by a domain wall, which consists of a charge monopole. The domain wall in a weakly coupled SL may move with or opposite to the electron flow or is pinned, depending on the value of the current [9]. This pinning of the domain wall occurs only in the discrete models. Under dc voltage bias, the non-linear behaviour of a weakly coupled SL is more complex than for strongly coupled SLs: formation of stationary EFDs, multistability of the current–voltage characteristics, current self-oscillations and high-frequency spikes due to discreteness effects. Pinning of domain walls in weakly coupled SLs for values of the current in certain intervals explains the periodic structure of the conductance in highly doped, weakly coupled SLs, which was initially observed by Esaki and Chang [5], and the current–voltage characteristics containing as many current branches as periods in the SL [10]. In the continuum limit described by continuous balance equations, the pinning interval shrinks to a point or completely disappears. Domain walls, which are wave front solutions of spatially discrete models, also occur in very different physical systems such as dislocations [11, 12], crack propagation and friction in solids [13] and propagation of nerve impulses along myelinated fibres [14].

Previously published reviews on this subject covered the theory of electric transport in SLs discussing miniband conduction, Wannier–Stark hopping, and sequential tunnelling, their relation to each other and a comparison with a quantum transport model based on non-equilibrium Green's functions [15]. Moreover, this work reviewed the occurrence of inhomogeneous electric field distributions, yielding either a characteristic sawtooth shape of the current–voltage characteristic or self-sustained current oscillations, and the effect of an additional ac-voltage in the terahertz range, demonstrating the existence of absolute negative conductance, photon-assisted tunnelling, the possibility of gain and a negative tunnelling capacitance. Another review, which appeared about the same time, presented the theory of non-linear charge transport, wave propagation and self-oscillations in weakly coupled SLs modelled by discrete equations and boundary conditions [16]. The focus of this work was the formation of EFDs, pinning or propagation of domain walls, self-sustained oscillations of the current and chaos. More recently, a review on photon-assisted transport in semiconductor nanostructures has appeared, which focuses on electronic transport through semiconductor nanostructures driven by ac fields [17]. This work includes the available experimental information on different nanostructures, such as resonant tunnelling diodes, SLs or quantum dots, together with different theoretical techniques used in the study of photon-assisted transport. The present review differs from the previous ones since it presents both theoretical and experimental results with similar weight and covers both weakly and strongly coupled SLs.

2. Vertical transport

2.1. General theoretical approach

Let us consider an n-doped SL formed by periodic alternation of two different semiconductors such as GaAs (quantum well, W) and AlAs (barrier, B). The SL cross section, S, is much larger than l^2, the square of the SL period. For n-doped SLs, we can restrict ourselves to studying electronic transport in the conduction band of the SL. We shall assume that the SL is under a dc voltage bias, which is equivalent to an external electric field directed along the SL growth direction. The corresponding Hamiltonian is

$$H = H_0 + H_{\text{e–e}} + H_{\text{sc}}. \tag{1}$$

We have separated the electron–electron interaction, $H_{\text{e–e}}$, and other scattering processes (impurity, phonon, etc), H_{sc}, from the one-electron Hamiltonian, H_0. Typically, the electron–electron interaction is treated in the Hartree approximation. Then we can find the spectrum of the Hamiltonian $H_0 + H_{\text{e–e}}$ by solving a non-linear stationary Schrödinger–Poisson system of equations. Their solutions yield a basis in which quantum kinetic equations describing the scattering processes out of equilibrium can be written, as shown below. The envelope wave function is [18]

$$\varphi_\nu(\boldsymbol{x},\boldsymbol{k}) \equiv \varphi_\nu(x,\boldsymbol{x}_\perp,k,\boldsymbol{k}_\perp) = \frac{1}{\sqrt{S}}\,\mathrm{e}^{\mathrm{i}\boldsymbol{k}_\perp\cdot\boldsymbol{x}_\perp}\varphi_\nu(x,k,\boldsymbol{k}_\perp). \tag{2}$$

At zero external field, φ_ν satisfies

$$\left[\mathcal{E}_{\text{c}} + V_{\text{c}}(x) - eW(x) - \frac{\hbar^2}{2}\frac{\partial}{\partial x}\frac{1}{m(x)}\frac{\partial}{\partial x} + \frac{\hbar^2\boldsymbol{k}_\perp^2}{2\,m(x)}\right]\varphi_\nu = \mathcal{E}_\nu(\boldsymbol{k})\,\varphi_\nu, \tag{3}$$

$$\varepsilon(x)\frac{\partial^2 W}{\partial x^2} = e[n_0 - N_{3\text{D}}(x)]. \tag{4}$$

Here $-e$ is the charge of the electron, $\mathcal{E}_{\text{c}}$ is the conduction band edge of material W (GaAs, well), $l = d_{\text{B}} + d_{\text{W}}$ is the SL period, $W(x)$ is the electric potential due to the electron–electron interaction, $N_{3\text{D}}(x) = N_{\text{D}}/l$ is the three-dimensional doping density (N_{D} is the two-dimensional doping density) and

$$m(x) = \begin{cases} m_{\text{W}} & \text{if } x \text{ corresponds to a quantum well W,} \\ m_{\text{B}} & \text{if } x \text{ corresponds to a barrier B,} \end{cases} \tag{5}$$

$$\varepsilon(x) = \begin{cases} \varepsilon_{\text{W}} & \text{if } x \text{ corresponds to a quantum well W,} \\ \varepsilon_{\text{B}} & \text{if } x \text{ corresponds to a barrier B} \end{cases} \tag{6}$$

are the masses and permittivities of the well and barrier. If V_{c} corresponds to the conduction-band offset between the well and barrier material, we have

$$V_{\text{c}}(x) = \begin{cases} 0 & \text{if } x \text{ corresponds to a quantum well W,} \\ V_{\text{c}} & \text{if } x \text{ corresponds to a barrier B.} \end{cases} \tag{7}$$

Moreover, the three-dimensional equilibrium electron density is

$$n_0(x) = \frac{1}{Sl}\sum_{\nu,k,\boldsymbol{k}_\perp} |\varphi_\nu(x,k,\boldsymbol{k}_\perp)|^2 n_{\text{F}}(\nu,k,\boldsymbol{k}_\perp), \tag{8}$$

where n_{F} denotes the Fermi function of the miniband ν. The boundary conditions at the well–barrier interfaces are that φ_ν and $m(x)^{-1}\partial\varphi_\nu/\partial x$ are both continuous. The electronic spectrum is continuous, consisting of *minibands* of energies $\mathcal{E}_\nu(k;\boldsymbol{k}_\perp)$ with $\nu = 1, 2, 3, \ldots$ (doubly degenerate because of spin) with an associated basis of spatially extended Bloch wave functions $\varphi_\nu(x,k;\boldsymbol{k}_\perp) = \mathrm{e}^{\mathrm{i}kx}u_\nu(x,k;\boldsymbol{k}_\perp)$ [18]. A more complete discussion of electronic states in SLs can be found in the book by Bastard [18].

Although we can discuss the effects of scattering using the previous basis of electronic states that solve a non-linear Schrödinger–Poisson system, we will for simplicity ignore the difference in mass and permittivity between barriers and wells and assume that the doping density is uniform. Then the model (equations (3)–(7)) becomes the Kronig–Penney model with $m_{\mathrm{W}} = m_{\mathrm{B}} = m^*$, $\varepsilon_{\mathrm{W}} = \varepsilon_{\mathrm{B}} = \varepsilon$ and $N_{3\mathrm{D}}(x) = N_{3\mathrm{D}}$ (constant). The Schrödinger–Poisson problem is simply $[H_0 - \mathcal{E}_\nu(\boldsymbol{k})]\varphi_\nu(\boldsymbol{x}, \boldsymbol{k}) = 0$ with $n_0 = N_{3\mathrm{D}}$, and its solutions have the form

$$\varphi_\nu(\boldsymbol{x}, \boldsymbol{k}) = \frac{1}{\sqrt{S}}\, \mathrm{e}^{\mathrm{i}\boldsymbol{k}_\perp \cdot \boldsymbol{x}_\perp} \varphi_\nu(x, k), \qquad \mathcal{E}_\nu(\boldsymbol{k}) = \frac{\hbar^2 \boldsymbol{k}_\perp^2}{2m^*} + \mathcal{E}_\nu(k). \tag{9}$$

The Bloch functions are $2\pi/l$-periodic in k, satisfying the orthogonality condition

$$\int_{-\infty}^{\infty} \varphi_\mu^*(x, k)\varphi_\nu(x, k')\, \mathrm{d}x = \delta_{\mu\nu}\delta(k - k') \tag{10}$$

and the closure condition

$$\int_{-\infty}^{\infty} \varphi_\mu^*(x, k)\varphi_\nu(x', k)\, \mathrm{d}k = \delta_{\mu\nu}\delta(x - x'), \tag{11}$$

provided the integral of $|\varphi_\nu|^2$ over one SL period is unity. Equivalently, a basis of orthogonal Wannier functions, each localized in a different quantum well, can be constructed from Bloch states with different wavenumbers [19, 20]. The Wannier function localized in the mth SL period is $\chi_\nu(x - ml)$, in which

$$\chi_\nu(x) = \frac{l}{2\pi} \int_{-\pi/l}^{\pi/l} \varphi_\nu(x, k)\, \mathrm{d}k \tag{12}$$

is the zeroth harmonic in the Fourier series of the Bloch function considered as a function of k. The orthogonality property is

$$\int_{-\infty}^{\infty} \chi_\mu^*(x - rl)\chi_\nu(x - sl)\, \mathrm{d}x = \delta_{\mu\nu}\delta_{rs}. \tag{13}$$

For weakly coupled SLs, the subbands of an isolated quantum well provide a convenient set of basic states, which approximate properly constructed Wannier functions [20], and it is used in sequential tunnelling theories as a useful alternative.

In the particular case of a non-zero constant applied electric field $E = -F$ (we prefer to write our equations in terms of $F = \partial W/\partial x$, which is the *negative* of the electric field, instead of the proper electric field, $E = -\partial W/\partial x$), the periodic part of the potential energy, $-eFx$, can be included in the periodic potential, $V_{\mathrm{c}}(x)$, and the solutions of the stationary Schrödinger equation are field-dependent Bloch or Wannier states. In this case, a third set of electron states, the *Wannier–Stark* (WS) states, is obtained from either the Bloch or the Wannier basis. The key observation to find them is that a wave function $\Phi_0(x)$ with energy E_0 generates a set of states $\Phi_0(x - jl)$ with energies $E_0 - jeFl$ (note that l denotes the SL period). Then, an infinite ladder of states is formed for each bound state of a single quantum well. This periodic energy spectrum is usually referred to as the *WS ladder*. The WS wave functions extend over several SL periods if the WS levels of neighbouring wells are in resonance. In this case, the electrons can tunnel between adjacent wells and spread coherently over a certain distance Λ. The condition for coherent tunnelling between two wells separated by a distance jl is $jeFl < \Delta$, in which the miniband width, Δ, gives a measure of the energetic broadening of the basic quantum well state. Then $\Lambda = jl = \Delta/(eF)$. Thus, the WS states become extended over the whole SL for vanishing fields (the same as for zero-field Bloch functions), whereas they become localized in one well if $eFl > \Delta$.

Scattering different from electron–electron scattering is usually treated by writing equations for the density matrix [21, 22], its Wigner transform [23–25] or the non-equilibrium Green's function (NGF) [15, 26, 27]. Whatever the chosen formulation, the equations for the one-electron functions depend on two-electron and higher functions, and we have the usual infinite hierarchy of coupled equations, which is well known in classical kinetic theory. Typically, the hierarchy is closed by assuming some dependence of the two-electron functions on one-electron functions, which is suggested by perturbation theory in the limit of weak scattering [27]. Assuming weak scattering, the differences between the equations corresponding to the different formulations are small. The trouble is that the kinetic equations are often used in the opposite *hydrodynamic* limit, in which collisions due to scattering are dominant. Then the results of using different formalisms are not equivalent, which has resulted in some discussion and confusion. In this review, we shall not discuss the difference between formulations in a precise way. Instead, we shall write kinetic equations for the one-electron matrix density or Wigner function, leaving unspecified the collision terms as much as we can, and discuss how to obtain reduced theories for electric field, electron density and current and so on. These theories are easier to analyse and to solve numerically, and they are the ones commonly used to understand non-linear phenomena in SLs.

To find a kinetic equation, we start writing equations for the coefficients $a_{\nu,\boldsymbol{k}}(t)$ in the expansion of the wave function

$$\psi(\boldsymbol{x},t) = \sum_{\nu,\boldsymbol{k}} a_{\nu,\boldsymbol{k}}(t)\varphi_\nu(\boldsymbol{x},\boldsymbol{k}) \equiv \sum_\nu \psi_\nu(\boldsymbol{x},t). \tag{14}$$

If we ignore the scattering term H_{sc} in equation (1), the coefficients $a_{\nu,\boldsymbol{k}}(t)$ become

$$\mathrm{i}\hbar\frac{\partial}{\partial t}a_{\nu,\boldsymbol{k}} = \mathcal{E}_\nu(\boldsymbol{k})a_{\nu,\boldsymbol{k}} - e\sum_{\nu',\boldsymbol{k}'}\langle\nu\boldsymbol{k}|W|\nu'\boldsymbol{k}'\rangle a_{\nu',\boldsymbol{k}'}. \tag{15}$$

The equations for the *band wave functions* ψ_ν of equation (14) can be obtained from this equation after some algebra:

$$\begin{aligned}\mathrm{i}\hbar\frac{\partial}{\partial t}\psi_\nu = &-\frac{\hbar^2}{2m^*}\frac{\partial^2}{\partial\boldsymbol{x}_\perp^2}\psi_\nu + \sum_{m=-\infty}^{\infty}E_\nu(m)\psi_\nu(x+ml,\boldsymbol{x}_\perp,t)\\ &- e\sum_{\nu'}\int\Phi_\nu(\boldsymbol{x},\boldsymbol{x}')W(\boldsymbol{x}')\psi_{\nu'}(\boldsymbol{x}',t)\,\mathrm{d}\boldsymbol{x}',\end{aligned} \tag{16}$$

$$\Phi_\nu(\boldsymbol{x},\boldsymbol{x}') = \sum_{\boldsymbol{k}}\varphi_\nu(\boldsymbol{x},\boldsymbol{k})\varphi_\nu^*(\boldsymbol{x}',\boldsymbol{k}), \tag{17}$$

$$\mathcal{E}_\nu(k) = \sum_{m=-\infty}^{\infty}E_\nu(m)\,\mathrm{e}^{\mathrm{i}mkl}. \tag{18}$$

Note that equation (2) implies

$$\begin{aligned}\Phi_\nu(\boldsymbol{x},\boldsymbol{x}') &= \delta(\boldsymbol{x}_\perp-\boldsymbol{x}'_\perp)\phi_\nu(x,x'),\\ \phi_\nu(x,x') &= \sum_k\varphi_\nu(x,k)\varphi_\nu^*(x',k)\end{aligned} \tag{19}$$

and the closure condition in equation (11) yields

$$\sum_\nu\Phi_\nu(\boldsymbol{x},\boldsymbol{x}') = \delta(\boldsymbol{x}-\boldsymbol{x}'). \tag{20}$$

Thus $\Phi_\nu(\boldsymbol{x},\boldsymbol{x}')$ can be considered as the projection of the delta function $\delta(\boldsymbol{x}-\boldsymbol{x}')$ onto the band ν.

After second quantization, the band density matrix is defined by

$$\rho_{\mu,\nu}(\boldsymbol{x},\boldsymbol{y},t) = \langle\psi_\mu^\dagger(\boldsymbol{x},t)\psi_\nu(\boldsymbol{y},t)\rangle, \tag{21}$$

so that the two-dimensional electron density is (the factor 2 is due to spin degeneracy)

$$n(\boldsymbol{x}, t) = 2l \sum_{\mu,\nu} \langle \psi_\mu^\dagger(\boldsymbol{x}, t)\psi_\nu(\boldsymbol{x}, t)\rangle = 2l \sum_{\mu,\nu} \rho_{\mu,\nu}(\boldsymbol{x}, \boldsymbol{x}, t). \tag{22}$$

Using equations (21) and (22), we can derive the following evolution equation for the band density matrix

$$\begin{aligned}
\mathrm{i}\hbar\frac{\partial}{\partial t}\rho_{\mu,\nu} &+ \frac{\hbar^2}{2m^*}\left(\frac{\partial^2}{\partial \boldsymbol{y}_\perp^2} - \frac{\partial^2}{\partial \boldsymbol{x}_\perp^2}\right)\rho_{\mu,\nu} \\
&- \sum_{m=-\infty}^{\infty} [E_\nu(m)\rho_{\mu,\nu}(\boldsymbol{x}, y + ml, \boldsymbol{y}_\perp, t) - E_\mu(m)\rho_{\mu,\nu}(x - ml, \boldsymbol{x}_\perp, \boldsymbol{y}, t)] \\
&+ e\sum_{\nu'}\int W(z)[\Phi_\nu(\boldsymbol{y}, z)\rho_{\mu\nu'}(\boldsymbol{x}, z, t) - \Phi_\mu(z, \boldsymbol{x})\rho_{\nu'\nu}(z, \boldsymbol{y}, t)] = Q[\rho],
\end{aligned} \tag{23}$$

with $Q[\rho] \equiv 0$ in the absence of scattering. The Hartree potential satisfies the Poisson equation

$$\varepsilon\frac{\partial^2 W}{\partial x^2} = \frac{e}{l}\,(n - N_\mathrm{D}). \tag{24}$$

When considering scattering, the right-hand side of equation (23) is equal to a non-zero functional of the band density matrix $Q[\rho]$, whose form depends on the closure assumption we have made to close the density matrix hierarchy. In the semiclassical limit, the kernel of the collision term $Q[\rho]$ is usually found by using leading order perturbation theory in the impurity potential, electron–phonon interaction, etc. For the time being, we shall not try to formulate collision models. Instead and in order to make contact with the kinetic equations in the semiclassical limit, we shall rewrite equation (23) in terms of the band Wigner function

$$w_{\mu,\nu}(\boldsymbol{x}, \boldsymbol{k}, t) = \int \rho_{\mu,\nu}\left(\boldsymbol{x} + \frac{1}{2}\boldsymbol{\xi}, \boldsymbol{x} - \frac{1}{2}\boldsymbol{\xi}, t\right)\mathrm{e}^{\mathrm{i}\boldsymbol{k}\cdot\boldsymbol{\xi}}\,\mathrm{d}\boldsymbol{\xi}. \tag{25}$$

The symmetry properties of the density matrix imply that the Wigner matrix is Hermitian,

$$w_{\mu,\nu}^*(\boldsymbol{x}, \boldsymbol{k}, t) = w_{\nu,\mu}(\boldsymbol{x}, \boldsymbol{k}, t). \tag{26}$$

The evolution equation for the Wigner function is

$$\begin{aligned}
\frac{\partial}{\partial t}w_{\mu,\nu} &+ \frac{\hbar\boldsymbol{k}_\perp}{m^*}\frac{\partial}{\partial \boldsymbol{x}_\perp}w_{\mu,\nu} + \frac{\mathrm{i}}{\hbar}\sum_{m=-\infty}^{\infty}\mathrm{e}^{\mathrm{i}mkl}\left[E_\nu(m)w_{\mu,\nu}\left(x + \frac{ml}{2}, \boldsymbol{x}_\perp, \boldsymbol{k}, t\right)\right. \\
&\left. - E_\mu(m)w_{\mu,\nu}\left(x - \frac{ml}{2}, \boldsymbol{x}_\perp, \boldsymbol{k}, t\right)\right] + \frac{\mathrm{i}e}{\hbar}\sum_{\nu'}\int\left[W\left(z + \frac{1}{2\mathrm{i}}\frac{\partial}{\partial k}, \boldsymbol{x}_\perp\right)\right. \\
&\times\phi_\mu(z, x)\,\mathrm{e}^{\mathrm{i}k(x-z)}w_{\nu',\nu}\left(\frac{x+z}{2}, \boldsymbol{x}_\perp, \boldsymbol{k}, t\right) - W\left(z - \frac{1}{2\mathrm{i}}\frac{\partial}{\partial k}, \boldsymbol{x}_\perp\right) \\
&\left.\times\phi_\nu(x, z)\,\mathrm{e}^{-\mathrm{i}k(x-z)}w_{\mu,\nu'}\left(\frac{x+z}{2}, \boldsymbol{x}_\perp, \boldsymbol{k}, t\right)\right]\mathrm{d}z = Q_{\mu,\nu}[w]
\end{aligned} \tag{27}$$

in which the collision term is again left unspecified. Note that the two-dimensional electron density is

$$n(\boldsymbol{x}, t) = \frac{2l}{8\pi^3}\sum_{\mu,\nu}\int w_{\mu,\nu}(\boldsymbol{x}, \boldsymbol{k}, t)\,\mathrm{d}\boldsymbol{k} \tag{28}$$

because of equation (22) and the definition in equation (25). From equations (27) and (28), we obtain the charge continuity equation,

$$\frac{e}{l}\frac{\partial n}{\partial t}+\frac{\partial}{\partial \boldsymbol{x}}\cdot\boldsymbol{J}=0, \tag{29}$$

$$\boldsymbol{J}_\perp=\frac{2e}{8\pi^3}\int\frac{\hbar\boldsymbol{k}_\perp}{m^*}\sum_{\mu,\nu}w_{\mu,\nu}(\boldsymbol{x},\boldsymbol{k},t)\,\mathrm{d}\boldsymbol{k}, \tag{30}$$

$$\begin{aligned}\frac{\partial J}{\partial x}=\frac{\mathrm{i}e}{4\pi^3\hbar}\sum_{\mu,\nu,m}\int \mathrm{e}^{\mathrm{i}mkl}\Big[&E_\nu(m)w_{\mu,\nu}\left(x+\frac{ml}{2},\boldsymbol{x}_\perp,\boldsymbol{k},t\right)\\&-E_\mu(m)w_{\mu,\nu}\left(x-\frac{ml}{2},\boldsymbol{x}_\perp,\boldsymbol{k},t\right)\Big]\,\mathrm{d}\boldsymbol{k},\end{aligned} \tag{31}$$

provided our collision model satisfies $\int\sum_{\mu,\nu}Q_{\mu,\nu}\,\mathrm{d}\boldsymbol{k}=0$.

A related formulation of the band Wigner functions (without collision terms) is due to Demeio *et al* [28]. One difficulty with our formulation is that the Wigner function in equation (25) is not $2\pi/l$-periodic in k. This can be corrected by using the following definition:

$$\begin{aligned}f_{\mu,\nu}(\boldsymbol{x},\boldsymbol{k},t)&\equiv\sum_{s=-\infty}^{\infty}w_{\mu,\nu}\left(\boldsymbol{x},k+\frac{2\pi s}{l},\boldsymbol{k}_\perp,t\right)\\&=\sum_{j=-\infty}^{\infty}\mathrm{e}^{\mathrm{i}jkl}l\int\rho_{\mu,\nu}\left(x+\frac{jl}{2},\boldsymbol{x}_\perp+\frac{1}{2}\boldsymbol{\xi}_\perp,x-\frac{jl}{2},\boldsymbol{x}_\perp-\frac{1}{2}\boldsymbol{\xi}_\perp,t\right)\mathrm{e}^{\mathrm{i}\boldsymbol{k}_\perp\cdot\boldsymbol{\xi}_\perp}\,\mathrm{d}\boldsymbol{\xi}_\perp.\end{aligned} \tag{32}$$

To derive this equation, we have used the identity

$$\sum_{j=-\infty}^{\infty}\delta(\xi-jl)=\frac{1}{l}\sum_{s=-\infty}^{\infty}\mathrm{e}^{\mathrm{i}2\pi\xi s/l}, \tag{33}$$

together with the definition of equation (25). From equations (28) and (32), we obtain the two-dimensional electron density in terms of $f_{\mu,\nu}$:

$$n(\boldsymbol{x},t)=\frac{2l}{8\pi^3}\sum_{\mu,\nu}\int_{-\pi/l}^{\pi/l}\int f_{\mu,\nu}(\boldsymbol{x},\boldsymbol{k},t)\,\mathrm{d}k\,\mathrm{d}\boldsymbol{k}_\perp. \tag{34}$$

Similarly, the transversal current density can be obtained from equations (30) and (32):

$$\boldsymbol{J}_\perp=\frac{2e}{8\pi^3}\int_{-\pi/l}^{\pi/l}\int\frac{\hbar\boldsymbol{k}_\perp}{m^*}\sum_{\mu,\nu}f_{\mu,\nu}(\boldsymbol{x},\boldsymbol{k},t)\,\mathrm{d}k\,\mathrm{d}\boldsymbol{k}_\perp. \tag{35}$$

The current density along the growth direction has the form

$$J=\frac{2e\hbar}{8\pi^3m^*}\sum_{\mu,\nu,s}\int_{-\pi/l}^{\pi/l}\int\left(k+\frac{2\pi s}{l}\right)w_{\mu,\nu}\left(\boldsymbol{x},k+\frac{2\pi s}{l},\boldsymbol{k}_\perp,t\right)\mathrm{d}k\,\mathrm{d}\boldsymbol{k}_\perp \tag{36}$$

from which we can also derive equation (31).

The definition of the periodic band Wigner function is related to that adopted by Bechouche *et al* [29]. These authors have rigorously proved that the collisionless Wigner–Poisson equations for a crystal become the crystal Vlasov–Poisson equations in the semiclassical limit, assuming that the initial conditions are concentrated in isolated bands. Scattering other than electron–electron scattering is not considered in these works.

Further progress can be made specifying models for the collision terms. It is convenient to distinguish two cases:

(a) miniband transport corresponding to field values, for which only the first miniband of the SL is populated, and
(b) transport in several minibands.

Strongly coupled SLs at relatively low fields are well described by case (a), whereas weakly coupled SLs typically require consideration of case (b). In both cases, non-linear phenomena are better described by reduced equations for moments of the Wigner functions, such as the electron density, the electric field and the electron average momentum and energy. For miniband transport, we can find these reduced equations using singular perturbation methods if we start from a sufficiently simple quantum kinetic equation. We shall describe this work in the following subsection and also indicate related approaches found in the literature. The study of transport in several minibands is less advanced. An important limiting case corresponds to sequential resonant tunnelling in weakly coupled SLs, which we shall describe in section 2.3. We shall see that a distinctive feature of a weakly coupled SL (supported by experiments) is that pinning and motion of EFDs may occur in them. Electric-field domains are pinned for values of the current in entire intervals. This is a characteristic feature of spatially discrete equations, which is absent in spatially continuous equations. Not surprisingly, discrete models have been used to describe non-linear phenomena in weakly coupled SLs, whereas continuous models are typically associated with strongly coupled SLs, for which EFDs always move except for single values of the current [16].

2.2. Miniband transport

Our goal in this subsection is to derive a reduced quantum drift–diffusion equation (QDDE) from the Wigner–Poisson equation for a SL with only one populated miniband, following the approach of Bonilla and Escobedo [30]. The resulting reduced QDDE will describe many non-linear phenomena in strongly coupled SLs. Let us first find an appropriate Wigner–Poisson description of transport in a single miniband. To this end, we sum all the Wigner equations (27) over the band indices and use the closure condition in equation (20), so as to find an equation for $w(\boldsymbol{x}, \boldsymbol{k}, t) = \sum_{\mu,\nu} w_{\mu,\nu}(\boldsymbol{x}, \boldsymbol{k}, t)$:

$$\frac{\partial}{\partial t}w + \frac{\hbar \boldsymbol{k}_\perp}{m^*}\frac{\partial}{\partial \boldsymbol{x}_\perp}w + \frac{\mathrm{i}}{\hbar}\sum_{m=-\infty}^{\infty} \mathrm{e}^{\mathrm{i}mkl}\sum_{\mu,\nu}\left[E_\nu(m)w_{\mu,\nu}\left(x + \frac{ml}{2}, \boldsymbol{x}_\perp, \boldsymbol{k}, t\right)\right.$$
$$\left. - E_\mu(m)w_{\mu,\nu}\left(x - \frac{ml}{2}, \boldsymbol{x}_\perp, \boldsymbol{k}, t\right)\right] + \frac{\mathrm{i}e}{\hbar}\left[W\left(x + \frac{1}{2\mathrm{i}}\frac{\partial}{\partial k}, \boldsymbol{x}_\perp\right)\right.$$
$$\left. - W\left(x - \frac{1}{2\mathrm{i}}\frac{\partial}{\partial k}, \boldsymbol{x}_\perp\right)\right] w = \sum_{\mu,\nu} Q_{\mu,\nu}[w]. \tag{37}$$

Let us now assume that only the first miniband is populated and that there are no transitions between minibands, $w(\boldsymbol{x}, \boldsymbol{k}, t) \approx w_{1,1}(\boldsymbol{x}, \boldsymbol{k}, t)$. Then equation (37) becomes

$$\frac{\partial}{\partial t}w + \frac{\hbar \boldsymbol{k}_\perp}{m^*}\frac{\partial}{\partial \boldsymbol{x}_\perp}w + \frac{\mathrm{i}}{\hbar}\sum_{m=-\infty}^{\infty} \mathrm{e}^{\mathrm{i}mkl}E_1(m)\left[w\left(x + \frac{ml}{2}, \boldsymbol{x}_\perp, \boldsymbol{k}, t\right) - w\left(x - \frac{ml}{2}, \boldsymbol{x}_\perp, \boldsymbol{k}, t\right)\right]$$
$$+ \frac{\mathrm{i}e}{\hbar}\left[W\left(x + \frac{1}{2\mathrm{i}}\frac{\partial}{\partial k}, \boldsymbol{x}_\perp\right) - W\left(x - \frac{1}{2\mathrm{i}}\frac{\partial}{\partial k}, \boldsymbol{x}_\perp\right)\right] w = Q_{1,1}[w]. \tag{38}$$

This yields the following equation for the periodic Wigner function in equation (32):

$$\frac{\partial}{\partial t} f + \frac{\hbar \boldsymbol{k}_\perp}{m^*} \frac{\partial}{\partial \boldsymbol{x}_\perp} f + \frac{\mathrm{i}}{\hbar} \sum_{m=-\infty}^{\infty} \mathrm{e}^{\mathrm{i}mkl} E_1(m) \left[f\left(x + \frac{ml}{2}, \boldsymbol{x}_\perp, \boldsymbol{k}, t \right) - f\left(x - \frac{ml}{2}, \boldsymbol{x}_\perp, \boldsymbol{k}, t \right) \right]$$
$$+ \frac{\mathrm{i}e}{\hbar} \left[W\left(x + \frac{1}{2\mathrm{i}} \frac{\partial}{\partial k}, \boldsymbol{x}_\perp \right) - W\left(x - \frac{1}{2\mathrm{i}} \frac{\partial}{\partial k}, \boldsymbol{x}_\perp \right) \right] f = Q[f]. \tag{39}$$

The dispersion relation $\mathcal{E}_1(k)$ is an even periodic function of k with period $2\pi/l$ that can be written as $\mathcal{E}_1(k) = \Delta_1[1 - \cos(kl)]/2$ plus a constant in the tight-binding approximation (Δ_1 denotes the width of the first miniband). Moreover, the field $\boldsymbol{F} = \partial W/\partial \boldsymbol{x}$ (note that the real electric field is $-\boldsymbol{F}$) satisfies

$$\varepsilon \left(\frac{\partial F}{\partial x} + \frac{\partial}{\partial \boldsymbol{x}_\perp} \boldsymbol{F}_\perp \right) = \frac{e}{l}(n - N_\mathrm{D}), \tag{40}$$

$$n(x, \boldsymbol{x}_\perp, t) = \frac{l}{4\pi^3} \int_{-\pi/l}^{\pi/l} \int_{-\infty}^{\infty} \int_{-\infty}^{\infty} f(x, \boldsymbol{x}_\perp, k, \boldsymbol{k}_\perp, t) \, \mathrm{d}k \, \mathrm{d}\boldsymbol{k}_\perp. \tag{41}$$

We want to explicitly derive reduced balance equations from the kinetic equation. For this purpose, we need a sufficiently simplified description of scattering. Scattering processes such as phonon scattering change the energy and momentum of the electrons, leading the distribution function towards thermal equilibrium. We can describe these processes using a Bhatnagar–Gross–Krook (BGK) collision model [31]:

$$Q_\mathrm{en}[f] = -\nu_\mathrm{en}(f - f^\mathrm{FD}), \tag{42}$$

$$f^\mathrm{FD}(\boldsymbol{k}; n) = \int_0^\infty \frac{\Gamma/\pi}{[E - \mathcal{E}(k) - \hbar^2 \boldsymbol{k}_\perp^2/2m^*]^2 + \Gamma^2} \frac{\mathrm{d}E}{1 + \exp((E - \mu)/k_\mathrm{B}T)}, \tag{43}$$

$$n(\boldsymbol{x}, t) = \frac{l}{4\pi^3} \int_{-\pi/l}^{\pi/l} \int_{-\infty}^{\infty} \int_{-\infty}^{\infty} f^\mathrm{FD}(k, \boldsymbol{k}_\perp; n) \, \mathrm{d}k \, \mathrm{d}\boldsymbol{k}_\perp. \tag{44}$$

Here Γ measures the finite width of the spectral function in thermal equilibrium due to scattering [15]. As $\Gamma \to 0$, the first factor in equation (43) becomes a delta function, and we recover the usual Fermi–Dirac distribution function with a chemical potential μ. As shown in figure 1, the chemical potential $\mu = \mu(x, \boldsymbol{x}_\perp, t)$ is a function of the exact electron density, n, of equation (41) that is calculated by solving equation (44). With these definitions, the integral of $Q_\mathrm{en}[f]$ over momentum vanishes, and the equation of charge continuity holds, as we shall show below. Other processes, such as impurity scattering, conserve the energy of the electron, change only its momentum and also preserve charge continuity. Gerhardts [32] used the following model,

$$Q_\mathrm{imp}[f] = -\frac{\tilde{\nu}_\mathrm{imp}}{4\pi^3} \int_{-\pi/l}^{\pi/l} \int_{-\infty}^{\infty} \int_{-\infty}^{\infty} \delta[E(k, \boldsymbol{k}_\perp) - E(k', \boldsymbol{k}'_\perp)][f(k, \boldsymbol{k}_\perp) - f(k', \boldsymbol{k}'_\perp)] \, \mathrm{d}k' \, \mathrm{d}\boldsymbol{k}'_\perp, \tag{45}$$

which can be rewritten as $Q_\mathrm{imp}[f] = -\nu_\mathrm{G}(f - \Phi_\mathrm{f}[E(k, \boldsymbol{k}_\perp)])$, provided $\Phi_\mathrm{f}[E] = \int \delta[E - E(\boldsymbol{k}')] f(\boldsymbol{k}') \, \mathrm{d}^3\boldsymbol{k}'/[4\pi^3 g(E)]$, $g(E) = \int \delta[E - E(\boldsymbol{k}')] f(\boldsymbol{k}') \, \mathrm{d}^3\boldsymbol{k}'/(4\pi^3)$ is the density of states and $\nu_\mathrm{G} = \tilde{\nu}_\mathrm{imp} g(E)$. Note that we have dropped the dependence of the Wigner function on space and time. This collision term couples the vertical motion of the electron to the lateral degrees of freedom. If we assume that the variation of the energy in the lateral direction is

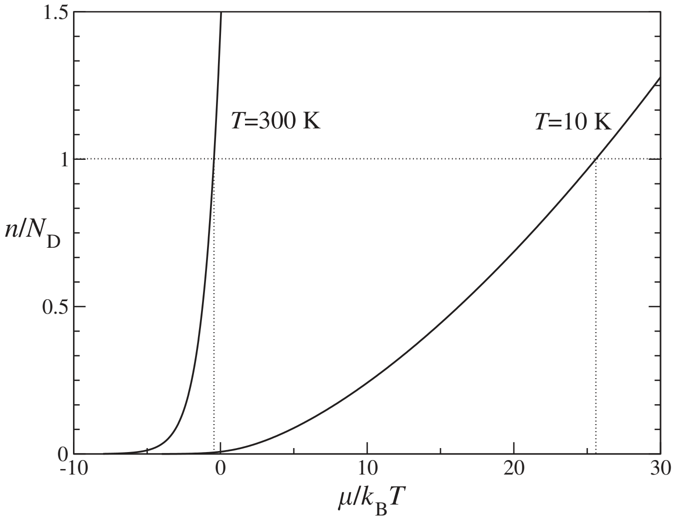

Figure 1. Electron density, n/N_D, versus chemical potential, μ/k_BT, for 10 K ($M = 25.59k_BT$) and 300 K ($M = -0.45k_BT$) with $\Gamma = 0$. From [34].

negligible, $E(k, \boldsymbol{k}_\perp) - E(k', \boldsymbol{k}'_\perp) \approx \mathcal{E}(k) - \mathcal{E}(k')$ and therefore

$$Q_{\mathrm{imp}}[f] \approx -\frac{\tilde{\nu}_{\mathrm{imp}}}{2\pi}\int_{-\pi/l}^{\pi/l} \delta[\mathcal{E}(k) - \mathcal{E}(k')][f(k) - f(k')]\,\mathrm{d}k'$$

$$= -\frac{\tilde{\nu}_{\mathrm{imp}}}{\pi\,\Delta_1 l\,\sin kl}[f(k) - f(-k)] \equiv -\frac{\nu_{\mathrm{imp}}}{2}[f(k) - f(-k)], \tag{46}$$

$$f(x, k, t) = \frac{1}{2\pi^2 S}\iint f(x, \boldsymbol{x}_\perp, k, \boldsymbol{k}'_\perp, t)\,\mathrm{d}\boldsymbol{k}'_\perp\,\mathrm{d}\boldsymbol{x}_\perp. \tag{47}$$

The approximate collision term in equation (46) was introduced by Ktitorov *et al* [33]. In terms of the one-dimensional Wigner function in equation (47), the following one-dimensional BGK–Poisson system of equations (independent of $\boldsymbol{x}_\perp$ if we assume that the initial Wigner function does not depend on $\boldsymbol{x}_\perp$) can be derived from equations (39)–(47):

$$\frac{\partial f}{\partial t} + \frac{\mathrm{i}}{\hbar}\sum_{j=-\infty}^{\infty} \mathrm{e}^{\mathrm{i}jkl} E_1(j)\left[f\left(x + \frac{jl}{2}, k, t\right) - f\left(x - \frac{jl}{2}, k, t\right)\right]$$
$$+\frac{\mathrm{i}e}{\hbar}\left[W\left(x + \frac{1}{2\mathrm{i}}\frac{\partial}{\partial k}, t\right) - W\left(x - \frac{1}{2\mathrm{i}}\frac{\partial}{\partial k}, t\right)\right] f$$
$$= -\nu_{\mathrm{en}}\left(f - f^{\mathrm{FD}}\right) - \nu_{\mathrm{imp}}\frac{f(x, k, t) - f(x, -k, t)}{2}, \tag{48}$$

$$\varepsilon\frac{\partial^2 W}{\partial x^2} = \frac{e}{l}(n - N_D), \tag{49}$$

$$n = \frac{l}{2\pi}\int_{-\pi/l}^{\pi/l} f(x, k, t)\,\mathrm{d}k = \frac{l}{2\pi}\int_{-\pi/l}^{\pi/l} f^{\mathrm{FD}}(k; n)\,\mathrm{d}k, \tag{50}$$

$$f^{\mathrm{FD}}(k; n) = \frac{m^* k_B T}{\pi^2\hbar^2}\left\{\tan^{-1}\left(\frac{\Gamma}{\mathcal{E}(k)}\right) + \int_0^\infty \frac{\Gamma}{[E - \mathcal{E}(k)]^2 + \Gamma^2}\ln\left[1 + \exp\left(\frac{\mu - E}{k_B T}\right)\right]\mathrm{d}E\right\}. \tag{51}$$

The semiclassical limit of these equations has been analysed in [34] in order to derive a reduced drift–diffusion model in the hydrodynamic limit. Particular solutions of the semiclassical model have been found by different authors. Ignatov and Shashkin [35] and Ignatov *et al* [36] found the stationary, space-independent semiclassical solution of equation (48) for a Boltzmann distribution function, the *Boltzmann limit* of equation (51). The integral of $v(k)$ times this solution was then used to find the SL drift velocity. The linear stability of this semiclassical, stationary, x-independent solution to plane wave disturbances in the field was studied by Ignatov and Shashkin [35]. The same equation with an additional source term modelling injection with a precise momentum was considered by Ryndyk *et al* [37]. These studies are relevant when we consider Bloch oscillations later on in this section.

Before we proceed, it is convenient to derive the charge continuity equation and a form of Ampère's law for the current density from equation (48). Since the Wigner function is periodic in k, we can write the second and third terms on the right-hand side of equation (48) in terms of its Fourier series:

$$f(x,k,t) = \sum_{j=-\infty}^{\infty} f_j(x,t)\,\mathrm{e}^{\mathrm{i}jkl}. \tag{52}$$

We have

$$W\left(x \pm \frac{1}{2\mathrm{i}}\frac{\partial}{\partial k}, t\right) f = \sum_{j=-\infty}^{\infty} W\left(x \pm \frac{jl}{2}, t\right) f_j\,\mathrm{e}^{\mathrm{i}jkl} \tag{53}$$

and therefore

$$\begin{aligned} W\left(x+\frac{1}{2\mathrm{i}}\frac{\partial}{\partial k}, t\right) f - W\left(x-\frac{1}{2\mathrm{i}}\frac{\partial}{\partial k}, t\right) f &= \sum_{j=-\infty}^{\infty}\left[W\left(x+\frac{jl}{2}, t\right) - W\left(x-\frac{jl}{2}, t\right)\right] f_j\,\mathrm{e}^{\mathrm{i}jkl} \\ &= \sum_{j=-\infty}^{\infty} jl\langle F\rangle_j\, f_j\,\mathrm{e}^{\mathrm{i}jkl}. \end{aligned} \tag{54}$$

Here we have defined the average

$$\langle F\rangle_j(x,t) = \frac{1}{jl}\int_{-jl/2}^{jl/2} F(x+s,t)\,\mathrm{d}s. \tag{55}$$

Note that differentiating an average, we obtain a finite difference

$$\frac{\partial}{\partial x}\langle g\rangle_j = \left\langle\frac{\partial g}{\partial x}\right\rangle_j = \frac{g(x+jl/2) - g(x-jl/2)}{jl}. \tag{56}$$

Then the second term in equation (48) is

$$\frac{\mathrm{i}}{\hbar}\sum_{j=-\infty}^{\infty}\left[f\left(x+\frac{jl}{2}, k, t\right) - f\left(x-\frac{jl}{2}, k, t\right)\right] E_1(j)\,\mathrm{e}^{\mathrm{i}jkl} = \sum_{j=-\infty}^{\infty}\frac{\mathrm{i}jl}{\hbar}\,\mathrm{e}^{\mathrm{i}jkl} E_1(j)\frac{\partial}{\partial x}\langle f\rangle_j, \tag{57}$$

which in the case of the tight-binding dispersion relation $\mathcal{E}_1(k) = \Delta_1(1-\cos kl)/2$ becomes $v(k)\partial\langle f\rangle_1/\partial x$, with the usual miniband group velocity,

$$v(k) \equiv \frac{1}{\hbar}\frac{\mathrm{d}\mathcal{E}_1}{\mathrm{d}k} = \frac{\Delta_1 l}{2\hbar}\sin(kl). \tag{58}$$

Inserting equations (54) and (57) into equation (48), we obtain the following equivalent form of the Wigner equation, which is particularly suitable for treating SL problems:

$$\frac{\partial f}{\partial t}+\sum_{j=-\infty}^{\infty}\frac{\mathrm{i}jl}{\hbar}\,\mathrm{e}^{\mathrm{i}jkl}\left(E_1(j)\frac{\partial}{\partial x}\langle f\rangle_j+e\langle F\rangle_j f_j\right)$$

$$=-\nu_{\mathrm{en}}(f-f^{\mathrm{FD}})-\nu_{\mathrm{imp}}\frac{f(x,k,t)-f(x,-k,t)}{2}. \qquad (59)$$

We now integrate this equation over k, thereby getting the charge continuity equation:

$$\frac{\partial n}{\partial t}+\frac{\partial}{\partial x}\sum_{j=1}^{\infty}\frac{2jl}{\hbar}\langle \mathrm{Im}(E_1(-j)f_j)\rangle_j=0. \qquad (60)$$

We can eliminate the electron density from equation (60) by using the Poisson equation (49) and integrating the result over x, thereby obtaining the non-local Ampère's law:

$$\varepsilon\frac{\partial F}{\partial t}+\frac{2e}{\hbar}\sum_{j=1}^{\infty}j\langle \mathrm{Im}(E_1(-j)f_j)\rangle_j=J(t). \qquad (61)$$

Here $J(t)$ is the total current density. Equations (59)–(61) are spatially non-local versions of the corresponding semiclassical equations. The charge continuity and Ampère's equations have their traditional form as derived from semiclassical Boltzmann equations, except that the electron current is averaged over the SL periods. This non-locality will be transmitted to the QDDE.

Large-signal studies of the Wigner–BGK–Poisson problem in equations (59) and (61) are lacking. A first step in this direction is to derive a QDDE for the electron density coupled with the Poisson equation for the electric field. To do so, we shall follow the Chapman–Enskog approach of Bonilla and Escobedo [30] (see also [34] for the semiclassical limit) and assume that the electric field contribution in equation (59) is comparable with the collision terms. Moreover, the electric-field contribution and the collision terms dominate over all other terms, which is known as the *hyperbolic limit* because the lowest-order approximation of the resulting reduced equation for the electric field is hyperbolic [34]. Let v_{M} and F_{M} denote the electron velocity and field scales, respectively, typical of the macroscopic phenomena described by the sought-after balance equation; for example, let them be the positive values at which the (zeroth order) drift velocity reaches its maximum. In the hyperbolic limit, the time t_0 it takes an electron with speed v_{M} to traverse a distance $x_0=\varepsilon F_{\mathrm{M}}l/(eN_{\mathrm{D}})$, over which the field variation is of order F_{M}, is much longer than the mean time between collisions, $\nu_{\mathrm{en}}^{-1}\sim\hbar/(eF_{\mathrm{M}}l)=t_1$. Note that $1/t_1$ is of the order of the Bloch frequency. We therefore define the *small parameter* $\eta=t_1/t_0=\hbar v_{\mathrm{M}}N_{\mathrm{D}}/(\varepsilon F_{\mathrm{M}}^2l^2)$ and formally multiply the first two terms on the left-hand side of equation (48) or (59) by η [34]. After obtaining the number of desired terms, we set $\eta=1$.

The solution of equation (59) for $\eta=0$ is the stationary space-independent solution that is easily found as a Fourier series,

$$f^{(0)}(k;n)=\sum_{j=-\infty}^{\infty}f_j^{(0)}\,\mathrm{e}^{\mathrm{i}jkl},\qquad f_j^{(0)}=\frac{1-ij\mathcal{F}/\tau_{\mathrm{e}}}{1+j^2\mathcal{F}^2}f_j^{\mathrm{FD}} \qquad (62)$$

in which

$$\mathcal{F}=\frac{\langle F\rangle_1}{F_{\mathrm{M}}},\qquad F_{\mathrm{M}}=\frac{\hbar\sqrt{\nu_{\mathrm{en}}(\nu_{\mathrm{en}}+\nu_{\mathrm{imp}})}}{el},\qquad \tau_{\mathrm{e}}=\sqrt{\frac{\nu_{\mathrm{en}}+\nu_{\mathrm{imp}}}{\nu_{\mathrm{en}}}}. \qquad (63)$$

Since f^{FD} is an even function of k, its Fourier coefficient, f_j^{FD}, is real. Note that equation (50) implies $f_0^{(0)}=f_0^{\mathrm{FD}}=n$.

The Chapman–Enskog ansatz consists of writing the distribution function as an expansion in powers of the book-keeping parameter η (recall that we have to set $\eta = 1$ after retaining the desired number of terms):

$$f(x, k, t; \eta) = f^{(0)}(k; F) + \sum_{m=1}^{\infty} f^{(m)}(k; F)\eta^m, \tag{64}$$

$$\varepsilon\frac{\partial F}{\partial t} + \sum_{m=0}^{\infty} J^{(m)}(F)\eta^m = J(t). \tag{65}$$

The coefficients $f^{(m)}(k; F)$ depend on the 'slow variables' x and t only through their dependence on the electric field and the electron density (which are related through the Poisson equation). The field obeys a reduced evolution equation (65), in which the functionals $J^{(m)}(F)$ are chosen so that $f^{(m)}(k; F)$ are bounded and $2\pi/l$-periodic in k. Differentiating Ampère's law in equation (65) with respect to x, we obtain the charge continuity equation. Moreover the condition

$$\int_{-\pi/l}^{\pi/l} f^{(m)}(k; n)\,\mathrm{d}k = \frac{2\pi f_0^{(m)}}{l} = 0, \qquad m \geqslant 1 \tag{66}$$

ensures that $f^{(m)}$ for $m \geqslant 1$ does not contain contributions proportional to the zero-order term $f^{(0)}$. Note that the insertion of equation (64) in Ampère's law in equation (61) yields

$$J^{(m)} = \frac{2e}{\hbar}\sum_{j=1}^{\infty} j\langle \mathrm{Im}[E_1(-j) f_j^{(m)}]\rangle_j, \tag{67}$$

which is also obtained by means of the above-mentioned boundedness condition.

Inserting equations (64) and (65) into equation (59) and equating all coefficients of η^m in the resulting series to zero, we find the hierarchy

$$\mathcal{L}f^{(1)} = -\left(\frac{\partial}{\partial t} + v(k)\frac{\partial}{\partial x}\right) f^{(0)}\bigg|_0, \tag{68}$$

$$\mathcal{L}f^{(2)} = -\left(\frac{\partial}{\partial t} + v(k)\frac{\partial}{\partial x}\right) f^{(1)}\bigg|_0 - \frac{\partial}{\partial t} f^{(0)}\bigg|_1 \tag{69}$$

and so on. We have defined

$$\mathcal{L}u(k) \equiv \frac{eF}{\hbar}\frac{\mathrm{d}u(k)}{\mathrm{d}k} + \left(\nu_{\mathrm{en}} + \frac{\nu_{\mathrm{imp}}}{2}\right) u(k) + \frac{\nu_{\mathrm{imp}} u(-k)}{2} \tag{70}$$

and the subscripts 0 and 1 in the right-hand side of these equations mean that $\varepsilon\partial F/\partial t$ is replaced by $J - J^{(0)}(F)$ and by $-J^{(1)}(F)$, respectively.

The linear equation $\mathcal{L}u = S$ has a bounded $2\pi/l$-periodic solution, provided $\int_{-\pi/l}^{\pi/l} S\,\mathrm{d}k = 0$. Equation (68) and this solvability condition yield equation (67) for $m = 0$. The solution of equation (68) is

$$f^{(1)}(k; F) = \sum_{j=-\infty}^{\infty} \frac{\mathrm{Re}\, S_j^{(1)} + \mathrm{i}\tau_{\mathrm{e}}^{-2}\mathrm{Im}\, S_j^{(1)} - \mathrm{i}j\mathcal{F}S_j^{(1)}/\tau_{\mathrm{e}}}{(1 + j^2\mathcal{F}^2)\nu_{\mathrm{en}}}\, \mathrm{e}^{\mathrm{i}jkl}, \tag{71}$$

in which $S_j^{(1)}$ is the jth Fourier coefficient of the right-hand side of equation (68). Using equation (71), we can now explicitly write two terms in equation (65), thereby obtaining the following QDDE for the field and the electron density given by the Poisson equation (49) (with

$\partial^2 W/\partial x^2 = \partial F/\partial x$). For the tight-binding dispersion relation, the QDDE is

$$\varepsilon\frac{\partial F}{\partial t} + \frac{eN_{\mathrm{D}}}{l}\mathcal{N}\left(F, \frac{\partial F}{\partial x}\right) = \varepsilon\left\langle D\left(F, \frac{\partial F}{\partial x}, \frac{\partial^2 F}{\partial x^2}\right)\right\rangle_1 + \left\langle A\left(F, \frac{\partial F}{\partial x}\right)\right\rangle_1 J(t), \tag{72}$$

$$A = 1 + \frac{2ev_{\mathrm{M}}}{\varepsilon F_{\mathrm{M}} l(\nu_{\mathrm{en}} + \nu_{\mathrm{imp}})}\frac{1-(1+2\tau_{\mathrm{e}}^2)\mathcal{F}^2}{(1+\mathcal{F}^2)^3} n\mathcal{M}, \tag{73}$$

$$\mathcal{N} = \langle nV\mathcal{M}\rangle_1 + \langle (A-1)\langle\langle nV\mathcal{M}\rangle_1\rangle_1\rangle_1 - \frac{l\tau_{\mathrm{e}}\Delta_1}{F_{\mathrm{M}}\hbar(\nu_{\mathrm{en}}+\nu_{\mathrm{imp}})}\left\langle\frac{B}{1+\mathcal{F}^2}\right\rangle_1, \tag{74}$$

$$V(\mathcal{F}) = \frac{2\mathcal{F}}{1+\mathcal{F}^2}, \qquad v_{\mathrm{M}} = \frac{l\mathcal{I}_1(M)\Delta_1}{4\hbar\tau_{\mathrm{e}}\mathcal{I}_0(M)}, \tag{75}$$

$$D = \frac{l^2\Delta_1^2}{8\hbar^2(\nu_{\mathrm{en}}+\nu_{\mathrm{imp}})(1+\mathcal{F}^2)}\left(\frac{\partial^2\langle F\rangle_1}{\partial x^2} - \frac{4\hbar v_{\mathrm{M}}\tau_{\mathrm{e}} C}{l\Delta_1}\right), \tag{76}$$

$$\begin{aligned} B = {} & \left\langle\frac{4\mathcal{F}_2 n\mathcal{M}_2}{(1+4\mathcal{F}_2^2)^2}\frac{\partial\langle F\rangle_2}{\partial x}\right\rangle_1 + \mathcal{F}\left\langle\frac{n\mathcal{M}_2(1-4\mathcal{F}_2^2)}{(1+4\mathcal{F}_2^2)^2}\frac{\partial\langle F\rangle_2}{\partial x}\right\rangle_1 \\ & - \frac{4\hbar v_{\mathrm{M}}(1+\tau_{\mathrm{e}}^2)\mathcal{F}(n\mathcal{M})'}{l\tau_{\mathrm{e}}(1+\mathcal{F}^2)\Delta_1}\left\langle n\mathcal{M}\frac{1-\mathcal{F}^2}{(1+\mathcal{F}^2)^2}\frac{\partial\langle F\rangle_1}{\partial x}\right\rangle_1, \end{aligned} \tag{77}$$

$$C = \left\langle\frac{(n\mathcal{M}_2)'}{1+4\mathcal{F}_2^2}\frac{\partial^2 F}{\partial x^2}\right\rangle_1 - 2\mathcal{F}\left\langle\frac{(n\mathcal{M}_2)'\mathcal{F}_2}{1+4\mathcal{F}_2^2}\frac{\partial^2 F}{\partial x^2}\right\rangle_1 + \frac{8\hbar v_{\mathrm{M}}(1+\tau_{\mathrm{e}}^2)(n\mathcal{M})'\mathcal{F}}{l\tau_{\mathrm{e}}(1+\mathcal{F}^2)\Delta_1}\left\langle\frac{(n\mathcal{M})'\mathcal{F}}{1+\mathcal{F}^2}\frac{\partial^2 F}{\partial x^2}\right\rangle_1. \tag{78}$$

$$\mathcal{M}\left(\frac{n}{N_{\mathrm{D}}}\right) = \frac{\mathcal{I}_1(\tilde{\mu})\mathcal{I}_0(M)}{\mathcal{I}_0(\tilde{\mu})\mathcal{I}_1(M)}, \qquad \mathcal{M}_2\left(\frac{n}{N_{\mathrm{D}}}\right) = \frac{\mathcal{I}_2(\tilde{\mu})\mathcal{I}_0(M)}{\mathcal{I}_0(\tilde{\mu})\mathcal{I}_1(M)}, \tag{79}$$

$$\begin{aligned} \mathcal{I}_{\mathrm{m}}(\tilde{\mu}) = \frac{1}{\pi}\int_{-\pi}^{\pi}\cos(mk)\Bigg[& \tan^{-1}\left(\frac{\tilde{\Gamma}/\delta}{1-\cos k}\right) \\ & + \int_0^{\infty}\frac{\tilde{\Gamma}}{(\tilde{E}-\delta+\delta\cos k)^2+\tilde{\Gamma}^2}\ln(1+\mathrm{e}^{\tilde{\mu}-\tilde{E}})\,\mathrm{d}\tilde{E}\Bigg]\mathrm{d}k. \end{aligned} \tag{80}$$

Here g' denotes $\mathrm{d}g/\mathrm{d}n$, $\delta = \Delta_1/(2k_{\mathrm{B}}T)$, $\tilde{\mu} = \mu/(k_{\mathrm{B}}T)$, $\tilde{\Gamma} = \Gamma/(k_{\mathrm{B}}T)$ and $n = N_{\mathrm{D}}$ at the value $\tilde{\mu} = M$, as indicated in figure 1. Figure 2 shows the coefficients $A(F, 0)$, $\mathcal{V}(F, 0)$ and $D(F, 0)$ for a GaAs/AlAs SL with $d_{\mathrm{W}} = 4.0$ nm, $d_{\mathrm{B}} = 0.9$ nm, $N_{\mathrm{D}} = 1.47 \times 10^{11}$ cm^{-2}, $\Delta_1 = 67$ meV, $\nu_{\mathrm{en}} = \nu_{\mathrm{imp}} = 10^{13}$ Hz and $\Gamma = 0$ [38]. If the electric field and the electron density do not change appreciably over two SL periods, $\langle F\rangle_j \approx F$, the spatial averages can be ignored and the *non-local* QDDE (72) becomes the *local* generalized DDE (GDDE) obtained from the semiclassical theory [34]. The boundary conditions for the QDDE (72), which contains triple spatial averages, need to be specified for the intervals $[-2l, 0]$ and $[Nl, Nl + 2l]$, and not just at the points $x = 0$ and $x = Nl$ (N denotes the number of SL periods), as in the case of the parabolic semiclassical GDDE. Similarly, the initial condition has to be defined on the extended interval $[-2l, Nl + 2l]$.

Equation (72) contains both differences and differentials, and it is strongly non-linear because $\mathcal{M}(n/N_{\mathrm{D}})$ and $\mathcal{M}_2(n/N_{\mathrm{D}})$ depend non-linearly on $\partial F/\partial x$ through their definitions and the Poisson equation (49). Despite its formidable appearance, the QDDE (72) is (in dimensionless units) a small perturbation of the drift equation $\varepsilon\partial F/\partial t = J - J^{(0)}$,

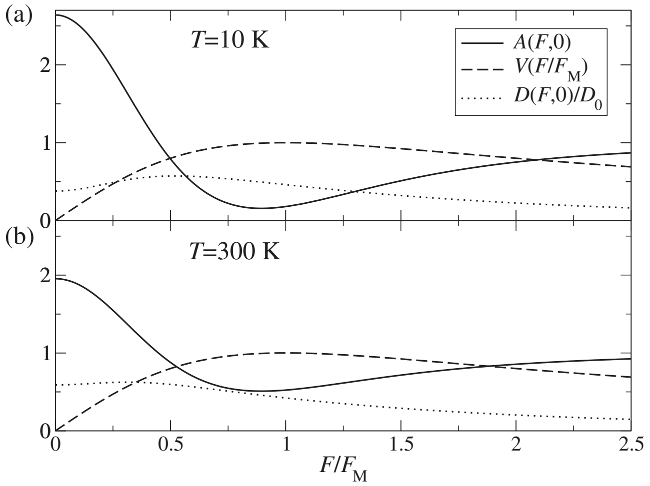

Figure 2. Coefficients $A(F,0)$, $\mathcal{V}(F,0)/[v_M A(F,0)] = V(F/F_M)$, and $D(F,0)/D_0$ with $D_0 = \Delta_1^2 l^2/[8\hbar^2(\nu_{en} + \nu_{imp})]$ appearing in equation (72) versus electric field, F/F_M, for (*a*) 10 K and (*b*) 300 K. We have considered the semiclassical limit and $\Gamma = 0$.

analysed in studies of the Gunn effect [39]. In the Boltzmann limit, $\mathcal{M}(n/N_D) = 1$ and $\mathcal{M}_2(n/N_D) = I_2(\delta)/I_1(\delta)$, in which $I_n(\delta)$ denotes the modified Bessel function of the nth order. Then, the Esaki–Tsu drift velocity in equation (76) has a maximum at $v_M = lI_1(\delta)\Delta_1/[4\hbar\tau_e I_0(\delta)]$ for a temperature-independent value of the field, F_M, given by equation (63) [36]. If $\nu_{imp} = 0$ and local averages are ignored (semiclassical limit), the diffusion coefficient in equation (76) becomes $D(F, 0, \partial^2F/\partial x^2) \equiv \mathcal{D}(F)\partial^2F/\partial x^2$, with $\mathcal{D}(F) = [v_0^2/(2\nu_{en})][1 + (I_2/I_0)(2\mathcal{F}^2 - 1)/(4\mathcal{F}^2 + 1) - 4(I_1/I_0)^2\mathcal{F}^2/(\mathcal{F}^2 + 1)^2]$, where $v_0 = l\Delta_1/(2\hbar)$, which coincides with the expression derived by Ignatov and Shashkin [40] from the dispersion relation for the BGK kinetic equation (cf their equation (3)). Experimentally, F_M depends on temperature, and Gerhardts [32] showed that the correct dependence is obtained by using the collision term in equation (45) to model elastic impurity scattering. By using the Chapman–Enskog method, it should be possible to derive a QDDE from the corresponding three-dimensional BGK–Poisson system of equations at the price of technical complications. A common alternative, implemented by Wacker in figure 8 of his review, is to fit temperature-dependent collision frequencies to equation (59) so that the resulting drift velocity mimics the result of Monte Carlo simulations of the three-dimensional semiclassical Boltzmann equation [15].

An interesting point is that the GDDE (semiclassical limit of the QDDE) becomes the usual Kroemer DDE with the Esaki–Tsu drift velocity in equation (76) and a diffusion coefficient obeying the Einstein relation

$$\varepsilon\frac{\partial F}{\partial t} + \frac{2v_M\mathcal{F}}{1+\mathcal{F}^2}\left(\frac{eN_D}{l} + \varepsilon\frac{\partial F}{\partial x}\right) = J(t) + \frac{2k_BTv_M\varepsilon}{eF_M(1+\mathcal{F}^2)}\frac{\partial^2 F}{\partial x^2} \tag{81}$$

only in the limit of large temperatures $k_BT \gg \max(\Delta_1, \pi\hbar^2N_D/m^*)$ in addition to the limit as $\eta \to 0$. This limit is not very realistic for many strongly coupled SLs, even at room temperature [34]. Figure 3 depicts the ratio $R(F) = eF\mathcal{D}(F)/[k_BT\mathcal{N}(F,0)]$ at two different temperatures, thereby showing how the Einstein relation breaks down. Note that the difference $|R(F) - 1|$ becomes smaller as the temperature increases. However, a numerical solution of the GDDE yields self-oscillations of the current, whose frequency agrees very well with experiments [34]. More phenomenological DDEs were used by Le Person *et al* [41].

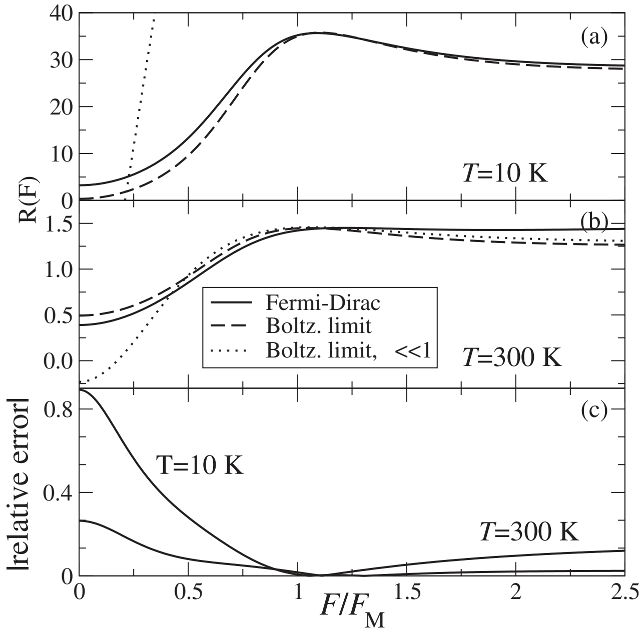

Figure 3. Ratio $R(F) = eF\mathcal{D}(F)/[k_B T\mathcal{N}(F, 0)]$ for (*a*) 10 K and (*b*) 300 K. (*c*) Relative error of the Boltzmann limit result with respect to using the Fermi–Dirac distribution. We have considered the semiclassical limit and $\Gamma = 0$. From [34].

In this subsection, we have described a one-dimensional Wigner–BGK–Poisson system of equations with a BGK collision term and a simplified description of impurity scattering. Then, we have used a systematic Chapman–Enskog method to derive a quantum drift–diffusion equation. In the limit of high temperatures, this equation becomes a DDE with the Esaki–Tsu drift velocity and a diffusivity that obeys the Einstein relation.

How can we generalize these results? In the general quantum description of single-miniband SLs, collision terms corresponding to many different scattering processes have been modelled within the NGF formulation [15,26,27,42]. In this formulation, closed equations for the one-electron NGFs are found by treating weak scattering processes up to second order in the scattering potential, thereby obtaining the Kadanoff–Baym equations [26,27]. Additional approximations yield closed equations for Wigner functions, although more work connecting both the NGF and the Wigner function approaches seems desirable [27]. Related work is due to Bryksin and coworkers. Bryksin and Firsov [43–45] derived a system of coupled equations for the two-point electron correlation function and the scattering transition probability, both written in the Wannier representation. More recently, Bryksin and Kleinert [25] extended the same formulation to obtain the drift velocity and the diffusion coefficient for constant applied electric fields. These transport coefficients are obtained by approximating the two first moments of the Wigner transform of the two-point correlation function. They have been used in a linear stability analysis of simple homogeneous field profiles [46]. Formulations using density matrices can be found in [21,22], and comparison between *non-equivalent* NGF and density matrix descriptions of single-miniband SLs can be found in appendices A and B of [15]. Laikhtman and Miller [47] derived equations for the NGF and subsequently for the density matrix of a single-miniband SL using the Wannier representation. Later, they calculated different approximations of the tunnelling current density (for high temperatures, considering hopping between next-neighbour WS states and SLs with two minibands) and studied the stability of the uniform field profile in an infinite SL. These authors calculated space-dependent electric field profiles via the Poisson equation and formulated a semidiscrete model, which treated the low- and high-field domains separately [48]. Lake *et al* [49] and Datta [42] have given a detailed self-consistent treatment within an NGF formulation for shorter devices such as the resonant tunnelling diode and a short n^+–n–n^+ diode, respectively. A general theory of self-consistent NGF for SLs with several minibands and realistic scattering mechanisms is still missing.

Within the semiclassical approach, we could improve the description of collision terms and then numerically solve the resulting Boltzmann equation using the Monte Carlo procedure [50–53] or using particle methods [54]. Thus, transport coefficients can be obtained and inserted in a model DDE, which results in an uncontrolled approximation unless we have a reasonable derivation of the reduced model. It is more difficult to implement a Chapman–Enskog method for non-local collision kernels and derive a GDDE, but, assuming that elastic processes are dominant, progress has been achieved in certain cases [55].

For general collision kernels, it is possible to derive a hydrodynamic model which is more general than DDEs. In the context of single-miniband SLs, Büttiker and Thomas [56] and later Lei and collaborators [57–64] have exploited the use of balance equations based on hydrodynamic variables. Lei [61] writes moment equations for the electron density, its average velocity and its average energy directly from a quantum theory. These equations are part of an infinite hierarchy, which is closed by assuming that the distribution function is a three-parameter Fermi–Dirac distribution depending on the electron density, an electron temperature and a moving wave vector within the lowest miniband described in the tight-binding approximation [64]. Balance equations are harder to study or solve numerically than DDEs but yield better quantitative results. The distribution function may be poorly described by hydrodynamic methods if it departs significantly from local equilibrium [15]. It might be interesting to investigate more general BGK collision models with local Fermi–Dirac distribution functions that depend on the exact electron density, average current density and energy and to derive hydrodynamic equations in the hyperbolic limit. In this limit, the electric field terms are of the same order as the collision operators, and the resulting zeroth-order distribution function (equivalent to the one in equation (62)) may be quite different from local equilibrium.

The experimental work on miniband transport in strongly coupled SLs has been reviewed by Sibille [7].

2.3. SLs with several minibands and sequential resonant tunnelling

Electronic transport in an SL with several minibands has been much less studied than the case of an SL with one miniband. In particular, reduced *non-local* QDDEs corresponding to equation (72) have not been derived for SLs with several minibands. Known results involve definitions of the current density that are not equivalent to equation (31) and therefore do not exactly satisfy the charge continuity equation (29). Bryksin *et al* [65] use a low-density approximation of the current density introduced by Bryksin and Firsov [43]: the current operator is determined by the density times the time derivative of the dipole moment. In a related definition of Kazarinov and Suris [66], the average current is the trace of the velocity operator times the density matrix multiplied by e (a similar definition is used in [47]). Wacker's definition of 'total current density well to well' does not even depend on the position $\boldsymbol{x}$ (cf equation (148) in [15]), and therefore its relation to the *space-dependent* current density in the charge continuity equation (29) is unclear.

The general quantum kinetic theory of electron transport in strongly or weakly coupled SLs with several minibands is not yet developed to the point in which systematic approximations to reduced balance equations are known. However, different calculations of approximate *stationary* current–field relations for weakly coupled SLs have been incorporated in *ad hoc* discrete balance equation models with great success in predicting and interpreting non-linear phenomena. Discrete equations are plausible candidates for reduced descriptions of weakly coupled SLs due to two reasons. First, the non-local QDDE describing single-miniband SLs contains finite differences, which are used in discrete equations. Second and more importantly, weakly coupled SLs display multistability of stationary field profiles having pinned domain walls (monopoles) separating different electric field domains, and this pinning occurs for entire intervals of the current. As we shall see later, pinning of domain walls is typical of discrete equations but not of continuous equations having differentials instead of differences.

An initial approach to calculating a stationary current–field relation for a weakly coupled SL is due to Kazarinov and Suris [67]. It is based on sequential resonant tunnelling of electrons between neighbouring wells of the SL. Kazarinov and Suris [66, 67] treated scattering within a density matrix formulation that used Wannier states as a basis. They considered a constant applied electric field and calculated an approximate stationary current density in different limits: close to resonance and far away from it. For fields close to resonant fields between different subbands of adjacent wells, their work shows that the current density is a Lorentzian function of the applied field. However, this formula is not applicable for hopping between the first subbands of adjacent wells. In what follows, we shall describe models involving discrete balance equations for weakly coupled SLs (whose main transport mechanism is sequential tunnelling) and explain why calculations of the stationary current density are important to completing the equations of these models. The limiting case of weakly coupled SLs is well understood in physical terms, and its description will probably play an important role in checking a future theory for all types of SLs.

In weakly coupled SLs, which contain wider barriers, the miniband widths, Δ_ν, are small compared with the broadening of the energy levels due to scattering, $\hbar/\tau_{\mathrm{sc}}$, and to the typical values of the electrostatic energy per SL period, eFl. Thus, the escape time from a quantum well $\tau_{\mathrm{esc}} \sim l/v_{\mathrm{M}} \sim \hbar/\Delta_\nu$ is much larger than the scattering time, τ_{sc}. This implies that the electron distribution in the wells is in local equilibrium [68]. Moreover, the dielectric relaxation time $\tau_{\mathrm{di}} \sim Nl_{\mathrm{di}}/v_{\mathrm{M}} \sim N\varepsilon F_{\mathrm{M}}\tau_{\mathrm{esc}}/(eN_{\mathrm{D}})$ (N is of the order of the number of SL periods), in which the current density across the SL reacts to sudden changes in the electric field profile, is typically larger than the escape time. Therefore, we can assume that the tunnelling current density between quantum wells is stationary on the longer timescale of the dielectric relaxation time [68]. A minimal theory of charge transport in weakly coupled SLs should therefore specify (i) which slowly varying magnitudes characterize the local Fermi–Dirac equilibrium distribution function in the wells (at least the electric field and the electrochemical potential), (ii) the equations relating these magnitudes (e.g. the charge continuity and the Poisson equation) and (iii) how to close these equations by calculating the necessary relations between magnitudes (e.g. the stationary tunnelling current between adjacent wells).

In 1974 itself, Esaki and Chang [5] explained their observation of periodic structures in the conductance of an SL with increasing dc voltage by the formation of two EFDs inside the SL. According to their interpretation, the electric field is very small in the low-field domain (LFD), and electronic transport is actually due to well-to-well hopping and not miniband conduction as originally assumed, since their SL was weakly coupled. However, the field in the high-field domain (HFD) has the appropriate value to almost align the first subband of one well with the second subband of the adjacent well. Thus, the transport process in the HFD consists of resonant tunnelling from the first subband across the barrier into the second subband in the adjacent well, followed by rapid scattering of the electrons out of the second subband into the first subband in the same well: *sequential resonant tunnelling*. The extent of the EFDs depends on the applied voltage across the SL. Esaki and Chang also recognized that the *discrete* nature in the expansion of the HFD yields the observed oscillatory behaviour of the conductance. Note that a little earlier Suris [69] had proposed a discrete model of charge transport in weakly coupled SLs that could have been used to explain the formation of EFDs. Instead, Suris discussed whether the homogeneous field and electron profiles could be unstable to the formation of moving dipole domains as in the Gunn effect or to the formation of a static inhomogeneous structure, whose period was twice the SL period [70]. Thus, the application of discrete models to the study of static domains in SLs did not occur until the work of Korotkov *et al* [71] and Laikhtman [72]. Korotkov *et al* [71] considered that quasi-zero-dimensional SLs of small lateral extent (quite different from the SLs considered in this work) were analogous to a one-dimensional array of metallic tunnel junctions studied earlier by Likharev *et al* [73]. Electronic transport in these structures was due to single-electron tunnelling events and coexistence between Bloch oscillations, and oscillations due to single-electron tunnelling was predicted. Laikhtman [72] wrote a discrete balance equation for the current through an equivalent circuit formed by a succession of capacitors and non-linear resistors in parallel. The current through each resistor played the role of the tunnelling current, and it was a function of the voltage drop therein but not of the electron density in adjacent wells. This unrealistic feature (absent in Suris's model) produced non-monotonic field profiles and was corrected in later models [47, 48, 68, 74, 75].

Following earlier work for undoped weakly coupled SLs [68], Bonilla [75] proposed a simple discrete model for non-linear charge transport in a doped, weakly coupled SL. This *discrete drift model* combines the discrete charge continuity and Poisson equations with a drift-type constitutive relation for the tunnelling current density across a barrier: the tunnelling current is equal to the product of the electron density at the well *before* the barrier and a non-linear function of the local electric field. Instead of working with the charge continuity equation, it is better to use an equivalent discrete Ampère equation that explicitly includes the total current density [68, 75]. The discrete drift model is the high electric-field limit of many other discrete models, and therefore it successfully describes phenomena occurring in the second and higher plateaus of the I–V characteristic.

Finding the constitutive relation requires calculation of the stationary tunnelling current across a barrier, which, according to the pioneering calculations of Kazarinov and Suris [66,67], is simply a Lorentzian function of $(\mathcal{E}_\nu - \mathcal{E}_1 - eFl)$ for fields comparable with or above the first resonant field. Knowing that the field profile in undoped SLs is uniform, one can fit the corresponding current–voltage characteristic with the stationary carrier density times a Lorentzian function of the electric field, as done by Bonilla *et al* [68]. When the Poisson equation is used to eliminate the electron density in Ampère's equation, the resulting discrete drift model for the field is first order in the spatial differences (unlike the higher-order model of Suris [69]). Instead of fitting data with Lorentzian functions, it is possible to find the discrete drift velocity by calculating the matrix element in the tunnelling current formula of Kazarinov and Suris [66]. Then, the resulting drift velocity can be inserted in the discrete drift model. This approach has been followed by other authors to analyse the coexistence between more than two EFDs [76] and the dependence of non-linear transport on an applied magnetic field [77].

In order to improve the simple discrete drift model, we need to add a contribution for low-field values to the tunnelling current formula. If the electric field is small, the tunnelling current across a barrier depends on the electron density in *both* wells, which are separated by the barrier. A useful analytical formula for this tunnelling current is derived in appendix A of the review by Bonilla [16] and given in equations (99) and (100). Wacker [15] gives an alternative formula for equation (100), which was also used by Amann *et al* [78]. The resulting constitutive relation yields a more elaborate *modified discrete model* for the field profile, which contains second-order differences, not just first-order differences as in the original discrete drift model. To systematically derive the modified discrete model (or a related one) from a quantum kinetic equation is an open problem.

Until 1998, Schöll and collaborators used a more elaborate discrete model to describe transport by sequential resonant tunnelling at low fields. Originally proposed by Prengel, Wacker and Schöll (PWS) [74], the PWS model consists of rate equations for the electron densities of the two first subbands of each quantum well plus a Poisson equation for the local electric field. The tunnelling rates in the PWS model are strongly non-linear functions of the subband populations. Simpler tunnelling rates appear in a later paper by Kastrup *et al* [79]. They combine expressions from miniband transport for tunnelling between the first subbands of adjacent wells with Lorentzian functions for resonant tunnelling between the first subband of one well and the second subband of the next well. The equations of the PWS model could have been simplified because the population of the first subband is always much larger than the one of the second subband for the usual weakly coupled SLs (which could be used to simplify the equations). More importantly, the Poisson equation in the PWS model contains *forward differences* instead of *backward differences* as in the discrete drift model. Thus, the PWS model in the limit of large fields (in which the tunnelling current becomes drift-like and therefore involves only first-order differences) requires an additional (and artificial) boundary condition at the last barrier of the SL, in addition to the boundary condition at the injecting region.

A different discrete model that describes sequential tunnelling for all field strengths is due to Aguado *et al* [80]. The model considers different electric field values in barriers and wells and describes the contact regions more precisely. The stationary tunnelling currents across the inner barriers and across the barriers confining the SL are calculated using the transfer Hamiltonian method. In this model, the stationary tunnelling current depends on the fields in the barrier and the neighbouring wells, which is more precise than the mere dependence of the tunnelling current on the average field in one SL period, as prescribed by the discrete drift model and related ones. The same can be said for the tunnelling current in the boundary conditions [81, 82]. This model is harder to analyse and solve numerically than the simple discrete models we describe in this review, but it has been used to derive the simpler discrete drift–diffusion equations [82] and the sequential tunnelling model explained later [16].

The sequential tunnelling discrete model that we describe here has been extended to predicting the formation of static spin domains in n-doped II–VI semiconductor SLs [83] and the undriven self-oscillations of the current under dc voltage bias in the same materials [84]. Kholod *et al* [85] have used a discrete model with forward differences in the Poisson equation to predict current self-oscillations in semiconductor–insulator SLs with localized states in the insulator barriers. Based upon their quantum kinetic calculations [47], Miller and Laikhtman [48] proposed a semidiscrete model to analyse static EFDs in weakly coupled SLs. They considered a semi-infinite SL and different equations for the LFD and the HFD.

Let us describe the discrete sequential tunnelling model for an SL with $N + 1$ barriers and N wells. The zeroth barrier separates the injecting region from the first SL well, whereas the Nth barrier separates the Nth well from the collecting region. Assume that F_i is the average field across one SL period (note that the actual electric field is $-F_i$), consisting of the ith well and the $(i - 1)$th barrier. Similarly, n_i is the two-dimensional electron density at the ith well, concentrated in a plane perpendicular to the growth direction inside the ith well. Then, the Poisson equation (averaged over the ith period) and the charge continuity equation are

$$F_i - F_{i-1} = \frac{e}{\varepsilon}(n_i - N_{\mathrm{D}}), \tag{82}$$

$$e\frac{\mathrm{d}n_i}{\mathrm{d}t} = J_{i-1\to i} - J_{i\to i+1}. \tag{83}$$

Here $J_{i\to i+1}$ is the tunnelling current density across the ith barrier, i.e. from well i to well $i+1$ with $i = 1, \ldots, N$.

Differentiating equation (82) with respect to time and inserting the result into equation (83), we obtain

$$\varepsilon \frac{\mathrm{d}F_i}{\mathrm{d}t} + J_{i\to i+1} = J(t) \tag{84}$$

in which the total current density, $J(t)$, is the same function for all i. Equation (84) is a discrete version of Ampère's equation. We shall now assume that $J_{i\to i+1}$ depends on F_i, n_i and n_{i+1}. The tunnelling current across the ith barrier clearly depends on the electrochemical potentials of the adjacent wells, thereby depending on n_i and n_{i+1}. That $J_{i\to i+1}$ depends on F_i, but not on F_{i+1}, is a simplifying assumption [82]. We complete our description by adding the voltage bias condition,

$$\frac{1}{N+1}\sum_{i=0}^{N} F_i = \frac{V(t)}{(N+1)l}, \tag{85}$$

for the known voltage $V(t)$.

Our discrete system of equations consists of equation (82) for $i = 1, \ldots, N$, equation (84) for $i = 0, \ldots, N$ and equation (85). In total, we have $(2N + 2)$ equations for the unknowns $n_1, \ldots, n_N, F_0, \ldots, F_N$ and $J(t)$. We need to derive the constitutive relations $J_{0\to 1}$ (tunnelling from the injecting region to the SL), $J_{i\to i+1}$ (tunnelling across an inner barrier of the SL) and $J_{N\to N+1}$ (tunnelling from the SL to the collecting region). Equation (84) evaluated for $i = 0$ and $i = N$ determines the boundary conditions.

We now indicate how to calculate the functions $J_{i\to i+1} = \mathcal{J}(F_i, n_i, n_{i+1})$. We can consider the energy states of isolated quantum wells or subbands $E_\nu(\boldsymbol{k}_\perp) = \mathcal{E}_\nu + \hbar^2\boldsymbol{k}_\perp^2/(2m^*)$, where $\mathcal{E}_\nu$ is now independent of k, as reasonable building blocks. First-order time-dependent perturbation theory indicates that the tunnelling rate through the ith barrier (from the μ subband of the ith well to the ν subband of the $(i+1)$th well) is given by Fermi's golden rule,

$$P_{i,i+1}^{\mu,\nu} = \frac{2\pi}{\hbar}|M_{i,i+1}^{\mu,\nu}|^2\delta(E_\mu(\boldsymbol{k}_{\perp,i}) - e\phi_i l - E_\nu(\boldsymbol{k}_{\perp,i+1}) + e\phi_{i+1} l) \tag{86}$$

assuming conservation of energy during tunnelling. Here $\phi_i l = \sum_{n=0}^{i} F_n$ is the electric potential at the ith well. The matrix element $M_{i,i+1}^{\mu,\nu}$ can be calculated by means of the transfer Hamiltonian method (THM) [86] or using Green's functions [87]. Here, we shall follow appendix B of Sánchez's PhD thesis [87] and choose the THM. Then

$$M_{i,i+1}^{\mu,\nu} = \frac{\hbar^2}{2m^*}\int_S (\psi_i \nabla\psi_{i+1}^* - \psi_{i+1}^*\nabla\psi_i)\,\mathrm{d}\boldsymbol{S} \tag{87}$$

in which $\psi_i(x, \boldsymbol{x}_\perp)$ is the wave function of an isolated well with energy $E_\mu(\boldsymbol{k}_{\perp,i})$ and lateral momentum $\boldsymbol{k}_{\perp,i}$. The surface integral in equation (87) is over any lateral surface inside the ith barrier that is perpendicular to the growth direction. Choosing the plane at the end of the barrier, an elementary calculation yields

$$|M_{i,i+1}^{\mu,\nu}|^2 = \frac{\pi\hbar^4}{2m^{*2}} B_{i-1,i} B_{i,i+1} T_i\, \delta(\boldsymbol{k}_{\perp,i} - \boldsymbol{k}_{\perp,i+1}), \tag{88}$$

$$B_{i,i+1} = \frac{k_{i+1}}{w + \alpha_i^{-1} + \alpha_{i+1}^{-1}}, \tag{89}$$

$$T_i = \frac{16 k_i k_{i+1} \alpha_i^2\, \mathrm{e}^{-2\alpha_i d_\mathrm{B}}}{(k_i^2 + \alpha_i^2)(k_{i+1}^2 + \alpha_i^2)}. \tag{90}$$

Here k_i and α_i are the wave vectors at the ith well and barrier, respectively, while T_i is the transmission coefficient through the ith barrier. To obtain the tunnelling current, we multiply $eP_{i,i+1}^{\mu,\nu}$ by a factor of 2 due to spin degeneracy and by the difference between the Fermi–Dirac distribution functions of the two wells. Then, we sum over energies and states in both wells. When transforming the sums over the lateral momenta and energies into integrals, we should include broadened densities of states for both wells due to scattering. To simplify matters, we can assume that the broadening functions do not depend on the lateral momentum. The result can be further simplified by noting that the lateral momentum is conserved according to equation (88) and that the integral over $\boldsymbol{k}_\perp$ affects only the distribution functions. We obtain

$$J_{i\to i+1} = \frac{\hbar k_{\mathrm{B}}T}{2m^*}\sum_{\nu=1}^{n_{\max}}\int_0^\infty A_1(\epsilon)A_\nu(\epsilon+eF_il)\mathcal{T}_i(\epsilon)\ln\left[\frac{1+\mathrm{e}^{(\mu_i-\epsilon)/k_{\mathrm{B}}T}}{1+\mathrm{e}^{(\mu_{i+1}-eF_il-\epsilon)/k_{\mathrm{B}}T}}\right]\mathrm{d}\epsilon. \tag{91}$$

In this formula, $n_{\max}$ is the number of subbands in the wells. The integral extends from the bottom of the ith well to infinity, and the bottom of the ith well is the origin of all the energies and the electrochemical potentials [82]. Then, μ_i and $\mu_{i+1} - eF_il$ are the electrochemical potentials of wells i and $(i + 1)$, respectively. μ_i is the *chemical potential* of the ith well referred to its bottom. It depends uniquely on the electron density, n_i, through the formula

$$n_i(\mu_i) = \frac{m^*k_{\mathrm{B}}T}{\pi\hbar^2}\int_0^\infty A_1(\epsilon)\ln[1+\mathrm{e}^{(\mu_i-\epsilon)/k_{\mathrm{B}}T}]\,\mathrm{d}\epsilon, \tag{92}$$

which is similar to equation (50) for miniband transport. The broadening due to scattering is a Lorentzian function centred at the energy of the νth subband, whose width is proportional to the inverse of the scattering time:

$$A_\nu(\epsilon) = \frac{\gamma_\nu/\pi}{(\epsilon-\mathcal{E}_\nu)^2+\gamma_\nu^2}. \tag{93}$$

Moreover, $\mathcal{T}_i(\epsilon)$ is

$$\mathcal{T}_i(\epsilon) = T_i(\epsilon)B_{i-1,i}(\epsilon)B_{i,i+1}(\epsilon) \tag{94}$$

and the wave vectors appearing in these formulae are

$$\begin{aligned}
&\hbar k_i = \sqrt{2m^*\epsilon}, \qquad \hbar k_{i+1} = \sqrt{2m^*[\epsilon+e(d_{\mathrm{W}}+d_{\mathrm{B}})F_i]},\\
&\hbar\alpha_{i-1} = \sqrt{2m^*\left[eV_{\mathrm{b}}+e\left(d_{\mathrm{B}}+\frac{d_{\mathrm{W}}}{2}\right)F_i-\epsilon\right]},\\
&\hbar\alpha_i = \sqrt{2m^*\left(eV_{\mathrm{b}}-\frac{ed_{\mathrm{W}}F_i}{2}-\epsilon\right)},\\
&\hbar\alpha_{i+1} = \sqrt{2m^*\left[eV_{\mathrm{b}}-e\left(d_{\mathrm{B}}+\frac{3d_{\mathrm{W}}}{2}\right)F_i-\epsilon\right]}.
\end{aligned} \tag{95}$$

Green's function calculations also yield equation (91), except that $\mathcal{T}_i(\epsilon)$ is given by a different formula, and the broadening depends on the lateral momentum [78].

The same type of argument leading to equation (91) yields the following formulae for the tunnelling current through the first and last barriers of the SL:

$$J_{0\to 1} = \frac{\hbar k_{\mathrm{B}}T}{2\hbar}\sum_{\nu=1}^{n_{\max}}\int_0^\infty A_\nu(\epsilon)B_{0,1}(\epsilon-eF_0l)T_0(\epsilon)\ln\left[\frac{1+\mathrm{e}^{(\varepsilon_{\mathrm{F}}+eF_0l-\epsilon)/k_{\mathrm{B}}T}}{1+\mathrm{e}^{(\mu_1-\epsilon)/k_{\mathrm{B}}T}}\right]\mathrm{d}\epsilon, \tag{96}$$

$$J_{N\to N+1} = \frac{\hbar k_{\mathrm{B}}T}{2\hbar}\int_0^\infty A_1(\epsilon)B_{N,N+1}(\epsilon+eF_Nl)T_N(\epsilon)\ln\left[\frac{1+\mathrm{e}^{(\mu_N-\epsilon)/k_{\mathrm{B}}T}}{1+\mathrm{e}^{(\varepsilon_{\mathrm{F}}'-eF_Nl-\epsilon)/k_{\mathrm{B}}T}}\right]\mathrm{d}\epsilon \tag{97}$$

in which $\epsilon = 0$ corresponds to the bottom of the first well in equation (96) and to the bottom of the Nth well in equation (97). $\varepsilon_{\rm F}$ and $\varepsilon'_{\rm F}$ are the Fermi energies of the injecting and the collecting regions, respectively.

The integrals in equations (91), (92), (96) and (97) can be approximately calculated in the limit of a scattering broadening that is small compared with subband energies and chemical potentials, thereby yielding explicit formulae. For example, the formulae for the electron density and for the tunnelling current across an inner barrier are [16]

$$n_i = \frac{m^* k_{\rm B} T}{\pi \hbar^2} \ln[1 + {\rm e}^{(\mu_i - \mathcal{E}_1)/k_{\rm B}T}], \tag{98}$$

$$J_{i\to i+1} = \frac{e v^{(f)}(F_i)}{l} \left\{ n_i - \frac{m^* k_{\rm B} T}{\pi \hbar^2} \ln[1 + {\rm e}^{-(eF_i l/k_{\rm B}T)} ({\rm e}^{(\pi \hbar^2 n_{i+1}/m^* k_{\rm B} T)} - 1)] \right\}, \tag{99}$$

$$v^{(f)}(F_i) = \sum_{\nu=1}^{n_{\rm max}} \frac{\hbar^3 l}{2m^{*2}} \frac{(\gamma_1 + \gamma_\nu)\mathcal{T}_i(\mathcal{E}_1)}{(\mathcal{E}_1 - \mathcal{E}_\nu + eF_i l)^2 + (\gamma_1 + \gamma_\nu)^2}. \tag{100}$$

Note that the *forward drift velocity*, $v^{(f)}(F_i)$, is a sum of Lorentzians centred at the resonant field values $F_\nu = (\mathcal{E}_\nu - \mathcal{E}_1)/(el)$. The tunnelling current is a linear function of n_i, but it is a strongly non-linear function of n_{i+1}. Moreover, $J_{i\to i+1} \sim ev^{(f)}(F_i)n_i/l$, for F_i of the order of the first resonant value or larger. For such values, the resulting tunnelling current density has the same shape as assumed in the original *discrete drift model* [68, 75].

In the limit $k_{\rm B}T \gg \pi\hbar^2 n_{i+1}/m^* \approx \pi\hbar^2 N_{\rm D}/m^*$, we can approximate equation (99) by

$$J_{i\to i+1} = \frac{v^{(f)}(F_i)}{l}(n_i - n_{i+1}\,{\rm e}^{-(eF_i l/k_{\rm B}T)}). \tag{101}$$

This equation can be rewritten as a discrete drift–diffusion electronic current density,

$$J_{i\to i+1} = \frac{e n_i v(F_i)}{l} - \frac{eD(F_i)}{l^2}(n_{i+1} - n_i), \tag{102}$$

$$v(F_i) = v^{(f)}(F_i)(1 - {\rm e}^{-(eF_i l/k_{\rm B}T)}), \tag{103}$$

$$D(F_i) = v^{(f)}(F_i) l\, {\rm e}^{-(eF_i l/k_{\rm B}T)} \tag{104}$$

in which $v^{(f)}(F_i)$ is given by equation (100). Note that the drift velocity in equation (103) is somewhat similar to the Lorentzian dependence given by the simpler theory of Kazarinov and Suris [66]. The additional prefactor in equation (100) yields a more complicated field dependence in our formulae. Our drift velocity is also similar to the escape time formula used by Rogozia and Grahn [88] to give an estimation of the frequency of current self-oscillations, provided that more precise expressions for $\mathcal{T}_i$ with different electron masses for the wells and barriers are used (cf section 5.2.2).

In the opposite limit $k_{\rm B}T \ll \pi\hbar^2 n_{i+1}/m^* \approx \pi\hbar^2 N_{\rm D}/m^*$, equation (99) becomes

$$J_{i\to i+1} = \frac{e v^{(f)}(F_i)}{l} \left[n_i - \left(n_{i+1} - \frac{m^* e F_i l}{\pi \hbar^2} \right) \theta \left(n_{i+1} - \frac{m^* e F_i l}{\pi \hbar^2} \right) \right]. \tag{105}$$

Here $\theta(x)$ denotes the Heaviside unit step function, and we have ignored an exponentially small term for $n_{i+1} < m^* e F_i l/(\pi\hbar^2)$.

We will use discrete model equations in sections 3–5 to describe EFD formation, switching of domains and current self-oscillations in weakly coupled SLs, respectively.

The experimental work on sequential resonant tunnelling in weakly coupled SLs has been reviewed by Grahn [89].

2.4. Wannier–Stark hopping

The WS states become increasingly localized as the applied constant electric field increases. For sufficiently high fields, each WS state is localized in a different well of the SL. Then, a master equation describing transitions between WS states due to scattering yields a description of non-resonant tunnelling, provided that only the lowest miniband is used as the basic state. Including more minibands, it is possible to describe resonant tunnelling as well [53, 90]. Historically, Tsu and Döhler [91] gave a description of WS hopping as a basis of calculating the electron drift velocity. They considered a basic state with only one miniband, hopping transitions between the first and the second neighbouring WS states, phonon scattering with an equilibrium distribution and an electron Fermi–Dirac distribution function at the lattice temperature. Later, Calecki *et al* [92] and Suris and Shchamkhalova [93] showed that the same formulae could be derived from a density matrix formulation using the WS states as a basis.

Transport by WS hopping is a very good counterpart of the Boltzmann description of miniband transport at constant electric field. At very low electric field values, the miniband quantitatively describes charge transport in strongly coupled SLs, whereas WS hopping gives an unphysical divergence of the electron drift velocity ($\propto 1/F$ as $F \to 0$). At high field values, deep in the region of negative differential conductivity (NDC), the miniband description becomes worse than WS hopping. Common to both descriptions is the possibility of a very accurate description of scattering processes using Fermi's golden rule of evaluating the scattering rates and good numerical tools [53]. Recently, Rott [53] and Rott *et al* [90,94] have extended WS hopping to lower field values so as to give a precise kinetic theory of charge transport in strongly coupled SLs (over a range of applied constant electric fields that overlaps with the outer field range, for which miniband transport holds). They assume that scattering times are much larger than tunnelling times, which is the opposite situation to sequential tunnelling in weakly coupled SLs. Rott [53] has considered the effects of electron heating by finding the stationary solution of the master equation for WS hopping transport and by using it to calculate the electron drift velocity. The results improve the ones obtained with a Fermi–Dirac distribution function [53].

The experimental work on WS localization and Bloch oscillations in strongly coupled SLs has been reviewed by Aguló-Rueda and Feldmann [3].

2.5. Bloch oscillations

Bloch oscillations are spatially homogeneous (coherent) self-oscillations of the electron distribution in an SL. The electric field profile inside the SL is independent of space during Bloch oscillations, and therefore electron transport can be seen as hopping between WS levels. The existence of these transitions between WS levels has been demonstrated experimentally by Feldmann *et al* [4]. From a theoretical perspective, there is some confusion due to the different theories and regimes that describe electron transport in SLs. Thus, it is better to rephrase the question about the existence of Bloch oscillations in a way that can be answered mathematically. *Is there a spatially homogeneous, time-periodic oscillation of the electron distribution that is stable*? This question should be *posed and answered* within the framework of a quantum kinetic theory for SLs with several minibands. Since this does not seem possible at the time of writing this paper, let us pose this question in the framework of semiclassical miniband transport. We would like to find a stable solution of the Boltzmann–Poisson system of equations

$$\frac{\partial f}{\partial t} + \frac{1}{\hbar}\frac{\mathrm{d}\mathcal{E}_1}{\mathrm{d}k}\frac{\partial f}{\partial x} + \frac{eF}{\hbar}\frac{\partial f}{\partial k} = -\nu_{\mathrm{en}}(f - f^{\mathrm{FD}}) - \nu_{\mathrm{imp}}\frac{f(x,k,t) - f(x,-k,t)}{2} \tag{106}$$

together with equations (49)–(51), for appropriate boundary conditions that are spatially homogeneous or almost homogeneous and time-periodic.

Boundary conditions (BCs) corresponding to contact regions can be posed for DDEs and then translated to BCs for the Boltzmann equation by using the ideas of Cercignani *et al* [95]. Let us start with a BC fixing the electron density at the collector to be N_{Dc} at $x = L = Nl$. If we define f^+ to be the distribution function at $x = L$ for $k > 0$ and similarly define f^-, equation (50) and the following BC,

$$f^+ = \frac{f^{(0)}}{(l/2\pi)\int_0^{\pi/l} f^{(0)}\,\mathrm{d}k}\left(N_{\mathrm{Dc}} - \frac{l}{2\pi}\int_{-\pi/l}^{0} f^-\,\mathrm{d}k\right) \tag{107}$$

yield $n(L, t) = N_{\mathrm{Dc}}$. The meaning of this BC is that the electrons that enter the contact, having a distribution f^+, become ‘thermalized’ to the leading order distribution in equation (62) with a factor that ensures charge neutrality at the contact doping density.

We would like to impose a BC at the injecting contact that is compatible with commonly used BCs for DDEs. In many studies of self-oscillations, the electronic current density is assumed to be a linear function of the electric field, according to Ohm’s law, i.e.

$$\frac{e}{2\pi}\int_{-\pi/l}^{\pi/l} v(k) f\,\mathrm{d}k = \sigma F \tag{108}$$

in which σ is the contact conductivity. We can recover this BC from the following one for the distribution function at $x = 0$:

$$f^- = -\frac{2\pi\hbar\sigma F}{e\Delta_1} - \frac{f^{(0)}}{\int_{-\pi/l}^{0} v(k) f^{(0)}\,\mathrm{d}k}\int_0^{\pi/l} v(k) f^+\,\mathrm{d}k. \tag{109}$$

Now the mathematical question on whether the Bloch oscillations can be obtained within the semiclassical miniband formulation can be phrased as follows. *Can we find a stable solution of the Boltzmann–Poisson system of equations (106) and (49)–(51), satisfying the BCs of equations (107)–(109) and the bias condition* $\int_0^L F\,\mathrm{d}x = V$, *that is spatially homogeneous or almost homogeneous and time-periodic*?

Within the semiclassical Boltzmann–Poisson framework, there has been no attempt to answer this question as we have formulated it here. However, incomplete answers can be gathered from previous work. Typically, previous authors have studied the linear stability of the stationary solution of equation (62) with constant electric field, *disregarding BCs*. They have also studied the response of the distribution function (and therefore of the current) to a small ac field superimposed on a large constant external field. These studies are relevant to deciding whether there exist stable space-independent high-frequency oscillations, once the BCs are included in studies of the appropriate solutions and their stability. Ktitorov *et al* [33] found that the real part of the high-frequency conductivity, $\sigma(\omega)$, is negative, until the frequency reaches the Bloch frequency $\omega_{\mathrm{B}} = eFl/\hbar$, and then it becomes positive. $\sigma(\omega)$ has a negative and sharp minimum close to ω_{B}, which may be important for designing a Bloch oscillator device [96]. Related work by Ignatov and Shashkin [35, 97], Ignatov *et al* [36] and Ryndyk *et al* [37] also ignores BCs, although Kroemer has pointed out the importance of studying the influence of BCs in deciding whether high-frequency, space-independent self-oscillations may occur in realistic devices.

In the framework of WS hopping transport, the question on the stability of Bloch oscillations cannot be answered because the mere existence of WS states already assumes that the electric field is space independent. To find out whether such states are stable, we should allow spatially inhomogeneous disturbances of the electron distribution function and see whether they become spatially homogeneous. The same can be said about density matrix theories that use accelerated Bloch states: such states presuppose a homogeneous electric field. This is not surprising: WS and accelerated Bloch states are equivalent bases of a Hamiltonian for an electron in the presence of a spatially periodic potential and a space independent electric field. WS states correspond to a representation of the electric field by means of a scalar potential, whereas accelerated Bloch states correspond to the representation by means of the vector potential [98, 99].

In the framework of sequential tunnelling theories, electron tunnelling is not coherent by definition. Therefore, the question of coherent oscillations does not make sense. However, we can investigate whether a stable space-independent and time-periodic field profile exists. The corresponding mathematical question and the related question about the existence of a driven space-independent oscillation can be answered by analysing equations (82), (84), (85), (91), (96) and (97) for different values of voltage and doping density. Although this general analysis has not been carried out, we can get an idea of the answer by examining previous work on simpler models. In principle, the field profile is almost uniform only if there is very little charge in the SL. Undriven, space-independent oscillations are possible only for small SLs or for large SLs with biases very close to the voltage threshold at which the stationary uniform profile ceases to be stable [100, 101]. Under these conditions, the frequency of the resulting undriven oscillations is not much larger than the one corresponding to monopole or even dipole recycling. We shall come back to these questions in sections 5 and 6.

3. Static domains

3.1. Pinning of wave fronts, static domains and theoretical considerations

The non-linear phenomenon in weakly coupled SLs are dominated by the formation and motion of EFDs. Domain walls separating two EFDs may be pinned because of the spatially discrete structure of a weakly coupled SL, thereby producing multistable branches of static EFDs under voltage bias conditions. By switching the voltage, we can probe the motion of domain walls and observe the complex non-linear behaviour of the EFDs.

This type of phenomenon does not occur in strongly coupled SLs, where the non-linear phenomena due to motion of EFDs are undriven, and driven self-oscillations of the current, which are akin to the Gunn effect in bulk semiconductors and will be reviewed in section 5. In strongly coupled SLs, the current self-oscillations are due to the periodic motion of charge dipoles (which are smooth pulses of the electric field) on an EFD. The multistable static domains studied in the remainder of this section occur only in weakly coupled SLs.

Typically, EFDs are regions of a weakly coupled SL having a uniform (or almost uniform) value of the electric field. An EFD is bounded by either a domain wall that connects it to a different domain or by the SL boundaries. To characterize the behaviour of EFDs, we should investigate the behaviour of their domain walls. Mathematically speaking, these domain walls are stable travelling wave front solutions for the chosen model equations describing the SL, in the absence of any boundaries and under dc current bias conditions. Wave fronts are transition regions, in which the electric field varies monotonically from its value in one EFD to its value in the other EFD. An increasing field profile corresponds to a charge accumulation layer (CAL), while a decreasing field profile corresponds to a charge depletion layer (CDL). Even pulses of the electric field can be described by the motion of two wave fronts, a CAL and a CDL, which form their leading and trailing edges.

What is the role of these idealized wave fronts in finite, voltage-biased SLs? In finite SLs, boundary conditions modify the extent and shape of EFDs, but wave fronts are still useful for describing their field profile. The reason for this is that static EFDs in a voltage-biased SL

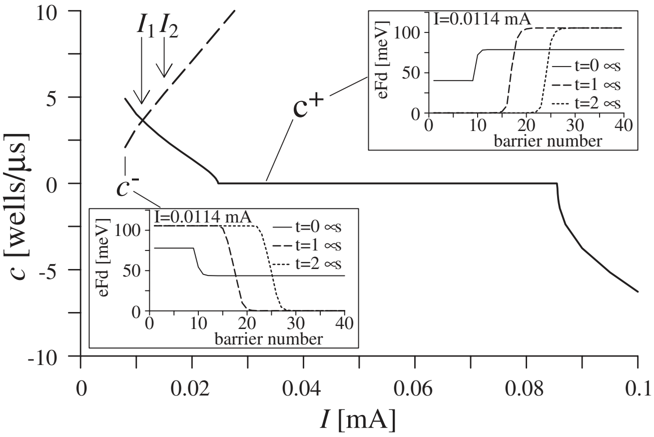

Figure 4. Velocities of wave fronts shown in the inset versus current bias, I. The parameters of the GaA/AlAs SL are $d_W = 9\,\text{nm}$, $d_B = 4\,\text{nm}$, $N_D = 1.5 \times 10^{11}\,\text{cm}^{-2}$ and $S = 1.13 \times 10^{-4}\,\text{cm}^2$ (courtesy of A Wacker).

occur naturally with constant current, and boundary conditions affect very small regions near the ends of a long SL. If the current is changing with time in a long voltage-biased SL, its envelope changes on timescales that are much longer than the dielectric relaxation time. Then, the electric field profile adjusts adiabatically to the instantaneous value of the average current. Such a profile can then be approximated by EFDs and by CALs or CDLs, defined as wave fronts of an infinite SL with a constant value of the current. This behaviour will be explained in more detail in sections 4 and 5.

3.1.1. Pinning in current-biased, infinite SLs. Let us consider the theory of wave fronts in current-biased, infinite SLs. The main difference between wave fronts of spatially discrete and continuous autonomous equations (no imperfections or spurious time- or space-dependent coefficients) is the phenomenon of pinning. Roughly speaking, wave fronts of continuous equations have to move (except at single values of a control parameter that characterizes their non-linearities), whereas wave fronts of discrete equations can be pinned for entire intervals of their control parameter [14, 102, 103]. In weakly coupled SLs, for appropriate values of the dc voltage, two stationary EFDs can coexist separated by a domain wall pinned at any given SL period [9]. This fact itself suggests that spatially discrete equations describe weakly coupled SLs. The absence of static EFDs in strongly coupled SLs very likely indicates that spatially continuous equations describe them well.

The pinning and the motion of wave fronts (domain walls) are illustrated in figures 4 and 5. The results shown in these figures have been obtained from stable solutions of the discrete model, with tunnelling currents given by equation (99) for figure 4 and its approximation in equation (101) for figure 5. Figure 4 depicts the velocity of a wave front moving at constant speed in a doped, infinite SL under constant current-bias conditions. For the doping density of this SL, wave fronts having a spatially decreasing profile of the electric field move from left to right, i.e. *downstream*, following the motion of individual electrons for any value of the current. These wave fronts correspond to moving CDLs. The behaviour of wave fronts having an increasing field profile, and thus corresponding to CALs, is more interesting. Below a first critical current, the wave front moves downstream too. There is an interval of currents, between the first and the second critical currents, in which the wave front has zero velocity: it is pinned in a well, whose position depends on the initial conditions of the numerical simulation.

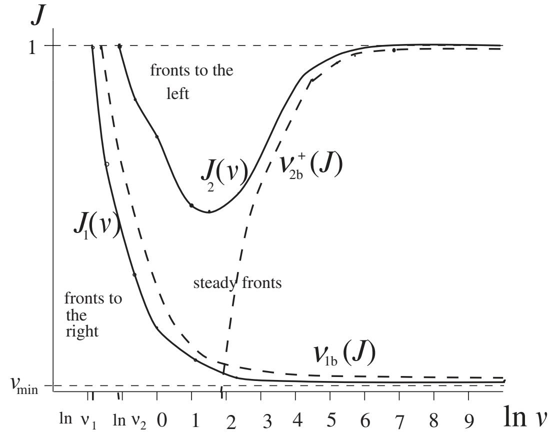

Figure 5. Critical currents, J_1 and J_2 (in units of eN_Dv_M/l), versus logarithm of the dimensionless doping density $\nu = eN_D/(\varepsilon F_M l)$. The dashed lines indicate the theoretical bounds $\nu_{1b}(J)$ and $\nu^+_{2b}(J)$. From [9].

For currents larger than the second critical current, the wave front moves *upstream*, against the motion of single electrons. These properties have been proven by Carpio *et al* [9]. Near the critical currents, the evolution of the electric field in a single well or in several wells determines the pinning/depinning transition according to the active well theory described in [16, 103, 104]. As the current approaches one of its critical values from the side corresponding to moving fronts, the electric field profile acquires a step-like appearance. The steps become infinitely long, and the wave front is pinned at the critical currents [104]. The critical exponent of the transition, $c \propto |I - I_c|^\gamma$, is $\gamma = \frac{1}{2}$ for perfect SLs and $\gamma = \frac{3}{2}$ if the doping density in the wells fluctuates weakly and randomly about its mean value [105].

Figure 5 shows that the existence of wave front pinning depends on the SL doping density. Below a first critical doping density, all CALs move downstream (just as in continuous models of strongly coupled SLs or in the Gunn effect). A useful lower bound for the first critical doping density is [9, 101]

$$N_D > \frac{\varepsilon(F_m - F_M)}{e} \frac{v_m}{v_M - v_m}, \tag{110}$$

provided that the local maximum and minimum of the drift velocity as a function of the field are (F_M, v_M) and (F_m, v_m), respectively. To obtain a lower bound of the doping density, above which pinning of CDLs is possible, we have to substitute v_M instead of v_m in the numerator of equation (110) [15, 101]. Between the first and a second critical doping density, CALs can be pinned or move downstream, depending on the current. Lastly, above the second critical doping density, the wave fronts may also move upstream [9]. Note that the pinning interval increases with an increasing SL doping density.

In discrete equations that are second order in the spatial differences, the nature of the pinning/depinning transition depends on the dynamics. Discrete SL models are dissipative and behave according to our previous discussion. The wave fronts of these equations either move or are pinned [102], depending on the value of the control parameter (the current in current-biased SLs). In models with inertia (such as chains of non-linear oscillators), the pinning/depinning transition may be much more complicated and involve the coexistence between moving and pinned wave fronts for some intervals of the control parameter [106].

3.1.2. Static domains and current spikes in voltage-biased SLs. We shall see in sections 4 and 5 that many non-linear phenomena in real SLs can be understood by analysing the motion of wave fronts in ideal current-biased, infinite SLs [16]. In finite, weakly coupled SLs under voltage bias, the motion and pinning of wave fronts leave two distinct traces in the experiments: I–V characteristics containing as many current branches as periods in the SL and current spikes as a CAL moves. These two features are absent in strongly coupled SLs. Both features occur in spatially discrete autonomous equations and not in spatially continuous equations, which help us select the correct SL theory for each case. Solutions of discrete models based on next-neighbour tunnelling currents and Poisson equations seem to have the same *qualitative behaviour*, notwithstanding the different scattering mechanisms or physical effects considered in the models. These mechanisms will be important when seeking quantitative agreement with experimental observations, precise control of devices, etc.

High-frequency current spikes accompany the well-to-well hopping motion of a CAL through the SL. They are observed in numerical simulations of discrete SL models and in experiments on relocation of EFDs (section 4) or self-sustained oscillations of the current (section 5). The number of spikes in a given time trace of the current tells us how many wells a mature CAL has traversed inside the SL [81, 107]. This is of fundamental importance for interpreting experimental results because the field profile inside the SL cannot be observed directly. In order to understand relocation of EFDs and self-oscillations in finite SLs under voltage bias, we shall describe in sections 4 and 5 how to use the adiabatic motion of wave fronts under slow variations of the current and the influence of the boundary conditions.

The simplest solutions of discrete models for doped, weakly coupled SLs under dc voltage bias are time-independent solutions. Their shape depends on the voltage range, the SL configuration (d_W, d_B) and the doping density. If the tunnelling current of the uniform field profile $F_i = F$, $n_i = N_\mathrm{D}$ and $J_{i\to i+1} = \mathcal{J}(F, N_\mathrm{D}, N_\mathrm{D})$ has several peaks corresponding to resonances between different subbands, the current–voltage characteristic of the SL exhibits different regions between peaks called plateaus. Restricting ourselves to a voltage range in one plateau, we need to consider a region with only a single maximum and a single minimum of the forward drift velocity in equation (100). In the second and successive plateaus, the tunnelling current is approximately proportional to the forward drift velocity times the electron density, and therefore we have the discrete drift model, which is first-order in the differences and easy to solve graphically [68, 75]. Equations (82), (84) and (102) with $D \equiv 0$ yield $lJ/e = v(F_i)[N_\mathrm{D} + \varepsilon(F_i - F_{i-1})/e]$, from which

$$F_{i-1} = F_i + \frac{eN_\mathrm{D}}{\varepsilon} - \frac{lJ}{\varepsilon v(F_i)} \equiv f(F_i; J) \tag{111}$$

for $i = 1, \ldots, N$. In order to determine the field, F_0, at the injecting contact, we equate the tunnelling current at the boundary to the total current density, i.e. $J_{0\to 1}(n_1, F_0) = J$, in which $n_1 = N_\mathrm{D} + \varepsilon\,(F_1 - F_0)/e$ according to equation (82) for $i = 1$. Solving this equation, we obtain F_0 as a function of F_1 and of J. Many calculations have assumed simpler boundary conditions, $n_1 = (1 + c)N_\mathrm{D}$ (constant electron density) [68, 101], or Ohm's law, $J_{0\to 1}(n_1, F_0) = \sigma F_0$ [15, 78].

The first-order difference equation (111) is easy to solve graphically once F_0 is known. Note that uniform field distributions solve $v(F) = \varepsilon lJ/(eN_\mathrm{D})$. Therefore, there are three such solutions for $v_\mathrm{m} < \varepsilon lJ/(eN_\mathrm{D}) < v_\mathrm{M}$. These solutions, $F^{(1)}(J) < F^{(2)}(J) < F^{(3)}(J)$, are the fixed points of the mapping in equation (111), which provides F_i as a multivalued function of F_{i-1}. Only $F^{(1)}(J)$ and $F^{(3)}(J)$ are stable solutions under the discrete dynamics generated by the mapping. Let us see now how to construct solutions of equation (111) that start from F_0 given by the boundary condition. If we are looking for solutions with an increasing field profile, we locate F_0, for example, on the first branch of $f(F_i; J)$ defined in equation (111), and graphically solve the mapping. Rapidly, F_i tends towards the stable fixed point of the mapping $F^{(1)}(J)$ as i increases. One possible solution is therefore a single EFD with $F_i = F^{(1)}(J)$, except in a small region near the cathode needed to accommodate the boundary condition. This is the solution having an almost uniform field profile, and it corresponds to an LFD covering the whole SL. The corresponding voltage is small. Are there other solutions having the same voltage?

Since F_i is a multivalued function of F_{i-1} according to equation (111), we find other solutions by allowing a jump from $F^{(1)}(J)$ (or its neighbourhood) towards a different branch of the mapping at any given SL period, $i = i_0$. Such jumps are possible only if the local minimum of the mapping $f(F_i; J)$ is smaller than $f(F^{(1)}(J); J)$, which occurs for sufficiently large doping densities. Below a critical doping density, which can be estimated using equation (110), the only stable static solution is the almost uniform one [75, 101]. For larger values of the doping density, jumps between branches of the discrete mapping in equation (111) are possible and give rise to different static solutions having the same J. Their field profile consists of two EFDs separated by a CAL. The second EFD has a field value $F_i = F^{(3)}(J)$, provided that the SL has a sufficient number of periods for the mapping to reach its second stable fixed point. Note that for a weakly coupled SL with small broadening due to scattering the value $F^{(1)}(J)$ in the LFD is close to a resonance, while the value $F^{(3)}(J)$ in the HFD can be quite far from resonance if the current at the second resonant peak of the plateau considered is much larger than the current at the first peak.

It turns out that only solutions with no jumps (corresponding to a single EFD) or with jumps from the first to the third branch of the mapping are stable solutions of the time-dependent problem. Solutions with one jump have one LFD and one HFD separated by a CAL that can be located at any $i = i_0$. The corresponding field profiles have the same J, but different voltages, as indicated by equation (85). In a diagram of J versus voltage, these stable solutions of the time-dependent problem form N disconnected curves that can be observed in the current–voltage characteristic of the SL. The branches of stable solutions are connected (at $J_{\mathrm{M}} = eN_{\mathrm{D}}v_{\mathrm{M}}/l$ and at some $J_{\min} = eN_{\mathrm{D}}v_{\min}/l$ depending on the doping density) to branches of unstable solutions, whose field profile displays one intermediate jump from the first to the second branch of the mapping [75, 101]. It is also clear that, by including more than two peaks of the drift velocity in our construction and choosing the appropriate SL doping density, we can construct solutions with more than two EFDs [76, 108]. For a sufficiently large doping density, solutions including CDLs can be similarly constructed [101]. For undoped weakly coupled SLs, Bonilla *et al* [68] constructed static domain solutions using similar theoretical ideas, but with the density of photoexcited carriers playing the role of the doping density in doped SLs.

For lower voltages on the first plateau, the term containing n_{i+1} in equation (99) cannot be ignored, and the stationary solutions solve a second-order difference equation. In this case, it is more convenient to numerically solve the time-dependent equations and find the stable stationary profiles. The results are similar for different discrete models, and the corresponding field profiles and current–voltage characteristics are similar to the ones obtained with the mapping in equation (111) for plateaus with higher voltages. The only qualitative difference is that the maximum current for field profiles in the first plateau is smaller than the current, J_{M}, corresponding to a uniform profile with $n_i = N_{\mathrm{D}}$ and $F_i = F$. Note that, except for small regions close to the boundaries, the constructed static solutions coincide with wave fronts pinned at the SL period $i = i_0$ corresponding to the CAL. Prengel *et al* [74] numerically solved a discrete model for voltages on the first plateau, and Kastrup *et al* [109] compared these solutions with experimental data. Similar results can be obtained with the tunnelling current in equation (99) as shown in figure 24 of [15], using an expression for the forward drift velocity slightly different from the one in equation (100).

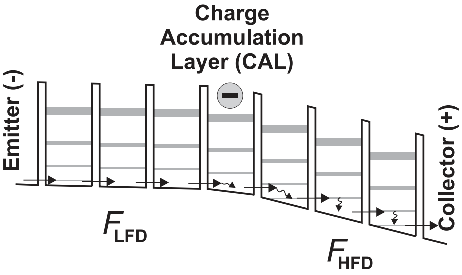

Figure 6. Schematic diagram of the distribution of the low- (F_{LFD}) and high-field domain (F_{HFD}) in a weakly coupled SL.

For all plateaus, plotting the current–voltage diagram of the stable solution branches yields a succession of disconnected curves, all having the same maximum and minimum values of the current. For a given voltage, two or more stable stationary solutions having different current values are possible. They are found by solving the time-dependent problem with different step-like initial conditions. One simple way of finding these branches is to follow in the numerical simulations the same procedure as in the experiments: sweep up or down systematically the current–voltage characteristic [109]. If we want to determine the influence of external parameters (doping density, temperature, etc) on the stable stationary or time-dependent solutions and their current–voltage diagram, it is better to use numerical continuation algorithms [80, 110].

3.2. Field distribution and I–V characteristics

The initial observation of the formation of static EFDs in semiconductor SLs goes back to the early days of molecular-beam epitaxy (MBE). The conductance of a doped GaAs/AlAs SL showed periodic structures as a function of the applied voltage [5]. Note that, although Esaki and Chang were searching for Bloch oscillations [1], which were discovered only in the early 1990s in strongly coupled SLs [4], they observed a very different effect, since they were investigating a weakly coupled SL. Static EFDs can be introduced either by doping the SL or using an undoped one under photoexcitation [111]. We will only discuss undoped and n-doped SLs, but not p-doped ones, since for holes the picture becomes more complicated due to the more complex structure of the valence band.

Under static EFD formation, the spatial distribution of the electric field inside the SL breaks up into two regions as shown in figure 6: the LFD consists of a region of a lower uniform electric field on the injecting contact side forming the emitter of the SL, while the HFD is formed by a region of a higher uniform electric field on the receiving contact side representing the collector. These two domains are separated by a domain boundary in the form of a CAL. The domain boundary is essentially confined to a single SL period, i.e. to one quantum well of the SL, since the SL is weakly coupled and charge can only reside in the wells and not in the barriers. When the applied bias sweeps across a discontinuity from one current branch to the next, the domain boundary moves by precisely one SL period [75]. The distribution for a given electric field can also contain three domains simultaneously as discussed by Grahn *et al* [108] and Mityagin *et al* [76]. If the doping density becomes larger than the charge density of the CAL at the domain boundary, it is also possible that a CDL is formed inside the SL in addition to the CAL. The spatial distribution of EFDs has been investigated using photoluminescence spectroscopy, varying the excitation energy in order to change the penetration depth of the light, as well using by cathodoluminescence spectroscopy and imaging. For typical carrier densities in the $10^{17}\,\mathrm{cm}^{-3}$ range and not too large electric-field strengths, the HFD is always located near the anode, i.e. the collector [112–114]. At the same time, a detailed analysis of the cathodoluminescence spectra [113] as well as cathodoluminescence images [114] proved that there is only a single CAL in the SL.

After the initial observation of EFDs in semiconductor SLs in 1974, it took about a decade before the subject was taken up again by Furuta *et al* [115] and Kawamura *et al* [116]. In both cases, weakly coupled SLs were investigated. Furuta *et al* [115] observed a splitting of the photoluminescence spectra in a doped GaAs/(Al,Ga)As SL. This splitting indicates the presence of two regions with different field strengths, since due to the quantum-confined Stark effect [117] the energy gap of a quantum well decreases with increasing electric field. Kawamura *et al* [116] investigated the transport properties of an (In,Ga)As/(In,Al)As SL grown lattice-matched on InP with the undoped SL embedded in a p–i–n-structure. This system showed EFD formation under forward bias. The voltage region where EFDs were observed increased with an increasing number of periods. Choi *et al* [118] also reported a correlation of the number of conductance peaks with the number of SL periods for a weakly coupled GaAs/(Al,Ga)As SL. Subsequently, it was realized that this topic is very important for devices based on weakly coupled SLs or multiple-quantum-well structures [119, 120]. Kawamura *et al* [121] and Vuong *et al* [122] reported the formation of EFDs due to higher electronic subbands, i.e. originating from resonant tunnelling between the first and second subbands (LFD) as well as between the first and third subbands (HFD). Choi *et al* [123] investigated the effect of a parallel and perpendicular magnetic field on the EFD formation, which will be discussed in more detail in section 3.4. Electric-field screening phenomena under photoexcitation were studied by Cavicchi *et al* [124] and Snow *et al* [125]. Further evidence for EFD formation was observed by Helm *et al* [126], Kawamura *et al* [127], Vuong *et al* [128], Helgesen and Finstad [129], Helm *et al* [130] and Helgesen *et al* [131]. By the early 1990s, EFDs had been identified in the systems GaAs/AlAs, GaAs/(Al,Ga)As, (In,Ga)As/(In,Al)As on InP and (In,Ga)As/InP. A comparison between EFD generation by doping and photoexcitation may be found in Grahn *et al* [111].

A direct proof for the coexistence of two or more regions with very different field strengths was derived from photoluminescence measurements in undoped SLs [108, 132]. In these experiments, the LFD and HFD were identified through separate PL lines, which did not change their position, but only their intensity, when the electric field was increased. Subsequently, electronic Raman scattering experiments showed that the intensity of the intersubband transition between the first and second subbands increases linearly with increasing electric field due the expanding HFD domain, while it remains nearly constant in the region of a single domain [133]. A splitting of the Raman line by intersubband excitations was reported by Murugkar *et al* [134] in the coexistence region of two EFDs of an undoped GaAs/AlAs SL under photoexcitation. Additional PL and Raman experiments directly demonstrated that the field strength of the LFD is very close to its resonance value, while the field strength of the HFD is significantly lower than the corresponding resonance field strength [135, 136]. The transport mechanism in the LFD is therefore sequential resonant tunnelling, while in the HFD the dominating transport mechanism is non-resonant tunnelling.

In 1991, Grahn *et al* [10] demonstrated that the I–V characteristics of highly doped, weakly coupled SLs exhibit as many well-defined branches on a current plateau as there are periods in the SL due to the formation of *static* domains. Two adjacent branches are separated by a discontinuous jump in the current level. The inset of figure 7 shows the I–V characteristic of a GaAs/AlAs SL with 40 periods, $d_{\mathrm{W}} = 9.0\,\mathrm{nm}$, $d_{\mathrm{B}} = 4.0\,\mathrm{nm}$ and a doping density of $3 \times 10^{17}\,\mathrm{cm}^{-3}$, corresponding to a sheet concentration of $N_{\mathrm{D}} = 1.5 \times 10^{11}\,\mathrm{cm}^{-2}$ per well recorded at 6 K for both sweep directions. The current plateau between 0.4 and 5 V

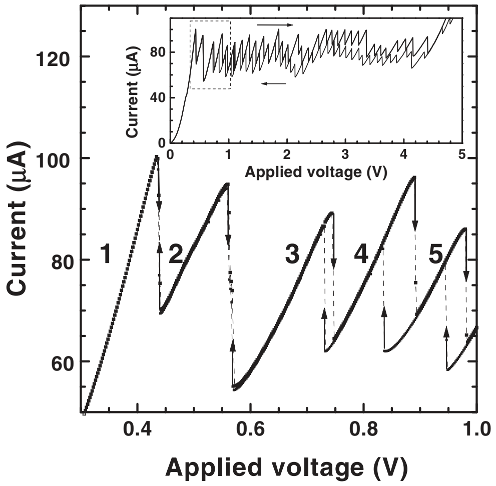

Figure 7. I–V characteristics of the first five branches (1, 2, 3, 4 and 5) for up and down sweeps as indicated by the arrows at 5 K. Inset: full I–V characteristics. From [184].

originates from EFD formation, where the LFD is associated with miniband transport or sequential resonant tunnelling between the ground-state subbands in adjacent wells and the HFD corresponds to sequential resonant tunnelling between the ground state of one well and the second subband in the adjacent well, as described by Grahn *et al* [10, 132] and Kastrup *et al* [109]. The domains are separated by a domain boundary in the form of a charge monopole, i.e. a negatively charged CAL. For every current jump in the up sweep, the CAL moves by one period towards the emitter. Figure 7 shows an enlarged section of the full I–V characteristic in the inset. The variations in the current minima and maxima are due to small fluctuations (below 5%) of the doping level between the different wells, while interface roughness and well width fluctuations result in a much smaller modulation of the branches [137–142]. The theoretical and experimental investigation of an intentionally perturbed SL, which has a single, significantly wider barrier in the 32nd period out of 40, demonstrated the impact of such a perturbation on the overall I–V characteristics [143]. When (Al,Ga)As contact layers are used as window layers for optical excitation, the actual voltage for the onset of EFD formation as well as for a particular current jump may shift between different measurements, especially after heating the sample to room temperature, due to the presence of *DX* centres in these contact layers [144].

The motion of the CAL through the SL has also been identified using capacitance–voltage measurements [145, 146], which allow determination of the charge density of the CAL at the domain boundary [147]. The two-dimensional charge density, $n_{2\mathrm{d}}$, at the domain boundary can be estimated from Poisson's equation,

$$n_{2\mathrm{d}} = \varepsilon\varepsilon_0 \frac{\Delta F}{e}, \tag{112}$$

where ε and ε_0 denote the dielectric constants of the material and of vacuum, respectively, and ΔF is the electric field change at the domain boundary. For a field difference of $\Delta F = 120\,\mathrm{mV}$ per 13 nm and an average dielectric constant $\varepsilon \sim 12$ for GaAs and AlAs, we obtain a carrier density of $n_{2\mathrm{d}} = 6.1 \times 10^{11}\,\mathrm{cm}^{-2}$ for a fully developed CAL. A typical nominal doping density of the GaAs wells corresponds to $n_{2\mathrm{d}} = 1.5 \times 10^{11}\,\mathrm{cm}^{-2}$, which is about a factor of 4 smaller than the carrier density necessary to form the domain boundary within a single well. Since the number of jumps in the I–V characteristic is correlated with the number of SL periods, the domain boundary in the static case is formed by a CAL within a single well. In contrast, a CDL would extend over at least four wells because the positive charge density is limited by the doping concentration.

The EFD formation is usually observed because of resonant coupling between the first subband in one well and the second, third or fourth subband in the adjacent well of the SL structure [108, 132]. However, in the investigations by Helm *et al* [126, 130], Stoklitskii *et al* [148], Mityagin and Murzin [149], Mityagin *et al* [76] and Rasulova *et al* [150], the wells were extremely wide, so that EFDs were formed due to resonant coupling not only between the first and the second, third and fourth subbands, but also between the first and the fifth, sixth, and in some cases even the seventh subbands. Xu *et al* [151] and Schneider *et al* [152] reported the observation of EFDs due to the coupling between a bound and a continuum state in n-doped multiple quantum wells with only a single bound state inside the wells. Han *et al* [153] investigated the formation of EFDs in a graded-gap SL, i.e. the GaAs well width increased from 3.0 to 9.5 nm in steps of 0.5 nm, while the (Al,Ga)As barrier width remained constant at 10.0 nm. Since the energy separation between the first and second subbands of the GaAs wells decreases with increasing well width, the separation of the current branches increases with increasing field.

All observations of EFDs discussed so far are based on sequential resonant tunnelling between Γ-states in adjacent wells. However, in GaAs/AlAs SLs with sufficiently narrow wells, the transport through the SL can also be dominated by Γ–X–Γ transfer from the GaAs well into the AlAs barrier and back to the GaAs well. Zhang *et al* [154] reported the observation of EFD formation in GaAs/AlAs SLs, where the ground state of the X band in the AlAs barrier is located between the first and second subbands of the GaAs well. The HFD in this system is due to resonant transfer from the ground state in the GaAs well to the lowest X state in the AlAs barrier and back via real-space transfer to the ground state in the next GaAs well. Sun *et al* [155] identified a transition for EFD formation as a function of pressure. Below a critical pressure, the HFD is due to sequential resonant tunnelling between Γ states, while above the critical pressure it is due to Γ–X transfer. Mimura *et al* [156] investigated a type-II SL, where the lowest electron state in the conduction band is the X state in the barrier. Here, the static domain formation is a result of resonant transfer between the first excited X state in the AlAs barrier and the ground Γ in the GaAs well.

3.3. Bi- and multistability

For a given applied voltage, the number of periods in the LFD and HFD is not uniquely determined. The current can vary between the maximum velocity of the LFD and the minimum velocity of the HFD. Therefore, the I–V characteristics exhibit a hysteresis or multistability [109] as already shown in figure 7. Another example with four stable operating points is shown in figure 8 for a GaAs/AlAs SL with 40 periods, $d_W = 9.0$ nm, $d_B = 4.0$ nm and a three-dimensional doping density of 1×10^{18} cm^{-3}. These four operating points can be reached by reversing the sweep direction of the voltage at different points. They correspond to four different locations of the domain boundary in the SL as shown in figure 9. For the operating point with the highest current (point 1 in figures 8 and 9), the electric-field strengths in the LFD and HFD are highest. At the same time, the LFD has the largest spatial extent. The situation is reversed for the operating point with the lowest current value (point 4 in figures 8 and 9), for which the electric-field strengths in the LFD and HFD are lowest and the HFD has the largest spatial extent. Rasulova *et al* [150] claim that the observation of bistability is related to a different spatial extent of the domain boundary, i.e. in the high-current state, the domain boundary is confined to more or less a single well, while for the low-current state it extends

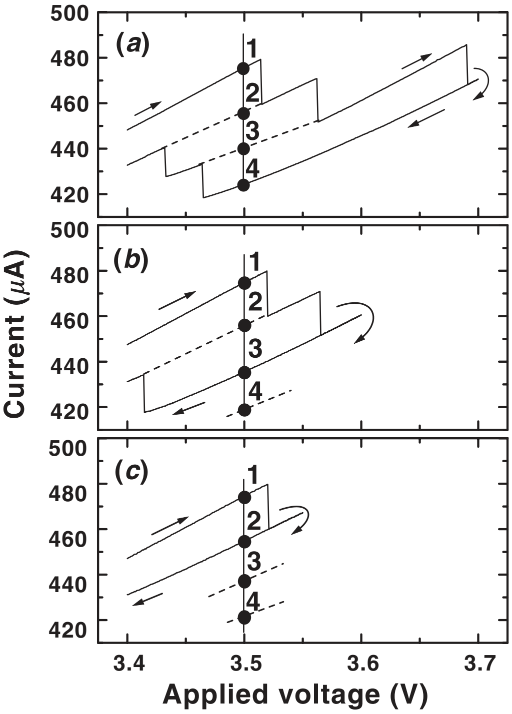

Figure 8. Enlarged section of the I–V characteristic of a doped, weakly coupled GaAs/AlAs SL with $d_W = 9.0$ nm, $d_B = 4.0$ nm and a volume doping density of Si in the wells of 1×10^{18} cm^{-3} under static domain formation showing multistability. The graphs in (*a*), (*b*) and (*c*) differ in the voltage position for reversing the sweep direction. From [109].

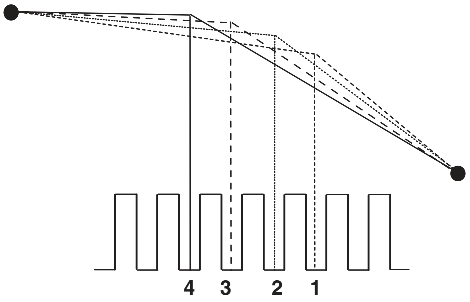

Figure 9. Voltage distribution for different locations of the domain boundary for a fixed applied voltage. The numbers indicate the location with respect to the operating points in figure 8.

over several periods. However, this may be just an additional side effect of the bistability in their particular system, which has a very small doping density in the SL. Mityagin and Murzin [149] showed that the extent of the domain boundary increases with decreasing doping concentration. Nevertheless, the main effect of the bistability is due to a different location of the CAL forming the domain boundary and not the extent of the domain boundary.

This bi- or multistability also exists in undoped, photoexcited SLs as already predicted theoretically by Bonilla *et al* [68] and observed experimentally by Tomlinson *et al* [157]. A different kind of bistability is observed when the sample exhibits current self-oscillations

[158], which will be discussed in section 5. Furthermore, a bistability between the static and oscillating states of EFDs is also possible [159] and will also be discussed in section 5.

3.4. External control parameters

There are several external control parameters which can influence the formation of EFDs in weakly coupled SLs. These are the carrier density, which can be varied within the same sample by photoexcitation, the temperature and a magnetic field applied perpendicular or parallel to the layers.

3.4.1. Carrier density. The first control parameter is the carrier density. For extremely low carrier densities, the field will be homogeneously distributed throughout the SL so that no domains are formed, while for very high carrier densities the EFDs will form as described in the previous subsections. In the intermediate density regime, the field distribution will become unstable. In this regime, current self-oscillations occur, which are reviewed in section 5. For investigating the carrier density dependence of EFD formation, optical excitation of an undoped structure has the advantage of a continuous variation of the electron density in the SL. In the case of doped structures, a large number of SL devices have to be fabricated, which still may be slightly different in some other parameter such as well and barrier width or composition. At very low carrier densities, tunnelling resonances between the different subbands are observed with increasing electric field strength. For intermediate carrier densities, the I–V characteristics contain plateaus, which do not exhibit any branch-like fine structure as shown in figure 7. This is the regime of unstable domain formation, i.e. current self-oscillations appear due to a recycling motion of the domain boundary (cf section 5). Finally, at very large carrier densities, we recover an I–V characteristic similar to the one shown in figure 7. This scenario has been confirmed by theoretical studies of undoped [68] and doped [75] SLs using the discrete drift model.

There have been several attempts to experimentally study the carrier density dependence of EFD formation. Grahn *et al* [108] varied the carrier density by changing the photoexcitation density in an undoped p–i–n structure with the SL forming the intrinsic layer. The homogeneous field distribution at low intensities can be identified through a single photoluminescence (PL) line, which is located between the two PL lines observed at high intensities, indicative of two regions of very different electric field. Hirakawa *et al* [160] and Shimada and Hirakawa [161] investigated two differently doped SLs. The SL with the higher doping density did not exhibit domain formation in the first plateau region, while both SLs exhibited domain formation in the second plateau. The results were interpreted in terms of an interplay between the tunnelling rate and the supply function for the electrons between adjacent quantum wells, which depends on the doping density. Hosoda *et al* [162] performed a detailed analysis of the EFD formation process in an undoped GaAs/AlAs SL under photoexcitation, in particular the regime of intermediate carrier densities. They showed how the field distribution inside the SL may evolve from the homogeneous field distribution at very low carrier densities to the two-domain picture at very high carrier densities. Using photoluminescence spectroscopy, they were able to obtain information about the field distribution, in particular for intermediate carrier densities. Detailed theoretical studies of stable field profiles as a function of the carrier density have used the discrete drift model to describe doped SLs [110] and undoped photoexcited SLs [163]. They confirm the transition from uniform field profiles to self-oscillations due to domain wall recycling, and then to static two-domain solutions as the carrier density increases.

3.4.2. Temperature. Another external control parameter is the sample temperature. With increasing temperature, the tunnelling resonances are gradually broadened [6]. At the same time, the peak velocity is lowered due to thermally activated transport mechanisms such as diffusion and thermionic emission above the barriers. As a result, static EFD formation is much more difficult to observe at room temperature than at liquid He or liquid N_2 temperatures. Kastrup [164] showed that the characteristic branches of static EFD formation disappear in a moderately doped GaAs/AlAs SL for temperatures above about 100 K. Xu *et al* [151] demonstrated that for a strongly doped GaAs/(Al,Ga)As multiple-quantum-well structure the formation of static EFDs is quenched above about 50 K. Wang *et al* [165] and Li *et al* [166] performed a detailed study of the temperature dependence of the I–V characteristics for a moderately doped GaAs/AlAs SL. In the investigation by Wang *et al* [165], there is a strong change in the shape of the I–V curves between 140 and 145 K. The fine structure of the I–V characteristics completely disappears above 156 K. At the same time, current self-oscillations as discussed in section 5 are already observed at 145 K so that a transition from static to dynamic EFD formation takes place between 140 and 156 K. In the investigation by Wang *et al* [167] and Li *et al* [166], who apparently used an identical structure, the fine structure in the I–V characteristics disappears above 170 K, and current self-oscillations appear for temperatures of 180 K and higher. Subsequently, Sánchez *et al* [168] performed a theoretical analysis of the temperature dependence of domain formation, which confirmed the breakdown of stationary EFDs in SLs above a certain temperature. We will return to the temperature dependence of the transition between dynamic and static domains in section 5.

3.4.3. Magnetic field. A magnetic field, which can be applied either parallel or perpendicular to the layers, i.e. perpendicular or parallel to the electric field, respectively, is very different external control parameter. Choi *et al* [123] demonstrated that a magnetic field applied perpendicular to the layers, which condenses the electrons in each well into Landau levels, does not have a significant influence on the formation of static EFDs. However, a magnetic field applied parallel to the layers, i.e. perpendicular to the electric field, causes several significant changes. It increases the onset voltage for the occurrence of the NDC structures, causes a splitting of these structures, suppresses them for large magnetic fields and increases the tunnelling current. The destruction of the branch-like structures in the I–V characteristics for a magnetic field parallel to the layers was confirmed by Grahn *et al* [10]. The onset of domain formation was shown to exhibit a quadratic dependence on the magnetic field, B. Shimada and Hirakawa [169] observed the formation of static EFDs in a magnetic field perpendicular to the layers for a GaAs/(Al,Ga)As SL with δ-doping at the centre of the (Al,Ga)As barriers. The spacing of the branches in the I–V characteristics varied with magnetic field, indicating that the field strengths of the domains are determined by resonant tunnelling between Landau levels of the lowest conduction subband, although the observed voltage spacings are systematically smaller than the cyclotron energy. However, for a GaAs/(Al,Ga)As SL with doping in the GaAs wells, Schmidt *et al* [170] showed that the EFD formation is governed by the subband spacing rather than by the cyclotron energy for magnetic fields up to 29 T, which again are applied perpendicular to the layers. The different observations by Shimada and Hirakawa [169] on the one hand and by Schmidt *et al* [170] on the other hand may be a result of the very different way of doping the SL structure, i.e. modulation doping with a δ-layer versus direct doping of the wells. At intermediate magnetic field strengths, additional resonances appear due to scattering-assisted inter-Landau-level tunnelling at the domain boundary [170]. The appearance of these additional structures was subsequently confirmed in the calculations of Aguado and Platero [171]. Sun *et al* [77], Wang *et al* [167, 172] and Sun *et al* [173] reported a quenching of the branch-like structures in the I–V characteristics due to static EFD formation with increasing magnetic field perpendicular to the layers. They interpreted their observation as a magnetic-field induced transition from a static to an oscillating electric-field distribution, which was supported by time-resolved measurements of the current. We will discuss this oscillation regime in more detail in section 5. Finally, Luo *et al* [174] observed that the typically irregular branch-like structure in the I–V characteristics becomes more regular with increasing magnetic field. A detailed analysis of the branches showed that the fluctuations for most of the branches are completely removed by a magnetic field of 9 T, indicating that the irregularities are connected to the non-resonant tunnelling process at the domain boundary. More theoretical investigations are necessary to clearly identify the effect of an external magnetic field on static domain formation.

4. Formation and switching of static domains

4.1. Formation

The formation times of static EFDs can be investigated experimentally in two ways. The first one takes an undoped SL under bias, which exhibits a homogeneous field distribution, and excites carriers inside the SL with an intense ultrashort light pulse. The evolution of a broad, single PL line, originating from the homogeneous field distribution, into two well-defined PL lines due to the presence of an LFD (PL line at higher energies) and HFD (PL line at lower energies) is monitored using time-resolved photoluminescence spectroscopy. The formation time for a weakly coupled GaAs/AlAs SL with $d_\mathrm{W} = 14.4$ nm and $d_\mathrm{B} = 3.4$ nm amounts to a few nanoseconds, indicating that the necessary space charge for forming the domain boundary is accumulated on a timescale much shorter than the characteristic transport time for electrons through the whole SL [175]. This rather short formation time can only be observed as long as the SL is biased in the region of NDC [176]. It increases by about one order of magnitude when the SL is biased in the positive differential conductivity region. Experiments performed with a step-like optical excitation of an undoped SL revealed current self-oscillations [177] since the excited carrier density for step-like excitation is about two orders of magnitude smaller than for excitation with an ultrashort light pulse so that static EFD formation could not be achieved.

The second way uses a doped SL and applies a short voltage pulse from zero field to a finite field strength in the static EFD region. Dynamical simulations showed that two formation mechanisms occur [79, 178]. When the SL is biased in the NDC regime, the domain boundary forms in place within a few microseconds for a doped, weakly coupled GaAs/AlAs SL with $d_\mathrm{W} = 9.0$ nm and $d_\mathrm{B} = 4.0$ nm, while for a bias in the region of positive differential conductivity the formation process consists of a well-to-well hopping starting from the cathode [79, 178]. The well-to-well hopping appears in the current-versus-time traces as small spikes. With increasing bias, the formation time decreases almost linearly in the positive differential conductivity region, because the distance from the cathode to the final position of the domain boundary decreases. Since the well-to-well hopping time depends on the coupling between adjacent wells, i.e. the barrier width and height, more strongly coupled SLs should exhibit formation times in the nanosecond time range. Subsequent measurements by Shimada and Hirakawa [179] confirmed the well-to-well hopping transients for the second and third plateau of the I–V characteristics of a doped GaAs/Al$_{0.3}$Ga$_{0.7}$As with $d_\mathrm{W} = 25.0$ nm and $d_\mathrm{B} = 10.0$ nm. An analysis of the formation time demonstrated that it can be described as the product of the capacitance of a single tunnelling barrier and the intrinsic tunnelling resistance in the LFD [179].

4.2. Theory of switching dynamics

While it is simple to find stable stationary solutions of discrete SL models containing two EFDs, a study of the transients in reaching them from certain initial conditions reveals many

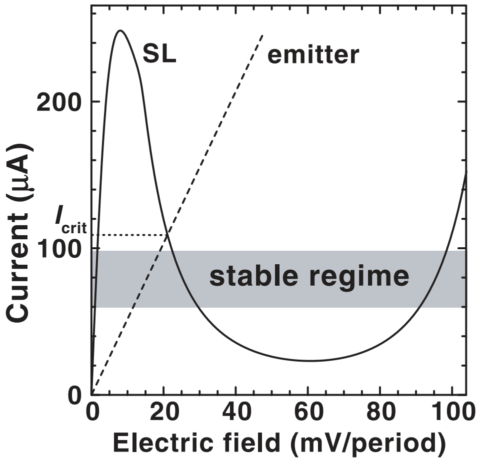

Figure 10. Schematic diagram of the current–field characteristics of the emitter contact and the SL. From [236].

important features of the dynamics of domains. Moreover, fluctuation phenomena, which we have ignored so far, can modify the predictions of the discrete models in ways that are experimentally observable. The theory of switching between different branches of stable static solutions in the first plateau of weakly coupled SLs is due to Amann *et al* [78, 180], and the effects of shot noise have been studied by Bonilla *et al* [181] using a stochastic discrete drift–diffusion model. These theoretical studies were motivated by experiments reported later in this section [182–185] and explained the observed experimental results quite well.

Let us explain in some detail the numerical simulations of the model based on equations (82) and (84), corresponding to discrete versions of Poisson's and Ampère's equations including the tunnelling current of equation (99). The calculations of Amann *et al* [78] use a forward drift velocity similar to equation (100), but with a different factor, $\mathcal{T}_i(\mathcal{E}_1)$, which is obtained from Green's function theory. The current densities at the boundaries are chosen as

$$J_{0\to 1} = \sigma F_0, \qquad J_{N\to N+1} = \sigma F_N \frac{n_N}{N_D}. \tag{113}$$

These functions are particular cases of tunnelling currents from the injecting contact to the SL and from the SL to the collecting contact [82]. The contact conductivity, σ, is selected as follows. Let us consider the tunnelling current density $J_{i\to i+1} = \mathcal{J}(F_i, n_i, n_{i+1})$ given by equations (99) and (100) with $n_{\max} = 2$ and evaluate it at $n_i = n_{i+1} = N_D$ for a fixed $F_i = F$. The curve $\mathcal{J}(F, N_D, N_D)$ is N-shaped: it has two local maxima, the first one at $F = F_M$ and J_M, and a local minimum at $F = F_m$ and J_m. We select σ so that the straight line $J = \sigma F$ intersects $\mathcal{J}(F, N_D, N_D)$ on its second decreasing branch at a point (F_c, J_c) with $F_M < F_c < F_m$. This condition is presented in figure 10, in which the homogeneous current–field characteristic, $S\mathcal{J}(F, N_D, N_D)$, is depicted, and $I_{\text{crit}} = SJ_c$ is explicitly shown. As we shall see, this condition allows the formation and motion of HFDs bounded by a CAL and a CDL (i.e. charge dipole waves). The key facts are as follows. The stationary field profile near the emitter corresponds to a CDL if its current is lower than $I_{\text{crit}} = SJ_c$, because the field in the LFD is smaller than in the emitting contact (cf figure 11(*a*)). This CDL contains a lower carrier density than the one at the domain boundary because the field change between the emitter and the LFD is much smaller than the field difference between the LFDs and HFDs.

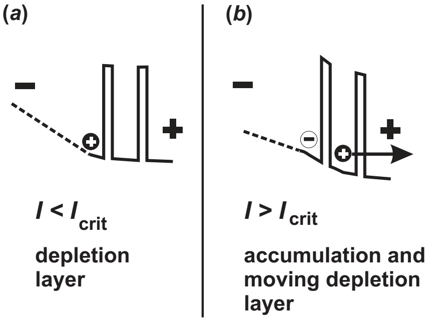

Figure 11. (*a*) For $I < I_{\rm crit}$ a CDL and (*b*) for $I > I_{\rm crit}$ a CAL exists between the emitter contact and the SL. For $I > I_{\rm crit}$ in (*b*), the initial CDL will move away from the emitter contact into the SL. From [236].

Figure 10 indicates that if the current is raised above $I_{\rm crit}$ during a short time interval, the field at the emitter would tend to increase as we move inside the SL. An embryonic CAL then appears near the emitter. However, the field in the LFD is still much lower, and therefore a CDL is still interposed between the emitter CAL and the LFD. The CDL will immediately begin to move into the SL (cf figure 11(*b*)), and this situation triggers a dipole formed by a CAL and a CDL if it persists long enough. The same result as in figure 10 can be obtained by appropriately modifying the contact doping density in the general expression of $J_{0\to 1}$ [81, 82]. The factor $n_N/N_{\rm D}$ in the expression for $J_{N\to N+1}$ avoids negative electron densities at the collector. The parameters in the numerical solution of the discrete model reported by Amann *et al* [78] correspond to the GaAs/AlAs SL studied by Luo *et al* [182] with 40 periods, $d_{\rm B} = 4.0\,{\rm nm}$, $d_{\rm W} = 9.0\,{\rm nm}$, $N_{\rm D} = 1.5 \times 10^{11}\,{\rm cm}^{-2}$, a cross section $S = 15\,000\,\mu{\rm m}^2$ and $T = 5\,{\rm K}$. Broadening due to scattering is taken into account using $\gamma_\nu = 8\,{\rm MeV}$ (independent of the subband index ν), and the conductivity, σ, is assumed to be 0.01 $(\Omega\ {\rm m})^{-1}$.

The stationary current–voltage characteristic for this doping density has the typical sawtooth pattern of figure 12, with the upper and lower branches corresponding to an up- and down-sweep of the external voltage, respectively. In the simulations, we start from the stable field configuration corresponding to a point on the upper branch of the first plateau of the I–V characteristic at $V_{\rm dc} = 0.75\,{\rm V}$. Then, we change the voltage to a final voltage $V_{\rm f} = V_{\rm dc} + V_{\rm step}$ and record the solution of the discrete model. We expect that the current evolves towards the value for one of the stable stationary solutions on the I–V characteristic at voltage $V_{\rm f}$ (in general there are several such branches due to the multistability as explained in section 3.3). We find that the final stationary current is on the upper branch if $V_{\rm step} = 0.1\,{\rm V}$, while it is on the lower branch if $V_{\rm step} = 0.18\,{\rm V}$ as indicated by the arrows in figure 12(*a*). Thus, fast switching allows us to reach the lower branch just by a sufficient increase in the voltage. This is a striking result. For conventional up- and down-sweeps, the point on the lower branch at 0.93 V can only be reached by increasing the voltage to more than 1.1 V and then decreasing it to 0.93 V.

In figure 13(*a*), we depict the current response to different positive values of $V_{\rm step}$ versus time. For $V_{\rm step} < V_{\rm crit}$ with $V_{\rm crit} \approx 0.175\,{\rm V}$, the current first increases abruptly and then relaxes monotonically to its final value. There is a fundamentally different current response if $V_{\rm step} \geqslant V_{\rm crit}$. Instead of relaxing monotonically after reaching a sharp peak, the current first drops to a level well below the lower stationary branch. Then, the current response exhibits a fast repetitive double peak pattern until about 3 μs. Subsequently, following one larger spike, only single peaks occur. The spiky structure ends about 7 μs after the voltage switch, and the

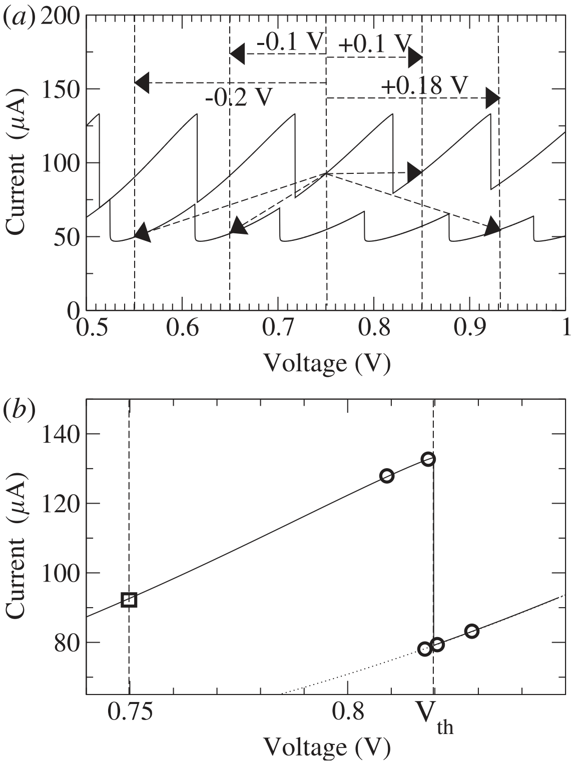

Figure 12. (*a*) Simulated sawtooth current–voltage characteristic of a GaAs/AlAs SL with $N = 40$, $d_{\mathrm{W}} = 9.0$ nm and $d_{\mathrm{B}} = 4.0$ nm. The upper branches correspond to a voltage up sweep, the lower branches to a down sweep. The arrows indicate the starting and end points of the voltage steps discussed in the text. (*b*) Enlarged section of the I–V characteristic in (*a*) indicating the initial operating point (□) and different final points (○). From [78].

current evolves to a stationary value on the lower branch. The total number of peaks is roughly equal to the number of wells in the SL. The frequency of the peak burst is about 15 MHz. This behaviour does not change significantly, provided $V_{\mathrm{step}} \geqslant V_{\mathrm{crit}}$, even for very different values of V_{step}. This effect is very similar to the experimental observations by Luo *et al* [182], except that the experimental total relaxation time is only about 2 μs. Better agreement can be achieved by choosing a larger scattering width $\gamma_\nu \approx 20$ MeV.

How can we explain this behaviour? The key lies in the motion of wave fronts, CALs and CDLs, at constant J studied in section 3.1. Consider the tunnelling current density, $\mathcal{J}(F, N_{\mathrm{D}}, N_{\mathrm{D}})$, of the uniform field profile and let $F^{(1)}(J)$, $F^{(2)}(J)$, as well as $F^{(3)}(J)$ be the solutions of $\mathcal{J}(F, N_{\mathrm{D}}, N_{\mathrm{D}}) = J$, with $J = I/S$ ordered from smaller to higher field values. The velocities of CALs and CDLs as a function of the current are $c_+(J)$ and $c_-(J)$, respectively, as depicted in figure 4. The current interval $(I_{\mathrm{l}}, I_{\mathrm{u}})$, corresponding to stationary CALs, depends on the location and size of the maximum and minimum values of the sequential tunnelling current. The point in figure 4 where the velocities of accumulation and depletion fronts intersect is of special interest. This point determines the velocity and current, at which a dipole wave consisting of a leading CDL and a trailing CAL can move rigidly [186].

Let us now consider a switching process with $0 < V_{\mathrm{step}} < V_{\mathrm{crit}}$. The dynamical evolution of the electron densities, n_i, is depicted in figure 14(*a*) for $V_{\mathrm{step}} = 0.1$ V. We observe that the CAL (light region) is shifted within a short time of 0.1 μs upstream towards the emitter, which

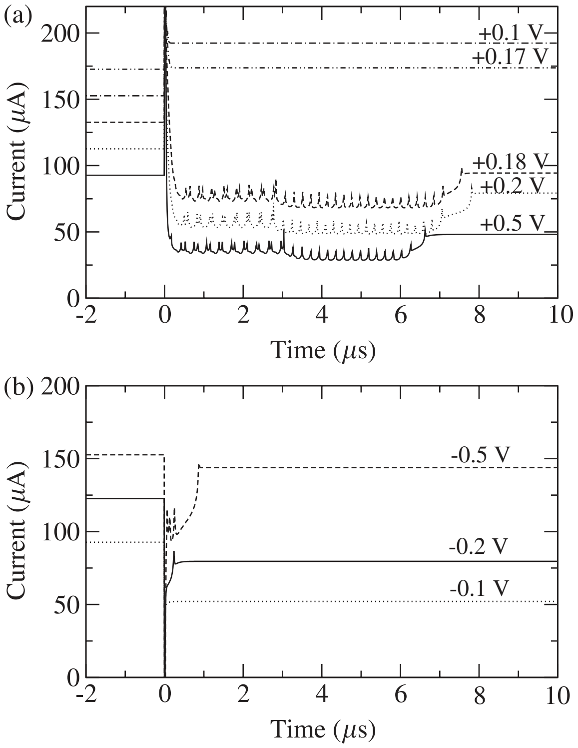

Figure 13. Current response versus time for various (*a*) positive and (*b*) negative voltage steps at $t = 0$. For $t < 0$, the initial voltage, V_{in}, is 0.75 V. The curves are shifted vertically in units of 20 μA in (*a*) and 30 μA in (*b*) for clarity. From [78].

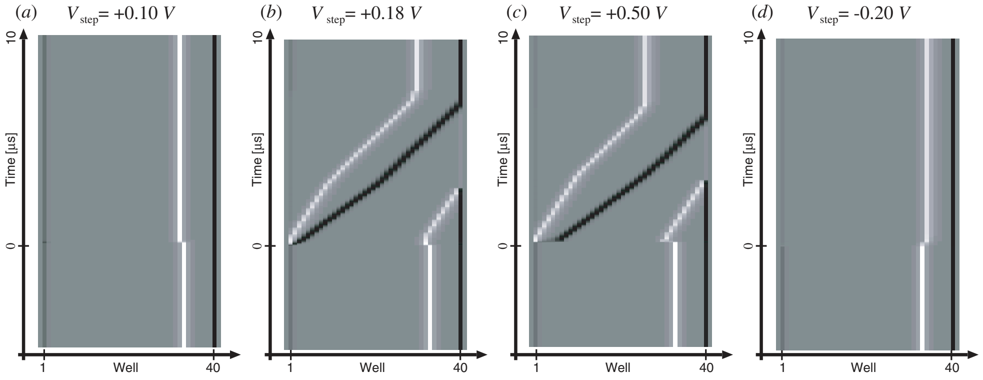

Figure 14. Evolution of the electron densities in the quantum wells during the switching process for various voltage steps, V_{step}, as indicated on the top, starting at $t = 0$ from $V_{\mathrm{in}} = 0.75$. The CALs (CDLs) are indicated by white (black) areas. In the grey area, the electron density is close to N_{D}. Well #1 is located at the emitter, well #40 at the collector. From [78].

explains the observed fast monotonic relaxation of the current after reaching its sharp peak. The switching to a higher external voltage has the effect that all fields in the SL are increased, and the current instantaneously rises above I_{u} to allow the upstream motion of the CAL. According to figure 4, the CAL moves with a negative velocity, consistent with the numerical results.

If $V_{\text{step}} \geqslant V_{\text{crit}}$, the situation is more complicated. For $V_{\text{step}} = 0.18$ and 0.50 V, the evolution of the electron density profile is depicted in figures 14(*b*) and (*c*), respectively. Before switching V_{step}, there is one CAL inside the sample, separating two coexisting EFDs. After switching the voltage, we observe four different dynamical phases: (1) upstream shift of the CAL and generation of new fronts at the emitter, (2) coexistence of three fronts (two CALs and one CDL) in downstream motion, (3) downstream motion of two fronts (one CAL and one CDL) and (4) pinning of the CDL at the collector, while the CAL moves until it reaches its final position. This relocation process involving two CALs and one CDL will be referred to as the *tripole/dipole* relocation scenario, and its four phases will now be described in detail.

Phase 1. Shortly after switching the voltage step, the initial CAL moves upstream towards the emitter. Simultaneously, a charge dipole wave appears at the emitter. Its leading CDL moves towards the collector, while its width increases. The trailing CAL of the dipole is pinned at the first SL well. Why and how can the charge dipoles be generated at the injecting contact?

In a stationary situation, the current through the injecting barrier is equal to the current through the first SL barrier. The field at the emitter can be calculated from equation (113). With our small contact conductivity, $F_0 > F_1$ if $0 < J < J_c$, the Poisson equation predicts electron depletion, $n_1 < N_D$. If we could suddenly change the current to a value larger than J_c, the field, F_1, would increase according to equation (84), trying to attain a value on the third branch of $\mathcal{J}(F, N_D, N_D)$. This would produce a CAL at this well, followed by the CDL that was there before changing J. The net outcome of this mechanism would be the creation of a dipole. As seen in figure 4, a depletion layer separated from the contacts moves towards the collector with a velocity $c_-(J)$. The CDL leaves a HFD in its wake that extends all the way to the injecting region. The width of this HFD increases as its leading edge (the CDL) advances. Since the total voltage is constant, the extra area gained by this region has to be compensated by lowering the current (since both the LFD and the HFD occur in a region of positive differential conductivity). Once the current has become smaller than J_c, the field in the immediate neighbourhood of the injecting region should correspond to another CDL, which implies that a CAL forming the back of the dipole wave has been created. Now the dipole is fully detached from the injecting region and a new phase starts.

The following observation about the contact conductivity is of paramount importance. Suppose that σ is so large that the line $J = \sigma F$ does not intersect $\mathcal{J}(F, N_D, N_D)$. The field profile of a stationary solution having $F_0 = J/\sigma$ needs to increase to the bulk value, $F^{(1)}(J)$, and therefore there is always a CAL near the injecting contact. This type of boundary condition can inject only CALs inside the SL for $J > J_c = J_M$. Then, the relocation of EFDs is quite different as discussed by Amann *et al* [78]. Similar considerations are well known in asymptotic studies of the Gunn effect [186, 187].

Phase 2. After about 0.2 μs, the current has dropped below I_1, and all fronts have positive velocities according to figure 4. Let us ignore the fast timescale responsible for the current spikes in figure 13(*a*) and try to find an equation for the envelope of the current time trace [16]. Then, we can consider that the field profile adjusts adiabatically to the instantaneous value of the envelope of the current time trace, $J(t)$, which evolves slowly. For an instantaneous value of $J(t) = J$, CALs move with velocity $c_+(J)$, whereas CDLs move with velocity $c_-(J)$. The electric field profile consists of an advancing HFD with field $F^{(3)}(J)$ (bounded by a CAL centred at $i = m_+^{(1)}(t)$ and a CDL centred at $i = m_-^{(1)}(t)$) and a CAL at $i = m_+^{(2)}(t)$ that encroaches on a HFD with $F = F^{(3)}(J)$ near the collector contact. We can mark the centre of a CAL at a time t as the well, at which there is a local maximum (or minimum in the case of a CDL) of the charge. Then the functions $m_\pm^{(j)}(t)$ are integer valued because the charge inside the wave front peaks at different wells as time changes. Consider the lifetime of a given wave front and denote the times at which $m_{\pm}^{(j)}(t)$ changes by $t_1, t_2, \ldots$. We may define a local velocity by $c_{\pm}^{i} = [m_{\pm}^{(j)}(t_{i+1}) - m_{\pm}^{(j)}(t_i)]/(t_{i+1} - t_i)$. Let us assume that we average these $c_{\pm}^{i}$ over a time interval that is short compared with the timescale typical of wave front motion, but sufficiently long compared with the mean value of $(t_{i+1} - t_i)$ for the wave front to have advanced over many wells. Moreover, as the envelope of the current time trace varies slowly, the average of $c_{\pm}^{i}$ can be approximated by $c_{\pm}(J)$ (J is the instantaneous value of the envelope of the current time trace). The average wave front velocities are

$$\left\langle \frac{\mathrm{d}m_{+}^{(j)}}{\mathrm{d}t} \right\rangle = c_{+}(J), \quad \left\langle \frac{\mathrm{d}m_{-}^{(j)}}{\mathrm{d}t} \right\rangle = c_{-}(J), \qquad j = 1, 2. \tag{114}$$

We can now easily calculate the voltage, V, corresponding to the field profile considered above (sometimes called a *tripole*—one pulse or charge dipole and one CAL, all of them advancing toward the collector). Ignoring transition regions and the contact voltage, $F_0 l$, in equation (85), we obtain for the average field $\Phi = V/(Nl)$

$$\Phi = \frac{1}{N}\sum_{j=1}^{N} F_i = F^{(1)}(J) + [F^{(3)}(J) - F^{(1)}(J)]\left(\frac{N - m_{+}^{(2)}}{N} + \frac{m_{-}^{(1)} - m_{+}^{(1)}}{N}\right). \tag{115}$$

We now differentiate this equation with respect to t, use $\mathrm{d}\Phi/\mathrm{d}t = 0$, average over short time intervals as indicated above and use equations (114) and (115) to simplify the result. Then we obtain

$$\begin{aligned} \frac{\mathrm{d}J}{\mathrm{d}t} &= \frac{2c_{+}(J) - c_{-}(J)}{N}\frac{[F^{(3)}(J) - F^{(1)}(J)]^2}{(F^{(3)}(J) - \Phi)/\mathcal{J}_{\mathrm{F}}^{(1)} + (\Phi - F^{(1)}(J))/\mathcal{J}_{\mathrm{F}}^{(3)}}, \\ \mathcal{J}_{\mathrm{F}}^{(i)} &\equiv \frac{\partial \mathcal{J}}{\partial F}(F^{(i)}, N_{\mathrm{D}}, N_{\mathrm{D}}), \qquad i = 1, 3. \end{aligned} \tag{116}$$

Note that, if we had started from a field profile comprising n_+ moving accumulation wave fronts and n_- depletion wave fronts, the same arguments would lead to the more general equation

$$\frac{\mathrm{d}J}{\mathrm{d}t} = \frac{n_{+}c_{+}(J) - n_{-}c_{-}(J)}{N}\frac{[F^{(3)}(J) - F^{(1)}(J)]^2}{(F^{(3)}(J) - \Phi)/\mathcal{J}_{\mathrm{F}}^{(1)} + (\Phi - F^{(1)}(J))/\mathcal{J}_{\mathrm{F}}^{(3)}}. \tag{117}$$

J evolves on the timescale t/N, which is slow, provided N is large. Clearly, J given by equation (116) changes until it reaches a value $J^{\dagger}$ such that $2c_{+}(J) = c_{-}(J)$, marked as $I_2 = SJ^{\dagger}$ in figure 4. Then, ignoring transients, this means that the two CALs of the tripole start advancing towards the collector with the same velocity, $c_{+}(J^{\dagger})$, while the CDL advances at a higher velocity, $c_{-}(J^{\dagger})$. Numerical simulations of different discrete models [78, 81, 107] show that each time a CAL advances by an SL period, a spike appears in the current. An asymptotic theory explaining this fact is still missing. If we accept it at face value, the double peak structure observed in the numerical simulation of figure 13(*a*) means that two CALs exist during that part of the period. Note that the transient region, where the current exhibits double spikes, has a flat appearance, indicating the constant *mean value* of the current density, $J^{\dagger}$. This is further corroborated by figures 14(*b*) and (*c*). In these figures, time traces of the positions of all wave fronts are recorded. Velocities are the reciprocal of the slopes. Note that the velocity of the CDL $c_{-}(J)$ is larger than the velocity of the two CALs in the tripole during a short time interval after the newly formed CAL leaves the injecting contact. Thus, the area lost by the shrinking HFD near the collector is gained by the growing HFD corresponding to the advancing dipole. When the rightmost CAL arrives at the collector, phase 2 ends and a new phase 3 starts.

Phase 3. After the HFD closest to the collector has disappeared at $t_o \approx 3\,\mu$s, only one CAL and one CDL, forming an advancing dipole, exist. Then the current response has a single-spike structure as depicted in figure 13(*a*). The same arguments as in phase 2 lead us to equation (117) with $n_+ = n_- = 1$. After a short transient, the velocities of the CAL and the CDL become equal, $c_+(J) = c_-(J)$. This occurs at a current density $J = J^* = I_1/S$, corresponding to the crossing point of the two front velocities in figure 4. In comparison with phase 2, the velocity of the CAL has almost doubled, while the velocity of the CDL is slightly decreased as shown in figures 14(*b*) and (*c*). This third stage ends when the CDL reaches the collector.

Phase 4. The CDL is pinned at the collector while the CAL advances to its final position, which it reaches in a short time. During this stage, the current increases, as described by equation (117), with $n_+ = 1$, $n_- = 0$. This short phase was apparently overlooked in earlier works [16, 78], although careful inspection of figures 13(*a*) and 14(*c*) clearly reveals its existence.

After these four stages of its evolution, the CAL finally reaches a stable stationary state: it becomes the domain wall separating two stationary EFDs. Of all possible stationary solutions having a voltage $V_{dc} + V_{step}$, the one having a CAL closer to the emitter is reached. Its current is lower than the initial one. This final situation can also be reached by conventional down-sweeping of the current–voltage characteristic. In the latter case, the CAL also moves towards the collector.

For $V_{step} < 0$, the CAL always travels towards the collector and stops at a position corresponding to the domain wall separating the two EFDs of a stationary solution. This solution can also be reached by down-sweeping to the final voltage as shown in figure 14(*d*). Figure 13(*b*) shows that the current has to decrease below its lower critical value so as to allow the downstream motion of the CAL with positive velocity. Note that the number of current spikes indicates the number of SL periods traversed by the CAL before reaching its final position. In contrast with the case of positive V_{step}, the resulting current response shows no threshold-like behaviour as in figure 13(*a*). Since all fields decrease during the switching process, no dipole wave can be generated at the emitter.

4.3. Switching between static branches

Switching experiments between static domains were initially reported by Rasulova *et al* [150]. A difference in the timescale for current jumps from a smaller to a larger current value versus from a larger to a smaller current value was found, which was about one order of magnitude longer for jumps to higher current values. However, a detailed analysis of switching across a single current discontinuity was not performed in this investigation.

Switching experiments investigating the relocation dynamics of the domain boundary over one or several periods were performed by Luo *et al* [182]. The transition process from one branch to the next was studied by adding a bias step with different amplitudes to a dc bias and recording the time-resolved current. A bias step increasing the applied dc voltage is referred to as an *up jump*, while a bias step decreasing the applied dc voltage is called a *down jump*. It was shown that the relocation time of the domain boundary for up jumps (down jumps) depends exponentially on the difference between the final static current and the maximum (minimum)

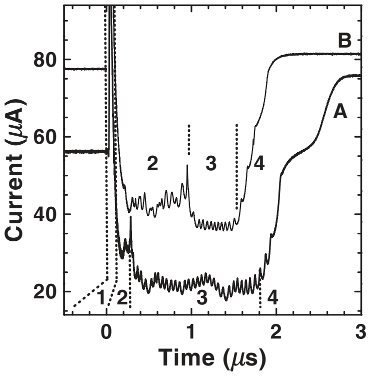

Figure 15. Ensemble-averaged current transients for switching from the third to the fifth branch (A) and from the tenth to the 13th branch (B) of the I–V characteristic. From [184].

current value of the initial branch. A universal scaling relationship between the relocation time and the current difference was found.

4.3.1. Voltage pulses decreasing or increasing the dc voltage. For down jumps, the relocation process of the domain boundary proceeds via a direct motion of the CAL in the direction of electron flow. This behaviour is confirmed by single-shot time traces of the current response: for values of the final voltage away from regions of bistability, there is an initial displacement current spike, after which the current rapidly switches to the stable value. Furthermore, when the final voltage is close to the bistable region, there is an additional intermediate period, in which the current fluctuates about a metastable value for a stochastically varying delay time τ_d before rapidly switching to the stable value in a time τ_s [182, 183]. However, for up jumps, the charge monopole at the domain boundary would have to move against the electron flow, and this is only possible for small-amplitude up jumps. Therefore, a different and more complex relocation scenario must apply for larger up jumps.

Figure 15 shows two current transients for the case of larger amplitude up jumps, i.e. from the third branch to the fifth branch (curve A) and from the tenth to the 13th branch (curve B). After the initial peak (phase 1), an interval of spikes with rather irregular amplitudes (phase 2) follows, which is terminated by a larger spike. The duration of phase 2 depends mainly on the final voltage, V_1. After this larger spike, a series of regular spikes (phase 3) appears with a lower current level, before the current rises (phase 4). The traces are ensemble averages of about 100 measurements for obtaining a better signal-to-noise ratio, i.e. the position of the individual spikes is essentially deterministic.

The separation of the regular spikes in region 3 is about 50 ns, which corresponds to a frequency of 20 MHz. This frequency falls into the same range of frequencies for the spikes of 10–20 MHz present in current self-oscillations, which have been observed in the same sample for opposite polarity [100, 188, 189] and will be discussed in section 5.3. This strongly suggests that these regular oscillations are due to the deterministic motion of the CAL over successive periods of the SL.

Several sets of measurements were performed to vary the number of regular spikes in phases 3 and 4. For each set, a starting voltage V_0 is selected on a particular initial branch (N_0), and the final voltage V_1 is varied to lie on different final branches (N_1) of the I–V curve. In these measurements, the number of regular spikes, N_rs, in phases 3 and 4 can be estimated by

$$N_\mathrm{rs} \approx N_\mathrm{SL} - N_0 - N_1 \qquad (118)$$

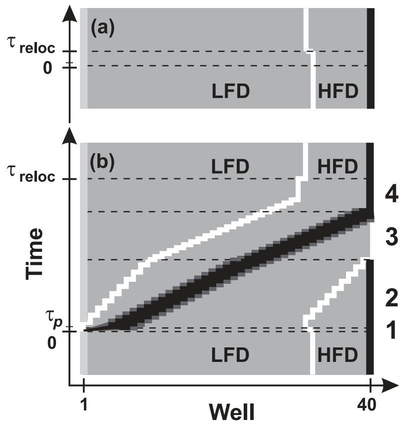

Figure 16. Schematic evolution of the electron densities in the quantum wells during the switching process via (*a*) the simple monopole and (*b*) the tripole/dipole relocation process for a jump from the eighth to the ninth branch. The CALs (CDLs) are indicated by white (black) areas. The labels 1, 2, 3 and 4 on the right-hand side refer to the phases in figure 15. From [184].

as long as $N_0 + N_1 < N_{\mathrm{SL}}$. The difference between the left- and right-hand sides of equation (118) varies typically between 1 and 3. Also, for jumps with $N_0 + N_1 > N_{\mathrm{SL}}$, phases 3 and 4 are not observed. These observations provide further support for the theoretical picture of a complex yet deterministic relocation scenario as described in section 4.2.

4.3.2. Comparison with theoretical results. According to the theoretical work of Amann *et al* [78, 180] described in section 4.2, the larger up jumps exhibit the more complex tripole/dipole relocation scenario. Figures 16(*a*) and (*b*) show the electron densities as a function of time and space for the simple monopole and the tripole/dipole relocation process, respectively. White and black areas depict CALs and CDLs, respectively. The simple monopole relocation displayed in figure 16(*a*) corresponds to a small up jump. The larger up jumps contain four different phases of the tripole/dipole relocation process. Phase 1 occurs during the initial displacement current peak. During this time, the CAL between the LFD and HFD tries to move upstream towards its final position. At the same time, the CDL at the emitter begins to move as described above, leaving an HFD behind, which grows with increasing time (cf region 1 in figure 16(*b*)). Since the number of SL periods in the HFD increases, while the applied voltage remains constant, the effective field strengths in both LFD and HFD must decrease, which implies a reduction in current level according to the homogeneous current–field characteristic.

Phase 2 begins after τ_{p}, when the current has dropped below a certain value. At this point in time, there are three travelling layers separating the low- and high-field regions in the SL (cf phase 2 in figure 16(*b*)). As explained in section 4.2, both CALs move with the same velocity towards the collector. Because of the constant total voltage, the number of periods under a high field at the average current density, which is quasistationary and approximately equal to $J^{\dagger}$, must now remain constant. Therefore, the sum of the velocities of the two CALs has to be the same as the velocity of the CDL, i.e. $2v_{\mathrm{CAL}} = v_{\mathrm{CDL}}$. Since the average current should have a value for which the CDL has twice the velocity of the CALs [78], a rather low current value, $SJ^{\dagger}$, is observed in figure 15. The jumps of the two CALs across individual quantum wells appear as irregular spikes within region 2 in figure 15 so that the details of their motion are not synchronized. This latter feature is different from the numerical results displayed in figure 13(*a*) and could be due to small fluctuations of the doping density or to imperfections in the different wells traversed by the two CALs.

After the original CAL reaches the collector, which is indicated by a larger spike in figure 15, the tripole reduces to a dipole and phase 3 begins (cf figure 16(*b*)). The velocities of the CAL and CDL are now the same. Since the CDL extends over several periods, the current transients are dominated by the motion of the CAL, which now appears as regular spikes in figure 15. When the CDL reaches the collector, phase 3 is completed.

In phase 4, only a CAL is present in the SL. Since now the number of periods in the HFD decreases with increasing time, the field strengths of the LFD and HFD must both increase, resulting in an increase in the current. The CAL continues to move towards its final position. After reaching the well adjacent to its final position, the situation becomes exactly the same as for the down jumps described earlier. As discussed by Rogozia *et al* [183], the current remains constant for a stochastically varying delay time, τ_{d}, in this well, before abruptly switching to the stable value.

4.4. Switching stochastics

4.4.1. Stochastic theory. In section 4.2, we have focused on the complex yet deterministic switching behaviour associated with domain boundary relocation. Another striking aspect of the switching behaviour is the statistical distribution of the relocation times. As explained below in section 4.5, experiments reveal that the *relocation time* it takes the CAL to relocate to its stable static position fluctuates randomly for $0 < V_{\mathrm{step}} \sim V_{\mathrm{M}} - V_{\mathrm{dc}}$, in which $(V_{\mathrm{M}}, I_{\mathrm{M}})$ is the point on the same branch of the current–voltage characteristic as the initial point that has the maximum possible value of the voltage. At this point, the corresponding stationary solution of the discrete model ceases to be stable. Typically, this point is a turning point, and the slope of the current–voltage characteristic becomes infinite there. There are no detailed studies in the literature clarifying this issue. Figure 5 in [80], obtained using a discrete sequential tunnelling model by using a numerical continuation algorithm, suggests that the turning point and the maximum of the I–V characteristic can be very close. For these SLs, the slope of the I–V characteristic varies considerably near the end of the stable static branch. At the turning point, one stable and one unstable branch of stationary solutions coalesce via a saddle–node bifurcation [190].

The effect of fluctuations is greater near bifurcation points, and therefore the described situation is not surprising. The origin of fluctuations in the present case of weakly coupled SLs at low temperatures is most likely shot noise. So far we have ignored the condition that the charge present in the SL should be an integer multiple of the electron charge, i.e. that only an integer number of electrons can tunnel. The obvious justification is that the number of electrons is very large due to the large cross section, S, of the SL. The strength of shot noise is small, but it will affect the dynamical behaviour, when it becomes comparable with $V_{\mathrm{M}} - V_{\mathrm{f}}$ in appropriate units. A theoretical study of shot noise effects on switching is due to Bonilla *et al* [181], although general considerations on shot noise [191] and a theory of switching times in double-barrier structures [192] are relevant.

The theory of Bonilla *et al* [181] simply adds Poissonian shot noise to the equations and boundary conditions of one's favourite deterministic discrete SL model. According to Blanter and Büttiker [191], this strategy has explained most of the relevant physics in many mesoscopic systems. The stochastic model consists of equations (82), (84) and (85) as well as expressions for the tunnelling currents across the inner and outer barriers of the SL. For an inner barrier, the tunnelling current density contains an additional random term besides the one in equation (99),

$$J_{i\to i+1} = \frac{e v^{(f)}(F_i)}{l}\left\{n_i - \frac{m^* k_{\mathrm{B}} T}{\pi\hbar^2}\ln\left[1 + \mathrm{e}^{-(eF_i l/k_{\mathrm{B}}T)}\left(\mathrm{e}^{(\pi\hbar^2 n_{i+1}/m^* k_{\mathrm{B}} T)} - 1\right)\right]\right\} + J^{(r)}_{i\to i+1}(t) \tag{119}$$

for $i = 1, \ldots, N-1$. Here $J^{(r)}_{i\to i+1}$ represents the random current, which satisfies

$$\langle J^{(r)}_{i\to i+1}\rangle = 0, \tag{120}$$

$$\langle J^{(r)}_{i\to i+1}(t)\, J^{(r)}_{j\to j+1}(t')\rangle = \frac{e^2}{Sl}\delta_{ij}\delta(t-t') \times\left\{ n_i v^{(f)}(F_i) + \frac{m^* k_{\mathrm{B}} T}{\pi\hbar^2}\ln[1 + \mathrm{e}^{-(eF_i l/k_{\mathrm{B}}T)}(\mathrm{e}^{(\pi\hbar^2 n_{i+1}/m^* k_{\mathrm{B}}T)} - 1)]\right\}. \tag{121}$$

The idea behind this form of random tunnelling current is that uncorrelated electrons are arriving at the ith barrier with a distribution function of time intervals between arrival times that is Poissonian. Moreover, the correlation time is of the same order as the tunnelling time, so that it is negligible on the longer timescale of dielectric relaxation.

Only numerical calculations of the high temperature limit in equations (99) and (121) have been reported [181]. They correspond to the discrete DD model given by equation (101). The tunnelling currents at the boundaries have the simplified form

$$J_{0\to 1} = j^{(f)}_{\mathrm{e}}(F_0) - \frac{en_1 w^{(b)}(F_0)}{l} + J^{(r)}_{0\to 1}, \tag{122}$$

$$J_{N\to N+1} = \frac{en_N w^{(f)}(F_N)}{l} + J^{(r)}_{N\to N+1} \tag{123}$$

in which the noise has zero mean and correlations

$$\langle J^{(r)}_{0\to 1}(t) J^{(r)}_{0\to 1}(t')\rangle = e\frac{j^{(f)}_{\mathrm{e}}(F_0)l + en_1 w^{(b)}(F_0)}{Sl}\delta(t-t'), \tag{124}$$

$$\langle J^{(r)}_{N\to N+1}(t) J^{(r)}_{N\to N+1}(t')\rangle = \frac{e^2 n_N w^{(f)}(F_N)}{Sl}\delta(t-t'). \tag{125}$$

The emitter current density, $j^{(f)}_{\mathrm{e}}$, the emitter backward velocity, $w^{(b)}$, and the collector forward velocity, $w^{(f)}$, are functions of the electric field depicted in figure 3 of Bonilla *et al* [82].

For parameter values corresponding to the SL studied in the experiments [182], a dimensionless measure of the noise amplitude is $a = \sqrt{e/(\varepsilon F_{\mathrm{M}} S)} \approx 3.232\times 10^{-4}$. The numerical simulations broadly confirm the experimental findings of Luo *et al* [182] and Rogozia *et al* [183]. Among them is the exponential dependence of the relocation time on the current difference, $|I - I_{\mathrm{M}}|$, as $\tau_{\mathrm{reloc}} \propto e^{\mathrm{b}|I-I_{\mathrm{M}}|/I_{\mathrm{M}}}$. Moreover, the distribution of switching times is a symmetric Gaussian density,

$$W(t, \bar{\tau}, \sigma)\,\mathrm{d}t = \frac{1}{\sigma\sqrt{2\pi}}\exp\left(-\frac{(t-\bar{\tau})^2}{2\sigma^2}\right)\mathrm{d}t \tag{126}$$

with $\bar{\tau} = \tau_{\mathrm{reloc}}$ denoting the mean relocation time for V_{f} far from V_{M} and σ its width, or an asymmetric first passage time (FPT) distribution,

$$W(t, y', \beta)\,\mathrm{d}t = \sqrt{y'\frac{2\beta}{\pi}}\exp\left(-\frac{\beta y' z^2}{2}\right)\mathrm{d}z, \tag{127}$$

in which

$$y' = \frac{y_0^2}{D} \qquad \text{and} \qquad z = \frac{1}{\sqrt{\exp(2\beta t) - 1}} \tag{128}$$

for V_{f} close to V_{M}. The parameters β and y_0^2/D are derived from the Fokker–Planck equation that describes a one-dimensional Brownian particle [193, 194].

The numerical findings have the natural uncertainty due to fitting noisy numerical data to presumed functional forms. In the particular case of the mean relocation time, an argument for choosing a different functional form is as follows. At the point $(V_{\rm M}, I_{\rm M})$, the branch of deterministic stationary solutions containing the initial point becomes unstable via a saddle–node bifurcation. If the bifurcation parameter, $\alpha = (V_{\rm f} - V_{\rm M})/(F_{\rm M}Nl)$, becomes comparable with the noise amplitude, a, the stochastic amplitude equation of the saddle–node bifurcation equation is

$$\frac{{\rm d}\varphi}{{\rm d}t} = \alpha\mu + \nu\varphi^2 + a\beta\xi(t). \tag{129}$$

In this expression, φ is proportional to $I - I_{\rm M}$ and $\xi(t)$ corresponds to zero-mean, delta-correlated white noise. The positive parameters μ, ν and β can be calculated using projection methods [190], but their precise form does not matter for the argument we want to make. Note that equation (129) has two stationary solutions with $|I - I_{\rm M}| \propto |V_{\rm f} - V_{\rm M}|^{1/2}$ if $a = 0$.

For $V_{\rm f} < V_{\rm M}$, equation (129) describes the escape of a Brownian particle from a potential well corresponding to the cubic potential $U(\varphi; \alpha) = \alpha\mu\varphi + \nu\varphi^3/3$. Provided the height of the barrier is large compared with the noise strength, the reciprocal of the mean escape time is proportional to the equilibrium probability density $P = {\rm e}^{-U/a^2}/Z$ evaluated at the maximum of the potential [195], i.e.

$$\tau_{\rm reloc} \propto \exp\left(\frac{2|\mu\alpha|^{3/2}}{3a^2\sqrt{\nu}}\right). \tag{130}$$

Thus, it seems that there exists a relatively large voltage interval $|\alpha|^{3/2} \gg a^2$ over which the logarithm of the relocation timescales superlinearly with $|\alpha|$. In terms of the current, $\ln(\tau_{\rm reloc}) \propto |I - I_{\rm M}|^3$. Therefore, it seems that fitting the numerical results for the relocation time to a linear function of $|I - I_{\rm M}|$ would not test these theoretical results [181].

Tretiakov *et al* [192] have derived the Fokker–Planck equation associated with equation (129) by analysing a master equation that models sequential tunnelling transport in a double-barrier structure. They assume tunnelling of one electron and carry out the Kramers–Moyal expansion of their equation in powers of the reciprocal cross section, S^{-1} [195]. The potential term in the Fokker–Planck equation is cubic near a turning point, which is then used to simplify the equation to a form equivalent to equation (129). Tretiakov *et al* [192] then infer that $\ln(\tau_{\rm reloc}) \propto |\alpha|^{3/2} \propto |I - I_{\rm M}|^3$, unless the inhomogeneous in-plane diffusion of the electrons in the well is considered. A saddle-point analysis of a functional Fokker–Planck equation modelling this motion yields $\ln(\tau_{\rm reloc}) \propto |\alpha| \propto |I - I_{\rm M}|^2$ for samples with large S. The authors conclude that $\ln(\tau_{\rm reloc}) \propto |\alpha|^{\zeta} \propto |I - I_{\rm M}|^{2\zeta}$, with $\zeta = \frac{3}{2}$ for structures of small cross section so that the electron density does not depend on the in-plane coordinates, and $\zeta = 1$ for structures of large cross section such as SLs. A crossover for intermediate cross section values is predicted.

While the arguments of Tretiakov *et al* [192] are very interesting and deserve further study, we are interested in the validity of equation (130) for weakly coupled SLs. The condition for equation (129) to hold is that all its terms must be of the same order. The balance between the two first terms of the right-hand side in equation (129) yields $\varphi = {\rm O}(|\alpha|^{1/2})$, and the balance with the left-hand side provides a rescaling of time to $\tau = |\alpha|^{1/2}t$. As $\delta(t) = |\alpha|^{1/2}\delta(\tau)$, the balance of the noise term with the others gives $a = {\rm O}(|\alpha|^{3/4})$. This means $|V_{\rm f} - V_{\rm M}|/(F_{\rm M}Nl) = {\rm O}([e/(\varepsilon F_{\rm M}S)]^{2/3})$. According to this argument, the exponent in equation (130) is of the order of $|\alpha|^{3/2}/a^2 = 1$ in the parameter region, where all the terms in equation (129) are of the same order. This implies that the scaling exponent $\zeta = \frac{3}{2}$ describes the behaviour of the relocation time in a voltage interval such that $|\alpha| \gg a^{3/4}$ (in which the barrier height is large compared with the noise). Whether the approximation also holds for $|\alpha| \approx a^{3/4}$

depends on the particular value of the unspecified numerical constants in the equation. At the turning point $\alpha = 0$, the barrier vanishes, and the approximation of equation (129) breaks down. These arguments do not determine the extent of the inner critical region, in which equation (129) no longer holds, nor the critical exponent there.

Recapitulating, the critical exponent, $\frac{3}{2}$, for the relocation time in discrete models of weakly coupled SLs that do not consider lateral motion of electrons seems to hold in an annular voltage region, $a^2 \ll |\alpha|^{3/2} \ll K$. The constant $K > 0$ characterizes the extension of the region, in which the current–voltage characteristic near the turning point can be approximated by a parabola. Unfortunately, such a region seems to be very narrow in known numerical calculations of I–V characteristics that include both stable and unstable branches. For example, figure 5 of [80] shows that the maximum and the turning point of the I–V characteristic are extremely close for all branches. In this case, it may very well happen that $K \ll 1$, or even that $K \ll a^2$. In the first case, the interval of voltages for which the critical exponent is $\frac{3}{2}$, is very narrow, which could very well mean that the experiment is probing a voltage region not described by the amplitude equation (129). Then the critical exponent, $\frac{3}{2}$, would not be observed. In the second case, the region in which the critical exponent is $\frac{3}{2}$ does not exist. What happens in such cases is not known at the present time.

The previous arguments indicate that the study of the effects of shot noise on voltage switching and relocation of EFDs is wide open from the theoretical point of view. The following additional theoretical studies seem necessary: (i) characterization of the turning points of discrete sequential tunnelling models for realistic parameter values using numerical continuation methods that find both stable and unstable static solution branches; (ii) study of the case $K \ll 1$, in which the parabolic region near the turning point is so narrow that the amplitude equation (129) breaks down (this case might be better approximated by analysing the effect of shot noise on a spiky turning point, at which the slope of the I–V characteristic is discontinuous, with a simple argument yielding $\ln(\tau_{\mathrm{reloc}}) \propto \alpha^2 \propto |I - I_{\mathrm{M}}|^2$); (iii) study of the case $|\alpha|^{3/2} \ll a^2$; and (iv) study of the effect of possible in-plane electron motion on relocation times in SLs. Comparison of the conclusions of these studies with existing and future experiments would greatly clarify the precise influence of shot noise on domain relocation after voltage switching.

4.4.2. Measured time distributions. In this subsection, we consider the experimentally observed statistical distribution of the relocation times. In order to analyse the switching times in terms of their statistics, the distribution functions have been directly measured using the built-in functions of a fast, digitizing oscilloscope. Two examples are shown as insets in figure 17. There is a very pronounced change in the shape of the distribution function going from larger to smaller values of the final voltage, $|V_1|$. The main part of figure 17 shows the ensemble-averaged switch times, $\bar{\tau}$ (dots), and the respective widths, σ (open squares), of the distributions on a logarithmic scale as a function of V_1. Both strongly increase with decreasing $|V_1|$. For values of V_1 far away from the current jump, the distribution function is very narrow (cf inset for $V_1 = -752.5$ mV in figure 17) and exhibits a Gaussian shape. However, for values of V_1 close to the current jump, the distribution function has a completely different, asymmetric shape with a steep increase at shorter times and a broad tail at longer times (cf inset for $V_1 = -732.0$ mV in figure 17). Also, the timescale has changed by more than one order of magnitude.

As against the deterministic switching behaviour discussed in section 4.3, we are now interested in the switching time distribution and its dependence on the final voltage, V_1. When V_1 is located on the adjacent higher branch, the domain boundary first remains in the same well. The current increases beyond the maximum of the initial branch of the I–V characteristic.

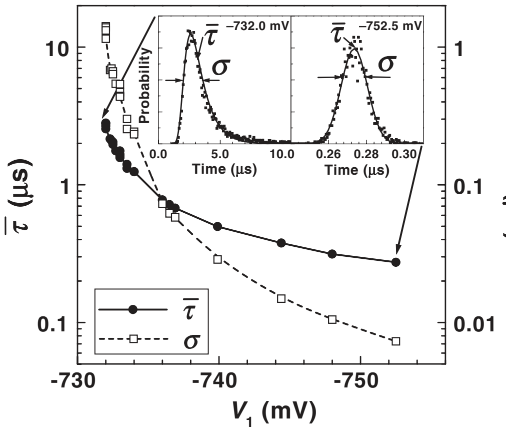

Figure 17. Average value, $\bar{\tau}$ (·) and width, σ (□), of the distribution of the relocation times for switching from $V_0 = -650$ mV on branch 3 to different final voltages on branch 4. The insets show two examples of the distribution functions measured at voltages of $V_1 = -732.0$ and -752.5 mV. From [183].

The field and charge profiles first begin to change without any spatial relocation of the CAL itself. However, the centre of mass of the total charge distribution moves upstream. During this time, the current remains almost constant. This intermediate state is metastable because the centre of mass of the charge distribution and the position of the CAL are located in different wells of the SL. When the distance between the centre of mass of the charge distribution and the accumulation layer reaches a critical value, the CAL moves almost instantaneously to the adjacent well.

The time to reach this critical charge distribution depends on stochastic processes of the system, primarily current shot noise. For large voltage jumps, the change in the electric-field distribution in the sample is relatively large, so that the centre of mass of the charge distribution is strongly affected and the critical charge distribution is reached rapidly. The resulting delay time is short and the corresponding time distribution is Gaussian. However, for values of V_1 close to the current jump, the field does not deviate very much from a stable distribution, and the centre of mass of the charge distribution will be affected much less; the system is quite sensitive to fluctuations [191], and both the mean value and the width of the distribution increase. The final abrupt switching event occurs when the critical charge distribution is reached *for the first time*. We consider a distribution function that describes the probability of a Brownian particle reaching $y = 0$ starting from y_0 for the first time in a time between t and $t + \mathrm{d}t$ by a one-dimensional random walk [193], commonly referred to as the first-passage time (FPT) distribution function. In this analogy, the variable y corresponds to the charge density in the quantum well associated with the domain boundary.

After normalizing the measured time distributions (area equal to 1), we fit them at large values of V_1 with the Gaussian function of equation (126) using $\bar{\tau}$ and σ as the fitting parameters. The resulting distribution function is shown in the inset of figure 17 for $V_1 = -752.5$ mV. Note that a Gaussian distribution would be expected when there is an effective Brownian potential that has only one local minimum. The motion towards that minimum is essentially deterministic and fast.

For small values of V_1 close to the current jump, we used the FPT distribution function of equation (127). The resulting distribution function is asymmetric and contains a steep initial increase and a broad tail as shown in the inset of figure 17 for $V_1 = -732.0$ mV. Increasing

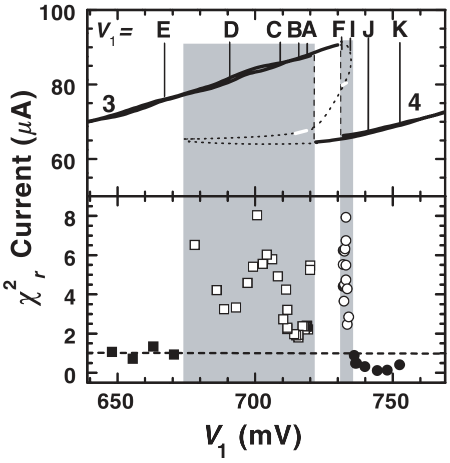

Figure 18. I–V characteristic as well as $\chi_\mathrm{r}^2 = \chi_\mathrm{Gauss}^2/\chi_\mathrm{FPT}^2$ as a measure of the type of distribution function for down (□, ■) and small up jumps (○, ●). The dotted line in the I–V characteristic depicts a possible form of the unstable branch. From [185].

β results in a narrower distribution, which at the same time is shifted to shorter times. An increase in y' mainly shifts the peak of the distribution to longer times in our parameter range.

For each measured distribution, we determined the quadratic deviation, χ^2, from the respective least square fits. If the ratio $\chi_\mathrm{r}^2 = \chi_\mathrm{Gauss}^2/\chi_\mathrm{FPT}^2$ is larger (smaller) than 1, the FPT (Gaussian) distribution fits the data points better. Figure 18 shows the experimentally determined χ_r^2 as a function of V_1 for down jumps (squares) and small up jumps (circles). In the case of down jumps, the ratio is considerably larger than 1 for $V_1 > 678$ mV, indicated by the open squares. The shaded area marks the region where the FPT distribution fits the measured distribution better. The dashed line indicates $\chi_\mathrm{r}^2 = 1$.

The *abrupt* change in χ_r^2 at 678 mV in figure 18 indicates the existence of an unstable branch in the shaded voltage region (with approximate width $\Delta V_1 = 45$ mV). For voltages below 678 mV, this unstable branch is not present. Small sections of the unstable branch have recently been extracted directly from time-trace data [185], and these are indicated in the I–V characteristic of figure 18 by the two short white segments. These values correspond to the instantaneous current level at the end of the stochastic time delay and just prior to the abrupt jump to the new stable current value. The short white segments correspond to the only values of the final voltage for which this current level can be determined from time traces using this technique. The dotted line indicates how the full unstable branch *might* connect with the stable parts of the characteristic. The extraction of the full unstable branch from time-trace data is an important objective, which needs further investigation.

For small up jumps, the voltage range for the unstable branch is only 4 mV (open circles in figure 18), which is much smaller than the one for down jumps. This is probably due to the different curvature of the homogeneous current-field characteristic in the field region for up and down jumps.

5. Current self-oscillations

5.1. Monopole versus dipole oscillations

Self-sustained oscillations of the electric current occur in both strongly and weakly coupled SLs. They can be best described by studying the simple non-linear models of section 2 and then, if necessary, extending the analysis to more complex models. As explained before, the main difference between strongly and weakly coupled SLs is that strongly coupled SLs are described by spatially continuous equations, whereas weakly coupled SLs are governed by spatially discrete equations. Let us first describe self-sustained current oscillations due to dipole domains in strongly coupled SLs.

5.1.1. *Dipole oscillations in strongly coupled SLs.*

The simplest description of self-oscillations in strongly coupled SLs uses DDEs. Neglecting the different physical origin of NDC (Bragg reflection due to the periodicity of the dispersion relation in SLs versus intervalley transfer of electrons in bulk GaAs), these equations are the same as the ones describing the Gunn effect in bulk n-GaAs, and therefore their analysis can go along the same lines. An early review of the Gunn effect was published by Kroemer [8]; Volkov and Kogan [196] as well as Shaw *et al* [197] are useful supplements. The main analytical results on self-oscillations in Gunn diodes are the following: (i) the description of a single charge dipole wave moving in an infinite sample under constant current bias conditions (e.g. the equal-area rule of Butcher [198] and the shock wave approximations of dipole waves of Knight and Peterson [39] as well as monopole waves of Murray [199]); (ii) linear stability (small signal) analysis of the inhomogeneous stationary field profile for a piecewise linear drift velocity [197] and for a general drift velocity in the limit of large samples [200]; (iii) bounds on the minimal device length necessary for self-oscillations [8]; (iv) characterization of the effect of different boundary conditions on self-oscillations [8, 197]; (v) analysis of the onset and end of the self-oscillations by means of amplitude equations [201]; and (vi) asymptotic analysis of self-oscillations mediated by charge monopole and dipole waves in the limit of samples that are large with respect to the spatial extent of the dipole [186, 187]. These later studies considered N-shaped drift velocities, which are very much related to weakly coupled SLs.

An early theoretical prediction (supported by analysis of model equations) of current self-oscillations due to Bragg reflections in single-band semiconductors is due to Büttiker and Thomas [56]. Their phenomenological hydrodynamic model has a relationship between a constant electric field and the current density it produces with the same functional dependence as the Esaki–Tsu drift velocity for strongly coupled SLs. Apparently these authors thought that their mechanism could be more important for the weakly coupled SLs studied by Esaki and Chang [5]. Many years later, simpler DDEs were used by Le Person *et al* [41] to model self-oscillations induced by picosecond light pulses in an undoped, strongly coupled SL and by Hofbeck *et al* [202] for the same purpose in a doped, strongly coupled SL. Cao and Lei [203] have described self-oscillations in doped, strongly coupled SLs by means of hydrodynamic balance equations.

In order to describe self-oscillations in a strongly coupled SL under dc voltage bias, we shall use the DDE (81)

$$\varepsilon\frac{\partial F}{\partial t} + v(F)\left(\frac{eN_{\mathrm{D}}}{l} + \varepsilon\frac{\partial F}{\partial x}\right) = J(t) + D(F)\varepsilon\frac{\partial^2 F}{\partial x^2}, \qquad (131)$$

$$v(F) = \frac{2v_{\mathrm{M}}\mathcal{F}}{1+\mathcal{F}^2} \equiv v_{\mathrm{M}}V(\mathcal{F}), \qquad D(F) = \frac{2k_{\mathrm{B}}Tv_{\mathrm{M}}}{eF_{\mathrm{M}}(1+\mathcal{F}^2)}, \qquad (132)$$

$$\frac{1}{L}\int_0^L F(x,t)\,\mathrm{d}x = \frac{V}{L} \qquad (133)$$

in which $\mathcal{F} = F/F_{\mathrm{M}}$ and $L = Nl$ is the SL length.

We derived equation (131) in section 2 as a high-temperature limit of the more realistic QDDE (72) (or its semiclassical limit, the GDDE [34]) that does not satisfy the Einstein relation

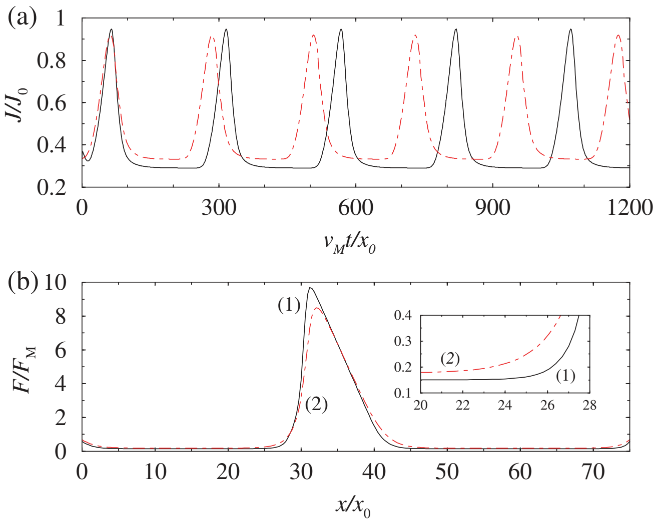

Figure 19. (*a*) Current ($J_0 = ev_{\mathrm{M}}N_{\mathrm{D}}/l$) versus time during self-oscillations for a 100-period SL at 300 K as described by the GDDE in the Boltzmann limit (——) and by the DDE (- - - -). (*b*) Comparison between the dipole wave for the GDDE (1) and the dipole wave for the DDE (2). From [34].

(This figure is in colour only in the electronic version)

between drift velocity and diffusion coefficient. There are quantitative differences between the simulations of self-oscillations using the GDDE and the DDE as shown in figure 19. These differences are greater for lower temperatures as explained in section 2. However, the qualitative features of the self-oscillations are similar, and we shall analyse the simpler DDE in this section to avoid technical complications. The DDE (131) is a particular case of the model commonly used to describe the one-dimensional Gunn effect in bulk n-GaAs. Therefore, many ideas that are already known for the case of the Gunn effect can be applied to our DDE. It is convenient to rewrite it in the following dimensionless form:

$$\frac{\partial \mathcal{F}}{\partial \tilde{t}} + V(\mathcal{F})\left(1 + \frac{\partial \mathcal{F}}{\partial \tilde{x}}\right) = \mathcal{J} + \delta \tilde{D}(\mathcal{F})\frac{\partial^2 \mathcal{F}}{\partial \tilde{x}^2}, \tag{134}$$

$$V(\mathcal{F}) = \frac{2\mathcal{F}}{1+\mathcal{F}^2}, \qquad \tilde{D}(\mathcal{F}) = \frac{2}{1+\mathcal{F}^2}, \tag{135}$$

$$\frac{1}{\mathcal{L}}\int_0^{\mathcal{L}} \mathcal{F}(\tilde{x},\tilde{t})\,\mathrm{d}\tilde{x} = \phi. \tag{136}$$

The variables, reference scales and typical numerical values (at 300 K) are listed in table 1. The dimensionless units are chosen so that the dimensionless drift velocity has a maximum at $\mathcal{F} = 1$ with $V(1) = 1$ (cf equation (75)) and the doping density, N_{D}, is the unit of the electron density. We also use $\delta = k_{\mathrm{B}}TN_{\mathrm{D}}/(\varepsilon F_{\mathrm{M}}^2 l) = 0.61$, $\mathcal{L} = NeN_{\mathrm{D}}/(\varepsilon F_{\mathrm{M}}) = 43$ and $\phi = V/(F_{\mathrm{M}}Nl)$ as dimensionless parameters. Dimensionless space and time variables are denoted by a tilde over the dimensional variables. To restore dimensional units, we multiply a given magnitude by its unit in table 1. Equations (134)–(136) contain three dimensionless parameters, $\mathcal{L}$, ϕ and δ, in addition to the dimensionless variables $\tilde{x}$, $\tilde{t}$, $\mathcal{F}$ and $\mathcal{J}$.

We now need to specify the boundary conditions. The boundary condition at $x = 0$ (the cathode) greatly affects the oscillation features as it determines the mechanism by which waves are injected into the SL. Three common boundary conditions are described in table 2,

Table 1. Variables, reference scales and typical numerical values used in the drift–diffusion model for a strongly coupled SL with $l = 5$ nm at 300 K [213] and for the first plateau of a weakly coupled SL with $l = 13$ nm at 4 K [100].

x (nm)	$\dfrac{\varepsilon F_M l}{e N_D}$	11.62	3.98
t	$\dfrac{\varepsilon F_M l}{e N_D v_M}$	0.375 ps	2.55 ns
F ($\mathrm{kV\,cm^{-1}}$)	F_M	14	6.92
n ($\mathrm{cm^{-2}}$)	N_D	0.4×10^{11}	1.5×10^{11}
v	v_M	$31\ \mathrm{km\,s^{-1}}$	$1.56\ \mathrm{m\,s^{-1}}$
D ($\mathrm{cm^2\,s^{-1}}$)	$\dfrac{k_B T v_M}{e F_M}$	5.73	$v_M l = 2.03 \times 10^{-4}$
J ($\mathrm{A\,cm^{-2}}$)	$\dfrac{e N_D v_M}{l}$	3.97×10^4	2.88

Table 2. Boundary conditions for the cathode.

Cathode	Boundary conditions	Injected charge density waves
Current–field characteristics	$j_c(F) = J(t) - \varepsilon \dfrac{\partial F}{\partial t}$	Dipoles (small σ)
(Ohmic)	$j_c(F) = \sigma F$	Monopoles (large σ and N-shaped $v(F)$)
n^+ region $-L_c < x < 0$	$\varepsilon \dfrac{\partial F}{\partial t} + \mu F \left(e N_{3D}^+ + \varepsilon \dfrac{\partial F}{\partial x} \right) - D\varepsilon \dfrac{\partial^2 F}{\partial x^2} = J(t)$, with $\dfrac{\partial F}{\partial x}(-L_c, t) = 0$	
Low mobility	$J = e N_{3D}^+ \mu F$ for constant J, F (high-resistivity cathode) $\left(\text{for } \mu N_{3D}^+ L_c < \dfrac{N_D v_M}{F_M} \right)$	Dipoles
Doping notch $-L_c < x < 0$	$\varepsilon \dfrac{\partial F}{\partial t} + v(F) \left(e N_{3D}^+ + \varepsilon \dfrac{\partial F}{\partial x} \right) - \varepsilon D(F) \dfrac{\partial^2 F}{\partial x^2} = J(t)$ with $\dfrac{\partial F}{\partial x}(-L_c, t) = 0$	
If $N_{3D}^+ \ll N_D/l$	$J \sim e N_{3D}^+ v(F) \sim 2 e v_M N_{3D}^+ \frac{F}{F_M}$ (low-conductivity cathode)	Dipoles

which provide a similar injection of waves at the cathode and can be analysed in the same way. As in section 4.1, we shall examine the simplest one, the Ohmic cathode current–field characteristics,

$$\frac{\partial \mathcal{F}(0, \tilde{t})}{\partial \tilde{t}} + \tilde{\sigma} \mathcal{F}(0, \tilde{t}) = \mathcal{J}, \tag{137}$$

$$\frac{\partial \mathcal{F}(\mathcal{L}, \tilde{t})}{\partial \tilde{t}} + \left(1 + \frac{\partial \mathcal{F}(\mathcal{L}, \tilde{t})}{\partial \tilde{x}} \right) \tilde{\sigma} \mathcal{F}(\mathcal{L}, \tilde{t}) = \mathcal{J} \tag{138}$$

in which $\tilde{\sigma} = \sigma F_M l / (e v_M N_D)$ is the dimensionless contact conductivity.

The asymptotic description of self-oscillations for an N-shaped drift-velocity is known in the limit $\mathcal{L} \gg 1$, in which the spatial extent of the wave fronts, CALs and CDLs or pulses (charge dipoles) are small compared with the SL length [186]. Let us describe what happens for the Esaki–Tsu drift velocity in equation (135). Typically, for small dc bias, $0 < \phi < \phi_\alpha$, equations (134)–(136) have a stable stationary solution. To construct this simple solution and more complicated ones, we proceed to rescale space and time in equations (134)–(136) as

$$\xi \equiv \frac{\tilde{x}}{\mathcal{L}} = \frac{x}{Nl}, \qquad \tau \equiv \frac{\tilde{t}}{\mathcal{L}} = \frac{v_\mathrm{M} t}{Nl}, \qquad \varsigma \equiv \frac{1}{\mathcal{L}} = \frac{\varepsilon F_\mathrm{M}}{e N_\mathrm{D} N} \ll 1. \tag{139}$$

The result is

$$\mathcal{J} - V(\mathcal{F}) = \varsigma \left(\frac{\partial \mathcal{F}}{\partial \tau} + V(\mathcal{F}) \frac{\partial \mathcal{F}}{\partial \xi} \right) - \varsigma^2 \delta\, \tilde{D}(\mathcal{F}) \frac{\partial^2 \mathcal{F}}{\partial \xi^2}, \tag{140}$$

$$\int_0^1 \mathcal{F}(\xi, \tau)\, \mathrm{d}\xi = \phi. \tag{141}$$

As $\varsigma \to 0$, equation (140) yields $V(\mathcal{F}) = \mathcal{J}$. This equation has two solutions for $0 < \mathcal{J} < 1$, $\mathcal{F}_1(\mathcal{J})$ and $\mathcal{F}_2(\mathcal{J})$ with $0 < \mathcal{F}_1(\mathcal{J}) < \mathcal{F}_2(\mathcal{J})$ for the Esaki–Tsu drift velocity in equation (135). Clearly $\mathcal{F}_2(\mathcal{J})$ is unstable, so that we should construct the appropriate solution satisfying boundary and bias conditions by correcting $\mathcal{F} = \mathcal{F}_1(\mathcal{J})$. The stationary field profile is $\mathcal{F}(x) \sim \mathcal{F}_1(\mathcal{J})$, except in a narrow boundary layer near the contact regions that we choose to ignore for the time being. The bias condition in equation (141) yields $\phi \sim \mathcal{F}_1(\mathcal{J})$, and therefore the current density corresponding to the average field, ϕ, is

$$\mathcal{J} \sim V(\phi). \tag{142}$$

This implies that the static current–voltage characteristic increases following the first branch of the drift velocity. Does the current increase all the way up to the end of the first branch of the drift velocity at $\phi = 1$? It depends on the boundary condition at the injecting contact. Let us go back to the original scaling of space and time as in equation (134) and consider the case of low contact conductivity, so that $\tilde{\sigma}\mathcal{F}$ intersects $V(\mathcal{F})$ on the second branch thereof. As in figure 16, the corresponding point $(\mathcal{F}_\mathrm{c}, \mathcal{J}_\mathrm{c})$ defines the critical values of field and current with $\tilde{\sigma}\mathcal{F}_2(\mathcal{J}_\mathrm{c}) = \mathcal{J}_\mathrm{c}$. For $0 < \mathcal{J} < \mathcal{J}_\mathrm{c}$, $\mathcal{F}(0) > \mathcal{F}_1(\mathcal{J})$, and there is a CDL whose field profile solves the time-independent equation (134) with $\mathcal{F}(0) = \mathcal{J}/\tilde{\sigma}$ and $\mathcal{F}(\infty) = \mathcal{F}_1(\mathcal{J})$. A similar layer joins $\mathcal{F}_1(\mathcal{J})$, with the other boundary value given by the mixed boundary condition in equation (138). These solutions can be constructed by using phase plane techniques as in [204]. The boundary layers yield corrections of the order of $\varsigma = 1/\mathcal{L}$ to the current in equation (142) that we ignore.

A linear stability analysis of this stationary solution shows that it loses stability at $\phi_\alpha = \mathcal{F}_1(\mathcal{J}_\mathrm{c}) + \mathrm{O}(\ln[\mathcal{L}]/\mathcal{L})$, if $\tilde{\sigma} < 1$, and at $\phi \sim 1$, if $\tilde{\sigma} > 1$ [200]. The intuitive reason is that, for $\mathcal{F}_1(\mathcal{J}_\mathrm{c}) < \phi < \mathcal{F}_\mathrm{c}$, the static field profile for $\mathcal{J} \sim \mathcal{J}_\mathrm{c}$ consists of a flat region near the cathode, where $\mathcal{F} \sim \mathcal{F}_2(\mathcal{J})$, and a CDL, at some $\tilde{x} = X$, that marks the transition to $\mathcal{F}_1(\mathcal{J})$ and solves $\phi = \mathcal{F}_1(\mathcal{J}_\mathrm{c}) + [\mathcal{F}_\mathrm{c} - \mathcal{F}_1(\mathcal{J}_\mathrm{c})]X$. The cathode field region has negative impedance, and any disturbance gets amplified and drifted towards the stable region $\tilde{x} > X$. At a critical value $X = \mathrm{O}(\ln \mathcal{L})$, the disturbances have sufficient space to generate a dipole wave that can move towards the anode. Note that $\mathcal{J} > \mathcal{J}_\mathrm{c}$ yields $\mathcal{F}(0) > \mathcal{F}_2(\mathcal{J})$. Phase plane considerations show that there is no stationary solution decaying from this cathode value to $\mathcal{F}_1(\mathcal{J})$ as $\tilde{x} \to \infty$. Stationary solutions having $\phi > \mathcal{F}_\mathrm{c}$ can be constructed assuming that the current is slightly greater than $\mathcal{J}_\mathrm{c}$. Their profile comprises a flat region with $\mathcal{F} \sim \mathcal{F}_2(\mathcal{J})$, going from the cathode to a point $\tilde{x} = X$, and a CAL having a field profile $\mathcal{F} \sim \mathcal{F}_\mathrm{c} \exp[\mathcal{J}_\mathrm{c}(\tilde{x} - X)/2]$. The CAL is logarithmically close to the anode, $(\mathcal{L} - X) \sim (2/\mathcal{J}_\mathrm{c}) \ln[(\phi - \mathcal{F}_\mathrm{c})\mathcal{J}_\mathrm{c}\mathcal{L}/(2\mathcal{F}_\mathrm{c})]$. These stationary solutions become stable above a certain bias $\phi_\omega > \mathcal{F}_2(\mathcal{J}_\mathrm{c})$, but no asymptotic calculation of ϕ_ω exists. On the basis of previous results of Bonilla *et al* [200], we expect $\phi_\omega = \mathcal{F}_2(\mathcal{J}_\mathrm{c}) + \mathrm{O}(\ln[\mathcal{L}]/\mathcal{L})$.

In the absence of an explicit calculation of ϕ_ω, several authors [205, 206] use a heuristic argument due to Guéret [207]. According to this argument, ϕ_ω corresponds to a uniform field profile F_0 such that

$$\frac{e|v_0'|N_\mathrm{D}}{\varepsilon l} = \frac{v_0^2}{4D_0} \tag{143}$$

in which $v_0' = v'(F_0)$, $v_0 = v(F_0)$ and $D_0 = D(F_0)$. Let us insert $F = F_0 + \varphi\,\mathrm{e}^{\lambda t + \mathrm{i}kx}$ and $J = J_0$ in equation (131) and ignore terms of the order of φ^2 in the result. We obtain the dispersion relation $\lambda = -\mathrm{i}v_0 k - v_0' e N_\mathrm{D}/(\varepsilon l) - D_0 k^2$. The uniform stationary state is unstable to an oscillatory state (Gunn oscillation) if $v_0' < 0$ and $k = 0$ (convective instability). If we write $k = \beta_1 + \mathrm{i}\beta_2$, the dispersion relation becomes

$$\lambda = v_0\beta_2 - \frac{v_0' e N_\mathrm{D}}{\varepsilon l} - D_0(\beta_1^2 - \beta_2^2) - \mathrm{i}\beta_1(v_0 + 2D_0\beta_2). \tag{144}$$

Bifurcation to stationary states requires real values of λ, which in turn happens provided that $\beta_2 = -v_0/(2D_0)$ for all values of β_1. Then $\lambda = -v_0^2/(4D_0) - v_0' e N_\mathrm{D}/(\varepsilon l) - D_0\beta_1^2$, and the homogeneous stationary state becomes unstable (absolute instability) at F_0, given by equation (143). Guéret [207] concludes from this calculation that the corresponding field profile $F = F_0 + \varphi\,\mathrm{e}^{v_0 x/(2D_0)}\,\mathrm{e}^{\lambda t}$ eventually gives rise to a stationary field profile having a CAL near the anode. Conclusions extracted from this argument and its usage should be examined with care.

If the sample length is small, i.e. $\mathcal{L} < \mathcal{L}_\mathrm{m}$, the stationary solution is stable for all bias values: written in dimensional units, a necessary condition for self-oscillations is that $N_\mathrm{D} L > \varepsilon F_\mathrm{M} \mathcal{L}_\mathrm{m}/e$, $L = Nl$, which is related to the usual N–L criterion for the Gunn effect [8]. For $\mathcal{L} > \mathcal{L}_\mathrm{m}$, the stationary state is linearly unstable in a bias interval $\phi_\alpha < \phi < \phi_\omega$. At ϕ_α and ϕ_ω, time-periodic solutions (which are current self-oscillations) are created from the stationary solution via sub- or supercritical Hopf bifurcations, depending on the value of $\mathcal{L}$ [201]. Near the bifurcation voltages, self-oscillations can be approximated by solving amplitude equations [201]. Far from bifurcation points, we can find the self-oscillations numerically or, in the limiting case $\mathcal{L} \gg 1$, using asymptotic methods, that we shall now describe.

The Esaki–Tsu drift velocity yields a non-linear source term in the DDE that has a single stable constant solution, not three as in the case of N-shaped velocity. The asymptotics of the latter case is well known in full detail [186, 208]. The case of a single stable constant field profile is novel and presents interesting aspects from the point of view of non-linear mathematics. We shall follow in our description recent work on a piecewise model related to the Gunn effect [209]. Let us assume that $\mathcal{F}_1(\mathcal{J}_\mathrm{c}) < \phi < \mathcal{F}_2(\mathcal{J}_\mathrm{c})$ and that the stationary state is unstable. As we know, the self-oscillations are due to a periodic motion of a charge dipole through the whole structure, i.e. from the cathode to the anode. The key of the asymptotic description is that *the current varies slowly*, on times of the order of $\tilde{t} = \mathcal{L}$ or $\tilde{t} = \sqrt{\mathcal{L}}$, *and the field profile follows adiabatically the evolution of* $\mathcal{J}$. We shall divide our description into three stages: (i) there is a single dipole far from the boundaries that advances towards the anode; (ii) the dipole arrives at the anode, and the increase in the current destabilizes the boundary layer at the cathode, that injects a new dipole; and (iii) the new dipole grows and moves towards the anode, while the old one disappears. After stage (iii), we return to stage (i), and one period of the oscillations has been completed.

Stage (i). The dipole is a pulse of the electric field comprising two wave fronts moving at different speeds. Its back is a wave-front solution advancing at speed c_+, $\mathcal{F} = \mathcal{F}(\chi + X_+; \mathcal{J}, c_+, \mathcal{F}_\mathrm{max})$, $\chi = \tilde{x} - c_+\tilde{t}$, $\mathcal{F}(0; \mathcal{J}, c_+, \mathcal{F}_\mathrm{max}) = 1$, such that $\mathcal{F}(-\infty; \mathcal{J}, c_+, \mathcal{F}_\mathrm{max}) = \mathcal{F}_1(\mathcal{J})$ and $\mathcal{F}(X_+; \mathcal{J}, c_+, \mathcal{F}_\mathrm{max}) = \mathcal{F}_\mathrm{max}$. The leading front of the pulse is a wave-front solution advancing at speed c_-, $\mathcal{F} = \mathcal{F}(\xi - X_-; \mathcal{J}, c_-, \mathcal{F}_\mathrm{max})$, $\chi = \tilde{x} - c_-\tilde{t}$, $\mathcal{F}(0; \mathcal{J}, c_-, \mathcal{F}_\mathrm{max}) = 1$, such that $\mathcal{F}(-X_-; \mathcal{J}, c_+, \mathcal{F}_\mathrm{max}) = \mathcal{F}_\mathrm{max}$ and $\mathcal{F}(\infty; \mathcal{J}, c_-, \mathcal{F}_\mathrm{max}) = \mathcal{F}_1(\mathcal{J})$. $\mathcal{F}_\mathrm{max}$ is the maximum value of the field in the pulse. According to equation (134), the wave fronts solve

$$-c\frac{\partial\mathcal{F}}{\partial\chi}+V(\mathcal{F})\left(1+\frac{\partial\mathcal{F}}{\partial\chi}\right)-\delta\tilde{D}(\mathcal{F})\frac{\partial^2\mathcal{F}}{\partial\xi^2}=\mathcal{J} \tag{145}$$

with appropriate boundary conditions. This equation has the following phase plane,

$$\begin{aligned}\frac{\partial\mathcal{F}}{\partial\chi}&=\mathcal{G},\\ \frac{\partial\mathcal{G}}{\partial\chi}&=\frac{V(\mathcal{F})-\mathcal{J}}{\delta\tilde{D}(\mathcal{F})}+\frac{V(\mathcal{F})-c}{\delta\tilde{D}(\mathcal{F})}\mathcal{G}\end{aligned} \tag{146}$$

or, equivalently,

$$\frac{\partial\mathcal{G}}{\partial\mathcal{F}}=\frac{V(\mathcal{F})-\mathcal{J}}{\delta\tilde{D}(\mathcal{F})\mathcal{G}}+\frac{V(\mathcal{F})-c}{\delta\tilde{D}(\mathcal{F})}. \tag{147}$$

In terms of the phase plane and for fixed values of $\mathcal{J}$ and $\mathcal{F}_{\max}$, $\mathcal{G}^+(\mathcal{F})$ is the trajectory having $\mathcal{G}>0$ that leaves the saddle point $\mathcal{F}=\mathcal{F}_1(\mathcal{J})$, $\mathcal{G}=0$ and reaches $\mathcal{F}=\mathcal{F}_{\max}$, $\mathcal{G}=0$. These two requirements are satisfied for a unique value of the front velocity, $c=c_+$. Similarly, $\mathcal{G}^-(\mathcal{F})$ is the separatrix with $\mathcal{G}<0$ that enters the saddle point $\mathcal{F}=\mathcal{F}_1(\mathcal{J})$, $\mathcal{G}=0$ having left $\mathcal{F}=\mathcal{F}_{\max}$, $\mathcal{G}=0$. Again these requirements uniquely determine the front speed $c=c_-$. Equation (145) implies that the pulse comprising these two wave fronts has a continuous second derivative with respect to χ for all values $-\infty<\chi<\infty$. On a slowly varying timescale, $\mathcal{J}$ and $\mathcal{F}_{\max}$ vary, and the pulse changes its size adiabatically to accommodate their instantaneous values (see below). The pulse width is

$$X_- - X_+ = \int_{-X_-}^{0}\mathrm{d}\chi-\int_0^{X_+}\mathrm{d}\chi=\int_1^{\mathcal{F}_{\max}}\left(\frac{1}{|\mathcal{G}^-(\mathcal{F})|}-\frac{1}{\mathcal{G}^+(\mathcal{F})}\right)\mathrm{d}\mathcal{F}. \tag{148}$$

It is possible to derive equations for $c_\pm$ as follows. Let us rewrite equation (147) as

$$\frac{\mathcal{G}\delta}{1+\mathcal{G}}\frac{\partial\mathcal{G}}{\partial\mathcal{F}}=\frac{V(\mathcal{F})-c}{\tilde{D}(\mathcal{F})}+\frac{c-\mathcal{J}}{\tilde{D}(\mathcal{F})(1+\mathcal{G})}. \tag{149}$$

Using $\mathcal{G}(\mathcal{F}_1)=0$, this equation yields

$$\delta[\mathcal{G}-\ln(1+\mathcal{G})]=\int_{\mathcal{F}_1}^{\mathcal{F}}\frac{V(E)-c}{\tilde{D}(E)}\mathrm{d}E+(c-J)\int_{\mathcal{F}_1}^{\mathcal{F}}\frac{\mathrm{d}E}{\tilde{D}(E)[1+\mathcal{G}(E)]}. \tag{150}$$

Since $\mathcal{G}(\mathcal{F}_{\max})=0$, we obtain

$$\int_{\mathcal{F}_1}^{\mathcal{F}_{\max}}\frac{V(E)-c_\pm}{\tilde{D}(E)}\mathrm{d}E+(c_\pm-\mathcal{J})\int_{\mathcal{F}_1}^{\mathcal{F}_{\max}}\frac{\mathrm{d}E}{\tilde{D}(E)[1+\mathcal{G}^\pm(E)]}=0. \tag{151}$$

In the particular case where $c_-=c_+$, we have a rigidly moving pulse that is a homoclinic orbit in the phase plane, leaving $(\mathcal{F}_1,0)$ for $\mathcal{G}>0$ and entering the same saddle point for $\mathcal{G}<0$. In such a case, we can subtract equation (151) for $\mathcal{G}^-$ from the same equation for $\mathcal{G}^+$ with $c_-=c_+=c_{\mathrm{h}}$. The result is

$$(c_{\mathrm{h}}-\mathcal{J})\int_{\mathcal{F}_1}^{\mathcal{F}_{\max}}\left(\frac{1}{1+\mathcal{G}^-(E)}-\frac{1}{1+\mathcal{G}^+(E)}\right)\frac{\mathrm{d}E}{\tilde{D}(E)}=0. \tag{152}$$

The integral in this expression is clearly positive, so that we have $c_{\mathrm{h}}=\mathcal{J}$ and therefore

$$\int_{\mathcal{F}_1}^{\mathcal{F}_{\max}}\frac{v(E)-\mathcal{J}}{\tilde{D}(E)}\mathrm{d}E=0, \tag{153}$$

$$\mathcal{G}-\ln(1+\mathcal{G})=\frac{1}{\delta}\int_{\mathcal{F}_1}^{\mathcal{F}}\frac{V(E)-\mathcal{J}}{\tilde{D}(E)}\mathrm{d}E \tag{154}$$

two well-known results in the Gunn effect literature [198].

Let us come back to the problem of finding $\mathcal{J}$ and $\mathcal{F}_{\text{max}}$ that determine uniquely the pulse. A relation between these variables can be obtained from the bias condition in equation (141). Ignoring contact layers, the bias condition becomes

$$\phi \sim \mathcal{F}_1 + \frac{1}{\mathcal{L}}\left[\int_{-\infty}^{0} (\mathcal{F} - \mathcal{F}_1)\,\mathrm{d}\chi + \int_{0}^{\infty} (\mathcal{F} - \mathcal{F}_1)\,\mathrm{d}\chi\right]$$
$$= \mathcal{F}_1 + \frac{1}{\mathcal{L}}\int_{\mathcal{F}_1}^{\mathcal{F}_{\text{max}}} \left(\frac{1}{\mathcal{G}^+(E)} + \frac{1}{|\mathcal{G}^-(E)|}\right)(E - \mathcal{F}_1)\,\mathrm{d}E. \tag{155}$$

Once $c_\pm$ are known as functions of $\mathcal{J}$ and $\mathcal{F}_{\text{max}}$, this equation determines $\mathcal{F}_{\text{max}}$ as a function of J and the bias, ϕ. From equations (151) and (155), we obtain the functions

$$c_\pm = \gamma_\pm(\mathcal{J}; \phi), \qquad \mathcal{F}_{\text{max}} = E_{\text{M}}(\mathcal{J}; \phi). \tag{156}$$

Inserting these functions in equation (148), we obtain the pulse width as a function of $\mathcal{J}$:

$$X_- - X_+ = \Lambda(\mathcal{J}; \phi). \tag{157}$$

An equation for $\mathcal{J}$ is easily found by time-differentiating this equation and using $\mathrm{d}X_\pm/\mathrm{d}\tilde{t} = c_\pm$ and $\mathrm{d}\phi/\mathrm{d}\tilde{t} = 0$,

$$\frac{\mathrm{d}\mathcal{J}}{\mathrm{d}\tilde{t}} = \frac{c_+ - c_-}{-(\partial\Lambda/\partial\mathcal{J})(\mathcal{J}; \phi)}. \tag{158}$$

If ϕ is also slowly varying, a term proportional to $\mathrm{d}\phi/\mathrm{d}\tilde{t}$ appears on the right-hand side of this equation. According to equation (158), the pulse evolves towards the homoclinic pulse with $c_+ = c_- = \mathcal{J}$ which satisfies the bias condition in equation (155).

The previous description becomes explicit in the limit $\delta \ll 1$. In such a case, $\mathcal{G}^+ = \mathrm{O}(1/\delta)$ and $\mathcal{G}^- = -1$ with $c_- = \mathcal{J}$ from equations (150) and (151). The pulse is approximately a straight isosceles triangle with height $(\mathcal{F}_{\text{max}} - \mathcal{F}_1) \sim \mathcal{F}_{\text{max}}$ because $\mathcal{F}_{\text{max}} \gg 1$. This is consistent with equation (148) which yields $X_- - X_+ = \mathcal{F}_{\text{max}} - 1 + \mathrm{O}(\delta) \sim \mathcal{F}_{\text{max}}$, from which $\mathrm{d}\mathcal{F}_{\text{max}}/\mathrm{d}\tilde{t} = c_- - c_+$. Equation (151) then yields the weighted equal-area rule condition for c_+,

$$\int_{\mathcal{F}_1}^{\mathcal{F}_{\text{max}}} \frac{V(E) - c_+}{\tilde{D}(E)}\,\mathrm{d}E = 0 \tag{159}$$

up to $\mathrm{O}(\delta)$ terms. The bias condition in equation (155) gives

$$\phi \sim \mathcal{F}_1 + \frac{(\mathcal{F}_{\text{max}} - \mathcal{F}_1)^2}{2\mathcal{L}}, \tag{160}$$

$$\mathcal{F}_{\text{max}} \sim \mathcal{F}_1 + \sqrt{2\mathcal{L}(\phi - \mathcal{F}_1)} \sim \sqrt{2\mathcal{L}(\phi - \mathcal{F}_1)}, \tag{161}$$

which is of the order of $\sqrt{\mathcal{L}} \gg 1$. Taking into account the fact that $V(\mathcal{F}_1) = \mathcal{J}$ implies $\mathrm{d}\mathcal{F}_1/\mathrm{d}\mathcal{J} = 1/V'(\mathcal{F}_1)$, the last equation together with $\mathrm{d}\mathcal{F}_{\text{max}}/\mathrm{d}\tilde{t} = c_- - c_+$ yields

$$\frac{\mathrm{d}\mathcal{J}}{\mathrm{d}\tilde{t}} = (c_+ - \mathcal{J})\,\frac{V_1'\sqrt{2(\phi - \mathcal{F}_1)}}{\sqrt{\mathcal{L}}}, \qquad V_1' = V'[\mathcal{F}_1(\mathcal{J})]. \tag{162}$$

This equation describes the evolution of the current density on a slowly varying timescale $\tilde{t}/\sqrt{\mathcal{L}}$. Equations (159)–(162) also hold in the large field case $\mathcal{F}_{\text{max}} = \mathrm{O}(\sqrt{\mathcal{L}}) \gg 1$, $\delta = \mathrm{O}(1)$. Then $\mathcal{F} = \mathrm{O}(\sqrt{\mathcal{L}})$ (inside the pulse), $\mathcal{G}^+ = \mathrm{O}(\mathcal{L})$, $\mathcal{G}^- \sim -1$, $c_+ \sim 3/\mathcal{F}_{\text{max}}$ for the Esaki–Tsu velocity in equation (135), $\mathcal{J} = \mathrm{O}(1/\sqrt{\mathcal{L}}) \ll 1$.

Note that the current density tends exponentially to

$$\mathcal{J} = c_+ \sim \frac{3}{\mathcal{F}_{\text{max}}} \sim \frac{3}{\sqrt{2\phi\mathcal{L}}}, \tag{163}$$

which corresponds to the homoclinic pulse described in detail in the Gunn effect literature [198]. This asymptotic description shows how a dipole moves and changes its shape, until it approaches its limiting form for constant current and speed. It also shows that the homoclinic pulse is stable under voltage bias. For a drift velocity with only two branches, this stability property of the dipole was assumed in previous work [187].

Stage (ii). The pulse moves until it reaches $\tilde{x} = \mathcal{L}$ and it starts disappearing. The description of this stage is more technical, and we shall give it for the large field case only. If the cathode has a very low conductivity, the critical current is small, the dipoles are very tall once they are detached from the boundary, and the simple description that follows is accurate except during short time intervals. The bias condition in equation (136) yields

$$\phi \sim \mathcal{F}_1 + \frac{(\mathcal{F}_{\max} - \mathcal{F}_1)^2}{2\mathcal{L}} - \frac{(\mathcal{F}_{\max} - \mathcal{F}_1 - \mathcal{L} + X_+)^2}{2\mathcal{L}} \tag{164}$$

and therefore

$$\mathcal{L} - X_+ \sim \mathcal{F}_{\max} - \mathcal{F}_1 - \sqrt{(\mathcal{F}_{\max} - \mathcal{F}_1)^2 - 2\mathcal{L}(\phi - \mathcal{F}_1)} \sim \mathcal{F}_{\max} - \sqrt{\mathcal{F}_{\max}^2 - 2\mathcal{L}\phi}. \tag{165}$$

Time-differentiating equation (164), using $\mathrm{d}\mathcal{F}_{\max}/\mathrm{d}t \sim \mathcal{J} - c_+$ and equation (165) in the result to eliminate X_+, we obtain

$$\frac{\mathrm{d}\mathcal{J}}{\mathrm{d}\tilde{t}} \sim \frac{V_1'\mathcal{F}_{\max}(c_+ - \mathcal{J})}{\mathcal{L}} + \frac{V_1'\mathcal{J}}{\mathcal{L}}\sqrt{\mathcal{F}_{\max}^2 - 2\mathcal{L}\phi}. \tag{166}$$

In this stage, $\mathcal{J} = \mathrm{O}(1/\sqrt{\mathcal{L}})$, $\mathcal{F}_{\max} = \mathrm{O}(\sqrt{\mathcal{L}})$, $c_+ \sim 3/\mathcal{F}_{\max}$ and timescales as $\mathcal{L}$. Then $\mathrm{d}\mathcal{J}/\mathrm{d}\tilde{t}$ is much smaller than the other terms in equation (166), and we get

$$\mathcal{J} \sim \frac{3}{\mathcal{F}_{\max} - \sqrt{\mathcal{F}_{\max}^2 - 2\mathcal{L}\phi}} \tag{167}$$

because we have used $c_+ \sim 3/\mathcal{F}_{\max}$. Then $\mathrm{d}\mathcal{F}_{\max}/\mathrm{d}\tilde{t} \sim \mathcal{J} - c_+ \sim \mathcal{J} - 3/\mathcal{F}_{\max}$ and equation (167) yield

$$\frac{\mathrm{d}\mathcal{F}_{\max}}{\mathrm{d}\tilde{t}} \sim \frac{3}{\mathcal{F}_{\max} - \sqrt{\mathcal{F}_{\max}^2 - 2\mathcal{L}\phi}} - \frac{3}{\mathcal{F}_{\max}}. \tag{168}$$

Thus $\mathcal{F}_{\max}$ and $\mathcal{J}$ increase until a new wave is injected at the cathode. This occurs when the boundary layer at the cathode becomes unstable.

A simple way of determining the current at which this happens is as follows. The quasistationary boundary layer at the cathode solves equation (134) with $\partial\mathcal{F}/\partial\tilde{t} = 0$, $\mathcal{F}(0) = \mathcal{J}/\tilde{\sigma}$ and $\mathcal{F}(\infty) = \mathcal{F}_1$. As explained earlier, this problem has a unique solution if $\mathcal{J} < \mathcal{J}_c$ (which is a CDL) and no solution if $\mathcal{J} > \mathcal{J}_c$. Before the current reaches $\mathcal{J} = \mathcal{J}_c$, there is a quasistationary CDL at the cathode that changes adiabatically with the instantaneous value of $\mathcal{J}$. Immediately after surpassing $\mathcal{J}_c$, the field at the cathode tries to increase from its value at $\tilde{x} = 0$, which would give rise to a CAL. This CAL has to join smoothly the existing large CDL that ends at $\mathcal{F} = \mathcal{F}_1$. The resulting situation is a dipole whose trailing CAL is pinned at the cathode. This developing dipole gains area, the current decreases below $\mathcal{J}_c$, and the trailing CAL of the dipole has to be detached from the cathode boundary layer, which is again a CDL. A description of the actual injection of a dipole wave after $\mathcal{J}$ has surpassed $\mathcal{J}_c$ uses the ideas of Bonilla *et al* [208] and will be omitted.

Stage (iii). A short time after J has first surpassed $\mathcal{J}_c$, there are two dipoles in the SL, one at the cathode, the other disappearing at the anode. Provided the critical current, $\mathcal{J}_c$, is sufficiently small, the new pulse created at the cathode acquires a triangular shape soon after its birth. Then the bias condition in equation (134) becomes

$$\phi \sim \mathcal{F}_1 + \frac{(\mathcal{F}_{\mathrm{max,n}} - \mathcal{F}_1)^2}{2\mathcal{L}} + \frac{(\mathcal{F}_{\mathrm{max}} - \mathcal{F}_1)^2}{2\mathcal{L}} - \frac{(\mathcal{F}_{\mathrm{max}} - \mathcal{F}_1 - \mathcal{L} + X_+)^2}{2\mathcal{L}} \tag{169}$$

and therefore

$$\mathcal{L} - X_+ \sim \mathcal{F}_{\mathrm{max}} - \mathcal{F}_1 - \sqrt{(\mathcal{F}_{\mathrm{max}} - \mathcal{F}_1)^2 + (\mathcal{F}_{\mathrm{max,n}} - \mathcal{F}_1)^2 - 2\mathcal{L}(\phi - \mathcal{F}_1)}, \tag{170}$$

where the subscripts n refer to the newly created pulse. Wave heights and locations obey

$$\frac{\mathrm{d}\mathcal{F}_{\mathrm{max}}}{\mathrm{d}\tilde{t}} = \mathcal{J} - c_+ \sim \mathcal{J} - \frac{3}{\mathcal{F}_{\mathrm{max}}}, \tag{171}$$

$$\frac{\mathrm{d}\mathcal{F}_{\mathrm{max,n}}}{\mathrm{d}\tilde{t}} = \mathcal{J} - c_{+n} \sim \mathcal{J} - \frac{3}{\mathcal{F}_{\mathrm{max,n}}}, \tag{172}$$

$$\frac{\mathrm{d}X_{-n}}{\mathrm{d}\tilde{t}} = \mathcal{J}, \qquad X_{+n} = X_{-n} - (\mathcal{F}_{\mathrm{max,n}} - \mathcal{F}_1). \tag{173}$$

Time-differentiating equation (170) yields

$$\frac{\mathcal{L}}{V_1'}\frac{\mathrm{d}\mathcal{J}}{\mathrm{d}\tilde{t}} \sim 6 - \mathcal{J}\mathcal{F}_{\mathrm{max}} - \mathcal{J}\mathcal{F}_{\mathrm{max,n}} + \mathcal{J}\sqrt{\mathcal{F}_{\mathrm{max}}^2 + \mathcal{F}_{\mathrm{max,n}}^2 - 2\mathcal{L}\phi}. \tag{174}$$

Provided that $\mathcal{J} = \mathrm{O}(1\sqrt{\mathcal{L}})$, $\mathcal{F}_{\mathrm{max}} = \mathrm{O}(\sqrt{\mathcal{L}}) = \mathcal{F}_{\mathrm{max,n}}$ and timescales as $\mathcal{L}$, the right-hand side of this equation can be set equal to zero, which gives

$$\mathcal{J} \sim \frac{6}{\mathcal{F}_{\mathrm{max}} + \mathcal{F}_{\mathrm{max,n}} - \sqrt{\mathcal{F}_{\mathrm{max}}^2 + \mathcal{F}_{\mathrm{max,n}}^2 - 2\mathcal{L}\phi}}. \tag{175}$$

Equations (171) and (172) together with equation (175) form a planar dynamical system that describes the evolution of the two pulses during the stage of their coexistence.

This stage ends when $X_+ = \mathcal{L}$, the old pulse exits at the anode and we are back at the initial stage with only one pulse. Thus, a period of the current oscillation under dc voltage bias is completed. The longest stage is (i), so that the frequency of the oscillations is approximately $\mathcal{J}/\mathcal{L} \sim 3/\sqrt{2\phi\mathcal{L}}$ or, in dimensional units,

$$f \approx \sqrt{\frac{9\varepsilon F_{\mathrm{M}}^2 l}{2eVN_{\mathrm{D}}}}\,\frac{v_{\mathrm{M}}}{Nl}. \tag{176}$$

Thus, the frequency is proportional to the peak velocity divided by the SL length, $v_{\mathrm{M}}/(Nl)$. The prefactor is the dimensionless velocity of the homoclinic dipole, $c_{\mathrm{h}} \sim 3/\sqrt{2\phi\mathcal{L}} < 1$, which is weakly dependent on the voltage, the SL doping density and the scattering frequencies through F_{M}. Table 3 compares the frequencies of self-oscillations measured experimentally with the ones calculated by solving numerically the GDDE for different strongly coupled SLs. We observe that the numerical solution of the GDDE reproduces very well the observed frequencies but that the numerical solution of the DDE and equation (176) give reasonable estimations thereof. By including the faster stages of the annihilation of a dipole at the anode and of the creation of the new dipole at the cathode, the period of the self-oscillation should decrease, and therefore it should improve the estimation given by equation (176) in table 3.

The observation of Gunn-like dipole oscillations in a strongly coupled SL was initially reported by Le Person *et al* [41]. They investigated the photocurrent of an undoped GaAs/AlAs SL excited with a picosecond light pulse and detected photocurrent self-oscillations of about

Table 3. Numerical values of the oscillation frequencies f_ν^{GDDE}, f_ν^{DDE} and $f_\nu^{(176)}$ according to the asymptotic formula in equation (176) in comparison with the experimental values, $f_\nu^{\exp}$, for five strongly coupled SLs investigated by Schomburg *et al* [213]. d_{W} denotes the well width, d_{B} the barrier width, N_{D}/l the three-dimensional doping density and V the corresponding applied voltage.

d_{W} (nm)	d_{B} (nm)	N_{D}/l ($10^{16}\,\mathrm{cm}^{-3}$)	$f_\nu^{\exp}$ (GHz)	f_ν^{GDDE} (GHz)	f_ν^{DDE} (GHz)	$f_\nu^{(176)}$ (GHz)	V (V)
5.13	0.87	14	19.44	19.5	21.8	16.73	0.95
4.80	0.90	8	29.12	29.1	34.16	24.75	1.07
4.00	1.00	8	46.35	46.5	52.96	38.77	1.2
3.64	0.93	10	52.79	52.8	62.35	42.33	1.24
3.54	0.96	9	65	65	70.32	54.00	1.73

20 GHz in real time. The frequency changed significantly when the applied bias or the photoexcited carrier density was varied. Hofbeck *et al* [202] reported the observation of current self-oscillations in doped, strongly coupled SLs with a frequency of 6 GHz. In a subsequent publication, the same group showed that these oscillations are due to a travelling dipole domain [210], i.e. Gunn-like domains. After the initial observation of current self-oscillations in a doped, strongly coupled SL by Hofbeck *et al* [202], the same group increased the frequency from 9 GHz [210] over 65 GHz [211] to 103 GHz [212] in GaAs/AlAs SLs. The dependence of the frequency on the miniband width was discussed by Schomburg *et al* [213], which we will return to in section 5.2. For (In,Ga)As/(In,Al)As SLs, the maximum frequency for current oscillations is expected to be considerably larger than for GaAs/AlAs SLs, since the electron mobility and therefore the domain velocity are higher in the (In,Ga)As/(In,Al)As materials system. The reported frequencies for (In,Ga)As/(In,Al)As SLs started at 55 GHz [214] and finally reached 147 GHz [215]. Note that all reported measurements on doped, strongly coupled SLs discussed earlier have been performed in the frequency domain.

5.1.2. Monopole and dipole oscillations in weakly coupled SLs. Self-sustained oscillations of the current in weakly coupled SLs have been studied extensively by solving numerically and asymptotically different discrete models. As in the case of DDEs describing strongly coupled SLs, the boundary condition at the injecting contact region selects the type of waves associated with self-oscillations. For example, the simple Ohmic condition $\mathcal{F}(0) = \mathcal{J}/\tilde{\sigma}$ (dimensionless units) with the Esaki–Tsu drift velocity $V(\mathcal{F}) = 2\mathcal{F}/(1+\mathcal{F}^2)$ selects dipole self-oscillations for poor contacts, $\tilde{\sigma} < 1$, and monopole self-oscillations for good contacts, $\tilde{\sigma} > 1$ [187]. Experimental evidence in strongly coupled SLs supports dipole self-oscillations. Therefore, we did not describe monopole self-oscillations in DDEs in the previous subsection. On the contrary, theory and experiments seem to support the idea that both monopoles and dipoles play an important role in electron dynamics in weakly coupled SLs. Consequently, we shall describe both types of self-oscillations in this subsection.

The theory of self-oscillations in long, doped, weakly coupled SLs under a dc voltage bias is now well understood in its main features, although many aspects merit further study. At a fixed temperature and an appropriate doping density (below the first critical doping density of section 4.1), there is an almost homogeneous stationary field profile that becomes unstable for one or more intervals of dc voltage. The analysis of the corresponding oscillatory instability can be performed using bifurcation theory, and the bifurcating branches can be found using numerical continuation methods [110]. These methods, or less exhaustive numerical simulations, give an idea of the influence of other parameters, such as doping density [110, 216], temperature [217], photoexcitation [68, 163] or magnetic fields [77, 173], on the self-oscillations. The dependence of the oscillation frequency on the SL parameters varies with the SL configuration and the plateau of the current–voltage diagram we study. These aspects will be discussed later in this section. However, an asymptotic analysis yields a physical picture of the fully developed self-oscillations that is worth keeping in mind and will be now described for the discrete model with the tunnelling current of equation (99).

As for relocation of EFDs, the key to describing self-oscillations lies in understanding wave front motion. In section 4, we indicated that whenever a CAL advances one SL period in a dc-voltage-biased, doped SL, a current spike appears. This fact is well documented by numerical simulations of different models [78, 81], although a mathematical understanding is lacking to this day. In the existing asymptotic theory, the current spikes are ignored, and the evolution of the current usually refers to a slow evolution of the envelope of the current traces as in section 4.1. Our task is simplified because self-oscillations occur only for a sufficiently low doping density, and fully developed waves, CALs, CDLs and dipoles can be seen unmasked by boundary effects, provided the SL is long. Thus, we can study weakly coupled SLs in the formal limit $eN_{\mathrm{D}}/(\varepsilon F_{\mathrm{M}}) \equiv \nu \to 0$, $N \to \infty$, so that $\mathcal{L} \equiv N\nu \gg 1$. In this limit, we can define $\tilde{x} = \mathrm{i}\nu$ as a continuous dimensionless space variable varying from $\tilde{x} = 0$ to $\tilde{x} = \mathcal{L}$. The resulting spatially continuous theory can then be adopted as a first-order approximation and be corrected by including the effects of discretization later [16, 75, 104, 218].

It is convenient to start by removing the dimensions from the model equations. Self-oscillations occurring at average fields larger than the first resonant field (in plateaus of the I–V characteristic higher than the first one) are described by the discrete drift model with a tunnelling current proportional to the electron density times a non-linear function of the local field. If the average field is smaller than the first resonant field, the tunnelling current is described by the strongly non-linear function in equation (99). Then the limiting, spatially continuous equation is a first-order hyperbolic equation with a strong non-linearity, and its analysis is a challenging mathematical problem. However, one would expect that the main qualitative features of self-oscillations appear in the discrete model that uses the high-temperature limit of equation (101), with $n_{\max} = 2$ in equation (100), as the tunnelling current. The resulting discrete DDE is easier to study [16]. Thus, we shall restrict our field values to the first plateau of the SL and denote by F_{M} and as v_{M} the values of field and current at the first local maximum of the drift velocity in equation (103). We shall define the reference scale of the dimensionless variables as in table 1. The resulting dimensionless equations are

$$\frac{\mathrm{d}\mathcal{F}_i}{\mathrm{d}\tilde{t}} + \tilde{v}(\mathcal{F}_i)\tilde{n}_i - \tilde{D}(\mathcal{F}_i)(\tilde{n}_{i+1} - \tilde{n}_i) = \mathcal{J}, \tag{177}$$

$$\mathcal{F}_i - \mathcal{F}_{i-1} = \nu(\tilde{n}_i - 1). \tag{178}$$

The dimensionless velocity and diffusivity are denoted by $\tilde{v}$ and $\tilde{D}$, respectively. To restore dimensional units, we just multiply each dimensionless quantity by its corresponding unit in table 1. With these definitions, the first local maximum of the drift velocity is $\tilde{v}(1) = 1$, whereas the local minimum is v_{m}, located at $\mathcal{F} = \mathcal{F}_{\mathrm{m}}$. Drift velocity and diffusion are related by $\tilde{v}^{(f)}(\mathcal{F}) = \tilde{v}(\mathcal{F}) + \tilde{D}(\mathcal{F})$, $\tilde{D}(\mathcal{F}) = \tilde{v}^{(f)}(\mathcal{F})\,\mathrm{e}^{-\beta\mathcal{F}}$, with $\beta = eF_{\mathrm{M}}l/(k_{\mathrm{B}}T)$. For the first plateau of the GaAs/AlAs SL with $d_{\mathrm{W}} = 9.0$ nm and $d_{\mathrm{B}} = 4.0$ nm at $T = 5$ K, $\nu = 3$ and $\beta = 21$. In the continuum limit, equations (177), (178) and (85) yield the following hyperbolic equation and bias condition,

$$\frac{\partial\mathcal{F}}{\partial\tilde{t}} + \tilde{v}(\mathcal{F})\left(1 + \frac{\partial\mathcal{F}}{\partial\tilde{x}}\right) = \mathcal{J}, \tag{179}$$

$$\frac{1}{\mathcal{L}}\int_0^{\mathcal{L}} \mathcal{F}(\tilde{x}, \tilde{t})\,\mathrm{d}\tilde{x} = \phi, \tag{180}$$

up to order 1 in terms of the dimensionless doping density, ν. Appropriate boundary conditions are equations (137) and (138), or equivalent ones. The hyperbolic equation (179) may have shock waves, i.e. moving discontinuities at $\tilde{x} = X(\tilde{t})$ such that the field becomes $\mathcal{F}_\pm$ as $\tilde{x} \to X(\tilde{t}) \pm 0$. The shock velocity is [16, 104]

$$V(\mathcal{F}_+, \mathcal{F}_-) = \frac{\int_{\mathcal{F}_-}^{\mathcal{F}_+} (\tilde{v}(E)/\tilde{v}^{(f)}(E))\,\mathrm{d}E}{\int_{\mathcal{F}_-}^{\mathcal{F}_+} (\mathrm{d}E/\tilde{v}^{(f)}(E))}. \tag{181}$$

This formula can be corrected by using the trapezoid rule to evaluate integrals, which typically reduces the discrepancy with direct numerical solutions of the discrete model to a maximum error of 3% [104].

Equation (179) is the same equation that describes the DDE for the Gunn effect in the absence of diffusion [39, 186, 187]. The only difference from the well-known asymptotic theory for the Gunn effect with an N-shaped velocity is the different shock condition in equation (181). Thus, we can directly use the description of self-oscillations for the Gunn effect with this different shock velocity. Rescaling equation (179) according to equation (139), we obtain

$$\mathcal{J} - \tilde{v}(F) = \varsigma \left[\frac{\partial \mathcal{F}}{\partial \tau} + \tilde{v}(\mathcal{F}) \frac{\partial \mathcal{F}}{\partial \xi} \right]. \tag{182}$$

For $\varsigma = 0$, this equation has three solutions in the interval $v_\mathrm{m} < \mathcal{J} < 1$, $\mathcal{F}^{(1)}(\mathcal{J})$, $\mathcal{F}^{(2)}(\mathcal{J})$ and $\mathcal{F}^{(3)}(\mathcal{J})$, ordered from smaller to higher field values. The main ingredients of the asymptotic theory are CALs and CDLs.

CDLs. We construct them by using the exact solution $\mathcal{F} = A + \mathcal{J}\tilde{t} - \tilde{x}$ of equation (179) to join $\mathcal{F}^{(3)}(\mathcal{J})$ to $\mathcal{F}^{(1)}(\mathcal{J})$. The regularization of the resulting corners should be done by means of the original discrete model. Clearly, CDLs are regions depleted of electrons that move with velocity $\mathcal{J}$.

CALs or 'monopoles'. The description of CALs for the DDE with vanishing diffusivity is due to Murray [199] in the case of the Gunn effect. We follow here Bonilla [16]. There is only one value of $\mathcal{J} = \mathcal{J}^*$, such that $V = \mathcal{J}$ with $\mathcal{F}_- = \mathcal{F}^{(1)}(\mathcal{J})$ and $\mathcal{F}_+ = \mathcal{F}^{(3)}(\mathcal{J})$. For $\mathcal{J}^*$, the unique shock joining $\mathcal{F}^{(1)}(\mathcal{J})$ and $\mathcal{F}^{(3)}(\mathcal{J})$ moves with the same speed, J, as a CDL. For $v_\mathrm{m} < \mathcal{J} < \mathcal{J}^*$, a CAL joining $\mathcal{F}^{(1)}(\mathcal{J})$ to $\mathcal{F}^{(3)}(\mathcal{J})$ consists of a shock wave having $\mathcal{F}_+ = \mathcal{F}^{(3)}(\mathcal{J})$, and $\mathcal{F}_-$ such that $V(\mathcal{F}^{(3)}(\mathcal{J}), \mathcal{F}_-) = \tilde{v}(\mathcal{F}_-)$. Furthermore, to the left of the shock wave, there is a *tail* region moving rigidly, with the shock wave described by

$$[\tilde{v}(\mathcal{F}) - V] \frac{\partial \mathcal{F}}{\partial \chi} = \mathcal{J} - \tilde{v}(\mathcal{F}) \tag{183}$$

for negative $\chi = \tilde{x} - V\tilde{t}$ and $\mathcal{F}(-\infty) = \mathcal{F}^{(1)}(\mathcal{J})$, $\mathcal{F}(0) = \mathcal{F}_-$. This whole structure (shock wave and tail region) is called a *monopole with left tail* [186]. Similarly, for $\mathcal{J}^* < \mathcal{J} < 1$, a CAL joining $\mathcal{F}^{(1)}(\mathcal{J})$ to $\mathcal{F}^{(3)}(\mathcal{J})$ becomes a *monopole with right tail.* This monopole consists of a shock wave having $\mathcal{F}_- = \mathcal{F}^{(1)}(\mathcal{J})$ as well as $\mathcal{F}_+$ such that $V(\mathcal{F}_+, \mathcal{F}^{(1)}(\mathcal{J})) = \tilde{v}(\mathcal{F}_+)$ and a tail region satisfying equation (183) for positive χ with the boundary conditions $\mathcal{F}(0) = \mathcal{F}_+$ and $\mathcal{F}(\infty) = \mathcal{F}^{(3)}(\mathcal{J})$ [186]. Thus, the velocity of a CAL as a function of J is determined by the following equations:

$$C(\mathcal{J}) = V(\mathcal{F}^{(3)}(\mathcal{J}), \mathcal{F}_-), \quad \text{with } \tilde{v}(\mathcal{F}_-) = V(\mathcal{F}^{(3)}(\mathcal{J}), \mathcal{F}_-), \quad \text{if } v_\mathrm{m} < \mathcal{J} < \mathcal{J}^*, \tag{184}$$

$$C(\mathcal{J}) = V(\mathcal{F}_+, \mathcal{F}^{(1)}(\mathcal{J})), \quad \text{with } \tilde{v}(\mathcal{F}_+) = V(\mathcal{F}_+, \mathcal{F}^{(1)}(\mathcal{J})), \quad \text{if } \mathcal{J}^* < \mathcal{J} < 1. \tag{185}$$

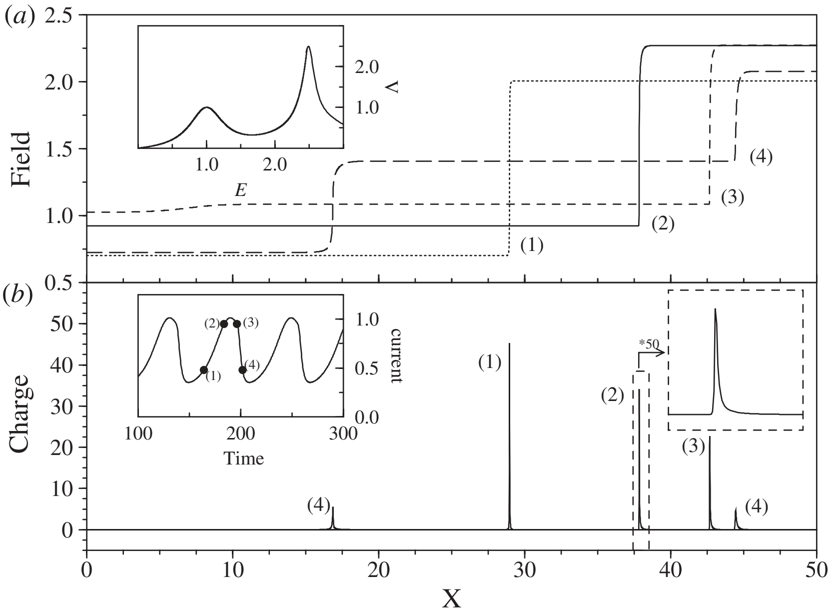

Figure 20. (*a*) Time evolution of the electric field profile in the SL using the velocity curve shown in the inset. (*b*) Charge density profiles ($n - 1 = \partial E(x, t)/\partial x$) showing the location of the wave front for different times. The total current density versus time is shown in the left inset, in which we have marked the times corresponding to the profiles depicted in (*a*). The right inset clearly shows a monopole with a right tail. From [218].

Monopole self-oscillations. Using CALs and CDLs as building blocks, we can now describe asymptotically one time period of the current self-oscillation starting from a given field configuration inside the SL. Let us start with the case of high contact conductivity, in which the Ohmic boundary condition selects monopoles (CALs) as the only waves responsible for the self-oscillations. This case was studied in detail by Bonilla *et al* [218], who used an equivalent boundary condition with a fixed electron density to trigger the monopoles. The initial profile will evolve with time following the current adiabatically, and our first goal will be to find an evolution equation for $\mathcal{J}$. As shown by the numerical solution depicted in figure 20, the easiest imaginable dynamic situation as an initial field profile is that of a single monopole inside the SL, at $\tilde{x} = X^+(\tilde{t})$ (equivalently, at $\xi = X^+/\mathcal{L} = \Xi^+$). Then, the bias in equation (180) is given by

$$\phi \sim \mathcal{F}^{(1)}(\mathcal{J})\, \Xi^+ + \mathcal{F}^{(3)}(\mathcal{J})\, (1 - \Xi^+). \tag{186}$$

If we time-differentiate this equation and use $\mathrm{d}X^+/\mathrm{d}\tilde{t} = \mathrm{d}\Xi^+/\mathrm{d}\tau = C(\mathcal{J})$ together with equation (186), we obtain

$$\frac{\mathrm{d}\mathcal{J}}{\mathrm{d}\tau} = \frac{[\mathcal{F}^{(3)}(\mathcal{J}) - \mathcal{F}^{(1)}(\mathcal{J})]^2}{(\mathcal{F}^{(3)}(\mathcal{J}) - \phi)/\tilde{v}'(\mathcal{F}^{(1)}(\mathcal{J})) + (\phi - \mathcal{F}^{(1)}(\mathcal{J}))/\tilde{v}'(\mathcal{F}^{(3)}(\mathcal{J}))} C(\mathcal{J}). \tag{187}$$

Since $C(\mathcal{J}) > 0$, the current increases as the monopole moves. Note that the dimensionless equation (187) is a particular case of equation (117) with $n_+ = 1, n_- = 0, J \leftrightarrow \mathcal{J}, c_+ \leftrightarrow C(\mathcal{J})$ and $t/N \leftrightarrow \tau$.

Near the injecting contact at $\tilde{x} = 0$, we have a boundary layer, where the field profile follows $\mathcal{J}(\tau)$ adiabatically according to

$$\frac{\partial\mathcal{F}}{\partial\tilde{x}} \sim \frac{\mathcal{J}}{\tilde{v}(\mathcal{F})} - 1, \qquad \mathcal{F}(0,\tau) = \frac{\mathcal{J}(\tau)}{\tilde{\sigma}}. \tag{188}$$

Note that we have ignored $\partial\mathcal{F}/\partial\tilde{t} = \varsigma\,\partial\mathcal{F}/\partial\tau \ll 1$. If $\tilde{\sigma} > 1$ and $j = \tilde{\sigma}\mathcal{F}$ does not intersect $j = \tilde{v}(\mathcal{F})$, the field profile near the cathode becomes that of a quasistatic CAL joining $\mathcal{F}(0,\tau) = \mathcal{J}(\tau)/\tilde{\sigma}$ to $\mathcal{F}(\infty,\tau) = \mathcal{F}^{(1)}(\mathcal{J})$. As $\mathcal{J}$ surpasses unity, a new monopole is triggered at the cathode, it moves to the anode, and J decreases again below unity. The field profile in the resulting situation comprises a new monopole joining $\mathcal{F}^{(1)}(\mathcal{J})$ to $\mathcal{F}^{(2)}(\mathcal{J})$ and the old monopole that now joins $\mathcal{F}^{(2)}(\mathcal{J})$ to $\mathcal{F}^{(3)}(\mathcal{J})$. Depending on the bias, the new monopole catches the old one, or the current drops to v_{m}, so that $\mathcal{F}^{(2)}(\mathcal{J}) = \mathcal{F}^{(3)}(\mathcal{J})$, and only one monopole remains. The situation is the same as during the first stage, and a period of self-oscillations is completed. It is interesting that a developing monopole takes a long time to grow to a mature size (having a shock wave and a tail) [218]. During this time, the monopole moves towards the anode. Consequently, in numerical simulations one gets the erroneous impression that monopoles are nucleated well inside the SL. This impression has an experimental backing too because only the well-to-well hopping motion of a mature monopole produces the characteristic current spikes detected in the experiments. The details of the monopole nucleation, its growth to mature size and the monopole coexistence are too technical to reproduce here, although the simplicity of equation (179) provides an analytical description [218]. The numerical solution of the discrete models can be interpreted with the help of the asymptotic description as shown by Kastrup *et al* [100] for the simple discrete drift model.

Dipole self-oscillations. In weakly coupled SLs, the field profile of a moving dipole comprises a HFD with $\mathcal{F} = \mathcal{F}^{(3)}(\mathcal{J})$, a trailing CAL and a leading CDL, all moving towards the anode. To fix our notation, the position of the trailing CAL is $\tilde{x} = X^{+}(\tilde{t})$ (equivalently, $\xi = X^{+}/\mathcal{L} = \Xi^{+}(\tau)$), and the position of the leading CDL is $\xi = \Xi^{-}(\tau)$. In a starting situation of a single dipole in the SL, the bias condition in equation (180) yields

$$\phi \sim \mathcal{F}^{(1)}(\mathcal{J}) + [\mathcal{F}^{(3)}(\mathcal{J}) - \mathcal{F}^{(1)}(\mathcal{J})](\Xi^{-} - \Xi^{+}). \tag{189}$$

If we time-differentiate this equation and use $\mathrm{d}\Xi^{+}/\mathrm{d}\tau = C(\mathcal{J})$ and $\mathrm{d}\Xi^{-}/\mathrm{d}\tau = \mathcal{J}$ together with equation (189), we obtain the dimensionless equation

$$\frac{\mathrm{d}\mathcal{J}}{\mathrm{d}\tau} = \frac{[\mathcal{F}^{(3)}(\mathcal{J}) - \mathcal{F}^{(1)}(\mathcal{J})]^2}{(\mathcal{F}^{(3)}(\mathcal{J}) - \phi)/\tilde{v}'(\mathcal{F}^{(1)}(\mathcal{J})) + (\phi - \mathcal{F}^{(1)}(\mathcal{J}))/\tilde{v}'(\mathcal{F}^{(3)}(\mathcal{J}))}[C(\mathcal{J}) - \mathcal{J}], \tag{190}$$

which is a particular case of equation (117) with $n_{+} = n_{-} = 1$, $J \leftrightarrow \mathcal{J}$, $c_{+} \leftrightarrow C(\mathcal{J})$, $c_{-} \leftrightarrow \mathcal{J}$ and $t/N \leftrightarrow \tau$. Now the current evolves towards $\mathcal{J} = \mathcal{J}^{*}$ such that $C(\mathcal{J}^{*}) = \mathcal{J}^{*}$. We observe that the dipole moves at constant current with velocity given by the equal-area rule in equation (181), $V(\mathcal{F}^{(1)}, \mathcal{F}^{(3)}) = \mathcal{J}$. After $\Xi^{-} = 1$, there is only one monopole in the SL, and we are back at equation (187). Again, the current increases as the monopole moves.

Let us assume that the cathode conductivity satisfies $1 < \tilde{\sigma} < v_{\mathrm{m}}/\mathcal{F}_{\mathrm{m}}$. Then the boundary line $j = \tilde{\sigma}\mathcal{F}$ intersects the second branch of the drift velocity at a point $(\mathcal{F}_{\mathrm{c}}, \mathcal{J}_{\mathrm{c}})$ with $\tilde{\sigma}\mathcal{F}^{(2)}(\mathcal{J}_{\mathrm{c}}) = \mathcal{J}_{\mathrm{c}}$, which defines the critical current and critical field at the cathode. As in the case of strongly coupled SLs, the current increases until it reaches $\mathcal{J}_{\mathrm{c}}$. Then a dipole wave is injected by the same mechanism, but an analytical description is possible using the simple first-order equation (179) [186]. This description can be used to calculate the time it takes to have a dipole detached from the cathode from the time J first surpasses $\mathcal{J}_{\mathrm{c}}$.

Until now, the asymptotic description of dipole self-oscillations in strongly and weakly coupled SLs has been the same. The fact that the drift velocity of weakly coupled SLs has a third branch introduces qualitatively new features. Let us look at them now. After a new wave is created, J decreases. Using the bias condition to derive an equation for the current rate, we again deduce equation (117) with $n_+ = 2$, $n_- = 1$, $J \leftrightarrow \mathcal{J}$, $c_+ \leftrightarrow C(\mathcal{J})$, $c_- \leftrightarrow \mathcal{J}$ and $t/N \leftrightarrow \tau$, corresponding to a charge tripole. The stable fixed point of this equation, $\mathcal{J} = \mathcal{J}^{\dagger}$, satisfies $2C(\mathcal{J}) = \mathcal{J}$. Depending on the contact conductivity, we can have (i) $\mathcal{J}^{\dagger} < \mathcal{J}_{\mathrm{c}}$, if $1 < \tilde{\sigma} < \mathcal{J}^{\dagger}/\mathcal{F}^{(2)}(\mathcal{J}^{\dagger})$ or (ii) $\mathcal{J}^{\dagger} > \mathcal{J}_{\mathrm{c}}$, if $\mathcal{J}^{\dagger}/\mathcal{F}^{(2)}(\mathcal{J}^{\dagger}) < \tilde{\sigma} < v_{\mathrm{m}}$.

In case (i), $\mathcal{J}$ stays at the value $\mathcal{J}^{\dagger}$ until the old monopole leaves the sample, and we are back at the initial situation. We have thus completed a period of the self-oscillation in a way very similar to that of self-oscillations in strongly coupled SLs. In case (ii), the current, $\mathcal{J}^{\dagger}$, is above the critical value and a new dipole is triggered. Once detached from the cathode and assuming a sufficiently large voltage bias, the situation is described by equation (117) with $n_+ = 3$, $n_- = 2$, $J \leftrightarrow \mathcal{J}$, $c_+ \leftrightarrow C(\mathcal{J})$, $c_- \leftrightarrow \mathcal{J}$ and $t/N \leftrightarrow \tau$, corresponding to a charge quintupole. As the CALs all move at the same speed and the same happens to the CDLs, this strange situation can occur during a finite time. There is again a different fixed point, $\mathcal{J}^{\ddagger}$, and different cathode conductivities, which allow the triggering of more dipoles. Numerical simulations have confirmed this picture in models of bulk semiconductors such as ultrapure p-Ge, whose local current–field relation is N-shaped [208]. For this material, undriven chaos results from chaotic firing of dipoles at the cathode [219]. Cantalapiedra *et al* [219] used the equivalent of equation (117) together with an estimate of the delay it takes to inject a dipole to formulate and check a discrete model of this undriven chaos. The same type of undriven chaos can be expected for weakly coupled SLs because the monopole dynamics in semiconductors with N-shaped current–field characteristics under dc voltage bias and described by scalar equations is universal [220]. This has been confirmed by numerical simulations of the discrete model with the tunnelling current of equation (99) [221], and the same ideas can be used as a basis of a discrete mapping model of this undriven chaos [222]. So far, the prediction of undriven chaos for average fields on the first plateau of a weakly coupled SL has not received experimental confirmation.

It is important to stress the far-reaching difference between monopole- and dipole-mediated self-oscillations we have mentioned earlier: dipoles are created fast and therefore contain noticeable charge accumulation and depletion layers that travel through the whole SL. However, monopoles are also created at the injecting contact, but the charge accumulation in them becomes noticeable only after a certain buildup time. This means that monopoles apparently traverse part of the SL during an oscillation period, whereas dipoles traverse the whole SL. Obviously this difference has important consequences that may be experimentally tested: monopole-mediated oscillations have higher frequencies. Furthermore, numerical simulations of discrete models show that each time a CAL jumps from well-to-well, a current spike is produced. Therefore, the number of current spikes per oscillation period (seen in simulations of discrete models, not in the continuum limit) is smaller for monopole self-oscillations than in the case of dipole self-oscillations as discussed in the numerical results of Sánchez *et al* [81].

The initial observation of current self-oscillations in weakly coupled SLs dates back to 1995, when Kwok *et al* [177] investigated an undoped SL under photoexcitation. Due to the excitation condition, the oscillations were damped. The frequency and the functional form of the time-resolved photocurrent exhibited a strong bias dependence. The initial report on current self-oscillations in a doped weakly coupled SL also appeared in 1995, when the authors directly showed by time-resolved photoluminescence measurements that the current oscillations are due to an oscillation of the field distribution inside the SL [223]. In the same year, it was shown that the frequency can vary within a single sample by more than one order of magnitude on increasing the bias voltage from the first to the second plateau [224]. By looking at different samples, the frequency could initially be varied by about one order of magnitude [225]. A more detailed discussion of the frequency dependence is given in section 5.2.2. Several years later, Rasulova [226] reported the observation of damped current self-oscillations with a frequency below 100 kHz in a weakly coupled GaAs/(Al,Ga)As SL with extremely wide wells.

Subsequently, undamped self-oscillations of the photocurrent in undoped SLs were observed for a type-II GaAs/AlAs [227, 228] and for a direct-gap GaAs/AlAs SL [229, 230]. For the type-II SL, the domain formation is due to resonant coupling between X states in the barrier. For the type-I SL, at least the transport in the LFD occurs by resonant tunnelling between Γ states, while the HFD is due to a resonant coupling between the lowest Γ state in the well and an X state in the barrier. However, the undamped nature of the photocurrent oscillations in these two systems may be connected with the rather long lifetime of electrons in the X state of the AlAs barrier, which at least for the HFD occurs in both samples. Tomlinson *et al* [231] detected undamped photocurrent oscillations in an undoped GaAs/$Al_{0.3}$ $Ga_{0.7}As$ SL, where the transport in the LFD as well as HFD is governed by resonant tunnelling between Γ states. Theoretical and experimental investigations of multiple-quantum-well structures have shown that under optical excitation with infrared light, which excites carriers from the lowest conduction subband into continuum states, periodic EFDs are formed due to the excitation of recharging waves [232–234].

Zhang *et al* [158] observed a bistability between different oscillation modes in a GaAs/AlAs SL, when the bias was swept in different directions. This bistability at the beginning of the oscillation regime is probably due to subcritical Hopf bifurcation. Kastrup *et al* [100] presented an oscillator based on doped weakly coupled SLs that reaches the gigahertz range. In addition, a number of different oscillation modes were discussed, which depend on the detailed shape of the drift velocity versus electric field relation and the doping level. Finally, Amann *et al* [235] have discussed the existence of tripole oscillations in weakly coupled SLs, mimicking the discussion in [186] for the Gunn effect and in [208] for ultrapure p-Ge. According to [236], there may be some experimental evidence for these tripole oscillations.

5.1.3. Effect of SL doping density on monopole self-oscillations. To determine the effect that the configuration and SL doping density have on the static and oscillatory solutions of a discrete model, it is convenient to draw a doping density–voltage phase diagram as in figure 21. This is a diagram for the second plateau, i.e. zero diffusivity, of a 20-period SL, assuming a cathode condition $n(0, t) = 1 + c$ with $c = 10^{-4}$ [110]. Besides this diagram, other comparable work for doped SLs is due to Patra *et al* [216], who solved the PWS discrete model for the first plateau with a doping density that fluctuated randomly about a constant value. Their results are similar to the ones of Moscoso *et al* [110] only if the random doping density is included; otherwise they differ qualitatively. Whether this difference is due to the different model used by Patra *et al* [216] can only be decided by calculating the phase diagram for the first plateau of a weakly coupled SL with the discrete model in equation (84) and the tunnelling current in equation (99).

Let us explain the phase diagram of figure 21 for the simpler discrete drift model. For a dimensionless doping density, ν, lower than the minimum of the solid line, the stable field profile is stationary and almost uniform. For larger doping densities, with $\nu < \nu_{\mathrm{TB}}$, the almost uniform stationary state is linearly stable outside a certain bias interval of average dimensionless field values $(\phi_\alpha, \phi_\omega)$. At the end points of this interval, a branch of self-oscillations stably bifurcates (supercritically), starting with zero amplitude and non-zero frequency (Hopf bifurcation). For $\nu > \nu_{\mathrm{TB}}$, a horizontal line of constant doping density

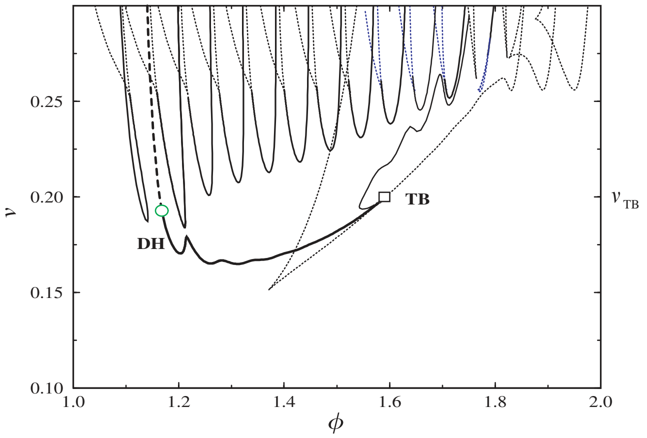

Figure 21. Total phase diagram of the model for $N = 20$ and $c = 10^{-4}$. The dotted lines are curves of stationary saddle nodes. For the sake of clarity, we have plotted only the main line of homoclinic orbits, which originates from the Takens–Bogdanov point, TB (thin solid line; at a Takens–Bogdanov point, lines of Hopf bifurcations, saddle–node bifurcations and homoclinic orbits intersect tangentially). We have not shown other homoclinic orbits, although there is one curve of homoclinic orbits for each Hopf curve. From [110].

intersects a number of different curves: (i) Hopf bifurcations (ii) saddle–node bifurcations and (iii) homoclines.

The intersection of the horizontal line with several Hopf bifurcation curves may indicate that there are intervals of self-oscillations alternating with intervals, in which the stable solution is a stationary state with two EFDs as described in section 3. There may be at most N intervals of stable stationary states, and the CAL separating the LFD and the HFD is pinned at a different well, i, in each different voltage interval. Let us consider the bias interval of self-oscillations located between intervals, whose corresponding static CALs are pinned at wells i and $(i + 1)$. The field profile for these oscillatory states corresponds to a recycling and motion of a CAL about the ith well. In some of the interior regions observed for such doping densities, there may be coexisting multistable states.

The interval of self-oscillations with largest bias ends at a homocline, i.e. the oscillation frequency tends to zero, while the amplitude remains finite. Another interesting feature of the phase diagram is the dashed line of Hopf bifurcations above the point marked DH. On this line, the Hopf bifurcation is subcritical, i.e. an unstable branch of self-oscillations bifurcates for $\phi < \phi_\alpha$. Typically this branch coalesces with a branch of stable oscillations at a smaller bias, ϕ_{LP}. Then there is a bias interval of bistability, in which both self-oscillations of finite amplitude and frequency and a stationary state are stable. Driving the bias adiabatically, we can obtain a hysteresis cycle. Finally, for a sufficiently large doping density, the self-oscillations disappear, and the result is multistability of stationary solutions corresponding to coexistence of EFDs separated by a pinned CAL.

The phase diagram in figure 21 may change substantially if we change the number of SL periods or c. For example, the branch of self-oscillations may disappear at the high-bias region either at a Hopf bifurcation (finite frequency) or at a homoclinic orbit (zero frequency), depending on the values of these parameters. The frequency may decrease or increase with increasing bias, as shown in the numerical results of Kastrup *et al* [100]. The first situation was observed in the experiments of Kastrup *et al* [100], while the second situation was reported by Wang *et al* [237], but for different weakly coupled SLs. Wang *et al* [237] claimed that an increase in the self-oscillation frequency with bias is anomalous, despite the explanation

Table 4. Sample parameters and oscillation frequencies for strongly coupled SLs [212–215]. Δ denotes the miniband width, d_W the well width, d_B the barrier width, L the total thickness of the SL, N_{3D} the three-dimensional doping density, v_M the measured peak velocity and f the measured oscillation frequency. Except for the samples 4.05/1.23 and 4.40/0.90, which are (In,Ga)As/(In,Al)As SLs grown lattice matched on InP, all other SLs are GaAs/AlAs.

Δ (meV)	d_W (nm)	d_B (nm)	L (μm)	N_{3D} (10^{17} cm^{-3})	v_M (10^5 cm s^{-1})	f (GHz)
16	3.10	1.96	0.55	0.8	2	2
22	4.86	1.30	0.74	1.3	9	9
43	5.13	0.87	0.60	1.4	20	20
46	4.80	0.90	0.57	0.8	27	29
55	4.00	1.00	0.50	0.8	31	46
72	3.64	0.93	0.64	1.0	41	53
160	4.05	1.23	0.53	0.8	50	55
72	3.54	0.96	0.45	0.9	34	65
120	4.00	0.60	0.60	0.9	75	103
—	4.40	0.90	0.64	0.8	150	147

to the contrary and numerical evidence of the earlier publication of Kastrup *et al* [100]. However, this conclusion was based on a discrete model of Laikhtman [72] and Wang and Niu [238], in which the stationary tunnelling current did not depend on the electron density. The transition between dynamic and static domain formation with increasing carrier density was experimentally investigated using undoped SLs under photoexcitation by Sun *et al* [239] and Ohtani *et al* [240–243]. It will be discussed in more detail in section 5.4.2.

5.2. Frequency dependence

5.2.1. Strongly coupled superlattices. The measured frequencies of current self-oscillations for strongly coupled SLs investigated by Schomburg *et al* [212–215] are summarized in the last column of table 4 for samples with different miniband widths, Δ_ν. The table also includes the well, d_W, and barrier, d_B, widths the total thickness of the SL, L, the three-dimensional doping density, N_{3D}, and the measured peak drift velocity, v_M. According to a simple transit time argument, the oscillation frequency, f, for travelling dipole domains is determined by

$$f = \frac{c_h}{L}. \tag{191}$$

Here, c_h denotes the velocity of the dipole domain advancing at constant speed towards the anode, when the current takes on the flat minimum value of its time trace during a period of oscillation. This velocity is always smaller than the peak drift velocity, v_M, so that $f = s v_M/L$, where s is a scaling factor, the dimensionless velocity of the uniformly moving dipole, which is smaller than 1. According to equation (176), s is equal to $\sqrt{9\varepsilon F_M^2 l/(2eVN_D)}$. When we plot the measured frequencies versus the ratio v_M/L as shown in figure 22, we obtain a value for s of 0.65, which is somewhat smaller than the value of 0.7 quoted by Schomburg *et al* [213]. However, first of all, they plotted f versus v_M, which is not very sensible. Second, we included some more recent data in figure 22, which was published after the publication by Schomburg *et al* [213] appeared. Since the peak drift velocity increases with increasing miniband width, we conclude that the dipole domain oscillation frequency increases for SLs with a larger miniband width. This analysis supports the idea that the current self-oscillations

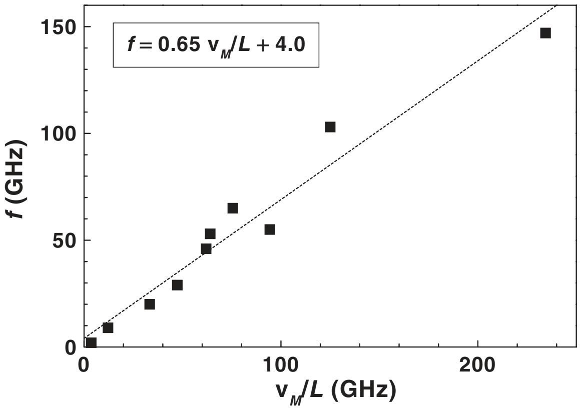

Figure 22. Current oscillation frequencies for strongly coupled SLs according to table 4 as a function of v_M/L (■). The dashed line indicates a least square fit of the data points to a linear function.

in strongly coupled SLs are due to travelling dipole domains, which traverse the complete SL from cathode to anode.

5.2.2. Weakly coupled superlattices. The measured frequencies of current self-oscillations for weakly coupled SLs investigated by Rogozia and Grahn [88] are summarized in the last column of table 5 for samples with different well, d_W, and barrier, d_B, widths. The table also includes the number of periods, N, the energy of the involved sub- or minibands, E_ν, as well as their widths, Δ_ν, which have been calculated using the Kronig–Penney model. The miniband width, Δ_ν, which is a measure of the resonant coupling between adjacent wells, is used in table 5 to order the samples from top to bottom. The index, ν, refers to the mini- or subband index. From table 5, in particular for the set of samples with a constant well width of 15 nm and different barrier widths (0.9, 1.7, 2.9 nm), it appears that the frequency of the current self-oscillations depends exponentially on the barrier width. The simplest approach to obtaining such a frequency dependence is to consider the coupling between different wells in the Wentzel–Kramers–Brillouin (WKB) approximation. In this case, the dominant term determining the tunnelling probability $T(E_\nu)$ between adjacent wells is given by

$$T(E_\nu) = \exp\left(-\frac{2d_B}{\hbar}\sqrt{2m_B^*(V_0 - E_\nu)}\right), \tag{192}$$

where m_B^* denotes the effective electron mass in the barrier and V_0 the conduction band offset between the well and barrier material. The difference, $V_0 - E_\nu$, is a measure of the effective barrier height, which decreases with increasing electric field. This very simple model was used to demonstrate that the frequency dependence of the current oscillations in weakly coupled SLs is dominated by the exponential dependence on the barrier width as well as on the effective barrier height [244].

In order to calculate not only the tunnelling probability, but also the frequency of the current oscillations, we introduce the classical round trip time, τ_{rt}, for an electron in a potential well of width d_W,

$$\tau_{rt}(E_1) = \frac{2d_W}{v(E_1)} = 2d_W\sqrt{\frac{m_W^*}{2E_1}}, \tag{193}$$

Table 5. Sample parameters and oscillation frequencies for weakly coupled SLs. d_W denotes the well width, d_B the barrier width, N the number of SL periods, ν the index of the corresponding plateau of the I–V characteristic, E_ν the energy and Δ_ν the width of the νth sub- or miniband and f_ν the measured oscillation frequency. All SLs consist of 40 periods except for the 13.3/2.7 sample, which has 50 periods. The symbols are used in figures 23 and 24 to distinguish different samples. Solid symbols refer to weakly coupled SLs, open symbols to more strongly coupled SLs. Except for the 10.0/4.0 sample ($*$), which is an (In,Ga)As/(In,Al)As SL grown lattice matched on InP, all other SLs are GaAs/AlAs. From [88].

d_W (nm)	d_B (nm)	Symbol	ν	E_ν (meV)	Δ_ν (meV)	f_ν (MHz)
9.0	1.4	□	1	44.3	4.5	5000
9.0	1.5	◇	1	44.5	3.7	1500
15.0	0.9	△	1	18.6	3.7	2500
10.1	1.4	▽	1	36.7	3.4	1800
10.0	4.0	$*$	1	48.0	2.0	1800
15.0	1.7	●	1	18.8	0.7	500
			2	75.8	2.8	8000
20.0	2.0	◆	1	11.3	0.2	—
			2	45.3	0.7	600
			3	102.2	1.7	1200
			4	182.4	3.2	2300
13.3	2.7	▼	1	23.3	0.1	25
			2	93.0	0.6	500
			3	211.0	1.6	1200
15.0	2.9	▲	1	19.0	<0.1	45
			2	75.8	0.3	500
			3	171	0.8	1700
			4	305	1.9	4000
9.0	4.0	■	1	44.4	<0.1	1
			2	180.0	0.1	20

where m_W^* denotes the effective electron mass in the well. For the energy, we use the value of the first subband, E_1, because for the applied doping concentrations the injecting level is always the ground level. The tunnelling probability through a rectangular barrier is given by [18]

$$T(E_\nu) = \frac{1}{1 + 1/4\ (x + x^{-1})^2\ \sinh^2(\kappa d_\mathrm{B})}, \tag{194}$$

where $\kappa = \sqrt{2m_\mathrm{B}^*(V_0 - E_\nu)}/\hbar$ and

$$x = \sqrt{\frac{m_\mathrm{B}^* E_\nu}{m_\mathrm{W}^*(V_0 - E_\nu)}}. \tag{195}$$

The escape time, $\tau_\mathrm{esc}(E_\nu)$, for a single well is determined by the round trip time, $\tau_\mathrm{rt}(E_1)$, divided by the tunnelling probability, $T(E_\nu)$, through the barrier [245]:

$$\tau_\mathrm{esc}(E_\nu) = \frac{\tau_\mathrm{rt}(E_1)}{T(E_\nu)}. \tag{196}$$

For the energy in the tunnelling probability, we use the value of the subband, E_ν, calculated within the Kronig–Penney model at zero electric field.

The frequency of the current oscillations, which is derived from this escape time model, is determined by the inverse of the product of the escape time and the number of periods, which

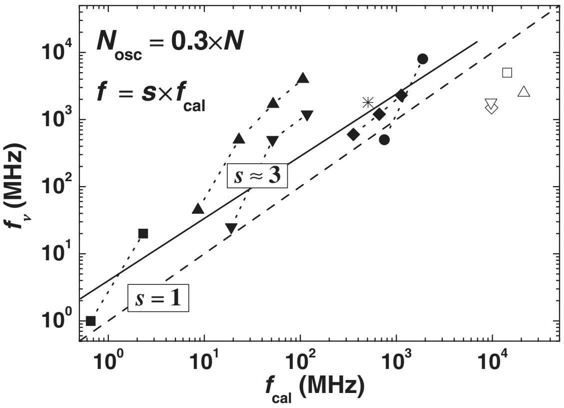

Figure 23. Measured (f_ν) versus calculated (f_{cal}) frequency for the weakly coupled SLs listed in table 5. The same symbols connected with dotted lines indicate oscillations within a single sample in different plateaus. The dashed line indicates the condition $f_{cal} = f_\nu$, the solid line is a least square fit to the solid data points. From [88].

are covered by the current oscillations. For weakly coupled SLs the recycling motion of the domain boundary includes only about 30% of all periods [188] so that $N_{osc} = 0.3 \times N$ and

$$f_{cal} = \frac{1}{N_{osc}\tau_{esc}(E_\nu)}. \tag{197}$$

The oscillation frequencies have been calculated for all samples listed in table 5 on the basis of equation (197). The measured versus the calculated frequencies are shown in figure 23. For weakly coupled SLs indicated by the solid symbols, the slope of the linear fit in the double-logarithmic plot is 0.92, which is in very good agreement with the expected value of 1. In order to directly compare the calculated and the measured values, a scaling factor s is introduced, which is determined by the ratio of measured and calculated frequencies, i.e. $s = f_\nu/f_{cal}$. For the weakly coupled SLs in figure 23, this factor is about 3, so that the observed frequencies are somewhat larger than the calculated ones.

The accuracy of the escape time model is reasonable for weakly coupled SLs because we use for the calculation of the oscillation frequency in the νth plateau of the I–V characteristic the νth energy level. However, in the HFD, the electrons tunnel into the (ν + 1)th level. For that reason, the actual oscillation frequency is expected to be somewhat higher than the calculated one. Another simplification is made with regard to the shape of the barriers since rectangular barriers are used and the energy levels are calculated within the Kronig–Penney model without any electric field. The variation of the data points between different samples and the consistently higher frequencies in some samples (solid triangles in figure 23) may originate from fluctuations of the doping density in the wells. Theoretical calculations show that the oscillation frequency increases by a factor of 5, if the doping density fluctuates by 3% in different wells [138]. Some oscillation frequencies listed in table 5 were only observed at higher temperatures. Between 5 and 300 K, the frequencies can differ by up to a factor of 3, resulting in some variation of the data points. Finally, another reason for the discrepancy between f_ν and f_{cal} could be the actual oscillation mode, which can vary between different SLs [81, 100, 216].

This simple model appears to be better than the more involved transfer model of Sánchez *et al* [81]. In that work, the calculated frequency, f_2, for the GaAs/AlAs SL with $d_W = 13.3$ nm and $d_B = 2.7$ nm is about 20 MHz. That value is more than one order of magnitude smaller than the experimental value of 500 MHz. Our model gives 90 MHz.

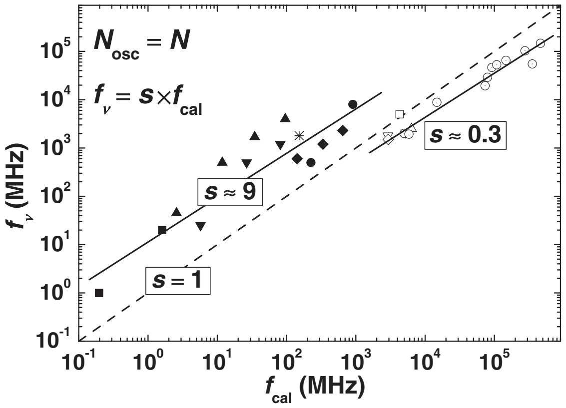

Figure 24. Measured (f_ν) versus calculated (f_{cal}) frequency for the weakly coupled SLs listed in table 5 and for some of the strongly coupled SLs listed in table 4 (⊙). Note that we used a different value for N_{osc} in comparison with figure 23. From [88].

Note that the four most strongly coupled SLs (open symbols) were not included in the linear fit of figure 23, which have calculated miniband widths of $\Delta_1 = 3.4$–4.5 MeV. For these samples, the observed oscillation frequencies are lower than the calculated ones. In order to verify this model for even more strongly coupled SLs, we have also calculated the frequencies for some of the strongly coupled SLs listed in table 4. In this case, a dipole domain travels through the entire SL. Therefore, we use $N_{osc} = N$ (instead of $N_{osc} = 0.3 \times N$) in equation (197). The dotted circles in figure 24 represent the measured versus calculated frequencies for strongly coupled SLs with miniband widths of $\Delta_1 = 16$–140 MeV. The escape time model also works for these samples since the fit in figure 24 also has a slope of about 1, but the observed oscillation frequencies are now smaller ($s \approx 0.3$) than the calculated ones. We also include all weakly coupled SLs from table 5 in figure 24. However, in order to compare the frequencies of weakly SLs with strongly ones, we now assume that the space–charge oscillations cover all periods so that the scaling factor for weakly coupled SLs becomes about 9. This analysis clearly shows that there is a fundamental difference in terms of the oscillation mechanism between strongly coupled SLs (open symbols), where travelling dipole domains are responsible for the current oscillations, and weakly coupled SLs (solid symbols), where the transport by sequential resonant tunnelling results in a recycling motion of a monopole domain boundary. The transition occurs for miniband widths of a few millielectronvolts, where the transition from weakly to strongly coupled SLs is expected.

5.3. Spiking

The discrete motion of the domain boundary can also be observed in the current self-oscillations of weakly coupled SLs. The recycling motion of the CAL usually covers 30%–40% of the entire SL. However, one complete period of the recycling motion should also contain the signature of the relocation process between two adjacent wells, which appears in the I–V characteristic under static domain formation and which was discussed in detail in section 4. This relocation of the CAL results in current spikes, which have been observed by Zhang *et al* [189], Kastrup *et al* [100] and Kantelhardt *et al* [188]. Numerical simulations [188] and a self-consistent microscopic model [81, 246] have provided a direct proof for the assertion that a single spike corresponds to the relocation of the domain boundary by exactly one period.

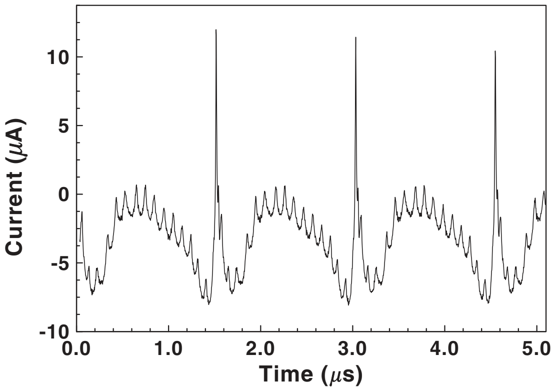

Figure 25. Ac component of the time-resolved current oscillation of a GaAs/AlAs SL with $d_W = 9.0$ nm and $d_B = 4.0$ nm at 2.77 V in the first plateau of the time-averaged I–V characteristic recorded at 6 K. From [188].

Figure 25 shows a time trace of the current oscillations for the GaAs/AlAs SL with $d_W = 9.0$ nm and $d_B = 4.0$ nm listed in table 5 recorded in the first plateau of the I–V characteristic. In addition to the fundamental frequency of 0.66 MHz, which is due to the monopole recycling motion, there are current spikes with a frequency of about 10 MHz [188]. The number of spikes within one period of the fundamental oscillation is directly related to the ratio of the two frequencies, which is 15 in this case. For the same sample, current oscillations with a fundamental frequency of 18.4 GHz are observed in the second plateau of the I–V characteristic, which also contains spikes, but with a frequency of 233 MHz, resulting in a ratio of 13. The number of spikes is a measure of the number of SL periods that are covered by the recycling motion of the CAL. We therefore conclude that about 35% of the SLs are covered by the recycling motion. Experimental results on several other samples with different well and barrier widths as well as a different number of periods confirm this conclusion [188].

Numerical simulations of a modified discrete model have shown that a single spike corresponds to the relocation of the domain boundary by a single period [188]. A detailed modelling of the dynamics of domain walls using a self-consistent microscopic model of sequential resonant tunnelling of Sánchez *et al* [81, 246] demonstrates that the peak of the electron density moves by exactly one SL period during a single current spike. The time dependence of the current is plotted in figure 26(*a*), while figure 26(*b*) shows the charge density profile at four different times of the current spike marked in figure 26(*a*). The spikes have a frequency of about 500 MHz and an amplitude of 2.5 μA. Note that the electron density in figure 26(*b*) is larger than the well doping density for only three wells (40, 41 and 42) during the times recorded in figure 26(*a*). The maximum of the electron density moves from well 40 to well 41 during this time interval, so that (i) tunnelling through the 41st barrier (between wells 40 and 41) dominates, when the total current density is increasing, whereas (ii) tunnelling through barriers 41 and 42 is important when $J(t)$ decreases. The contributions of the tunnelling and displacement currents to $J(t)$ are depicted in figures 26(*c*) and (*d*).

The spikes reflect a two-stage hopping motion—short timescale—of the domain wall: at time (1) (minimum of the current), the charge accumulates mainly in the ith well. As time elapses, electrons tunnel from this well to the next one, the $(i + 1)$th, where most of the charge is located at time (3) (maximum of the current). This corresponds to a hop of the monopole. As the monopole moves, it leaves a lower potential drop in its wake. The reason is that the electrostatic field in the $(i + 1)$th well and barrier become abruptly flat between times (1) and

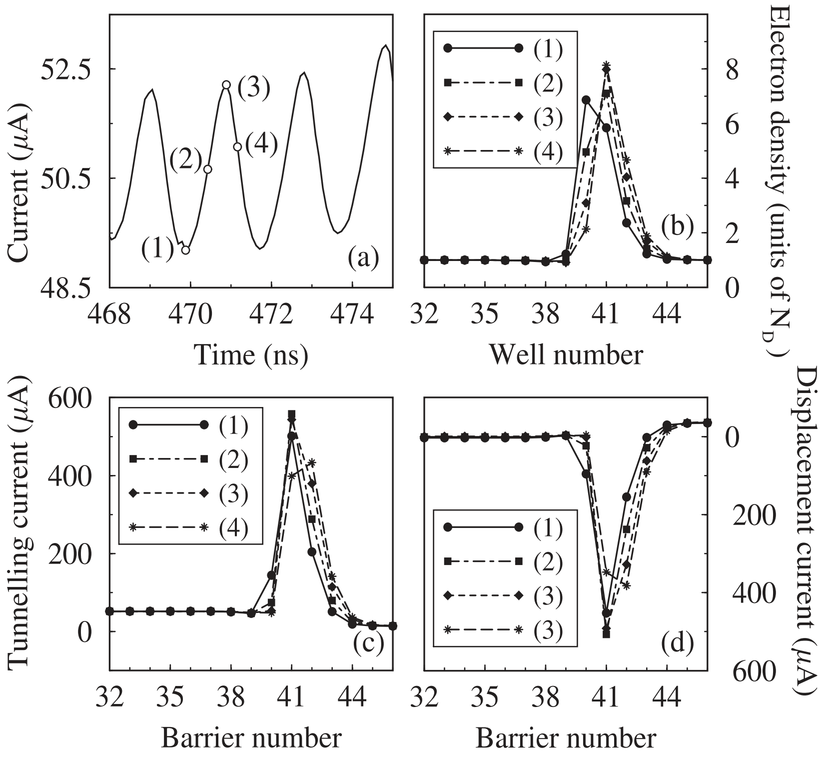

Figure 26. (*a*) Enlarged section of a calculated time trace showing the spikes of the current. (*b*) Electron density profiles (in units of the doping density in the wells), (*c*) tunnelling current and (*d*) displacement current versus barrier number within the monopole at the times marked in (*a*). From [81].

(3), as they pass from the HFD to the LFD. This means that a negative displacement current has its peak at the $(i + 1)$th barrier, near the wells, where most of the charge resides. Between times (1) and (3), the tunnelling current is maximal, while the displacement current is minimal and the total current increases. After that, some charge flows to the next well (time (4)), but both tunnelling and displacement currents are smaller than previously. This occurs because the potential drop at barrier $(i + 2)$ (in the HFD) is larger than the one at barrier $(i + 1)$. Then there is a smaller overlap between the resonant levels of nearby wells—the tunnelling current decreases—as well as the displacement current, and eventually $J(t)$ decreases. This stage lasts, until well i is drained, and most of the charge is concentrated at wells $(i + 1)$ (the local maximum of charge) and $(i + 2)$ (slightly smaller charge). Then, the next current spike starts.

5.4. External control parameters

External control parameters such as voltage bias, carrier density, temperature and magnetic field have different effects on the current self-oscillations. The voltage bias can change the frequency within a plateau and between different plateaus. The carrier density can be varied within a single sample by photoexcitation. An increasing carrier density can induce a transition from dynamic to static EFD formation, while an increasing temperature or magnetic field perpendicular to the layers can induce a transition from static to oscillating domains.

5.4.1. Voltage bias. The variation of the oscillation frequency as a function of voltage bias for doped SLs was discussed by Kastrup *et al* [100]. Within a plateau region, the frequency can be tuned in some samples by a factor of 2 to 3. This magnitude of the frequency tunability depends on the actual oscillation mode. When the frequency is basically bias independent, the current self-oscillation are due to the typical monopole recycling mode as described in section 5.1.2. However, when the frequency decreases with increasing bias within the plateau, the electric-field profile oscillates around an almost uniform stationary state [100], which is typical for a rather low doping density. The bias dependence of the frequency for photocurrent oscillation in undoped, photoexcited SLs was also investigated experimentally by Kwok *et al* [177], Hosoda *et al* [227], Mimura *et al* [228], Ohtani *et al* [229, 230, 241–243] and Tomlinson *et al* [231]. Unfortunately, there is no unique trend observed. In many cases, the frequency decreases very rapidly at the beginning of the plateau, remains constant for most voltages in the plateau and increases somewhat at the end of the plateau, before the oscillations disappear.

A much larger tunability can be observed when the voltage is increased from one plateau to the next. Table 5 lists the frequency not only for different samples, but also for different plateaus of a single sample. For example, in the GaAs/AlAs SL with $d_{\mathrm{W}} = 15.0\,\mathrm{nm}$ and $d_{\mathrm{B}} = 2.9\,\mathrm{nm}$ the frequency can be increased by almost two orders of magnitude going from the first to the fourth plateau. This increase within one sample was already discussed in connection with the model for the frequency dependence described in section 5.2.2. The origin for this frequency increase is a decreasing effective barrier height due to the larger electric field because the tunnelling current is determined by both, the barrier width, which is constant for a given sample, and the effective barrier height, which decreases with increasing plateau index.

5.4.2. Carrier density. The carrier density can be varied most easily by exciting electron–hole pairs with above-band-gap light. Additional photoexcitation applied to a doped SL can result in a decreasing frequency with increasing laser intensity, which at the time was not reproduced by the model [224]. For photoexcitation of an undoped, type-II SL, the frequency strongly increases for carrier densities just above the lower critical density and reaches a plateau at higher carrier densities [227, 228]. However, for type-I SLs, there is usually little variation of the oscillation frequency with increasing carrier density [229, 231].

The transition between dynamic and static domain formation as a function of carrier density has been studied theoretically [68, 163] as well as experimentally for a number of undoped, photoexcited SLs [239, 240, 242, 243]. A phase diagram of the carrier density versus bias voltage has been constructed. It shows that the transition between dynamic and static domain formation is not independent of the applied bias voltage. While the experiments exhibit a certain modulation of this transition region with bias, the theoretical investigations show a very detailed structure of this transition region, which is shown in figure 21.

Photoexcitation of undoped SLs acts qualitatively on self-oscillations in a manner similar to that of varying the doping density for doped SLs. The discrete models become rather complicated in this case since we have to include the two-dimensional hole density in the Poisson equation and add a rate equation for the holes [68, 223]. In order to understand the experimentally observed phase diagrams of photoexcited SLs, more theoretical work is necessary.

Finally, the evolution from a static state at low carrier densities to an oscillating domain at higher carrier densities was demonstrated in an undoped, photoexcited SL by increasing the laser power [159]. Several distinct bifurcation scenarios were observed in connection with a controllable bistability. In the bistable regime, the oscillations disappear via a subcritical Hopf bifurcation with increasing reverse bias. When the bistability is absent at low (high)

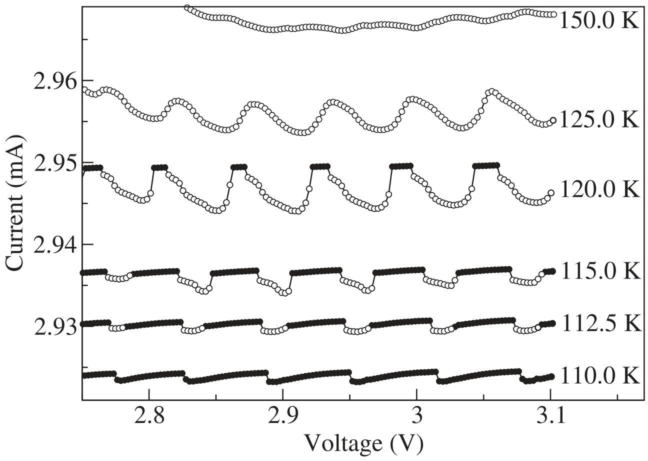

Figure 27. I–V characteristics for different temperatures showing stationary (dynamic) states with full (empty) circles. The boundary condition parameter $c = 10^{-3}$ has been used in the numerical simulations. The curve corresponding to 150 K has been shifted by −0.04 mA for clarity. The lines are only added for purposes of guiding the eye. From [217].

laser powers, the oscillations disappear via a supercritical Hopf bifurcation (homoclinic connection).

5.4.3. Temperature. Temperature changes both the Fermi functions and the scattering amplitudes in the expressions for the tunnelling currents. As a consequence, the drift velocity and the diffusion coefficient in the DDD model can be substantially changed, which in turn can drastically affect self-oscillations. In addition, thermionic emission above the barrier can also alter the drift velocity. However, in contrast with an increasing doping density, which can stabilize oscillating domains, an increasing temperature can facilitate self-oscillations.

Experiments inducing current self-oscillations by increasing the temperature have been reported by Ohtani *et al* [240], Wang *et al* [165, 167, 172] and Li *et al* [166]. In most of these experiments, the time-averaged I–V characteristics show a transition from the branch-like modulation with increasing temperature which is typical for static EFD formation, to a rather featureless plateau-like structure which is typically observed for current self-oscillations. A detailed analysis of the transition region demonstrates that within a certain temperature range there is a coexistence between static and dynamic domains [165, 237].

The temperature–voltage phase diagram is similar to the doping density–voltage diagram, except that an increase in the doping density stabilizes the domains, while an increase in the temperature may lead to current self-oscillations. This can be seen from the numerically calculated current–voltage characteristics for temperatures between 110 and 150 K shown in figure 27. It was calculated for a GaAs/AlAs SL with 40 periods, $d_W = 14.0$ nm, $d_W = 4.0$ nm and a well doping density of $N_D = 2 \times 10^{11}$ cm^{-2}. The voltage regime shown in figure 27 corresponds to the second plateau of the SL used in the experiments of Wang *et al* [165]. The numerical calculations were performed by Sánchez *et al* [168, 217]. They are based on the discrete drift model with a drift velocity computed directly from equation (91) by means of the procedure reported by Bonilla *et al* [82]. However, in order to study the influence of temperature, the scattering amplitude, γ, was linearly interpolated between the values $\gamma = 18$ MeV at 1.6 K and $\gamma = 23$ MeV at 140 K, taken directly from the experimental data as explained by Sánchez *et al* [217]. $\gamma(T)$ was assumed to be the same for all resonances.

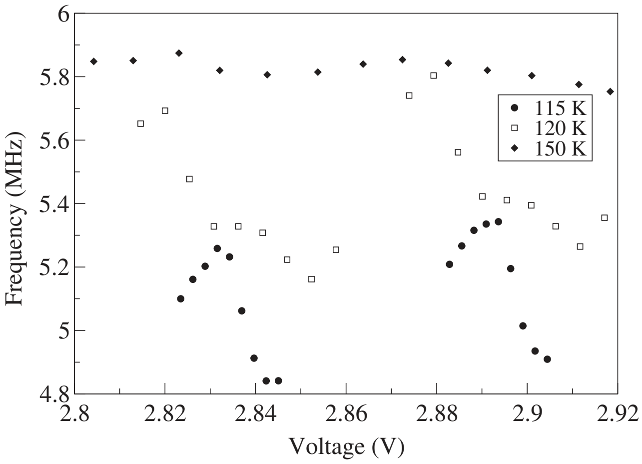

Figure 28. Current oscillation frequencies versus voltage for some dynamic dc bands of the curves shown in figure 27. From [217].

In this SL, the first peak of the drift velocity disappears rapidly as the temperature increases above 50 K. In the second plateau, the maximum and minimum of the resulting drift velocity both increase with temperature, and their positions are shifted to lower field values. The minimum drift velocity increases faster with temperature than the maximum, which tends to wash out the difference between them [217]. This behaviour of the drift velocity is reflected in the observed multistable static EFDs and self-oscillations. For example, multistable solution branches of the current–voltage characteristic should also shift to lower voltages and higher currents as the temperature increases, as observed in the experiments of Li *et al* [166]. These effects could not be obtained from the fitted drift velocity used by Li *et al* [166]. The numerical solution of the discrete drift model with constant electron density at the cathode shows that the voltage intervals of static EFDs shrink as the temperature increases and disappear above 120 K as shown in figure 27. The I–V curve contains intervals in which the average current increases with voltage, followed by intervals in which the average current decreases. At lower temperatures, the intervals of increasing current are wider, whereas the opposite occurs at higher temperatures. Correspondingly, the frequency of the self-oscillations in such an interval starts increasing, but it drops to a smaller value than the initial one at the upper limit of the interval, which is shown in figure 28. The amplitude of the self-oscillations (not shown here) vanishes at the upper and lower limits of each voltage interval. This suggests that the branches of self-oscillations begin and end at supercritical Hopf bifurcations. As the temperature increases, the region of NDC in the drift velocity becomes shallower, and the frequency of the self-oscillations increases (cf figure 28).

5.4.4. Magnetic field. The effect of an external magnetic field on the current self-oscillations has been studied experimentally by Sun *et al* [77, 173] and Wang *et al* [167, 172]. As with increasing temperature, an increasing magnetic field applied parallel to the layers, i.e. perpendicular to the electric field, can induce a transition from static domains to oscillating domains. With increasing magnetic field, the time-averaged I–V characteristic loses its branch-like structure, which is observed at $B = 0$, indicating the presence of a propagating domain wall. Increasing B both shifted the plateaus to larger voltages and diminished the length of the branches in the I–V characteristics as well as the peak current. Above a critical field B_1, the I–V curve became flat and self-oscillations started. When a second, even higher, critical B_2 was surpassed, the self-oscillations and the corresponding plateau disappeared again. These observations were explained by simulations of the discrete drift model with parameters corresponding to the second plateau of the SL [77, 173]. For the drift velocity, they used the expression of Kazarinov and Suris [66], but with an increased Lorentzian width $\Gamma(B)$ and its centre, eFl, shifted to $eFl - e^2l^2B^2/(2m^*)$. The transitions between static and dynamic domains as well as between dynamic and no domains at all are attributed to a magnetic-field-induced modification of the negative differential velocity (NDV). The peak-to-valley ratio decreases between 0 and B_2, while above B_2 the NDV disappears. A detailed analysis of the effect of a magnetic field applied parallel to the electric field on the dynamics of EFD formation is still missing. In this context, it would be interesting to compare the experimental results with simulations based on the drift velocity given in equations (100) and (103).

6. Driven systems and chaos

6.1. Theory

Both strongly and weakly coupled SLs exhibit self-sustained oscillations of the current under dc voltage bias, given appropriate values of doping density, well and barrier widths and material composition. These oscillations are accompanied by a rich dynamics of EFDs, indicating the possibility of more complex behaviour, including chaotic attractors and spatiotemporal chaos. This possibility has been investigated by a number of authors, as reviewed in this section. Theoretical studies predominantly interpret numerical solutions of model equations for SLs driven by an ac voltage bias in addition to the given dc voltage difference between the SL ends (ac + dc voltage bias). Theoretical studies of chaos in driven or undriven SLs are much less complete than all the other non-linear phenomena so far described.

6.1.1. Weakly coupled SLs. Bulashenko and Bonilla [247] predicted chaos in driven, weakly coupled SLs by solving the discrete drift model under ac + dc voltage bias with fixed excess electron density in the first SL well. Their results [247–250] can be illustrated as follows. Let the dc voltage be fixed at a value on the second plateau of the I–V characteristics of a 40-period SL such that, in the absence of ac driving, there are self-oscillations of the current due to the periodic monopole motion. The drift velocity is a sum of Lorentzian functions that corresponds to the SL studied by Grahn *et al* [223]. Then, add a driving voltage with a frequency equal to the natural oscillation frequency times the inverse golden mean, $(1 + \sqrt{5})/2 \approx 1.618$ (an irrational number that is most poorly approximated by rational numbers). To find aperiodic attractors, it is convenient to plot a measure of the amplitude of the solutions as a function of the control parameter, the amplitude of the driving voltage. The current density or the current corresponding to a solution is a natural measure of the amplitude of the solution, which is easily observed in experiments. Thus, a natural bifurcation diagram depicts the current at integer multiples of the period of the driving voltage, T_{d}, as a function of the dimensionless amplitude of the driving voltage, a (measured in units of $F_{\mathrm{M}}Nl$). Periodic solutions with the same frequency as that of the driving voltage (frequency-locked solutions) appear as a single point in this diagram, solutions with twice the period T_d appear as two points, etc.

Figure 29 shows that there appear windows of chaotic solutions as the amplitude of the driving voltage increases. We see that the SL starts in a quasiperiodic state (with first Lyapunov exponent $\lambda_1 = 0$) at $a = 0$, as it should be for an irrational frequency ratio. Then at $a \approx 0.005$, the SL locks to a period-5 orbit ($\lambda_1 < 0$) terminated by several chaotic windows at the relatively small driving amplitude $a \approx 0.01$ ($\lambda_1 > 0$). After $a > 0.085$, period doubling cascades and several chaotic windows can be seen. For even larger a, the solution becomes quasiperiodic

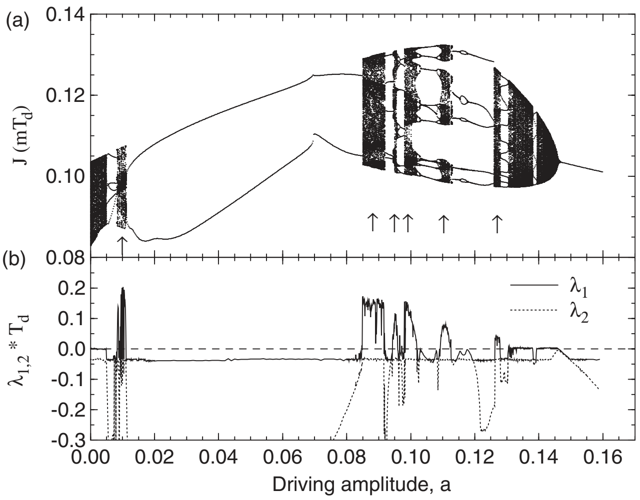

Figure 29. (*a*) Bifurcation diagram of the current obtained by means of Poincaré mapping each driving-force period, T_d, and (*b*) the first two Lyapunov exponents versus the driving-force amplitude, a, for the golden-mean ratio between natural and driving frequencies. Windows of chaotic solutions are marked by arrows. The Lyapunov exponents are scaled to the driving period, T_d. From [248].

again (as it was at $a = 0$), before locking to the driving frequency, f_d, at $a \approx 0.145$. The chaotic attractors are low-dimensional, and their corresponding electric field profiles show nucleation and motion of monopoles at different places inside the SL [247]. A detailed description of chaos and quasiperiodic attractors in the discrete drift SL model was presented by Bulashenko *et al* [248], which includes Lyapunov exponents and fractal dimensions of attractors, Arnol'd tongues in the phase diagram of driving amplitude versus driving frequency, Fourier spectra of different attractors and first return maps of the current density at successive times mT_d and $(m+1)T_d$. Zwolak *et al* [251] have recently extended this analysis to predicting chaotic transport in dc+ac-voltage-biased arrays of quantum dots or quantum wires described by discrete drift models.

As described in section 6.4, the experimentally observed chaos is more complex than the one of the discrete drift model. In particular, the Fourier spectrum of the self-oscillations is richer in the experiments. Moreover, for voltages in the second plateau of one SL, undriven chaos has been observed (cf section 6.3). The motion of CALs in the discrete drift model is accompanied by very small current spikes, whereas these spikes are much larger in other models [15, 81]. The high-frequency current spikes will yield additional peaks in the Fourier spectrum of self-oscillations, and so it is natural to study driven oscillations with these models and to compare their numerical solutions with experimental results. Unfortunately, there are very few studies in this direction. Sánchez *et al* [107] used the discrete model of Aguado *et al* [80] to show that the high-frequency current spikes give rise to distorted Poincaré first return maps of the current at successive times mT_d and $(m+1)T_d$, as observed by Luo *et al* [182] (cf section 6.4). A systematic study of this model, or of the simpler discrete model with the tunnelling current of equation (99) and realistic boundary conditions yielding both dipole and monopole mediated self-oscillations, is still lacking.

An intriguing and unsolved question is the explanation of undriven chaos in the second plateau of the time-averaged I–V characteristics in the GaAs/AlAs SL with $d_W = 9.0\,\mathrm{nm}$ and $d_B = 4.0\,\mathrm{nm}$ [252]. Two possible explanations have been proposed. Kantelhardt *et al* [188] suggest that non-stationary tunnelling effects may cause current spiking for high fields. They introduced a phenomenological time delay in the tunnelling current (which is of pure drift type) and showed that the resulting model displays current spikes and complex dynamics as the tunnelling delay time increases. Undriven chaos might thus be caused by frequency locking between the slow drifting motion of monopoles and internal frequencies arising from the time lag. No theory of the origin of time lag has been advanced, and no model of non-stationary tunnelling current is known. Therefore, these arguments have not been substantiated by a consistent theory.

The other explanation is based upon the mechanism of dipole self-oscillations of section 5.1. If the contact resistivity is finely tuned, more than one dipole can be present in the SL at a given time interval. Undriven chaos can then arise from the random creation of dipoles at the cathode, as initially proposed by Bonilla *et al* [208] for a model of ultrapure p-Ge. Using the asymptotics of wave fronts as in section 5.1 and taking into account the finite time it takes to create a dipole at the injecting contact, Cantalapiedra *et al* [219] derived a discrete model of wave front dynamics to explain these chaotic oscillations. Following this lead, Amann *et al* [221] solved numerically the discrete tunnelling model with the current of equation (99) and appropriate cathode conductivity to find undriven chaos caused by random firing of dipoles. Further elaboration on the relation of the reduced wave front dynamics to a tent map is due to Amann *et al* [222]. That these theoretical results explain the observed undriven chaos in SLs is rather unlikely. First, undriven chaos was observed for voltages on the second plateau of the I–V characteristic, not on the first plateau, as in the calculations of Amann *et al* [221]. For the corresponding high electric fields, the tunnelling current density is purely of drift type, for which undriven chaos has not been found. Secondly, chaotic motion of wave fronts might be observable for voltages in the first plateau of the SL I–V characteristic. However, this chaotic motion should be demonstrated to persist if the Ohmic cathode condition is changed to a more realistic boundary condition, such as equation (96) or (122). The delicate tuning of the cathode conductivity needed for chaotic motion is not a good indication of the robustness of this mechanism as an explanation of the origin of undriven chaos in SLs.

6.1.2. Strongly coupled SLs. Chaos in strongly coupled SLs has been investigated using numerically solving balance equation models. If the SL is driven at terahertz frequencies, the field and electron densities may be considered spatially homogeneous. Thus, the simplest models for this regime ignore the spatial dependence of the electric field and the electron density and analyse chaotic and quasiperiodic oscillations of the resulting non-autonomous (driven chaos) system of differential equations. Authors following this approach include Alekseev *et al* [253, 254] and Romanov and Romanova [255].

After the prediction and observation of chaos in weakly coupled SLs, Cao and Lei [256] characterized chaos in hydrodynamic models of strongly coupled SLs driven by gigahertz frequencies. Cao *et al* [257, 258] extended this work to models of quantum dot arrays and of terahertz-driven semiconductors with negative effective mass, respectively. In these investigations, undriven self-oscillations are due to periodic motion of charge dipoles, as in the Gunn effect. Chaotic oscillations in driven SLs appear through complex bifurcation scenarios [256]. Simpler models based on the QDDE (72) or its semiclassical limit [34] might prove easier to analyse. These models are similar to the ones of the Gunn effect in bulk GaAs. Numerical studies of the Gunn effect under ac + dc voltage bias exhibiting driven chaos have been carried out by Mosekilde *et al* [259,260] and by Oshio and Yahata [261]. These authors used different drift–diffusion models with zero-charge boundary conditions at the contacts, and they included a notch in the doping density near the cathode (which acted as a nucleation site for dipoles (cf table 2)). It is interesting that models of the Gunn effect including dynamics of traps in addition to the electron transport have undriven chaotic oscillations among their solutions [262].

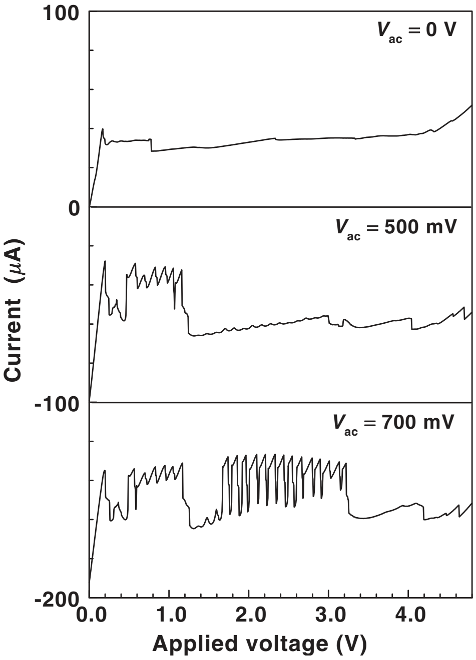

Figure 30. Time-averaged I–V characteristics for different driving amplitudes (*a*) $V_{\mathrm{ac}} = 0\,\mathrm{mV}$, (*b*) 500 mV and (*c*) 700 mV with a frequency of 50 MHz in the GaAs/AlAs SL with $d_{\mathrm{W}} = 9.0\,\mathrm{nm}$ and $d_{\mathrm{B}} = 4.0\,\mathrm{nm}$ at 6 K. The traces in (*b*) and (*c*) have been shifted by $-100\,\mu$A and $-200\,\mu$A, respectively. From [189].

6.2. *Quenching of current self-oscillations in weakly coupled superlattices*

The current oscillations shown in figure 25 contain two timescales, the oscillation, of the order of a microsecond, and the hopping of the domain boundary between adjacent wells, of the order of 100 ns. If this system is driven by an oscillating voltage with a large amplitude and a frequency much higher than the hopping frequency between adjacent wells, the domain boundary will be localized again within a single well [189]. Under this condition, the system should exhibit static domain formation. In figure 30, the first plateau of the time-averaged I–V characteristics in the GaAs/AlAs SL with $d_{\mathrm{W}} = 9.0\,\mathrm{nm}$ and $d_{\mathrm{B}} = 4.0\,\mathrm{nm}$ is shown for different amplitudes with a driving frequency of 50 MHz at 6 K. The trace in figure 30(*a*) has been recorded without any driving signal, and the traces in figures 30(*b*) and (*c*) with an amplitude, V_{ac}, of 500 mV and 700 mV, respectively. While the trace in figure 30(*a*) does not show any sign of static domain formation, the trace in figure 30(*c*) resembles to a large extent the I–V characteristic in the inset of figure 7. The changes for the low-voltage regime are already visible in figure 30(*b*). The oscillations are quenched by the driving signal with a high frequency and large amplitude. This interpretation is confirmed when we look at the frequency spectra recorded for different amplitudes of the driving signal. In figure 31, the frequency spectra for the GaAs/AlAs SL with $d_{\mathrm{W}} = 9.0\,\mathrm{nm}$ and $d_{\mathrm{B}} = 4.0\,\mathrm{nm}$ recorded at 2.77 V are shown for $V_{\mathrm{ac}} = 0$, 200, 500, 740 and 800 mV. The fundamental frequency of the low-frequency oscillation is denoted f_0. The spectra for $V_{\mathrm{ac}} = 0$, 200 and 500 mV show many higher harmonics with almost equal amplitude since the low-frequency oscillation in figure 25 is not sinusoidal but contains a large number of spikes. The high-frequency component from the hopping motion is not shown on this frequency scale. A strong change in the frequency

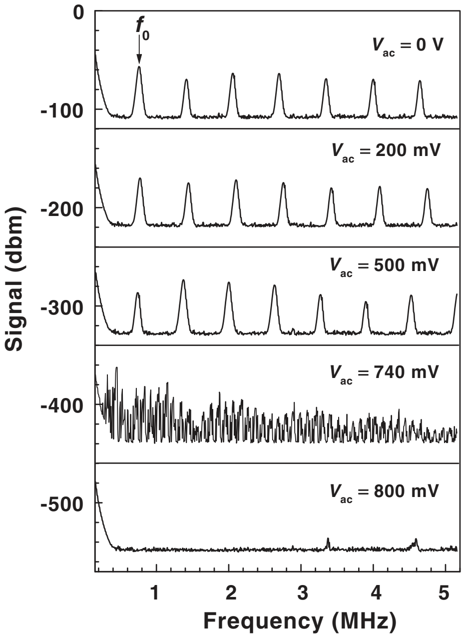

Figure 31. Frequency spectra of the current oscillations for an applied voltage of 2.77 V in the GaAs/AlAs SL with $d_W = 9.0$ nm and $d_B = 4.0$ nm using different amplitudes of the driving voltage, V_{ac}, with a frequency of 50 MHz at 6 K. The spectra at $V_{ac} = 200$ mV, 500 mV, 740 mV and 800 mV have been shifted by −110 dbm, −220 dbm, −330 dbm and −440 dbm, respectively. From [189].

spectra is observed between $V_{ac} = 500$ and 740 mV. For $V_{ac} = 800$ mV, the oscillations are completely quenched. The quenching is not observed if the frequency of the driving signal is smaller than 10 MHz, which is the hopping frequency between adjacent wells. We therefore conclude that even in the unstable regime static domains can be observed, if the system is driven by an ac voltage with a large amplitude and a frequency which is much higher than the well-to-well hopping time of the domain boundary. Dynamic EFDs can be transformed back into static EFDs by an external driving frequency with the appropriate frequency and amplitude.

6.3. *Undriven chaos in weakly coupled superlattices*

In this subsection, we will look more closely at the voltage dependence of the frequency spectra in an undriven system. In figure 32, the oscillations in the GaAs/AlAs SL with $d_W = 9.0$ and $d_B = 4.0$ nm are shown for two different applied voltages, V_{dc}. While for $V_{dc} = 7.6$ V in figure 32(*a*) the oscillations are periodic, the time trace for $V_{dc} = 7.491$ V in figure 32(*b*) has a more complicated time dependence [252]. These oscillations occur in the second plateau of the time-averaged I–V characteristic in this sample. The corresponding frequency spectrum for $V_{dc} = 7.6$ V contains only two sharp peaks at 22 and 44 MHz, while the one for $V_{dc} = 7.491$ V consists of a broad-band noise spectrum. We conclude that the trace in figure 32(*a*) corresponds to a fully periodic regime with several higher harmonics, while the trace in figure 32(*b*) has the signature of undriven chaos.

The existence of chaotic windows in the frequency spectra becomes more evident when the power spectra for the GaAs/AlAs SL with $d_W = 9.0$ nm and $d_B = 4.0$ nm recorded at 30 K

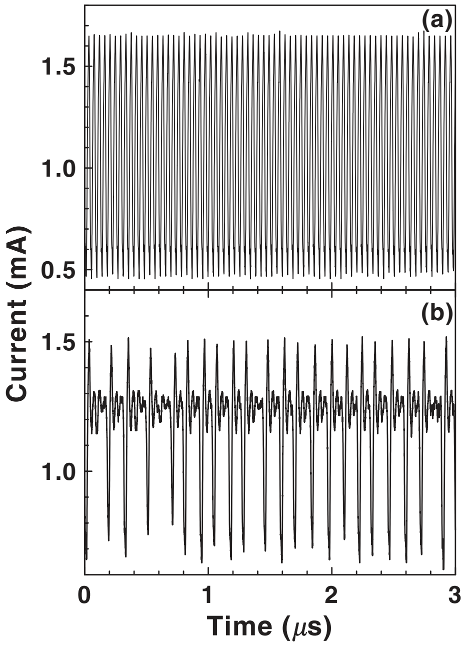

Figure 32. Current oscillations in (*a*) the periodic regime at $V_{dc} = 7.6$ V and (*b*) the chaotic regime at $V_{dc} = 7.941$ V for the GaAs/AlAs SL with $d_W = 9.0$ nm and $d_B = 4.0$ nm recorded at 30 K. From [252].

are plotted versus the applied voltage on a grey scale as in figure 33(*a*). Dark areas correspond to a large amplitude of the oscillations. The corresponding time-averaged I–V characteristic is shown in figure 33(*b*) on the same voltage scale at the same temperature [252, 263]. With increasing bias, several chaotic windows exist, which are separated by periodic windows containing only the fundamental frequency and several higher harmonics. The transition from the chaotic to the periodic window occurs over a very narrow voltage range, e.g. at $V_{dc} = 7.6$ V. However, the transition from a periodic to a chaotic window usually consists of a random-enhancing process covering a broader voltage range. Comparing the voltage ranges of the chaotic windows with the time-averaged I–V characteristic in figure 33(*b*), there is a clear correlation between the existence of a chaotic window and a large NDC in the time-averaged current. The periodic windows, however, appear for positive differential conductivity (PDC). The sharp transitions from the chaotic to the periodic window correspond to the minimum value of the average current, i.e. the onset of PDC. The regions with a PDC are characterized by attractive coupling between the different degrees of freedom of the different quantum wells. The SL behaves as a self-synchronized unit with spontaneous periodic current oscillations. However, in the regions with a large NDC, the coupling becomes strongly repulsive. With increasing repulsion, the synchronized oscillations become more and more destabilized, until the SL enters a chaotic state. With increasing temperature, the chaotic windows become smaller and smaller until they completely disappear at 60 K [252]. As the temperature increases, other scattering mechanisms such as optic phonon scattering become more and more likely, thereby reducing the effective non-linearity of the system. The structures in the time-averaged I–V characteristic disappear completely for temperatures above 60 K, so that the structureless current plateau corresponds to a large periodic window. In contrast, a magnetic field applied perpendicular to the layers, i.e. parallel to the electric field, has the opposite effect on the chaotic windows [264]. With increasing magnetic field, B, the chaotic windows become wider and

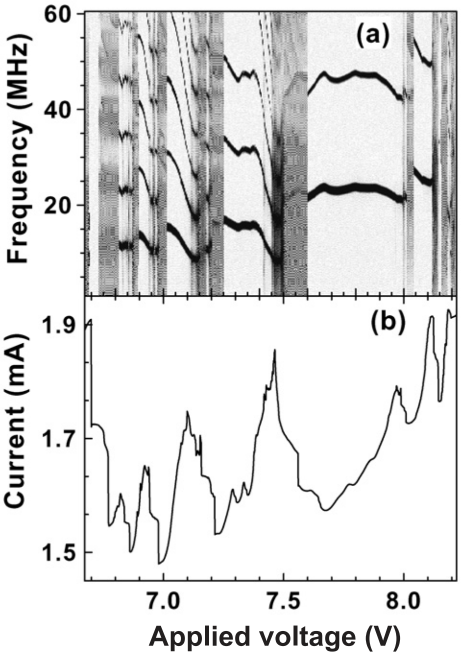

Figure 33. (*a*) Frequency spectra of the spontaneous current oscillations and (*b*) time-averaged current versus applied voltage for the GaAs/AlAs SL with $d_W = 9.0\,\text{nm}$ and $d_B = 4.0\,\text{nm}$ recorded at 30 K. In the power spectra, dark areas correspond to large amplitudes. From [252].

the structures in the time-averaged I–V characteristics less pronounced. At $B = 9\,\text{T}$, almost the whole oscillatory regime exhibits chaotic oscillations. This observation was interpreted as an equalization of the transport process over the whole SL resulting in a suppression of any disorder effects between different periods. The undriven chaos itself is probably generated by the presence of the finite timescale of the sequential resonant tunnelling process between adjacent wells.

6.4. Frequency locking, quasiperiodicity and chaos driven by an external ac voltage

6.4.1. Weakly coupled superlattices. The application of an external driving voltage with a frequency close to the intrinsic frequency of the current self-oscillations can result in a rather complex behaviour with increasing amplitude, V_{ac}, of the driving frequency [263,265]. Figure 34 displays the frequency bifurcation diagram (frequency spectra as a function of V_{ac}) of the GaAs/AlAs SL with $d_W = 9.0\,\text{nm}$ and $d_B = 4.0\,\text{nm}$ for a dc bias voltage, V_{dc}, near the centre of the second plateau of the corresponding I–V characteristics. The driving frequency, f_d, was chosen to be $(1 + \sqrt{5})/2 \times f_0 = 18.4\,\text{MHz}$, so that the ratio f_d/f_0 corresponds to the golden mean. For $V_{ac} = 75\,\text{mV}$, 125 mV, 145 mV, 155 mV and 180 mV, the frequency spectra indicate frequency locking at ratios $\frac{5}{8}$, $\frac{7}{11}$, $\frac{9}{14}$, $\frac{11}{17}$ and $\frac{2}{3}$, respectively, i.e. the winding number of the frequency-locked states increases according to $(2m + 1)/(3m + 2)$ with $m = 2, 3, 4, 5, \ldots$. For very low values of V_{ac}, the ratio $\frac{3}{5}$ can be observed, which corresponds to $m = 1$. Note that the inverse of the initial ratio, $\frac{3}{5}$, is numerically close to the golden mean, with a value of about 1.618. The regions between the frequency-locked windows correspond to quasiperiodic oscillations. This conclusion was drawn from real-time traces, which were then used to construct Poincaré maps between the current amplitudes I_{n+1} and I_n, where I_n

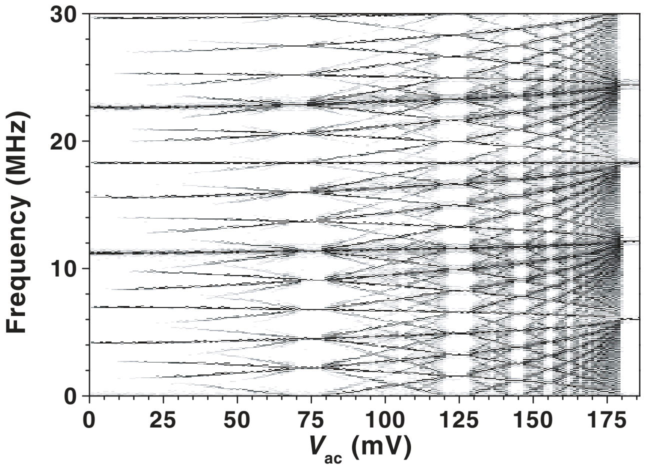

Figure 34. Frequency bifurcation diagram for $V_{dc} = 7.080$ V and $f_d = 18.4$ MHz for the GaAs/AlAs SL with $d_W = 9.0$ nm and $d_B = 4.0$ nm recorded at 5 K. The current power spectra are shown as density plots versus the amplitude of the driving voltage, V_{ac}, where dark areas correspond to large amplitudes. From [265].

is obtained by sampling the current trace, $I(t)$, at a fixed phase (usually the maximum of the amplitude of the driving frequency signal) in the nth period of the driving voltage [265]. The Poincaré maps in the frequency-locked regime consist of $3m + 2$ isolated points (except for large values of m, where they contain only three isolated points), while in the quasiperiodic regime they are closed loops [266]. Due to the presence of higher harmonics in the undriven frequency spectrum of figure 34, the Poincaré maps of the frequency-locked (discrete set of points) as well as quasi-periodic windows (closed loops) are highly distorted [267]. This distortion was connected in a theoretical investigation to the presence of the high-frequency spikes in the current traces discussed in section 5.3, which together with the much lower driving and natural frequency yields a much richer power spectrum [107]. With increasing V_{ac}, the separation between frequency-locked and quasiperiodic windows becomes smaller and smaller. For V_{ac} between 155 and 180 mV, the frequency spectra become more and more smeared out, indicating the presence of chaotic oscillations in this regime. The route to chaos follows an alternation between frequency locking and quasiperiodicity, until the chaotic state is reached, just before the system returns to the final frequency-locked state. This bifurcation process is considered to be explosive, since the attractor dimension changes rather abruptly [268]. When the dc bias voltage, V_{dc}, is changed to the beginning of the second plateau in the corresponding I–V characteristic, the route to chaos changes completely as evidenced by the dependence of the frequency spectra and Poincaré maps [265] as well as the multifractal dimension [268] on V_{ac}. It now follows the route quasiperiodicity → synchronized chaos → frequency locking → chaos → chaos with higher complexity. This very different route is probably due to the fact that for a voltage close to the edge of the current plateau the driving amplitude will move the system periodically out into the static regime and back into the oscillating regime. In contrast, when the system is biased near the centre of the plateau, the system will completely remain in the oscillating regime for the driving amplitudes applied.

An investigation of the bifurcation diagrams for undoped photoexcited SL also demonstrated the existence of a transition between periodic and chaotic oscillations [269].

However, the actual form of the bifurcation diagram depends strongly on the laser intensity, indicating a strong effect of the carrier density on the bifurcation diagram [269].

6.4.2. Strongly coupled superlattices. The response of an ac driving voltage has also been investigated experimentally and theoretically for strongly coupled SLs with frequencies in the same range as the intrinsic oscillation frequency [270–272]. However, due to the much higher intrinsic frequency for strongly coupled SLs in comparison with weakly coupled ones, experimental results are only possible in the frequency domain and not in real time. In particular, single-shot real time traces, which are necessary for constructing Poincaré maps, cannot be performed for frequencies larger than 10 GHz. Nevertheless, the frequency spectra for strongly coupled SLs, i.e. for propagating dipole domains, also indicate the presence of synchronization, frequency locking and quasiperiodicity. The locked and disturbed dipole domain propagation state can be described by a 'devil's staircase', where in the locked state the ratio of the external frequency and the intrinsic domain transit frequency becomes a rational number [270]. A theoretical analysis indicates that the external ac field controls the domain propagation by a modification of both the domain velocity and the shedding of domains from the cathode.

A separate theoretical investigation focused on the evolution of the impedance of the SL circuit with the frequency of the ac driving voltage [271, 272], which exhibits strong variations of its amplitude and phase. In addition, Jappsen *et al* [271, 272] found frequency-locked and quasiperiodic propagating dipole domains as well as a phase synchronization of the travelling dipole domains.

6.5. Photon-assisted domain formation

There is a very different range for the external driving frequencies, which can strongly affect the domain formation in SLs. EFD formation induced by photon-assisted tunnelling has been observed in a weakly coupled SL with the photon field in the terahertz regime [273]. New virtual states serve a role similar to that of unperturbed, real quantum well states in the description of the resonant transport process underlying the domain formation. In a more strongly coupled SL under terahertz radiation, the same authors observed dynamic localization, absolute negative conductance and stimulated, multiphonon emission [274]. Subsequently, a theoretical investigation by Aguado and Platero [275, 276] using a self-consistent microscopic model of sequential tunnelling through multiple quantum wells in the presence of terahertz fields showed how the EFDs can be supported by virtual photonic sidebands due to multiple photon emission and absorption. Very recently, the same authors [17] published a detailed review of photon-assisted transport in semiconductor nanostructures.

The interaction of high-frequency fields with the miniband electrons has been experimentally investigated by Winnerl *et al* [277] in a strongly coupled SL that shows negative differential resistance at room temperature. They observed a field-induced reduction of the current through the SL with a different bias dependence below and above a characteristic frequency of 1 THz. A transition from a quasistatic to a dynamic interaction with the high-frequency field was interpreted as a transition from a classical to a quantum response, in analogy with a corresponding transition of irradiated SLs that showed sequential resonant tunnelling [278]. Very recently, the action of a terahertz field on the motion of electrons performing Bloch oscillations was investigated theoretically for a strongly coupled SL [279]. An amplification of the terahertz field can occur via phase-locked k-space bunches of Bloch oscillating electrons for a driving frequency that is smaller than the Bloch frequency. This study may lead to a development of a Bloch laser for terahertz radiation.

Photo-assisted dynamical transport in highly doped, weakly coupled SLs and its consequences for EFD formation were theoretically investigated by López *et al* [280, 281]. The results indicate that the terahertz field induces with increasing intensity a transition from a stationary configuration to a dynamic state with an ac-induced recycling motion of the domain walls, possibly via a supercritical Hopf bifurcation. The oscillation frequency lies in the megahertz regime and is therefore much smaller than the frequency of the driving photon field. By a further increase in the intensity of the terahertz field, the current becomes stationary again. At the same time, the electric field is homogeneously distributed over the whole sample. The ac field can therefore be used to induce and control oscillations. This is not done by special triggering but rather by driving the system to a distinct dynamical state.

7. Applications

In this section, we will briefly discuss several devices such as oscillators, detectors and quantum-cascade lasers, for which non-linear transport in SLs and its consequences for the field distribution have a significant importance for the device performance.

7.1. Gigahertz oscillators

The original idea of semiconductor SLs of Esaki and Tsu [1] was to use this artificial structure for the development of a Bloch oscillator. However, although Bloch oscillations have been observed experimentally [4], there is no device which uses electrical injection based on this original concept. Nevertheless, the existence of NDV in strongly coupled SLs due to miniband transport resembling Bloch oscillations has led to the observation of oscillations caused by travelling dipole domains with extremely high frequencies as summarized in section 5.2.1. A complete device based on a strongly coupled SL was reported by Schomburg *et al* [282]. A millimetre wave oscillator was developed with a quasiplanar design using a GaAs/AlAs SL built into a waveguide, which allows easy integration into a planar millimetre wave circuit. The device was tunable by about 10% around 70 GHz with an output power of $100\,\mu$W. Depending on the applied voltage, additional oscillation lines up to 180 GHz were observed. (In,Ga)As/(In,Al)As SLs were used to design amplifiers and oscillators with frequencies of up to 74 GHz [283, 284]. The advantage of this material is that it can be directly utilized for applications above 30 GHz in connection with optical telecommunications wavelengths (1.3–$1.6\,\mu$m).

In order to develop high-power SL oscillators for submillimetre radiation, the impact of electron heating and of the mesa size on the I–V characteristics was investigated theoretically [285, 286] and experimentally [286, 287] for strongly coupled SLs. The relatively large miniband width in strongly coupled SLs causes an additional heating instability, which appears as an S-shaped I–V characteristic in addition to the conventional N-type one occurring at lower electric fields [285]. The combination of these two instabilities alters the structure of the dipole domain associated with the self-generated gigahertz oscillations, resulting in a more complex dynamical behaviour [286]. Since the electron heating is much larger for strongly coupled SLs than for weakly coupled ones, this effect is much more important for oscillators based on travelling dipole domains. Increasing the mesa size also increases the electron temperature by Joule heating [287]. For large mesa sizes, the current jumps in the I–V characteristics disappear, indicating the suppression of propagating dipole domains. A proper heat management is therefore necessary for large-area SL oscillators based on propagating dipole domains [287].

7.2. Detectors

There are two kinds of detectors that are based on non-linear transport in semiconductor SLs. The first one uses strongly coupled SLs for detection of terahertz signals. The second one is a photodetector for the infrared spectral region and is based on weakly coupled SLs or multiple-quantum-well structures.

Winnerl *et al* [288,289] developed a detector and an autocorrelator for picosecond terahertz radiation pulses based on a wide miniband GaAs/AlAs SL. The detection at room temperature employed a terahertz field-induced change in the conductivity of the SL, while the correlation used the non-linearity of the conductivity change at strong terahertz-field pulse powers. The non-linear conductivity change was attributed to two effects, the dynamical localization of miniband electrons and the ionization of deep impurity centres. This type of detector with a frequency range up to about 5 THz was then used to characterize short terahertz pulses with a poorly defined trigger signal [290] and to detect the emission of a copper-doped germanium terahertz laser [291]. Subsequently, the range of the detector was extended up to 10 THz by using a different SL with a wider miniband [292]. A detector based on an SL with submonolayer barriers showed a dynamic range of more than six orders of magnitude, indicating that it should be possible to reach a responsivity comparable with that of a Schottky diode [293]. A strongly coupled SL can also lead to frequency doubling or tripling of terahertz radiation due to the frequency modulation of damped Bloch oscillations of the miniband electrons [294]. The non-linear response of strongly coupled GaAs/AlAs SLs to terahertz radiation was analysed theoretically by Ignatov *et al* [295]. While the current responsivity is small for the infrared-active, transverse polar-optic phonon due to dynamic screening of the terahertz fields by the lattice, the responsivity is strongly increased at the longitudinal polar-optic phonon frequency due to a resonant enhancement of the terahertz field inside the SL. Strongly coupled semiconductor SLs may therefore be useful for development of ultrafast detectors for a desired region of the terahertz frequency range.

The work on EFDs in weakly coupled SLs in the 1980s was mainly triggered by the interest in intersubband photodetectors for the mid-infrared spectral range [119]. In a multistack GaAs/(Al,Ga)As quantum well infrared detector, special switching properties were observed, which were attributed to the formation and readjustment of HFDs in the structure [296]. Subsequently, Shakouri *et al* [297] discussed the important parameters which govern the formation, expansion and readjustment of EFDs in multi-quantum-well structures. The pattern of EFD formation can be manipulated by a careful design of the device. Using an infrared photodetector based on a weakly coupled SL with bound-to-continuum transitions, Xu *et al* [298] demonstrated that the electric-field strength in the HFD is below the resonant field strength as already discussed in section 3.2. Gravé and An [299] published a more detailed review on the switching and control of electric-field configurations along multi-quantum-well structures.

The formation of periodic EFDs was investigated theoretically for optically excited multi-quantum-well structures under bias triggering bound-to-continuum transitions [232]. In particular, an electric-field distribution with a period equal to twice the structure period was shown to be possible. The origin of these periodic EFDs was associated with the excitation of recharging waves due to a decreasing capture rate of electrons with their heating by the electric field. The formation of periodic electric-field and charge distributions in these quantum-well structures becomes possible when the intensity of the infrared radiation is sufficiently high for the photoexcitation to prevail over the thermionic emission of electrons from the quantum wells [233]. The threshold intensity of the EFD formation depends on the donor concentration in the quantum wells and the characteristic capture and generation fields [233]. The dynamics of the electric-field distributions and photocurrent were found to be different for structures with even and odd numbers of quantum wells [234].

7.3. Quantum-cascade lasers

In 1994, the inverse of the infrared photodetector based on semiconductor SLs or multiple quantum wells, the infrared emitter, was demonstrated by Faist *et al* [300]. This infrared emitter is called a quantum-cascade laser (QCL). Structurally, QCLs are SLs with typically 30 periods, in which the unit cell consists of up to 20 individual layers. In some versions of the QCL, the unit cell contains a graded-gap or chirped SL, which is strongly coupled. At the same time, the coupling between two periods is smaller than the coupling within a single period. Therefore, QCLs are SLs with intermediate coupling between adjacent wells. For a detailed review of QCLs, see Gmachl *et al* [301]. In a recent investigation of the carrier transport and the carrier distribution in GaAs/(Al,Ga)As quantum-cascade structures (QCSs) by Ohtsuka *et al* [302], it was shown that the dark j–F characteristics of undoped QCSs exhibit distinct current maxima, resulting in regions of NDC, while a plateau-like feature appears under illumination. For doped QCSs, a plateau with sawtoothlike structures appears, which are well known from doped, weakly coupled SLs under EFD formation as described in section 3. However, in contrast to the splitting of the PL line that is observed for doped, weakly coupled SLs, no splitting has been observed in doped QCSs. The j–F characteristic of an undoped QCS with thicker barriers than the original QCS exhibits a much more pronounced current maximum in the dark. Under illumination, the j–F characteristic of this structure shows a clear plateau-like feature, which contains additional fine structure, indicating the existence of electric-field inhomogeneities within each period due to the separation of electrons and holes. These results indicate that the formation of static EFDs as well as current self-oscillations due to propagating monopole or dipole domains may also be important for the operation of QCLs. However, there is also clear evidence that these features are strongly suppressed in working lasers, because otherwise the lasing operation would be much more difficult to achieve. Nevertheless, at this point in time, the influence of static as well as dynamic domain formation on the lasing properties of QCLs has been investigated neither experimentally nor theoretically.

8. Summary and outlook

In terms of their theoretical description of non-linear dynamics, semiconductor SLs have to be divided into two groups, weakly and strongly coupled SLs. While the non-linear transport in strongly coupled SLs can be described by spatially continuous partial differential equations, the description of non-linear transport in weakly coupled SLs has to be based on spatially discrete differential-difference equations. Due to this discreteness, non-linear transport in weakly coupled SLs contains a rather rich spectrum of non-linear phenomena such as the formation of stationary electric-field domains, multistability of the I–V characteristic, complex switching scenarios between static domains including a tripole/dipole relocation process, current self-oscillations due to a monopole recycling motion, spiking in the switching transients and in the current self-oscillations due to the discontinuous motion of the charge monopole between two adjacent wells, undriven chaos, frequency locking, quasiperiodicity and chaos for an external driving voltage. In contrast, due to the continuous nature of the underlying equations, strongly coupled SLs exhibit mainly current self-oscillations, which in this case are due to a dipole propagating through the whole SL as in the Gunn effect, and frequency locking. Stationary domains and multistability as well as the switching processes associated with stationary domains are not present in the non-linear transport of strongly coupled SLs.

The derivation of discrete and continuous balance equations from quantum kinetic theory is still lacking for a unified description of non-linear transport in semiconductor SLs. Furthermore, the stability of the solutions describing Bloch oscillations and driven terahertz oscillations against space-dependent disturbances needs additional investigation. In terms of further experimental work, the effect of some external control parameters such as the magnetic field on the stationary domain formation and the current self-oscillations is still poorly understood. Furthermore, an investigation of the non-linear transport characteristics as a function of mesa size down into the submicrometre regime seems in view of some recent theoretical work an interesting direction for future work. The theoretical description of the switching processes and their stochastic aspects in weakly coupled SLs clearly need further investigation. Experimentally, the reconstruction of unstable branches from switching experiments seems to be an interesting challenge. Open questions remaining include the microscopic theoretical description of the spiking and the existence of undriven chaos in weakly coupled SLs. For devices, a complete theory for non-linear transport in quantum-cascade lasers is still lacking.

Acknowledgments

We would like to thank R Aguado, A Amann, O M Bulashenko, A Carpio, R Escobedo, A Fischer, K-J Friedland, J Galán, R Hey, F J Higuera, M Hosoda, J W Kantelhardt, J Kastrup, M Kindelan, R Klann, P Kleinert, K von Klitzing, H Kostial, S H Kwok, K J Luo, R Merlin, M Moscoso, W Müller, N Ohtani, A Perales, G Platero, K H Ploog, M Rogozia, D Sánchez, O Sánchez, H Schneider, J Soler, S W Teitsworth, S Venakides, A Wacker and Y H Zhang for fruitful collaborations and discussions as well as their invaluable contributions to this work. This work was supported in part by the DGES grant PB98-0142-C04-01, by the MCyT grant BFM2002-04127-C02-01 and by the European Union under grant HPRN-CT-2002-00282.

References

[1] Esaki L and Tsu R 1970 Superlattice and negative differential conductivity in semiconductors *IBM J. Res. Dev.* **14** 61

[2] Fujiwara K 1995 Growth and characterization *Semiconductor Superlattices: Growth and Electronic Properties* ed H T Grahn (Singapore: World Scientific) pp 1–27

[3] Agulló-Rueda F and Feldmann J 1995 Wannier–Stark localization and Bloch oscillations *Semiconductor Superlattices: Growth and Electronic Properties* ed H T Grahn (Singapore: World Scientific) pp 99–153

[4] Feldmann J, Leo K, Shah J, Miller D A B, Cunningham J E, Meier T, von Plessen G, Schulze A, Thomas P and Schmitt-Rink S 1992 Optical investigation of Bloch oscillations in a semiconductor superlattice *Phys. Rev.* B **46** 7252

[5] Esaki L and Chang L L 1974 New transport phenomenon in a semiconductor 'superlattice' *Phys. Rev. Lett.* **33** 495

[6] Capasso F, Mohammed K and Cho A Y 1986 Sequential resonant tunneling through a multiquantum well superlattice *Appl. Phys. Lett.* **48** 478

[7] Sibille A 1995 Miniband transport *Semiconductor Superlattices: Growth and Electronic Properties* ed H T Grahn (Singapore: World Scientific) pp 29–97

[8] Kroemer H 1972 Gunn effect—bulk instabilities *Topics in Solid State and Quantum Electronics* ed W D Hershberger (New York: Wiley) pp 20–98

[9] Carpio A, Bonilla L L, Wacker A and Schöll E 2000 Wave fronts may move upstream in semiconductor superlattices *Phys. Rev.* E **61** 4866

[10] Grahn H T, Haug R J, Müller W and Ploog K 1991 Electric-field domains in semiconductor superlattices: a novel system for tunneling between 2D systems *Phys. Rev. Lett.* **67** 1618

[11] Nabarro F R N 1987 *Theory of Crystal Dislocations* (New York: Dover)

[12] Braun O M and Kivshar Y S 1998 Nonlinear dynamics of the Frenkel–Kontorova model *Phys. Rep.* **306** 1

[13] Gerde E and Marder M 2001 Friction and fracture *Nature (London)* **413** 285

[14] Keener J P 1987 Propagation and its failure in coupled systems of discrete excitable cells *SIAM J. Appl. Math.* **47** 556

[15] Wacker A 2002 Semiconductor superlattices: a model system for nonlinear transport *Phys. Rep.* **357** 1

[16] Bonilla L L 2002 Theory of nonlinear charge transport, wave propagation, and self-oscillations in semiconductor superlattices *J. Phys.: Condens. Matter* **14** R341

[17] Platero G and Aguado R 2004 Photon-assisted transport in semiconductor nanostructures *Phys. Rep.* **395** 1

[18] Bastard G 1988 *Wave Mechanics Applied to Semiconductor Heterostructures* (New York: Halsted)

[19] Kohn W 1959 Analytic properties of Bloch waves and Wannier functions *Phys. Rev.* **115** 809

[20] Pedersen F B, Einevoll G T and Hemmer P C 1991 Wannier functions for the Kronig–Penney model *Phys. Rev.* B **44** 5470

[21] Bryksin V V and Kleinert P 1997 An analytic approach to the real-space transfer in semiconductor superlattices with highly doped barriers *J. Phys.: Condens. Matter* **9** 7391

[22] Fischetti M V 1998 Theory of electron transport in small semiconductor devices using the Pauli master equation *J. Appl. Phys.* **83** 270

Fischetti M V 1998 Theory of electron transport in small semiconductor devices using the Pauli master equation *J. Appl. Phys.* **83** 6202 (erratum)

[23] Rossi F, Di Carlo A and Lugli P 1998 Microscopic theory of quantum-transport phenomena in mesoscopic systems: a Monte Carlo approach *Phys. Rev. Lett.* **80** 3348

[24] Bordone P, Pascoli M, Brunetti R, Bertoni A, Jacoboni C and Abramo A 1999 Quantum transport of electrons in open nanostructures with the Wigner-function formalism *Phys. Rev.* B **59** 3060

[25] Bryksin V V and Kleinert P 2003 Theory of quantum diffusion in biased semiconductors *J. Phys.: Condens. Matter* **15** 1415

[26] Kadanoff L P and Baym G 1989 *Quantum Statistical Mechanics: Green's Function Methods in Equilibrium and Nonequilibrium Problems* (Redwood City: Addison-Wesley)

[27] Haug H and Jauho A P 1996 *Quantum Kinetics in Transport and Optics of Semiconductors* (Berlin: Springer)

[28] Demeio L, Barletti L, Bertoni A, Bordone P and Jacoboni C 2002 Wigner-function approach to multiband transport in semiconductors *Physica* B **314** 104

[29] Bechouche P, Mauser N J and Poupaud F 2001 Semiclassical limit for the Schrödinger–Poisson equation in a crystal *Commun. Pure Appl. Math.* **54** 851

[30] Bonilla L L and Escobedo R 2004 Nonlocal drift–diffusion description of one-miniband strongly coupled superlattices *Phys. Rev. Lett.* submitted

[31] Bhatnagar P L, Gross E P and Krook M 1954 A model for collision processes in gases: I. Small amplitude processes in charged and neutral one-component systems *Phys. Rev.* **94** 511

[32] Gerhardts R R 1993 Effect of elastic scattering on miniband transport in semiconductor superlattices *Phys. Rev.* B **48** 9178

[33] Ktitorov S A, Simin G S and Sindalovskii V Ya 1971 Bragg reflections and the high-frequency conductivity of an electronic solid-state plasma *Fiz. Tverd. Tela (Leningrad)* **13** 2230

Ktitorov S A, Simin G S and Sindalovskii V Ya 1972 *Sov. Phys.—Solid State* **13** 1872 (Engl. Transl.)

[34] Bonilla L L, Escobedo R and Perales A 2003 Generalized drift–diffusion model for miniband superlattices *Phys. Rev.* B **68** 241304(R)

[35] Ignatov A A and Shashkin V I 1987 Bloch oscillations of electrons and instability of space–charge waves in semiconductor superlattices *Zh. Eksp. Teor. Fiz.* **93** 935

Ignatov A A and Shashkin V I 1987 Bloch oscillations of electrons and instability of space–charge waves in semiconductor superlattices *Sov. Phys.—JETP* **66** 526 (Engl. Transl.)

[36] Ignatov A A, Dodin E P and Shashkin V I 1991 Transient response theory of semiconductor superlattices: connection with Bloch oscillations *Mod. Phys. Lett.* B **5** 1087

[37] Ryndyk D A, Demarina N V, Keller J and Schomburg E 2003 Superlattice with hot electron injection: an approach to a Bloch oscillator *Phys. Rev.* B **67** 033305

[38] Scheuerer R, Schomburg E, Renk K F, Wacker A and Schöll E 2002 Feasibility of a semiconductor superlattice oscillator based on quenched domains for the generation of submillimeter waves *Appl. Phys. Lett.* **81** 1515

[39] Knight B W and Peterson G A 1966 Nonlinear analysis of the Gunn effect *Phys. Rev.* **147** 617

[40] Ignatov A A and Shashkin V 1984 Diffusion coefficient of heated carriers, spectrum of space-charge waves, and characteristic instability frequencies of semiconductor superlattices *Fiz. Tekh. Poluprov.* **18** 721

Ignatov A A and Shashkin V 1984 Diffusion coefficient of heated carriers, spectrum of space-charge waves, and characteristic instability frequencies of semiconductor superlattices *Sov. Phys.—Semicond.* **18** 449 (Engl. Transl.)

[41] Le Person H, Minot C, Boni L, Palmier J F and Mollot F 1992 Gunn oscillations up to 20 GHz optically induced in GaAs/AlAs superlattice *Appl. Phys. Lett.* **60** 2397

[42] Datta S 2000 Nanoscale device modeling: the Green's function method *Superlatt. Microstruct.* **28** 253

[43] Bryksin V V and Firsov Yu A 1971 General theory of transport phenomena in a semiconductor with a strong electric field *Fiz. Tverd. Tela (Leningrad)* **13** 3246

Bryksin V V and Firsov Yu A 1972 *Sov. Phys.—Solid State* **13** 2729 (Engl. Transl.)

[44] Bryksin V V and Firsov Yu A 1972 General theory of transport processes in strong electric fields *Zh. Eksp. Teor. Fiz.* **61** 2373

Bryksin V V and Firsov Yu A 1972 General theory of transport processes in strong electric fields *Sov. Phys.—JETP* **34** 1272 (Engl. Transl.)

[45] Bryksin V V and Firsov Yu A 1973 Transport in arbitrary electric and magnetic fields in the absence of electron–phonon correlations *Fiz. Tverd. Tela (Leningrad)* **15** 3235

Bryksin V V and Firsov Yu A 1974 *Sov. Phys.—Solid State* **15** 2158 (Engl. Transl.)

[46] Bryksin V V and Kleinert P 2003 Diffusion and electric field domain formation in one-dimensional superlattices *Phys. Lett.* A **308** 202

[47] Laikhtman B and Miller D 1993 Theory of current–voltage instabilities in superlattices *Phys. Rev.* B **48** 5395

[48] Miller D and Laikhtman B 1994 Theory of high-field-domain structures in superlattices *Phys. Rev.* B **50** 18426

[49] Lake R, Klimeck G, Bowen R C and Jovanovic D 1997 Single and multiband modeling of quantum electron transport through layered semiconductor devices *J. Appl. Phys.* **81** 7845

[50] Andersen D L and Aas E J 1973 Monte Carlo calculation of the electron drift velocity in GaAs with a superlattice *J. Appl. Phys.* **44** 3721

[51] Price P J 1973 Transport properties of the semiconductor superlattice *IBM J. Res. Dev.* **17** 39

[52] Artaki M and Hess K 1985 Monte Carlo calculations of electron transport in GaAs/AlGaAs superlattices *Superlatt. Microstruct.* **1** 489

[53] Rott S 1999 Theory of electronic transport in semiconductor superlattices *PhD Thesis* Friedrich-Alexander-Universität, Erlangen-Nürnberg

[54] Palmier J F, Etemadi G, Sibille A, Hadjazi M, Mollot F and Planel R 1992 High field miniband conduction in GaAs/AlAs superlattices *Surf. Sci.* **267** 574

[55] Dmitruk P, Saúl A and Reyna L G 1992 High electric field approximation to charge transport in semiconductor devices *Appl. Math. Lett.* **5** 99

[56] Büttiker M and Thomas H 1977 Current instability and domain propagation due to Bragg scattering *Phys. Rev. Lett.* **38** 78

[57] Lei X L, Cai W and Ting C S 1985 Balance equations in nonlinear electronic transport for electron–phonon-impurity systems in the presence of crossed electric and magnetic fields *J. Phys. C: Solid State Phys.* **18** 4315

[58] Lei X L, Horing N J M and Cui H L 1991 Theory of negative differential conductivity in a superlattice miniband *Phys. Rev. Lett.* **66** 3277

[59] Lei X L, Horing N J M and Cui H L 1992 Balance-equation analysis of hot-carrier Bloch transport in a superlattice miniband *J. Phys.: Condens. Matter* **4** 9375

[60] Lei X L 1992 Miniband Bloch transport through a one-dimensional semiconductor superlattice *J. Phys.: Condens. Matter* **4** 9367

[61] Lei X L 1995 Balance equations for hot-electron transport in a general energy band in crossed magnetic and electric fields *Phys. Rev.* B **51** 5184

[62] Lei X L 1995 Distribution functions and balance equations of drifting Bloch electrons in an electric field *Phys. Rev.* B **51** 5526

[63] Lei X L 1995 Investigation of the Büttiker–Thomas momentum balance equation from the Heisenberg equation of motion for Bloch electrons *J. Phys.: Condens. Matter* **7** L429

[64] Lei X L, Horing N J M and Cui H L 1995 Convective instability of a biased semiconductor superlattice *J. Phys.: Condens. Matter* **7** 9811

[65] Bryksin V V, Voloshin V S and Raĭtsev A V 1980 Theory of transport effects in strong electric fields taking account of interband transitions *Fiz. Tverd. Tela (Leningrad)* **22** 3076

Bryksin V V, Voloshin V S and Raĭtsev A V 1980 Theory of transport effects in strong electric fields taking account of interband transitions *Sov. Phys.—Solid State* **22** 1796 (Engl. Transl.)

[66] Kazarinov R F and Suris R A 1972 Electric and electromagnetic properties of semiconductors with a superlattice *Fiz. Tekh. Poluprov.* **6** 148

Kazarinov R F and Suris R A 1972 Electric and electromagnetic properties of semiconductors with a superlattice *Sov. Phys.—Semicond.* **6** 120 (Engl. Transl.)

[67] Kazarinov R F and Suris R A 1971 Possibility of the amplification of electromagnetic waves in a semiconductor with a superlattice *Fiz. Tekh. Poluprov.* **5** 797

Kazarinov R F and Suris R A 1971 Possibility of the amplification of electromagnetic waves in a semiconductor with a superlattice *Sov. Phys.—Semicond.* **5** 707 (Engl. Transl.)

[68] Bonilla L L, Galán J, Cuesta J A, Martínez F C and Molera J M 1994 Dynamics of electric-field domains and oscillations of the photocurrent in a simple superlattice model *Phys. Rev.* B **50** 8644

[69] Suris R A 1973 Electrical instabilities in semiconductors with one-dimensional superlattices *Fiz. Tekh. Poluprov.* **7** 1540

Suris R A 1974 *Sov. Phys.—Semicond.* **7** 1030 (Engl. Transl.)

[70] Suris R A 1973 Inhomogeneous structures in semiconductors with superlattices *Fiz. Tekh. Poluprov.* **7** 1549

Suris R A 1974 *Sov. Phys.—Semicond.* **7** 1035 (Engl. Transl.)

[71] Korotkov A N, Averin D V and Likharev K K 1993 Single-electron quantization of electric field domains in slim semiconductor superlattices *Appl. Phys. Lett.* **62** 3282

[72] Laikhtman B 1991 Current–voltage instabilities in superlattices *Phys. Rev.* B **44** 11260

[73] Likharev K K, Bakhvalov N S, Kazacha G S and Serdyukova S I 1989 Single-electron tunnel junction array: an electrostatic analog of the Josephson transmission line *IEEE Trans. Magn.* **25** 1436

[74] Prengel F, Wacker A and Schöll E 1994 Simple model for multistability and domain formation in semiconductor superlattices *Phys. Rev.* B **50** 1705

Prengel F, Wacker A and Schöll E 1995 Simple model for multistability and domain formation in semiconductor superlattices *Phys. Rev.* B **52** 11518 (erratum)

[75] Bonilla L L 1995 Dynamics of electric field domains in superlattices *Nonlinear Dynamics and Pattern Formation in Semiconductors and Devices* ed F-J Niedernostheide (Berlin: Springer) pp 1–20

[76] Mityagin Yu A, Murzin V N, Efimov Yu A and Rasulova G K 1997 Sequential excited-to-excited states resonant tunneling and electric field domains in long period superlattices *Appl. Phys. Lett.* **70** 3008

[77] Sun B Q, Wang J N, Ge W K, Wang Y, Jiang D S, Zhu H J, Wang H L, Deng Y M and Feng S L 1999 Current self-oscillation induced by a transverse magnetic field in a doped GaAs/AlAs superlattice *Phys. Rev.* B **60** 8866

[78] Amann A, Wacker A, Bonilla L L and Schöll E 2001 Dynamic scenarios of multistable switching in semiconductor superlattices *Phys. Rev.* E **63** 066207

[79] Kastrup J, Prengel F, Grahn H T, Ploog K and Schöll E 1996 Formation times of electric-field domains in doped GaAs–AlAs superlattices *Phys. Rev.* B **53** 1502

[80] Aguado R, Platero G, Moscoso M and Bonilla L L 1997 Microscopic model for sequential tunneling in semiconductor multiple quantum wells *Phys. Rev.* B **55** R16053

[81] Sánchez D, Moscoso M, Bonilla L L, Platero G and Aguado R 1999 Current self-oscillations, spikes, and crossover between charge monopole and dipole waves in semiconductor superlattices *Phys. Rev.* B **60** 4489

[82] Bonilla L L, Platero G and Sánchez D 2000 Microscopic derivation of transport coefficients and boundary conditions in discrete drift–diffusion models of weakly coupled superlattices *Phys. Rev.* B **62** 2786

[83] Sánchez D, MacDonald A H and Platero G 2002 Field-domain spintronics in magnetic semiconductor multiple quantum wells *Phys. Rev.* B **65** 035301

[84] Béjar M, Sánchez D, Platero G and MacDonald A H 2003 Spin-polarized current oscillations in diluted magnetic semiconductor multiple quantum wells *Phys. Rev.* B **67** 045324

[85] Kholod A N, Borisenko V E, Zaslavsky A and Arnaud d'Avitaya F 1999 Current oscillations in semiconductor-insulator multiple quantum wells *Phys. Rev.* B **60** 15975

[86] Bardeen J 1961 Tunnelling from a many-particle point of view *Phys. Rev. Lett.* **6** 57

[87] Sánchez Martín D 2002 Nonlinear dynamics and spin-related properties of semiconductor nanodevices *PhD Thesis* Universidad Autónoma de Madrid, Madrid

[88] Rogozia M and Grahn H T 2001 Escape time model for current self-oscillation frequencies in weakly coupled semiconductor superlattices *Appl. Phys.* A **73** 459

[89] Grahn H 1995 Resonant tunneling *Semiconductor Superlattices: Growth and Electronic Properties* ed H T Grahn (Singapore: World Scientific) pp 155–203

[90] Rott S, Linder N and Döhler G H 2002 Field dependence of the hopping drift velocity in semiconductor superlattices *Phys. Rev.* B **65** 195301

[91] Tsu R and Döhler G 1975 Hopping conduction in a 'superlattice' *Phys. Rev.* B **12** 680

[92] Calecki D, Palmier J F and Chomette A 1984 Hopping conduction in multiquantum well structures *J. Phys. C: Solid State Phys.* **17** 5017

[93] Suris R A and Shchamkhalova B S 1984 Heating of electrons in superlattice semiconductors *Fiz. Tekh. Poluprov.* **18** 1178

Suris R A and Shchamkhalova B S 1984 Heating of electrons in superlattice semiconductors *Sov. Phys.—Semicond.* **18** 738 (Engl. Transl.)

[94] Rott S, Binder P, Linder N and Döhler G H 1999 Combined description for semiclassical and quantum transport in superlattices *Phys. Rev.* B **59** 7334

[95] Cercignani C, Gamba I M and Levermore C D 2001 A drift-collision balance for a Boltzmann–Poisson system in bounded domains *SIAM J. Appl. Math.* **61** 1932

[96] Ignatov A A, Renk K F and Dodin E P 1993 Esaki–Tsu superlattice oscillator: Josephson-like dynamics of carriers *Phys. Rev. Lett.* **70** 1996

[97] Ignatov A A and Shashkin V I 1983 A simplified approach to nonlinear hf response theory of superlattice materials *Phys. Lett.* A **94** 169

[98] Rossi F 1998 Bloch oscillations and Wannier–Stark localization in semiconductor superlattices *Theory of Transport Properties of Semiconductor Nanostructures* ed E Schöll (London: Chapman and Hall) pp 283–320

[99] Rossi F 1998 Coherent phenomena in semiconductors *Semicond. Sci. Technol.* **13** 147

[100] Kastrup J, Hey R, Ploog K H, Grahn H T, Bonilla L L, Kindelan M, Moscoso M, Wacker A and Galán J 1997 Electrically tunable GHz oscillations in doped GaAs–AlAs superlattices *Phys. Rev.* B **55** 2476

[101] Wacker A, Moscoso M, Kindelan M and Bonilla L L 1997 Current–voltage characteristic and stability in resonant-tunneling n-doped semiconductor superlattices *Phys. Rev.* B **55** 2466

[102] Carpio A, Chapman S J, Hastings S and McLeod J B 2000 Wave solutions for a discrete reaction–diffusion equation *Eur. J. Appl. Math.* **11** 399

[103] Carpio A and Bonilla L L 2001 Wave front depinning transition in discrete one-dimensional reaction–diffusion systems *Phys. Rev. Lett.* **86** 6034

[104] Carpio A, Bonilla L L and Dell'Acqua G 2001 Motion of wave fronts in semiconductor superlattices *Phys. Rev.* E **64** 036204

[105] Carpio A, Bonilla L L and Luzón A 2002 Effects of disorder on the wave front depinning transition in spatially discrete systems *Phys. Rev.* E **65** 035207(R)

[106] Carpio A and Bonilla L L 2003 Oscillatory wave fronts in chains of coupled nonlinear oscillators *Phys. Rev.* E **67** 056621

[107] Sánchez D, Platero G and Bonilla L L 2001 Quasiperiodic current and strange attractors in ac-driven superlattices *Phys. Rev.* B **63** 201306(R)

[108] Grahn H T, Schneider H and von Klitzing K 1990 Optical studies of electric field domains in GaAs–$\mathrm{Al}_x\mathrm{Ga}_{1-x}\mathrm{As}$ superlattices *Phys. Rev.* B **41** 2890

[109] Kastrup J, Grahn H T, Ploog K, Prengel F, Wacker A and Schöll E 1994 Multistability of the current–voltage characteristics in doped GaAs–AlAs superlattices *Appl. Phys. Lett.* **65** 1808

[110] Moscoso M, Galán J and Bonilla L L 2000 Bifurcation behavior of a superlattice model *SIAM J. Appl. Math.* **60** 2029

[111] Grahn H T, Müller W, von Klitzing K and Ploog K 1992 Electric-field domains in superlattices: a comparison of transport and optical generation *Surf. Sci.* **267** 579

[112] Grahn H T, Schneider H and von Klitzing K 1990 Spatial distribution of high-field domains in GaAs–AlAs superlattices *Surf. Sci.* **228** 84

[113] Kwok S H, Jahn U, Menniger J, Grahn H T and Ploog K 1995 Spatial distribution of electric-field domains in n-doped semiconductor superlattices *Appl. Phys. Lett.* **66** 2113

[114] Kwok S H, Jahn U, Kostial H, Menniger J, Grahn H T and Ploog K 1996 Cathodoluminescence imaging of electric-field domains in semiconductor superlattices *Solid-State Electron.* **40** 527

[115] Furuta T, Hirakawa K, Yoshino J and Sakaki H 1986 Splitting of photoluminescence spectra and negative differential resistance caused by the electric field induced resonant coupling of quantized levels in GaAs–AlGaAs multi-quantum well structures *Japan. J. Appl. Phys.* **25** (part 2) L151

[116] Kawamura Y, Wakita K, Asahi H and Kurumada K 1986 Observation of room temperature current oscillation in InGaAs/InAlAs MQW pin diodes *Japan. J. Appl. Phys.* **25** (part 2) L928

[117] Miller D A B, Chemla D S, Damen T C, Gossard A C, Wiegmann W, Wood T H and Burrus C A 1984 Band-edge electroabsorption in quantum well structures: the quantum-confined Stark effect *Phys. Rev. Lett.* **53** 2173

[118] Choi K K, Levine B F, Malik R J, Walker J and Bethea C G 1987 Periodic negative conductance by sequential resonant tunneling through an expanding high-field superlattice domain *Phys. Rev.* B **35** 4172

[119] Choi K-K, Levine B F, Bethea C G, Walker J and Malik R J 1987 Multiple quantum well 10 μm GaAs/$\mathrm{Al}_x\mathrm{Ga}_{1-x}\mathrm{As}$ infrared detector with improved responsivity *Appl. Phys. Lett.* **50** 1814

[120] Newman H S and Kirchoefer S W 1987 Electronic properties of symmetric and asymmetric quantum-well electron barrier diode *J. Appl. Phys.* **62** 706

[121] Kawamura Y, Wakita K and Oe K 1987 Current oscillations related to the $N = 3$ subband levels up to room temperature in InGaAs/InAlAs MQW diodes *Japan. J. Appl. Phys.* **26** (part 2) L1603

[122] Vuong T H H, Tsui D C and Tsang W T 1988 High-field transport in an InGaAs–InP superlattice grown by chemical beam epitaxy *Appl. Phys. Lett.* **52** 981

[123] Choi K K, Levine B F, Jarosik N, Walker J and Malik J 1988 Anisotropic magnetotransport in weakly coupled GaAs–$Al_xGa_{1-x}As$ multiple quantum wells *Phys. Rev.* B **38** 12362

[124] Cavicchi R E, Lang D V, Gershoni D, Sergent A M, Temkin H and Panish M B 1988 Sequential screening layers in a photoexcited $In_{1-x}Ga_xAs$/InP superlattice *Phys. Rev.* B **38** 13474

[125] Snow E S, Kirchoefer S W and Glembocki O J 1989 Spectrally dependent photocurrent measurements in n^+–n–n^+ heterostructure devices *Appl. Phys. Lett.* **54** 2023

[126] Helm M, England P, Colas E, DeRosa F and Allen S J Jr 1989 Intersubband emission from semiconductor superlattices excited by sequential resonant tunneling *Phys. Rev. Lett.* **63** 74

[127] Kawamura Y, Asasi H, Wakita K, Mikami O and Naganuma M 1989 Resonant tunneling characteristic in InGaAs/InAlAs MQW diodes with Si-doped quantum wells *Japan. J. Appl. Phys.* **28** (part 2) L1104

[128] Vuong T H H, Tsui D C and Tsang W T 1989 Transport through InGaAs–InP superlattices grown by chemical beam epitaxy *J. Appl. Phys.* **66** 3688

[129] Helgesen P and Finstad T G 1990 Sequential resonant and non-resonant tunneling in GaAs/AlGaAs multiple quantum well structures: high field domain formation *Proc. 14th Nordic Semiconductor Meeting (Aarhus, Denmark)* ed O Hansen (Aarhus: University of Aarhus) p 323

[130] Helm M, Golub J E and Colas E 1990 Electroluminescence and high-field domains in GaAs/AlGaAs superlattices *Appl. Phys. Lett.* **56** 1356

[131] Helgesen P, Finstad T G and Johannessen K 1991 Sequential resonant and nonresonant tunneling in GaAs/AlGaAs multiple quantum wells *J. Appl. Phys.* **69** 2689

[132] Grahn H T, Schneider H and von Klitzing K 1989 Optical detection of high-field domains in GaAs/AlAs superlattices *Appl. Phys. Lett.* **54** 1757

[133] Murugkar S, Kwok S H, Ambrazevičius G, Grahn H T, Ploog K and Merlin R 1994 Growth of electric field domains in quantum-well structures: correlation with intersubband Raman scattering *Phys. Rev.* B **49** 16849

[134] Murugkar S, Merlin R, Kwok S H, Grahn H T and Hey R 1996 Correlation between intersubband Raman scattering and electric-field domains in quantum-well structures *Solid-State Electron.* **40** 153

[135] Kwok S H, Merlin R, Grahn H T and Ploog K 1994 Electric-field domains in semiconductor superlattices: resonant and nonresonant tunneling *Phys. Rev.* B **50** 2007

[136] Kwok S H, Grahn H T, Ramsteiner M, Ploog K, Prengel F, Wacker A, Schöll E, Murugkar S and Merlin R 1995 Nonresonant carrier transport through high-field domains in semiconductor superlattices *Phys. Rev.* B **51** 9943

[137] Wacker A, Schwarz G, Prengel F, Schöll E, Kastrup J and Grahn H T 1995 Probing growth-related disorder by high-field transport in semiconductor superlattices *Phys. Rev.* B **52** 13788

[138] Schwarz G, Wacker A, Prengel F, Schöll E, Kastrup J, Grahn H T and Ploog K 1996 The influence of imperfections and weak disorder on domain formation in superlattices *Semicond. Sci. Technol.* **11** 475

[139] Schöll E, Schwarz G, Patra M, Prengel F and Wacker A 1996 Oscillatory instabilities and field domain formation in imperfect superlattices *Proc. 9th International Conf. on Hot Carriers in Semiconductors (Chicago, IL, USA)* ed K Hess *et al* (New York: Plenum) p 177

[140] Schöll E, Schwarz G and Wacker A 1998 Nonlinear and oscillatory electronic transport in superlattices as a probe of structural imperfections *Physica* B **249–251** 961

[141] Schwarz G, Patra M, Prengel F and Schöll E 1998 Multistable current–voltage characteristics as fingerprints of growth-related imperfections in semiconductor superlattices *Superlatt. Microstruct.* **23** 1353

[142] Wacker A and Jauho A-P 1998 Impact of interface roughness on perpendicular transport and domain formation in superlattices *Superlatt. Microstruct.* **23** 297

[143] Schwarz G, Prengel F, Schöll E, Kastrup J, Grahn H T and Hey R 1996 Electric field domains in intentionally perturbed semiconductor superlattices *Appl. Phys. Lett.* **69** 626

[144] Rogozia M, Krispin P and Grahn H T 2001 Giant resistance changes in (Al,Ga)As contact layers of GaAs/AlAs superlattices due to deep donors *J. Appl. Phys.* **90** 4560

[145] Zhang Y H, Li Y X, Jiang D S, Yang X P and Zhang P H 1994 Giant capacitance oscillations related to the quantum capacitance in GaAs/AlAs superlattices *Appl. Phys. Lett.* **64** 3416

[146] Han Z Y, Yoon S F, Radhakrishnan K and Zhang D H 1995 Investigation of high-field domain formation in tight-binding superlattices by capacitance–voltage measurements *Appl. Phys. Lett.* **67** 1908

[147] Han Z Y, Yoon S F, Radhakrishnan K and Zhang D H 1995 Space charge buildup in tight-binding superlattices induced by electron sequential tunneling *Superlatt. Microstruct.* **18** 83

[148] Stoklitskiĭ S A, Murzin V N, Rasulova G K, Mityagin Yu A, Perestoronin A P, Monemar B, Holz P O and Singh M 1995 Optical observation of the formation of an electric-field domain in an n^+–i–n^+ GaAs/AlGaAs superlattice with wide quantum wells *Pis. Zh. Éksp. Teor. Fiz.* **61** 399 (*JETP Lett.* **61** 405)

[149] Mityagin Yu A and Murzin V N 1996 Current hysteresis collapse and the formation condition for electric-field domains in lightly doped superlattices *Pis. Zh. Éksp. Teor. Fiz.* **64** 146 (*JETP Lett.* **64** 155)

[150] Rasulova G K, Efimov Yu A and Murzin V N 1997 Current bistability and switching in weakly coupled superlattices GaAs/AlGaAs *J. Appl. Phys.* **82** 3381

[151] Xu Y J, Shakouri A and Yariv A 1997 The effect of temperature on the resonant tunneling and electric field domain formation in multiple quantum well superlattices *J. Appl. Phys.* **81** 2033

[152] Schneider H, Mermelstein C, Rehm R, Schönbein C, Sa'ar A and Walther M 1998 Optically induced electric-field domains by bound-to-continuum transitions in n-type multiple quantum wells *Phys. Rev.* B **57** R15096

[153] Han Z Y, Yoon S F, Radhakrishnan K and Zhang D H 1995 High-field domain formation in GaAs/AlGaAs superlattices *Appl. Phys. Lett.* **66** 1120

[154] Zhang Y H, Yang X P, Liu W, Zhang P H and Jiang D S 1994 New formation mechanism of electric field domain due to Γ-X sequential tunneling in GaAs/AlAs superlattices *Appl. Phys. Lett.* **65** 1148

[155] Sun B Q, Jiang D S, Liu Z X, Zhang Y H and Liu W 1996 Evidence of $\Gamma - X$ sequential resonant tunneling in GaAs/AlAs superlattices *Appl. Phys. Lett.* **69** 520

[156] Mimura H, Hosoda M, Ohtani N, Tominaga K, Fujita K, Watanabe T, Grahn H T and Fujiwara K 1996 Electric-field domain formation in type-II superlattices *Phys. Rev.* B **54** R2323

[157] Tomlinson A M, Fox A M and Foxon C T 2000 Domain bistability in photoexcited GaAs multiple quantum wells *Phys. Rev.* B **61** 12647

[158] Zhang Y H, Klann R, Ploog K H and Grahn H T 1997 Observation of bistability in GaAs/AlAs superlattices *Appl. Phys. Lett.* **70** 2825

[159] Luo K J, Teitsworth S W, Kostial H, Grahn H T and Ohtani N 1999 Controllable bistabilities and bifurcations in a photoexcited GaAs/AlAs superlattice *Appl. Phys. Lett.* **74** 3845

[160] Hirakawa K, Shimada Y and Ikoma T 1996 Supply-function dependent sequential resonant tunneling in semiconductor multiple quantum well diodes *Physica* B **227** 202

[161] Shimada Y and Hirakawa K 1997 High-field domain formation conditions in semiconductor multiple quantum well sequential resonant tunneling structures *Japan. J. Appl. Phys.* **36** (part 1) 1012

[162] Hosoda M, Ohtani N, Domoto C and Aida T 2001 Formation process of high-field domain in superlattices observed by photoluminescence spectra branch *Japan. J. Appl. Phys.* **40** (part 1) 3023

[163] Perales A, Bonilla L L, Moscoso M and Galán J 2001 Spatiotemporal structures in undoped photoexcited semiconductor superlattices *Int. J. Bifur. Chaos* **11** 2817

[164] Kastrup J 1996 The superlattice oscillator: from stable to unstable electric-field domains *PhD Thesis* Humboldt-Universität, Berlin

[165] Wang J N, Sun B Q, Wang X R, Wang Y, Ge W K and Wang H L 1999 Dynamic dc voltage band observed within each current branch in the transition from static to dynamic electric-field domain formation in a doped GaAs/AlAs superlattice *Appl. Phys. Lett.* **75** 2620

[166] Li C Y, Sun B Q, Jiang D S and Wang J N 2001 Analysis of the temperature-induced transition to current self-oscillations in doped GaAs/AlAs superlattices *Semicond. Sci. Technol.* **16** 239

[167] Wang J N, Sun B Q, Wang X R and Wang H L 1999 Negative differential resistance and the transition to current self-oscillation in GaAs/AlAs superlattices *Solid State Commun.* **112** 371

[168] Sánchez D, Bonilla L L and Platero G 2002 Temperature-induced breakdown of stationary electric field domains in superlattices *Physica* E *(Amsterdam)* **13** 798

[169] Shimada Y and Hirakawa K 1997 Sequential resonant magnetotunneling through Landau levels in GaAs/AlGaAs multiple quantum well structures *Phys. Status Solidi* b **204** 427

[170] Schmidt T, Jansen A G M, Haug R J, von Klitzing K and Eberl K 1998 Magnetic control of electric-field domains in semiconductor superlattices *Phys. Rev. Lett.* **81** 3928

[171] Aguado R and Platero G 1998 Magnetic field induced charge instabilities in weakly coupled superlattices *Physica* B **256–258** 233

[172] Wang J N, Sun B Q, Wang X R, Wang Y, Ge W K, Jiang D S and Wang H L 2000 Static and dynamic electric field domain formation in a doped GaAs/AlAs superlattice *Physica* E *(Amsterdam)* **8** 141

[173] Sun B Q, Wang J N, Jiang D S, Wu J Q, Wang Y Q and Ge W K 2000 Self-sustained oscillations caused by magnetic field in a weakly-coupled GaAs/AlAs superlattice *Physica* B **279** 220

[174] Luo K J, Friedland K-J, Grahn H T and Ploog K H 2000 Magnetotransport investigations of structural irregularities in a weakly coupled GaAs/AlAs superlattice under domain formation *Phys. Rev.* B **61** 4477

[175] Grahn H T, Klann R and Rühle W W 1995 Temporal evolution of electric field domain formation in semiconductor superlattices *Proc. 22nd International Conf. on The Physics of Semiconductors (Vancouver, British Columbia, Canada)* ed D J Lockwood (Singapore: World Scientific) p 1169

[176] Klann R, Kwok S H, Grahn H T and Hey R 1995 Time-resolved photoluminescence investigations of electric-field domain formation in GaAs–AlAs superlattices *Phys. Rev.* B **52** R8680

[177] Kwok S H, Norris T B, Bonilla L L, Galán J, Cuesta J A, Martínez F C, Molera J M, Grahn H T, Ploog K and Merlin R 1995 Domain-wall kinetics and tunneling-induced instabilities in superlattices *Phys. Rev.* B **51** 10171

[178] Prengel F, Wacker A, Schwarz G, Schöll E, Kastrup J and Grahn H T 1995 Dynamics of domain formation in semiconductor superlattices *Lith. J. Phys.* **35** 404

[179] Shimada Y and Hirakawa K 1997 Time constant for high-field domain formation in multiple quantum well sequential resonant tunneling diodes *Japan. J. Appl. Phys.* **36** (part 1) 1944

[180] Amann A, Wacker A, Bonilla L L and Schöll E 2001 Field domains in semiconductor superlattices: dynamic scenarios of multistable switching *Proc. 25th International Conf. on The Physics of Semiconductors (Osaka, Japan)* ed N Miura and T Ando (Berlin: Springer) p 801

[181] Bonilla L L, Sánchez O and Soler J 2002 Nonlinear stochastic discrete drift–diffusion theory of charge fluctuations and domain relocation times in semiconductor superlattices *Phys. Rev.* B **65** 195308

[182] Luo K J, Grahn H T and Ploog K H 1998 Relocation time of the domain boundary in weakly coupled GaAs/AlAs superlattices *Phys. Rev.* B **57** R6838

[183] Rogozia M, Teitsworth S W, Grahn H T and Ploog K H 2001 Statistics of the domain-boundary relocation time in semiconductor superlattices *Phys. Rev.* B **64** 041308(R)

[184] Rogozia M, Teitsworth S W, Grahn H T and Ploog K H 2002 Relocation dynamics of domain boundaries in semiconductor superlattices *Phys. Rev.* B **65** 205303

[185] Rogozia M, Grahn H T, Teitsworth S W and Ploog K H 2002 Time distribution of the domain-boundary relocation in superlattices *Physica* B **314** 427

[186] Bonilla L L, Cantalapiedra I R, Gomila G and Rubí J M 1997 Asymptotic analysis of the Gunn effect with realistic boundary conditions *Phys. Rev.* E **56** 1500

[187] Higuera F J and Bonilla L L 1992 Gunn instability in finite samples of GaAs: II. Oscillatory states in long samples *Physica* D **57** 161

[188] Kantelhardt J W, Grahn H T, Ploog K H, Moscoso M, Perales A and Bonilla L L 1997 Spikes in the current self-oscillations of doped GaAs/AlAs superlattices *Phys. Status Solidi* b **204** 500

[189] Zhang Y H, Klann R, Ploog K H and Grahn H T 1996 Quenching of the spontaneous current oscillations in GaAs/AlAs superlattices under domain formation *Appl. Phys. Lett.* **69** 1116

[190] Iooss G and Joseph D D 1980 *Elementary Stability and Bifurcation Theory* (New York: Springer)

[191] Blanter Ya M and Büttiker M 2000 Shot noise in mesoscopic conductors *Phys. Rep.* **336** 1

[192] Tretiakov O A, Gramespacher T and Matveev K A 2003 Lifetime of metastable states in resonant tunneling structures *Phys. Rev.* B **67** 073303

[193] Wang M C and Uhlenbeck G E 1945 On the theory of the Brownian motion II *Rev. Mod. Phys.* **17** 323

[194] Montroll E W and West B J 1979 On an enriched collection of stochastic processes *Studies in Statistical Mechanics vol VII: Fluctuation Phenomena* ed E W Montroll and J L Lebowitz (Amsterdam: North-Holland) pp 61–175

[195] van Kampen N G 1981 *Stochastic Processes in Physics and Chemistry* (Amsterdam: North-Holland)

[196] Volkov A F and Kogan Sh M 1968 Physical phenomena in semiconductors with negative differential conductivity *Usp. Fiz. Nauk* **96** 633
Volkov A F and Kogan Sh M 1969 *Sov. Phys.—Usp.* **11** 881 (Engl. Transl.)

[197] Shaw M P, Grubin H L and Solomon P R 1979 *The Gunn–Hilsum Effect* (New York: Academic)

[198] Butcher P N 1967 The Gunn effect *Rep. Prog. Phys.* **30** 97

[199] Murray J D 1970 On the Gunn effect and other physical examples of perturbed conservation equations *J. Fluid Mech.* **44** 315

[200] Bonilla L L, Higuera F J and Venakides S 1994 The Gunn effect: instability of the steady state and stability of the solitary wave in long extrinsic semiconductors *SIAM J. Appl. Math.* **54** 1521

[201] Bonilla L L and Higuera F J 1995 The onset and end of the Gunn effect in extrinsic semiconductors *SIAM J. Appl. Math.* **55** 1625

[202] Hofbeck K *et al* 1996 High-frequency self-sustained current oscillation in an Esaki–Tsu superlattice monitored via microwave emission *Phys. Lett.* A **218** 349

[203] Cao J C and Lei X L 1999 Hydrodynamic balance-equation analysis of spatiotemporal domains and negative differential conductance in a voltage-biased GaAs superlattice *Phys. Rev.* B **59** 2199

[204] Bonilla L L and Higuera F J 1991 Gunn instability in finite samples of GaAs: I. Stationary states, stability and boundary conditions *Physica* D **52** 458

[205] Ignatov A A, Piskarev V I and Shashkin V I 1985 Instability (formation of domains) of an electric field in multilayer quantum structures *Fiz. Tekh. Poluprov.* **19** 2183

Ignatov A A, Piskarev V I and Shashkin V I 1986 *Sov. Phys.—Semicond.* **19** 1345 (Engl. Transl.)

[206] Lei X L and Cui H L 1997 Suppression of absolute instability by elastic scattering in semiconductor superlattices *J. Phys.: Condens. Matter* **9** 4853

[207] Guéret P 1971 Convective and absolute instabilities in semiconductors exhibiting negative differential mobility *Phys. Rev. Lett.* **27** 256

[208] Bonilla L L, Hernando P J, Herrero M A, Kindelan M and Velázquez J J L 1997 Asymptotics of the trap-dominated Gunn effect in p-type Ge *Physica* D **108** 168

[209] Bonilla L L, Kindelan M and Keller J B 2004 Periodically generated propagating pulses *SIAM J. Appl. Math.* at press

[210] Blomeier T *et al* 1997 Current oscillations in n-doped GaAs/AlAs superlattice devices due to traveling field domains *Phys. Status Solidi* b **204** 485

[211] Schomburg E *et al* 1998 Generation of millimeter waves with a GaAs/AlAs superlattice oscillator *Appl. Phys. Lett.* **72** 1498

[212] Schomburg E, Henini M, Chamberlain J M, Steenson D P, Brandl S, Hofbeck K, Renk K F and Wegscheider W 1999 Self-sustained current oscillation above 100 GHz in a GaAs/AlAs superlattice *Appl. Phys. Lett.* **74** 2179

[213] Schomburg E *et al* 1998 Current oscillation in superlattices with different miniband widths *Phys. Rev.* B **58** 4035

[214] Brandl S *et al* 1998 Millimeter wave generation by a self-sustained current oscillation in an InGaAs/InAlAs superlattice *Appl. Phys. Lett.* **73** 3117

[215] Schomburg E, Scheurer R, Brandl S, Renk K F, Pavel'ev D G, Koschurinov Yu, Ustinov V, Zhukov A, Kovsh A and Kop'ev P S 1999 InGaAs/InAlAs superlattice oscillator at 147 GHz *Electron. Lett.* **35** 1491

[216] Patra M, Schwarz G and Schöll E 1998 Bifurcation analysis of stationary and oscillating domains in semiconductor superlattices with doping fluctuations *Phys. Rev.* B **57** 1824

[217] Sánchez D, Bonilla L L and Platero G 2001 Temperature dependence of current self-oscillations and electric-field domains in sequential-tunneling doped superlattices *Phys. Rev.* B **64** 115311

[218] Bonilla L L, Kindelan M, Moscoso M and Venakides S 1997 Periodic generation and propagation of traveling fronts in dc voltage biased semiconductor superlattices *SIAM J. Appl. Math.* **57** 1588

[219] Cantalapiedra I R, Bergmann M J, Bonilla L L and Teitsworth S W 2001 Chaotic motion of space charge wave fronts in semiconductors under time-independent voltage bias *Phys. Rev.* E **63** 056216

[220] Bonilla L L and Cantalapiedra I R 1997 Universality of the Gunn effect: self-sustained oscillations mediated by solitary waves *Phys. Rev.* E **56** 3628

[221] Amann A, Schlesner J, Wacker A and Schöll E 2002 Chaotic front dynamics in semiconductor superlattices *Phys. Rev.* B **65** 193313

[222] Amann A, Peters K, Parlitz U, Wacker A and Schöll E 2003 Hybrid model for chaotic front dynamics: from semiconductors to water tanks *Phys. Rev. Lett.* **91** 066601

[223] Grahn H, Kastrup J, Ploog K, Bonilla L, Galán J, Kindelan M and Moscoso M 1995 Self-oscillations of the current in doped semiconductor superlattices *Japan. J. Appl. Phys.* **34** (part 1) 4526

[224] Kastrup J, Klann R, Grahn H T, Ploog K, Bonilla L L, Galán J, Kindelan M, Moscoso M and Merlin R 1995 Self-oscillations of domains in doped GaAs–AlAs superlattices *Phys. Rev.* B **52** 13761

[225] Kastrup J, Grahn H T, Ploog K and Merlin R 1996 Oscillating electric field domains in GaAs/AlAs superlattices *Solid-State Electron.* **40** 157

[226] Rasulova G K 2000 Dynamic characteristics of weakly coupled GaAs/AlGaAs superlattices *J. Appl. Phys.* **88** 4170

[227] Hosoda M, Mimura H, Ohtani N, Tominaga K, Watanabe T, Fujiwara K and Grahn H T 1996 Current self-oscillations in photoexcited type-II GaAs–AlAs superlattices *Appl. Phys. Lett.* **69** 500

[228] Mimura H, Hosoda M, Ohtani N, Grahn H T and Yokoo K 1997 Subband-resonance oscillations in undoped GaAs/AlAs type-II superlattices under photoexcitation *Appl. Surf. Sci.* **113/114** 85

[229] Ohtani N, Hosoda M and Grahn H T 1997 Photocurrent self-oscillations in a direct-gap GaAs–AlAs superlattice *Appl. Phys. Lett.* **70** 375

[230] Ohtani N, Egami N, Kuroyanagi K, Ando M, Hosoda M, Grahn H T and Ploog K H 1997 Current self-oscillations in undoped, photoexcited GaAs/AlAs type-I superlattices *Phys. Status Solidi* b **204** 489

[231] Tomlinson A M, Fox A M, Cunningham J E and Jan W Y 1999 Photocurrent self-oscillations in a spatially direct GaAs/AlGaAs superlattice *Appl. Phys. Lett.* **75** 2067

[232] Ryzhii M, Ryzhii V, Suris R and Hamaguchi C 2000 Periodic electric-field domains in optically excited multiple-quantum-well structures *Phys. Rev.* B **61** 2742

[233] Ryzhii V, Khmyrova I, Ryzhii M, Suris R and Hamaguchi C 2000 Phenomenological theory of electric-field domains induced by infrared radiation in multiple quantum well structures *Phys. Rev.* B **62** 7268

[234] Ryzhii V and Ryzhii M 2000 Nonlinear dynamics of recharging processes in multiple quantum well structures excited by infrared radiation *Phys. Rev.* B **62** 10292

[235] Amann A, Wacker A and Schöll E 2002 Tripole current oscillations in superlattices *Physica* B **314** 404

[236] Rogozia M 2002 Oszillatoren aus schwach gekoppelten Halbleiterübergittern für den MHz- und GHz-Bereich: Domänendynamik und Stromoszillationen *PhD Thesis* Humboldt-Universität, Berlin

[237] Wang X R, Wang J N, Sun B Q and Jiang D S 2000 Anomaly of the current self-oscillation frequency in the sequential tunneling of a doped GaAs/AlAs superlattice *Phys. Rev.* B **61** 7261

[238] Wang X R and Niu Q 1999 General analysis of instabilities and oscillations of the sequential tunneling in superlattices *Phys. Rev.* B **59** R12755

[239] Sun B Q, Jiang D S and Wang X J 1997 Current oscillations and stable electric field domains in doped GaAs/AlAs superlattices *Semicond. Sci. Technol.* **12** 401

[240] Ohtani N, Egami N, Grahn H T, Ploog K H and Bonilla L L 1998 Transition between static and dynamic electric-field domain formation in weakly coupled GaAs/AlAs superlattices *Phys. Rev.* B **58** R7528

[241] Ohtani N, Egami N, Grahn H T and Ploog K H 1998 Carrier density dependence of transitions between chaotic and periodic photocurrent oscillations in undoped GaAs/AlAs superlattices *Physica* B **249–251** 878

[242] Ohtani N, Egami N, Grahn H T and Ploog K H 1999 Phase diagram of static and dynamic electric field domain formation in semiconductor superlattices *Physica* B **272** 205

[243] Ohtani N, Egami N, Grahn H T and Ploog K H 2000 Phase diagram of static- and dynamic-domain formation in weakly coupled GaAs/AlAs superlattices *Phys. Rev.* B **61** R5097

[244] Rogozia M, Hey R, Kostial H and Grahn H T 2000 Tunable GHz oscillations in weakly coupled GaAs/AlAs superlattices *Proc. 26th International Symp. on Compound Semiconductors (Berlin, Germany)* (*Inst. Phys. Conf. Ser. No. 166*) ed K H Ploog *et al* (Bristol: Institute of Physics Publishing) p 147

[245] Wichmann E H 1971 *Quantum Physics* (*Berkeley Physics Course* vol 4) (New York: McGraw-Hill)

[246] Sánchez D, Moscoso M, Bonilla L L, Platero G and Aguado R 2000 Dynamics of electric field domain walls in semiconductor superlattices *Physica* E (*Amsterdam*) **7** 299

[247] Bulashenko O M and Bonilla L L 1995 Chaos in resonant-tunneling superlattices *Phys. Rev.* B **52** 7849

[248] Bulashenko O M, García M J and Bonilla L L 1996 Chaotic dynamics of electric-field domains in periodically driven superlattices *Phys. Rev.* B **53** 10008

[249] Bonilla L L, Bulashenko O M, Galán J, Kindelan M and Moscoso M 1996 Dynamics of electric-field domains and chaos in semiconductor superlattices *Solid-State Electron.* **40** 161

[250] Bonilla L L and Bulashenko O M 1998 Forcing of chaos in semiconductor superlattices *Superlatt. Microstruct.* **23** 13

[251] Zwolak M, Ferguson D and Ventra M D 2003 Chaotic transport in low-dimensional superlattices *Phys. Rev.* B **67** 081303(R)

[252] Zhang Y H, Klann R, Grahn H T and Ploog K H 1997 Transition between synchronization and chaos in doped GaAs/AlAs superlattices *Superlatt. Microstruct.* **21** 565

[253] Alekseev K N, Berman G P, Campbell D K, Cannon E H and Cargo M C 1996 Dissipative chaos in semiconductor superlattices *Phys. Rev.* B **54** 10625

[254] Alekseev K N, Cannon E H, McKinney J C, Kusmartsev F V and Campbell D K 1998 Symmetry-breaking and chaos in electron transport in semiconductor superlattices *Physica* D **113** 129

[255] Romanov Yu A and Romanova Yu Yu 2000 Self-oscillations in semiconductor superlattices *Zh. Éksp. Teor. Fiz.* **118** 1193 (*J. Exp. Theor. Phys.* **91** 1033)

[256] Cao J C and Lei X L 1999 Synchronization and chaos in miniband semiconductor superlattices *Phys. Rev.* B **60** 1871

[257] Cao J C, Liu H C and Lei X L 2000 Chaotic dynamics in quantum-dot miniband superlattices *Phys. Rev.* B **61** 5546

[258] Cao J C, Liu H C, Lei X L and Perera A G U 2001 Chaotic dynamics in terahertz-driven semiconductors with negative effective mass *Phys. Rev.* B **63** 115308

[259] Mosekilde E, Feldberg R, Knudsen C and Hindsholm M 1990 Mode locking and spatiotemporal chaos in periodically driven Gunn diodes *Phys. Rev.* B **41** 2298

[260] Mosekilde E, Thomsen J S, Knudsen C and Feldberg R 1993 Phase diagrams for periodically driven Gunn diodes *Physica* D **66** 143

[261] Oshio K and Yahata H 1993 Chaotic current oscillations in the Gunn-effect device under the dc and the rf bias voltages *J. Phys. Soc. Japan* **62** 3639

[262] Oshio K and Yahata H 1996 Current oscillations induced by recombination instability in semiconductors *J. Phys. Soc. Japan* **65** 1490

[263] Zhang Y H, Kastrup J, Klann R, Ploog K H and Grahn H T 1996 Synchronization and chaos induced by resonant tunneling in GaAs/AlAs superlattices *Phys. Rev. Lett.* **77** 3001

[264] Luo K J, Friedland K-J, Grahn H T and Ploog K H 2000 Magnetic-field effects on undriven chaos in a weakly coupled GaAs/AlAs superlattice *Appl. Phys. Lett.* **76** 2913

[265] Luo K J, Grahn H T, Ploog K H and Bonilla L L 1998 Explosive bifurcation to chaos in weakly coupled semiconductor superlattices *Phys. Rev. Lett.* **81** 1290

[266] Grahn H T 1999 Current self-oscillations and chaos in semiconductor superlattices *Superlatt. Microstruct.* **25** 7

[267] Luo K J, Grahn H T, Teitsworth S W and Ploog K H 1998 Influence of higher harmonics on Poincaré maps derived from current self-oscillations in a semiconductor superlattice *Phys. Rev.* B **58** 12613

[268] Bulashenko O M, Luo K J, Grahn H T, Ploog K H and Bonilla L L 1999 Multifractal dimension of chaotic attractors in a driven semiconductor superlattice *Phys. Rev.* B **60** 5694

[269] Ohtani N, Egami N, Fujiwara K and Grahn H T 1998 Photocurrent self-oscillations in undoped GaAs/AlAs superlattices modulated by an external AC voltage *Solid-State Electron.* **42** 1509

[270] Schomburg E *et al* 2002 Control of the dipole domain propagation in a GaAs/AlAs superlattice with a high-frequency field *Phys. Rev.* B **65** 155320

[271] Jappsen A-K, Amann A, Wacker A, Schöll E and Schomburg E 2002 High-frequency impedance of driven superlattices *J. Appl. Phys.* **92** 3137

[272] Jappsen A-K, Amann A, Wacker A, Schomburg E and Schöll E 2003 Synchronization of dipole domains in GHz driven superlattices *Proc. SPIE—Int. Soc. Opt. Eng.* **5023** 220

[273] Keay B J, Allen S J Jr, Galán J, Kaminski J P, Campman K L, Gossard A C, Bhattacharya U and Rodwell M J W 1995 Photon-assisted electric field domains and multiphonon-assisted tunneling in semiconductor superlattices *Phys. Rev. Lett.* **75** 4098

[274] Keay B J, Zeuner S, Allen S J Jr, Maranowski K D, Gossard A C, Bhattacharya U and Rodwell M J W 1995 Dynamic localization, absolute negative conductance, and stimulated, multiphoton emission in sequential resonant tunneling semiconductor superlattices *Phys. Rev. Lett.* **75** 4102

[275] Aguado R and Platero G 1997 Electric field domain formation and multistability in semiconductor multiple quantum wells in the presence of THz radiation *Phys. Status Solidi* a **164** 235

[276] Aguado R and Platero G 1998 Photoinduced multistable phenomena in the tunneling current through doped superlattices *Phys. Rev. Lett.* **81** 4971

[277] Winnerl S *et al* 1997 Quasistatic and dynamic interaction of high-frequency fields with miniband electrons in semiconductor superlattices *Phys. Rev.* B **56** 10303

[278] Zeuner S, Keay B J, Allen S J, Maranowski K D, Gossard A C, Bhattacharya U and Rodwell M J W 1996 Transition from classical to quantum response in semiconductor superlattices at THz frequencies *Phys. Rev.* B **53** R1717

[279] Schomburg E, Demarina N V and Renk K F 2003 Amplification of a terahertz field in a semiconductor superlattice via phase-locked k-space bunches of Bloch oscillating electrons *Phys. Rev.* B **67** 155302

[280] López R, Sánchez D and Platero G 2002 Photo-assisted dynamical transport in multiple quantum wells *Physica* E (*Amsterdam*) **12** 319

[281] López R, Sánchez D and Platero G 2003 Dynamical instability of electric-field domains in ac-driven superlattices *Phys. Rev.* B **67** 035330

[282] Schomburg E *et al* 1997 Millimeter wave oscillator based on a quasiplanar superlattice electronic device *Appl. Phys. Lett.* **71** 401

[283] Minot C, Sahri N, Le Person H, Palmier J F, Harmand J C, Medus J P and Esnault J C 1998 Millimetre-wave negative differential conductance in GaInAs/AlInAs semiconductor superlattices *Superlatt. Microstruct.* **23** 1323

[284] Palmier J F, Minot C, Harmand J C, Sibille A, Tanguy D and Penard E 1999 Recent results on superlattice transport and optoelectronics applications *Superlatt. Microstruct.* **25** 13

[285] Steuer H, Wacker A and Schöll E 1999 Complex behavior due to electron heating in superlattices exhibiting high-frequency current oscillations *Physica* B **272** 202

[286] Steuer H, Wacker A, Schöll E, Ellmauer M, Schomburg E and Renk K F 2000 Thermal breakdown, bistability, complex high-frequency current oscillations due to carrier heating in superlattices *Appl. Phys. Lett.* **76** 2059

[287] Scheuerer R, Renk K F, Schomburg E, Wegscheider W and Bichler M 2002 Nonlinear superlattice transport limited by Joule heating *J. Appl. Phys.* **92** 6043

[288] Winnerl S *et al* 1998 Ultrafast detection and autocorrelation of picosecond THz radiation pulses with a GaAs/AlAs superlattice *Appl. Phys. Lett.* **73** 2983

[289] Winnerl S *et al* 1999 A GaAs/AlAs superlattice autocorrelator for picosecond THz radiation pulses *Superlatt. Microstruct.* **25** 57

[290] Hovenier J N, van Es R W, Klaassen T O, Wenckebach W Th, Krätschmer M, Klappenberger F, Schomburg E, Winnerl S, Knippels G M H and van der Meer A F G 2000 Differential electronic gating: a method to measure the shape of short THz pulses with a poorly defined trigger signal *Appl. Phys. Lett.* **77** 1762

[291] Hovenier J N, de Kleijn R M, Klaassen T O, Wenckebach W Th, Chamberlin D R, Bründermann E and Haller E E 2000 Mode-locked operation of the copper-doped germanium terahertz laser *Appl. Phys. Lett.* **77** 3155

[292] Klappenberger F, Ignatov A A, Winnerl S, Schomburg E, Wegscheider W, Renk K F and Bichler M 2001 Broadband semiconductor superlattice detector for THz radiation *Appl. Phys. Lett.* **78** 1673

[293] Schomburg E *et al* 2000 Miniband transport in a GaAs/AlAs superlattice with submonolayer barriers in a static and THz electric field *Physica* E (*Amsterdam*) **7** 814

[294] Winnerl S *et al* 2000 Frequency doubling and tripling of terahertz radiation in a GaAs/AlAs superlattice due to frequency modulation of Bloch oscillations *Appl. Phys. Lett.* **77** 1259

[295] Ignatov A A, Klappenberger F, Schomburg E and Renk K F 2002 Detection of THz radiation with semiconductor superlattices at polar-optic phonon frequencies *J. Appl. Phys.* **91** 1281

[296] Gravé I, Shakouri A, Kuze N and Yariv A 1992 Voltage-controlled tunable GaAs/AlGaAs multistack quantum well infrared detector *Appl. Phys. Lett.* **60** 2362

[297] Shakouri A, Gravé I, Xu Y, Ghaffari A and Yariv A 1993 Control of electric field domain formation in multiquantum well structures *Appl. Phys. Lett.* **63** 1101

[298] Xu Y J, Shakouri A and Yariv A 1995 Quantum interference effect and electric field domain formation in quantum well infrared photodetectors *Appl. Phys. Lett.* **66** 3307

[299] Gravé I and An S 1998 Switching and control of electric field configurations along multi-quantum well structures *Pure Appl. Opt.* **7** 409

[300] Faist J, Capasso F, Sivco D L, Sirtori C, Hutchinson A L and Cho A Y 1994 Quantum cascade laser *Science* **264** 553

[301] Gmachl C, Capasso F, Sivco D L and Cho A Y 2001 Recent progress in quantum cascade lasers and applications *Rep. Prog. Phys.* **64** 1533

[302] Ohtsuka T, Schrottke L, Hey R, Kostial H and Grahn H T 2003 Investigation of carrier transport and carrier distribution in GaAs/(Al, Ga)As quantum-cascade structures *J. Appl. Phys.* **94** 2192